



Pb(Yb $\frac{1}{2}$ Nb $\frac{1}{2}$)O -PbTiO : a model solid solution for the study of the different polar orders

Charlotte Cochard

► To cite this version:

Charlotte Cochard. Pb(Yb $\frac{1}{2}$ Nb $\frac{1}{2}$)O -PbTiO : a model solid solution for the study of the different polar orders. Other. Ecole Centrale Paris, 2015. English. NNT : 2015ECAP0027 . tel-01187385

HAL Id: tel-01187385

<https://theses.hal.science/tel-01187385>

Submitted on 26 Aug 2015

HAL is a multi-disciplinary open access archive for the deposit and dissemination of scientific research documents, whether they are published or not. The documents may come from teaching and research institutions in France or abroad, or from public or private research centers.

L'archive ouverte pluridisciplinaire **HAL**, est destinée au dépôt et à la diffusion de documents scientifiques de niveau recherche, publiés ou non, émanant des établissements d'enseignement et de recherche français ou étrangers, des laboratoires publics ou privés.



CentraleSupélec

THÈSE

présentée par

Charlotte COCHARD

Pour l'obtention du

GRADE DE DOCTEUR

Spécialité : Sciences des Matériaux

Laboratoire d'accueil : Structures, Propriétés et Modélisation des Solides

SUJET:

**$\text{Pb}(\text{Yb}_{1/2}\text{Nb}_{1/2})\text{O}_3\text{-PbTiO}_3$:
a Model Solid Solution for the Study of
the Different Polar Orders**

Soutenue le : 16 avril 2015

devant un jury composé de :

Dragan Damjanovic
Benoit Froelich
Orland Guedes
Torsten Granzow
Pierre-Eymeric Janolin
Marc Lethieq
Martin Lüling

Rapporteur
Examineur
Co-encadrant de Thèse
Rapporteur
Directeur de Thèse
Examineur
Examineur

2015ECAP0027

REMERCIEMENTS

Je tiens, tout d'abord, à remercier les membres de mon jury de thèse et en particulier, Dragan Damjanovic et Torsten Granzow pour avoir accepté d'être les rapporteurs de mon travail de thèse. Leurs remarques sur mon travail m'ont permis d'indéniablement améliorer la qualité de mon manuscrit ainsi que ma compréhension des différents phénomènes. Je les remercie donc pour leur travail et leurs remarques très pertinentes.

Merci aussi à Marc Lethiecq d'avoir accepté dans des délais très courts de présider mon jury de thèse.

Je remercie aussi Martin Lüling et Benoit Froelich pour avoir accepté de faire partie de mon jury de thèse et de m'avoir fait confiance pour mener à bien ce projet. Je souhaite, d'autre part, remercier Martin Lüling et Kenneth Liang pour la relecture de mon manuscrit de thèse.

Je remercie aussi mes deux encadrants Pierre-Eymeric Janolin et Orland Guedes pour l'intérêt qu'ils ont porté à ma thèse tout au long de ces trois ans (et demi). Je remercie, en particulier, Pierre-Eymeric Janolin pour sa présence, ses conseils et son soutien inconditionnel. Et je le remercie aussi chaleureusement d'avoir supporté mon besoin de clarifier les choses et d'avoir réussi à limiter mon envie de faire toujours plus de manip'.

Ce travail de thèse a été réalisé au laboratoire SPMS de l'École Centrale Paris et je tiens à remercier Jean-Michel Kiat, puis par la suite Guilhem Dezanneau, de m'avoir accueillie au sein du laboratoire. Je remercie aussi Jean-Michel Kiat de ses conseils avisés qui m'ont permis d'acquérir les connaissances nécessaires à la compréhension et la détermination de la structure. Je remercie Ingrid Cañero-Infante pour son énergie et les expériences réalisées ensemble.

Ici, je souhaite aussi signaler à Brahim Dkhil que "non, le café n'est pas prêt".

Je tiens à remercier sincèrement Michel Gramond sans qui je n'aurais pu réaliser les mesures électriques si importantes dans mon travail de thèse et à Xavier Bril qui a pris la relève après le départ de Michel.

Sans l'aide de Fabienne Karolak et Chrsitine Bogicevic, je n'aurais jamais pu préparer les échantillons nécessaires à ma thèse et qui ont donc rendu possible mon travail (car sans échantillons, on ne fait pas grand chose...). Je les remercie donc d'avoir pris le temps de m'apprendre la préparation de céramiques.

Je remercie aussi vivement Nicolas Guiblin pour ses explications sur la diffraction et en particulier sur la technique d'affinement Rietveld, mais aussi pour les conseils en mécanique auto. Je remercie aussi ses bras droits, Christopher Luneau et Hubert Jubeau, pour l'avoir admirablement

secondé.

Je voudrais dire un grand merci à Christine Vinée-Jacquin de tous ses conseils éclairés (professionnels ou personnels). Merci aussi à Pascale Gemeiner pour les mesures Raman faites sur mes échantillons et toutes les informations très importantes qu'elle m'a donnée dans le couloir...

Je remercie aussi Pascale Salvini, Claire Roussel, Gilles Boemare, Thierry Martin, Jean-Michel Gillet, Guilhem Dezanneau, Pierre Becker, Sandrine Geiger, Igor Kornev et Agnès Benard d'avoir assuré le bon déroulement de cette thèse en glissant de petits mots gentils au café ou au détour d'un couloir.

Je tiens aussi à remercier Doru Lupascu de m'avoir accueillie quelques jours dans son laboratoire de Essen (Allemagne) et Vladimir Shvarstmann pour les mesures de PFM et les discussions sur les relaxeurs.

Je remercie aussi Nour-Eddine Ghermani pour m'avoir aidée (pour avoir fait) des mesures de diffraction sur monocristal.

Un grand merci à Hichem Dammak de m'avoir éclairée sur les mesures piézoélectriques et d'avoir pris le temps de répondre à toutes mes questions.

Je souhaite remercier Hana Uršič et Tadej Rojac du Jozef Stefan Institute (Slovénie) et Jani Peräntue de l'université d'Oulu (Finlande) pour la synthèse de couches épaisses. De l'université d'Oulu, je remercie aussi Marina Tyunina pour ses conseils sur l'interprétation de mes mesures électriques et les discussions que nous avons pu avoir sur les relaxeurs.

Je souhaite dire merci à Florence Porchet du Laboratoire Léon Brillouin, à Yves Watier de l'European Synchrotron Research Facility, à Emmanuelle Suard de l'Institut Laue Langevin et à Lluís López Conesa du Laboratory of Electron Nanoscopies pour toutes les mesures de diffraction.

Je pense évidemment à tous mes compagnons de labeur qui ont partagé ou non mon bureau pour m'avoir supportée tout ce temps sans se plaindre (ou alors pas à moi...): Yang Hu, Mickaël Anoufa, Yang Liu, Alistar Ottochian, Clement Gilles, Marie Benoit, Xiaofei Bai, Gentien Thorner, Desire Ciria, Cintia Hartmann, Fabien Briec, Bertrand Clair et Mohammed Ben Assine.

Je remercie plus particulièrement Charles Paillard pour l'incompréhension de nos conversations et Anastasia Iakovleva pour les sorties culturelles.

Un grand merci aussi à Romain Faye de m'avoir encouragée dans ma pratique sportive et de m'avoir supportée dans nos (longs) week-ends touristiques.

Bien entendu, Camille Rabache (devenue Exare après la fin de ma thèse, elle reste donc Rabache ici) pour tous les fous rires (qu'Ingrid qualifie de "résonance") et son soutien inébranlable dans les moments difficiles comme dans les plus joyeux.

D'un point de vue personnel, je voudrais remercier l'auto-proclamé "génial" Tobias Rödel pour le soutien moral et logistique apporté tout au long de la thèse et en particulier lors de la rédaction.

Au moment de conclure, une pensée me vient pour ma famille qui s'est déplacé en nombre pour ma soutenance (mais je pense aussi aux autres membres de ma famille qui n'ont pas pu faire le déplacement) et m'a soutenue pendant ces trois ans.

CONTENTS

1	Literature Review	15
1.1	Macroscopic properties	16
1.1.1	Piezoelectricity	16
1.1.2	Ferroelectricity	18
1.1.3	Antiferroelectricity	19
1.1.4	Relaxors	19
1.1.5	Applications	23
1.2	Perovskite structure	25
1.2.1	Chemical Ordering in Perovskites	27
1.2.2	Effect of Chemical Ordering on the Macroscopic Properties	32
1.3	High-Temperature Piezoelectric Materials	35
1.4	$\text{Pb}(\text{Yb}_{1/2}\text{Nb}_{1/2})\text{O}_3\text{-PbTiO}_3$ (PYN-PT)	37
1.4.1	$\text{Pb}(\text{Yb}_{1/2}\text{Nb}_{1/2})\text{O}_3$ (PYN)	37
1.4.2	The Solid-Solution $(1-x)\text{Pb}(\text{Yb}_{1/2}\text{Nb}_{1/2})\text{O}_3\text{-}x\text{PbTiO}_3$	46
1.4.3	System Similar to $(1-x)\text{PYN-}x\text{PT}$: $\text{Pb}(\text{Yb}_{1/2}\text{Ta}_{1/2})\text{O}_3\text{-PbTiO}_3$	48
2	Properties	53
2.1	Introduction	54
2.1.1	Ferroelectrics	54
2.1.2	Relaxors	56
2.1.3	Antiferroelectrics	57
2.1.4	Use of the derivative of the inverse of the dielectric constant	59
2.2	Dielectric Measurements	60
2.2.1	Influence of composition	61
2.2.2	Influence of frequency	64
2.2.3	Conclusion about dielectric measurements	67
2.3	Influence of Large Electric-Field on the Polarization and Strain at Room-Temperature	68
2.4	Phase Transitions	69
2.4.1	AFE	71
2.4.2	Relaxors	75
2.4.3	FE	91

2.5	Summary and Conclusion on the phase diagram	92
3	Structure	97
3.1	Structural features related to different polar orders	98
3.1.1	Ferroelectrics	98
3.1.2	Antiferroelectrics	99
3.1.3	Relaxors	102
3.1.4	Superstructure Reflections	103
3.2	Methodology	104
3.2.1	Experimental Conditions	104
3.2.2	Rietveld refinement	105
3.2.3	Single peak fitting	106
3.3	Overview of the PYN-PT structure	107
3.3.1	Distortions	107
3.3.2	Presence and type of SSRs	113
3.3.3	Quantification of the chemical order on the B-site	114
3.3.4	Positional disorder on the A-site	121
3.3.5	New knowledge about the structure in the PYN-PT solid solution	127
3.4	Room Temperature Structures for $(1-x)$ PYN- x PT	129
3.4.1	Structure with SSRs due to antiparallel displacements: $x = 0-0.10$	129
3.4.2	Structure with small distortions: $x = 0.16-0.30$	139
3.4.3	Structure with large distortions: $x = 0.35-0.60$	146
3.4.4	O-Octahedra Tilting for $x = 0.30$ and $x = 0.40$	153
3.4.5	Summary and conclusion	155
3.5	Phase transitions	158
3.5.1	Structure with SSRs due to antiparallel displacements: $x = 0-0.10$	158
3.5.2	Structure with low distortions: $x = 0.16-0.30$	162
3.5.3	Structure with strong distortions: with $x = 0.35-0.60$	165
3.6	Summary and Conclusion on the phase diagram	168
4	Structure-Properties Relationship	173
4.1	Phase diagrams proposed from properties and structural investigations	174
4.1.1	Phase diagram proposed from properties measurements	174
4.1.2	Phase diagram proposed from structural investigations	176
4.2	Putting in perspective	177
4.3	Understanding of the phase diagram of PYN-PT	179
4.3.1	Evolution of the structure at room temperature	182
4.3.2	Thermal evolution of the structure and properties	187
4.3.3	Summary and Conclusion	192
5	Applications	195
5.1	Introduction	196
5.2	Evolution of the piezoelectric properties with temperature	199
5.2.1	Measurement techniques	199

5.2.2	Results and Discussion	205
5.3	Applications of PYN-PT	210
5.3.1	Piezoelectric applications	210
5.3.2	Electrostriction	213
5.3.3	Ferroelectric Memory devices	217
5.4	Further Improvement of the Material	218
5.5	Conclusion	221
6	Summary and unified phase diagram	223
A	Influence of the processing method on the $\text{Pb}(\text{Yb}_{1/2}\text{Nb}_{1/2})\text{O}_3\text{-PbTiO}_3$ solid solution	237
A.1	Introduction	237
A.2	Experimental procedure	238
A.2.1	Solid-State reaction	238
A.2.2	Mechanosynthesis	238
A.2.3	Reactive sintering	239
A.2.4	Characterization methods	239
A.3	Results and discussion	239
A.3.1	Chemical reaction mechanism	239
A.3.2	Influence of powder processing method on dielectric properties	240
A.3.3	Influence of microstructure and grain size on dielectric properties	242
A.4	Conclusion	244
B	Calculation of the derivative of the inverse of the dielectric constant: ξ	248
C	Refined parameters for compositions in the range $0.40 \leq x \leq 0.60$	249

INTRODUCTION

Piezoelectric materials have attracted a lot of attention due to the versatility of its potential applications. The present work has been done with the participation of Schlumberger, major actor in the worldwide Oil and Gas industry, which is extensively using piezoelectric materials in a very wide variety of tools: pulse echo ultrasonic transducers, hydrophones and geophones for seismic applications, mechanical actuators, acoustic sensors, etc. Most of these tools are using commercial $\text{Pb}(\text{Zr,Ti})\text{O}_3$ (PZT) materials with a Curie temperature above 300 °C, since most of the mission profiles are requiring temperatures up to 200 °C. A step forward the improvement of the piezoelectric properties was, first, considered by using single crystals based on $\text{Pb}(\text{Mg}_{1/3}\text{Nb}_{2/3})\text{O}_3\text{-PbTiO}_3$ (PMN-PT). The distinct improvement of the piezoelectric properties were obtained using PMN-PT single crystals, however the limit in its usage for temperatures above 100 °C excludes the use of this material in most of Schlumberger's applications. Therefore, materials combining high-operating temperature and high-piezoelectric properties appeared necessary.

Based on an extended literature survey of high-temperature piezoelectrics (Sec.1.3), the perovskite solid solution $(1-x)\text{Pb}(\text{Yb}_{1/2}\text{Nb}_{1/2})\text{O}_3\text{-}x\text{PbTiO}_3$ (PYN-PT) appears to present the best temperature-properties compromise for the targeted application. Thus, this PhD thesis aims at processing ceramic samples of various compositions in that solid solution and at characterizing their piezoelectric and structural properties to assess the applicative potential of this material.

To this end, twelve compositions throughout the PYN-PT solid solutions were prepared using a specially developed processing method: mechanosynthesis. This processing method had never been used for PYN-PT despite having been already used to prepare other Pb-based complex perovskites (such as $\text{Pb}(\text{Zr,Ti})\text{O}_3$ or $\text{Pb}(\text{Mg}_{1/3}\text{Nb}_{2/3})\text{O}_3\text{-PbTiO}_3$) and is commonly used in industrial production of piezoelectric powders. The details of the original synthesis route has been the object of an article submitted and reproduced in Appendix A.

The dielectric and piezoelectric responses of these compositions as a function of temperature are examined in Chapter 2. On the other hand, the thermal evolution of the various structures present in the phase diagram are investigated in Chapter 3. These two studies of the solid solution from a property and structural points of view will enable us to propose two phase diagrams accounting for the evolution of the polar orders and structure as a function of composition and

temperature.

These two phase diagrams will be compared and put in perspectives in Chapter 4. In this chapter, a model explaining the link between the structure and properties and its evolution within the PYN-PT solid solution will be proposed.

Finally, the understanding of the solid solution gained in these chapters will lead us to discuss the potential applications of the PYN-PT solid solution (Chapter 5).

- CHAPTER 1 -

LITERATURE REVIEW

The perovskite solid solution $\text{Pb}(\text{Yb}_{1/2}\text{Nb}_{1/2})\text{O}_3\text{-PbTiO}_3$ (PYN-PT) presents the peculiarity of exhibiting all polar orders at room temperature: antiferroelectricity, relaxor and ferroelectricity. Therefore, before turning to the study of the phase diagram of $\text{Pb}(\text{Yb}_{1/2}\text{Nb}_{1/2})\text{O}_3\text{-PbTiO}_3$ (PYN-PT), the various polar orders will be introduced in Sec.1.1.

PYN-PT also exhibits chemical order on the B site of the perovskite. Hence, after presenting some of the structural features of the perovskite structure (Sec.1.2), chemical ordering on the B site will be discussed, as well as methods to quantify the chemical ordering in double perovskites and their solid solutions. The influence of the chemical order on the macroscopic properties will also be examined.

In Sec.1.3, the evolution of the piezoelectric properties as a function of the Curie temperature will be examined. This will enable to explain the choice of the PYN-PT solid solution as high-piezoelectric high-temperature material.

Finally, the literature on the PYN-PT solid solution will be introduced (Sec.1.4). The polar orders and structures proposed for the various compositions will be the starting point of my examination of the PYN-PT solid solution.

1.1 MACROSCOPIC PROPERTIES

1.1.1 Piezoelectricity

For ordinary solids, a moderate stress causes a proportional strain related by the elastic modulus [1]. In *piezoelectric* materials, the application of a stress not only leads to strain in the material but also to the creation of electric charges directly proportional to the force. Conversely an applied electric field produces a proportional strain in piezoelectric materials. The proportionality between stress and charges and between electric field and strain is described by the piezoelectric coefficient d such as

$$\text{direct piezoelectric effect} \quad D = Q/A = d \cdot T$$

$$\text{converse piezoelectric effect} \quad S = d \cdot E$$

Where D is the dielectric displacement (charge Q per unit area A), T is the stress, S is the strain and E is the electric field. For both direct and converse effects, the piezoelectric constant d is identical.

Several piezoelectric coefficients, namely d , g , e , h , can be defined depending on the boundary conditions: short/open-circuit, free/clamped samples.

Microscopically, piezoelectricity can be described using a simple one-dimensional spring model of the crystal lattice. When an electric field is applied in one direction (to the right in Fig.1.1(a)) cations are displaced along the electric field whereas anions are displaced in the opposite direc-

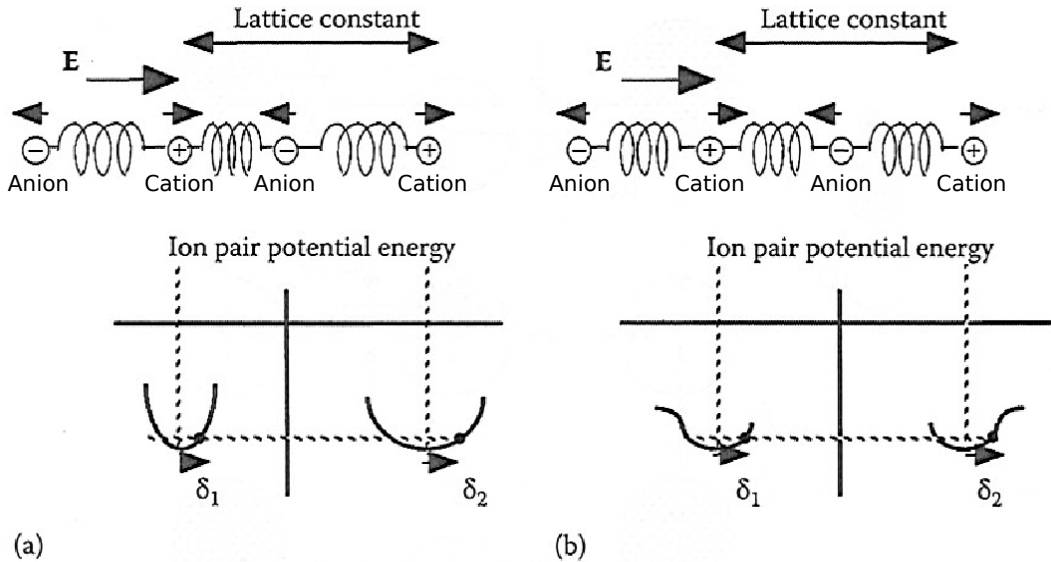


Figure 1.1: Microscopic explanation of the (a) piezoelectric strain and (b) electrostriction. Adapted from [2]

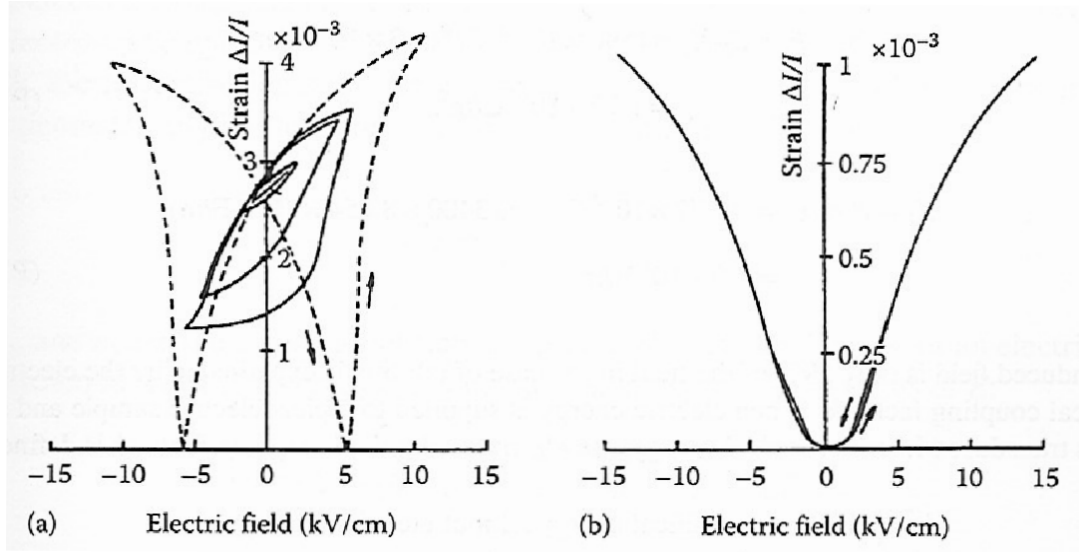


Figure 1.2: Typical strain-electric field curves for piezoelectric (a) and electrostrictive (b) ceramics [2]

tion. If, between ions, hard and soft springs exist alternatively, then the ionic displacements lead to relative changes in the interionic distance and therefore to strain. On the contrary, no strain is generated if the springs are all identical since the displacements of the cations and anions compensate each other leading to no change in the interionic distance. Hence, in this simple one-dimensional model, piezoelectricity requires the existence of hard and soft springs. In three dimensions, this means that the piezoelectric crystals must be noncentrosymmetric.

This simple model assumes that the springs mimicking the bonds between ions are perfectly harmonic. However springs possess anharmonicity (bottom of Fig.1.1(b)), that is they are somewhat easier to extend than to contract [2]. Such subtle difference in the displacements causes a change in the interionic distance, i.e. produces a strain which is independent of the direction of application of the electric field (+E/left or -E/right) and hence is an even function of the electric field (see Fig.1.2(b)). This is the *electrostrictive* effect and can be expressed by rewriting the strain-electric field relation as

$$S = \underbrace{d \cdot E}_{\text{piezoelectricity}} + \underbrace{M \cdot E^2}_{\text{electrostriction}} \quad (1.1)$$

Since electrostriction only derives from anharmonicity of the springs, having non-centrosymmetric crystals is not necessary for its manifestation. For materials with strong piezoelectric coefficient the effect of electrostriction in the strain-electric field relation can be neglected (see Fig.1.2(a)). Electrostriction is commonly used for actuators, but not as much as piezoelectric materials for sensors because a bias must be applied to get a strong response.

In the general case, the electric field/strain and stress/dielectric displacement relationship de-

pend on the orientation of the crystal. The previous relation (1.1) then becomes

$$S_{jk} = \sum_i d_{ijk} \cdot E_i + \sum_{i,j} M_{ijkl} \cdot E_i E_j$$

where the piezoelectric coefficient d_{ijk} and the electrostrictive coefficient M_{ijkl} are third and forth rank tensor respectively.

or when the electrostriction is neglected: $S_{jk} = d_{ijk} \cdot E_i$ using the Einstein summation convention.

To facilitate the reading of these coefficients the Voigt notation is commonly used. In this notation the second and third suffixes are replaced by a single suffix, as follows

Tensor notation	11	22	33	23,32	31,13	12,21
Matrix notations	1	2	3	4	5	6

However, when using the suffixes 4, 5 and 6 in the Voigt notation, special care must be taken since the piezoelectric coefficient using the Voigt notation is half of the one using the full notation (see Sec.2.14. in [2] for more details).

Because of crystal symmetry, the piezoelectric crystal matrix and the electrostrictive crystal matrix can be simplified: some coefficients are zero and some are equals (see for example Table 2.1 and Table 2.2 in Ref.[2]).

In ceramics, grains are randomly distributed and, in practice, the only indices used to describe the piezoelectric coefficients are 33, 31 and 15. For example, in ceramics, d_{33} refers to the piezoelectric coefficient in which the strain, the electric-field and the polarization directions are parallel, d_{31} refers to the piezoelectric coefficient in which the strain is perpendicular to the electric-field and polarization directions, d_{15} refers to the piezoelectric coefficient in which the strain, the electric-field and the polarization are all orthogonal. Thus, the indices refer more to macroscopic directions rather than to crystallographic directions.

1.1.2 Ferroelectricity

If we consider the 32 crystal point groups into which all crystalline material can be divided, 20 of the 21 which lack an inversion center may exhibit piezoelectricity. The 21st, the cubic class 432, although non-centrosymmetric does not allow piezoelectricity.

A further subdivision of the point groups may be made, consisting of the ten point groups which contain a unique polar axis leading to the appearance of an electric dipole moment also called spontaneous polarization. Hence, in materials from such classes, charges can be created not only by stress but also by changes in temperature. Such materials are called *pyroelectric*.

Furthermore, when the spontaneous polarization can be reversed by an applied electric field the material falls into an even narrower subdivision: *ferroelectric* materials. Hence a ferroelectric crystal has at least two directions of spontaneous polarization in the absence of an electric field and the polarization can be reversed from one direction to the other by an electric field.

Piezoelectricity, pyroelectricity and ferroelectricity require the shifting of cations and anions in opposite directions. This shift should be energetically unfavorable [2] and when the temperature is high enough the unit cell transforms into a centrosymmetric phase: the *paraelectric* phase. The critical temperature at which the phase transforms from non-centrosymmetric to centrosymmetric is called the Curie temperature (T_C). This transformation is accompanied by an increase of the properties such as the dielectric constant (ability of a material to store electrical energy compared to the one of vacuum).

1.1.3 Antiferroelectricity

The definition of antiferroelectricity is in general complex since only certain classes of materials have well-defined localized electric dipoles (e.g. hydrogen-bonded antiferroelectrics and antiferroelectric liquid crystals). Hereafter, these materials will not be discussed.

Kittel [3] postulated that an antiferroelectric is a material whose cells show a polar arrangement, but in which adjacent cells are oppositely polarized, giving a zero net polarization. The antiparallel pattern of dipole displacements leads to the appearance of a center of symmetry, so that the unit cell of the antiferroelectric material becomes a multiple of the unit cell without the dipole moments.

In his simple model, Kittel describes the antiferroelectric lattice to be composed of two sublattices with similar atoms and unit cells but with dipole moments directed in opposite directions. In this definition the dielectric constant at the Curie temperature does not need to be large.

Later, Jona and Shirane [4] have further developed the concept of antiferroelectricity by adding that an antiferroelectric crystal is “an antipolar crystal whose free energy is comparable to the one of a polar crystal”. In this case, the value of the dielectric constant at the Curie temperature is directly linked to the closeness in energy of the antipolar and polar crystals.

Later, Rabe [5] interpreted the definition of Jona and Shirane [4] in terms of instabilities of a high-temperature phase. In this case, the antiferroelectric phase can be described by a group of coupled modes with a primary unstable antipolar mode accompanied by other distortions such as oxygen octahedra rotations. A competing polar phase can be driven from the same high-temperature phase by applying an electric field. This polar phase would be generated by a zone-center polar mode that may be accompanied by other modes. The definition by Rabe [5] does not rely on a structural criterion, as almost any non-polar distortion of a high-temperature phase could satisfy the requirement, but on energetic criteria.

1.1.4 Relaxors

Relaxor ferroelectrics (RFE) or relaxors are usually identified on the basis of the evolution of their dielectric constant as a function of temperature and frequency. Indeed, in relaxors, the dielectric constant presents a wide frequency-dependent peak (see for example Fig.1.3(a)) explaining the origins of the first designation of relaxors: “diffuse ferroelectrics”. The difference in the evolution of the dielectric constant with temperature is even more striking when com-

pared to the evolution of classical ferroelectrics (Fig.1.3(d) with no frequency dependence above $T_m = T_c$).

Furthermore, in relaxors, the maximum of the dielectric constant (at the temperature T_m) is not necessarily accompanied by a structural phase transformation whereas in classical ferroelectrics this maximum is always associated with a phase transformation.

Typical relaxor materials are $\text{Pb}^{2+}(\text{Mg}_{1/3}^{2+}\text{Nb}_{2/3}^{5+})\text{O}_3$, $\text{Pb}^{2+}(\text{Sc}_{1/2}^{3+}\text{Nb}_{1/2}^{5+})\text{O}_3$, $\text{Ba}^{2+}(\text{Ti}_{1-x}^{4+}\text{Sn}_x^{4+})\text{O}_3$ or $\text{Pb}_{1-x}^{2+}\text{La}_x^+(\text{Zr}_{1-y}^{4+}\text{Ti}_y^{4+})_{1-x/4}\text{O}_3$.

At high temperature, relaxors exist in a non-polar paraelectric phase which is similar to the paraelectric phase of classical ferroelectrics. Upon cooling, they transform into the ergodic relaxor state (ER in Fig.1.3) at the Burns temperature (T_B) in which polar regions of nanometer scale with randomly distributed directions of dipole moments appear: the polar nanoregions (PNRs). In the ergodic relaxor state, the polar nanoregions are mobile and the system is ergodic (the average over time and space is the same). While cooling, the dielectric constant goes through a maximum at T_m (see Sec.2.1 page 54, for more details), the dynamics of the polar nanoregions decrease and, and at a temperature typically hundred degrees below the Burns temperature, the PNRs become frozen leading to the appearance of a non-ergodic relaxor state. This temperature is called the freezing temperature: T_f .

In the non-ergodic state, the application of a strong-enough electric field transforms the non-ergodic relaxor state into a stable classical ferroelectric one that will, upon heating, transform back into the ergodic state at the Curie temperature, usually close to the freezing temperature. This stable transformation into a classical ferroelectric phase under the application of an electric field is the main difference between a relaxor and a dipolar glass.

Some relaxors do not require the application of an external electric field to transform into a classical ferroelectric state. This transition can be diffuse (Fig.1.3(b)) or sharp (Fig.1.3(c)) and can take place at the maximum of the dielectric constant or at a lower temperature.

The main difference between a material undergoing a relaxor-to-ferroelectric transition at the maximum of the dielectric constant and a classical ferroelectric material is the behavior above the Curie temperature: is the transition a simple paraelectric-ferroelectric transition or does the transition goes through an ergodic relaxor state?

Models proposed for relaxors

Several models have been proposed to explain the behavior of relaxors and all of them assume the existence of polar nanoregions (PNRs).

Some models (usually referred to as Random-Bond models) propose that PNRs result from local transitions or local fluctuations. In these models, the PNRs are entities (islands, regions, etc.) dispersed into a matrix (Fig.1.4(a)). Such models are, for example, the chemical fluctuation model proposed by Smolenskii et al. [7], the superparaelectric model proposed by Cross [8] and the dipolar glass model proposed by Viehland et al. [9].

On the other hand, Westphal et al. [10] proposed that the transition is not local, but occurs in the entire crystal. In this model, the entire crystal is tiled with polar nanodomains (also called PNRs) without any matrix (Fig.1.4(b)). This is the Random-Field model.

This model disagrees with the previously described models on the type of transition leading

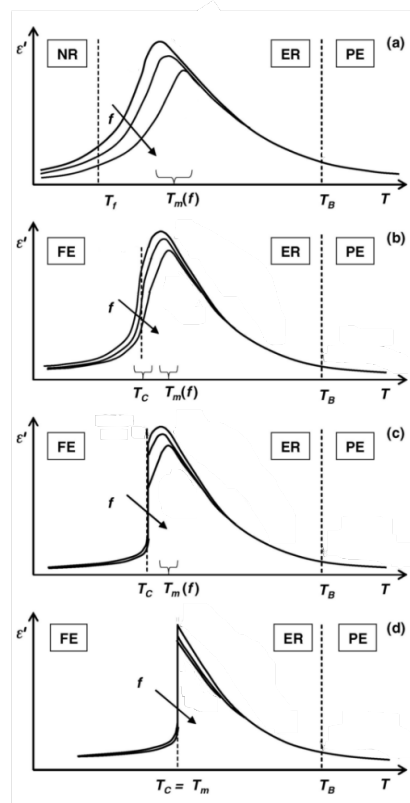


Figure 1.3: Various possibilities for the temperature evolution of structure and dielectric properties in compositionnaly disordered perovskites: (a) canonical relaxor; (b) crystal with a diffuse relaxor-to-ferroelectric phase transition at $T_c < T_m$; (c) crystal with a sharp relaxor-to-ferroelectric phase transition at $T_c < T_m$; (d) crystal with a sharp relaxor-to-ferroelectric phase transition at $T_c = T_m$. The temperature dependencies of the dielectric constant at different frequencies are schematically shown. The type of structure [paraelectric (PE), non-ergodic relaxor (NR), ergodic relaxor (ER), ferroelectric (FE)] are identified. Note the similar behavior at high temperature in all cases. [6]

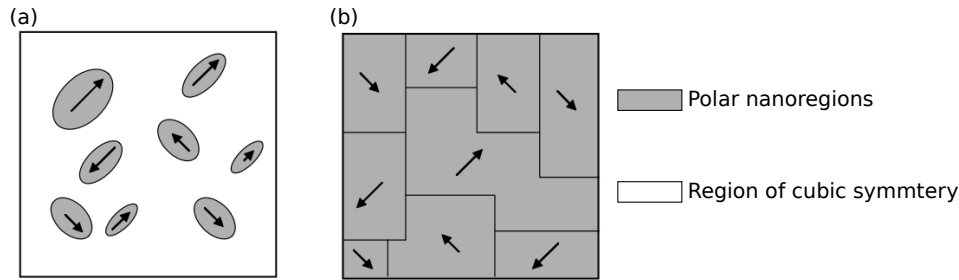


Figure 1.4: Schematic representation of PNRs in relaxors according to different models

to the appearance of the polar nanoregions and therefore on the micro(nano)structure in the non-ergodic phase.

Finally, Pirc et al. [11] proposed the Spherical Random Bond Random Field (SRBRF) model that unifies the Random-Bond and Random-Fields models. This rather complicated model is however extremely powerful since it can reproduce most of relaxor properties. In this model, the chemical inhomogeneities present in the materials are not only responsible for creating random electric field (as in the Random-Field model), but also random elastic constraints. In this case, it is the presence of both electric and elastic fields that leads to the appearance of PNRs.

Local chemical ordering

The first model to be proposed (Smolenskii et al. (1961) [7]) suggested that it is the presence of regions of different chemical compositions that leads to the frequency-dependent dielectric constant because of the different sizes of the regions and to the wide dielectric peak because of the superimposition of several "classical ferroelectric peaks". This model is partially adequate in the sense that later works found regions of local chemical ordering in relaxors, using for example diffuse-scattering experiments. The local chemically ordered regions are composed of double-perovskite cells (described in details in Sec.1.2.1), i.e. neighboring unit cells have different B-cations in their center. This local chemically-ordered regions, that are present up to very high temperature, are dispersed in a matrix of disordered perovskite cells (Fig.1.5).

Below the Burns temperature, a different type of nanoregions appears. This second type of nanoregions has been identified because of a different shape of the diffuse scattering has been observed. This different type of nanoregions is believed to be the polar nanoregions described previously.

The difference above and below the Burns temperature is noticeable when looking at the results of the diffuse scattering measurements (reported in Fig.1.6) carried out on $\text{Pb}(\text{Mg}_{1/3}\text{Nb}_{2/3})\text{O}_3$ crystals for which $T_B \sim 420$ K. At 650 K ($\gg T_B$), the diffuse scattering has a bow-tie shape whereas it has a butterfly shape at 300 K ($\ll T_B$). The butterfly diffuse scattering depends strongly on temperature and appears on cooling at a temperature close to the Burns temperature. This butterfly-shape diffuse scattering is hence associated with polar nanoregions. On the other hand, the bow-tie shape of the diffuse scattering is associated with the presence of local chemical

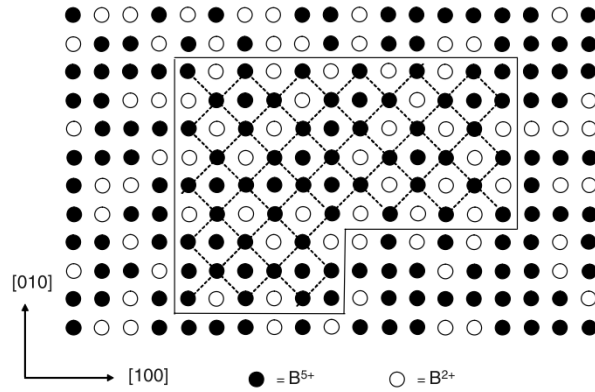


Figure 1.5: Schematic representation of the local chemically ordered regions (the area delimited by the solid line) within the disordered matrix in $\text{Pb}(\text{B}_{1/3}^{2+}\text{B}_{2/3}^{5+})\text{O}_3$ perovskites. One of the two sublattices inside the local chemically ordered regions is formed by B^{5+} ions only. Pb and O ions are not shown. [6]

ordering because this scattering is almost temperature-independent. The difference in shapes and temperature dependence of the diffuse scattering shows that the regions of local chemical order and the polar nanoregions are indeed different entities. But, by producing local strain and electric field, the local chemically-ordered regions are believed to facilitate (if not trigger) the appearance of polar nanoregions.

1.1.5 Applications

Piezoelectric, pyroelectric, antiferroelectric, ferroelectric and relaxors materials are not only interesting because of fundamental issues but also from an application point of view. Many applications use these materials because of the large variety of properties available. Some of the most common applications are listed below

Applications of strain-electric field relationship Piezoelectricity is extensively utilized in the fabrication of various devices such as transducers, sensors, actuators, surface and bulk acoustic wave (SAW and BAW) devices, frequency control, ultrasonic motors and much more. Piezoelectric materials have also gained a lot of interest because of the possible harvesting of the energy produced by vibrations.

Electrostrictive materials have also been used for optical correction instead of piezoelectric materials because of the absence of hysteresis in electrostrictive materials.

Applications of polarization-temperature relationship Pyroelectric materials are commonly used for infrared or temperature sensors.

Heating/cooling devices using the converse effect of pyroelectricity (*electrocaloric* effect) have been developed taking advantage of the change of temperature induced by a change

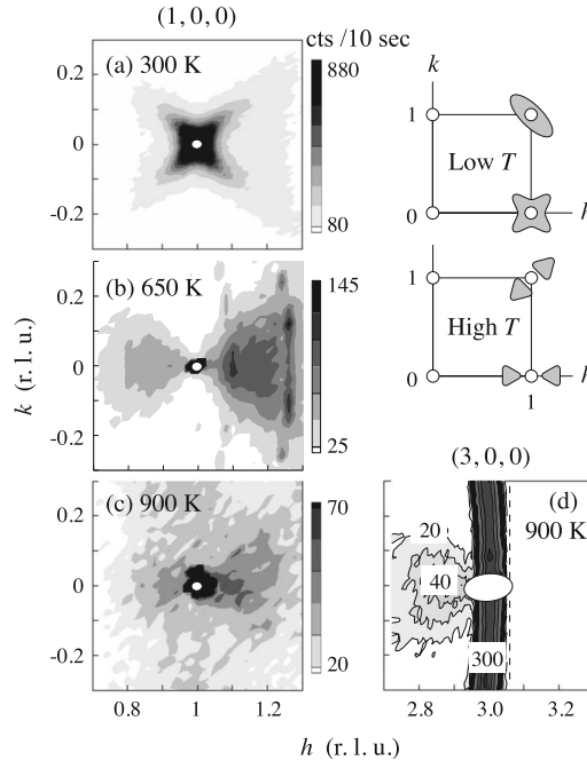


Figure 1.6: Diffuse scattering intensity contours in $\text{Pb}(\text{Mg}_{1/3}\text{Nb}_{2/3})\text{O}_3$ measured near (100) are shown using a linear gray scale at (a) 300 K, (b) 650 K, (c) 900 K. (d) Diffuse scattering intensity contours at 900 K near (300) using thermal neutrons. Schematic diagrams of the diffuse scattering intensity contours are shown in the upper right panel [12].

The bow-tie shape of diffuse scattering that is temperature-independent is associated with local chemical order whereas the butterfly-shape diffuse scattering (300 K) is associated with the presence of polar nanoregions.

of electric-field.

Applications of polarization-electric field relationship Ferroelectric materials are used as memory devices (FeRAMs) because of the possibility to return the polarization by applying an electric field.

Ferroelectric tunnel junctions have been build based on the change of the tunneling effect due to the reversal of the spontaneous polarization in ferroelectrics.

Applications of electric-field induced phase transitions Applications of electric-field induced phase transition have been mainly developed in antiferroelectric materials. Indeed the large volume change associated with phase transition is used for actuators with great displacements. The phase transition can also be used to store electric energy.

Other applications Because of their extremely large dielectric constant and low temperature-dependence, relaxors are often used in supercapacitors especially in the context of miniaturization.

Thermistors using the positive temperature coefficient of resistivity effect present in some ferroelectrics have been developed.

The electro-optic effect (change of the absorption and/or refractive index by an electric field), in particular the Pockels effect, observed in relaxors show promising applications such as light valves, beam deflectors and optical displays for optical communications in conjunction with solid-state laser chips and optical fibers.

Applications have also driven research on piezoelectric, pyroelectric, antiferroelectric, ferroelectric and relaxor materials. In particular, applications have motivated studies focusing on the size effect in all these materials and on the effect of doping. Moreover, to fit as closely as possible to the needs, novel material geometries have been developed: multilayers, single crystals, composites, films and so on.

Some of the potential applications of PYN-PT will be discussed in Chapter 5 with a particular interest on the application of strain-electric field relationship (piezoelectricity and electrostriction).

1.2 PEROVSKITE STRUCTURE

The most common structure for piezoelectric, ferroelectric, antiferroelectric and relaxors materials is the perovskite structure with the general formula ABX_3 where A and B are cations and X is an anion typically oxygen (but can also be fluorine). The ideal perovskite cell is cubic with A-cations on the corners of the cube, B-cations in the center, and X-anions in the center of the faces creating an octahedron around the B-site (Fig.1.7). The perovskite unit cell can also be described by shifting the origin of the cell so that the B cations are situated on the corners of the cube.

The perovskite structure has been extensively studied because of its versatility: the structure is stable for a lot of different chemical elements on the A-, B- or X-sites, hence allowing a lot of

different macroscopic properties to appear. The stability of the structure is usually described by the Goldschmidt factor t :

$$t = \frac{r_A + r_X}{\sqrt{2}(r_B + r_X)} \quad \text{where } r \text{ are the different ionic radii}$$

The Goldschmidt factor describes the facility of a chemical compound ABX_3 to form into the perovskite structure: if $t = 1$, the ionic radii are such that the structure filling the most space is the perovskite structure. When t deviates from 1, the structure becomes less and less stable. In this case, the perovskite structure can become distorted or may not be stabilized at all and the chemical compound will form in a different structure.

When the perovskite structure is distorted, there is a temperature for which the thermal vibrations of the atoms are so large that it becomes energetically favorable for the structure to transform into a cubic cell. This temperature is the Curie temperature (the same Curie temperature as the one introduced in the context of ferroelectricity). For some material, the Curie temperature is not experimentally observed because the decomposition temperature of the perovskite is lower than the Curie temperature.

As aforementioned the perovskite structure can accommodate many different cations on the various sites leading to different macroscopic properties. In the following, we will focus mainly on complex Pb-based perovskites, i.e. materials with the chemical formula $Pb(B', B'')O_3$ where B' and B'' may be cations of different valences. The effect of the type of B cations on the perovskite structure, on the chemical ordering and on the macroscopic properties is discussed in Sec.1.2.1.

Morphotropic Phase Boundary: MPB

To combine the advantages of different perovskite materials, solid solutions have been investigated. The study of such solid solutions have lead to the discovery of a compositional range over which the properties are enhanced: the morphotropic phase boundary (MPB).

The first morphotropic phase boundary was discovered, in 1951 [1], in $PbZrO_3$ - $PbTiO_3$ (PZT) solid solution. This phase boundary between the rhombohedral and tetragonal phases in the PZT solid solutions was named "morphotropic" in reference to alloys because of its (nearly)

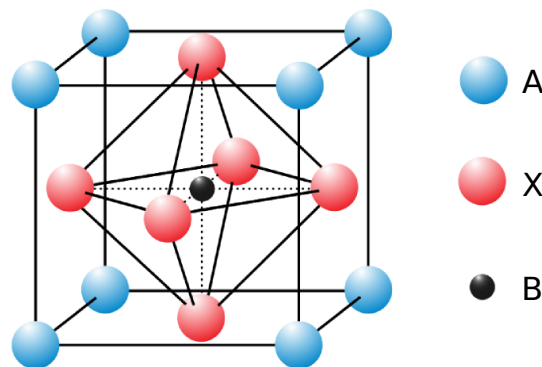


Figure 1.7: Schematic representation of the perovskite unit cell.

temperature independence.

At the morphotropic phase boundary, in addition to a change in the crystallographic structure, a large enhancement of the dielectric constant and of the electromechanical coupling coefficient was found. Therefore, compositions in other solid solutions that were later found to present an enhancement of the dielectric and piezoelectric properties at the frontier between a rhombohedral and tetragonal phase were named morphotropic phase boundary in reference to the PZT solid solution (even though some of these phase boundaries are not so temperature-independent). Morphotropic phase boundaries were discovered in relaxor-lead titanate solid solutions (e.g. $\text{Pb}(\text{Mg}_{1/3}\text{Nb}_{2/3})\text{O}_3$ - PbTiO_3 , $\text{Pb}(\text{Zn}_{1/3}\text{Nb}_{2/3})\text{O}_3$ - PbTiO_3 or $\text{Pb}(\text{Sc}_{1/2}\text{Nb}_{1/2})\text{O}_3$ - PbTiO_3). Relaxors- PbTiO_3 solid solutions have attracted a considerable amount of interest because their morphotropic phase boundaries present dielectric and piezoelectric properties even higher than the ones of PZT. Presently MPBs are investigated in many systems including lead-free solid solutions (e.g. $(\text{Bi}_{1/2}\text{Na}_{1/2})\text{TiO}_3$ - NaNbO_3) and ternary solid-solutions (e.g. $\text{Pb}(\text{Mg}_{1/3}\text{Nb}_{2/3})\text{O}_3$ - PbTiO_3 - PbZrO_3).

For a long time the enhancement of the properties had been thought to come from the co-existence or frustration of the two structures existing on either side of the morphotropic phase boundary. In 1999, the discovery of a monoclinic phase in the morphotropic phase boundary of PZT [13] (followed by its discovery in other Pb-based solid solutions such as $\text{Pb}(\text{Mg}_{1/3}\text{Nb}_{2/3})\text{O}_3$ - PbTiO_3 [14] or $\text{Pb}(\text{Sc}_{1/2}\text{Nb}_{1/2})\text{O}_3$ - PbTiO_3 [15]) gave new keys to understand the enhancement of the properties in this compositional range. Indeed this monoclinic phase is characterized by a symmetry plane ((011) in Cm case) which does not constrain the polarization along a fixed direction but rather allows an easy rotation path between the [111] and the [001] axes, i.e. the direction of the polarization in the rhombohedral and tetragonal phases, respectively (Fig.1.8). The monoclinic phase existing at the morphotropic phase boundary has also been proposed to be an “adaptive” phase between the different symmetries, rhombohedral or tetragonal. This new understanding of the properties based on a structural features illustrates well the intrinsic structure/properties relation.

1.2.1 Chemical Ordering in Perovskites

Perovskite structure $\text{A}(\text{B}'_{1/2}\text{B}''_{1/2})\text{O}_3$ can present three different B-cations arrangements: random, rock-salt and layered (Fig.1.9).

In the random case, B' and B'' cations are randomly distributed on the B-site which means that the type of cation on one site is not influenced by the type of cation on neighboring sites. In the rock-salt arrangement, cations are of different chemical nature on neighboring sites, hence the chemical formula becomes $\text{A}_2(\text{B}'\text{B}'')\text{O}_6$ and these compounds are usually referred to as double perovskites. In the layered arrangement, within one plane (the (001) plane) all sites are occupied by the same cation whereas in neighboring planes the B cations are different. Only one compound is known to present a layered structure: $\text{La}(\text{Cu}_{1/2}\text{Sn}_{1/2})\text{O}_3$.¹

¹Another type of chemical arrangement can be imagined: columns of one type of B site cations with different cations on neighboring sites within one plane, i.e. a layered arrangement with layers of (110) planes. Such

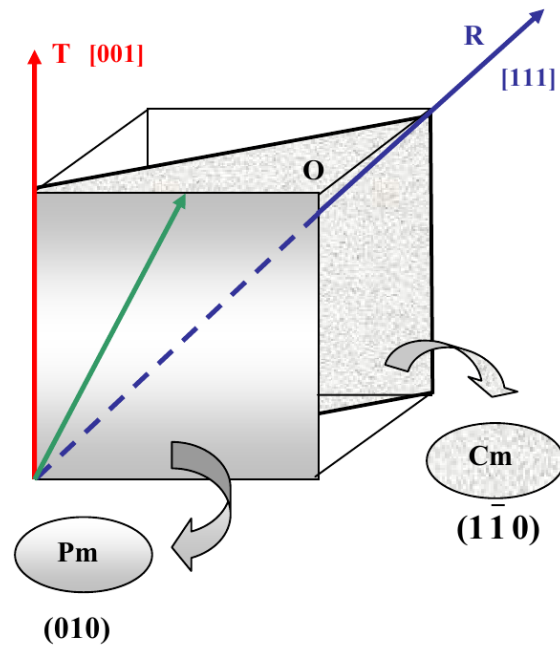


Figure 1.8: Schematic representation of the polarization direction in tetragonal (T), rhombohedral (R) and monoclinic (Pm and Cm) phases [16]. The polarization is directed along the $[001]$ axis in the tetragonal structure and along the $[111]$ axis in the rhombohedral structure. In the two monoclinic structures (Pm and Cm) the polarization lies into planes (010) and $(1\bar{1}0)$, respectively) and the polarization can rotate freely within these planes. Hence the monoclinic phases are a structural bridge between the rhombohedral and tetragonal phases for which the polarization is constrained into one direction ($[111]$ and $[001]$ respectively).

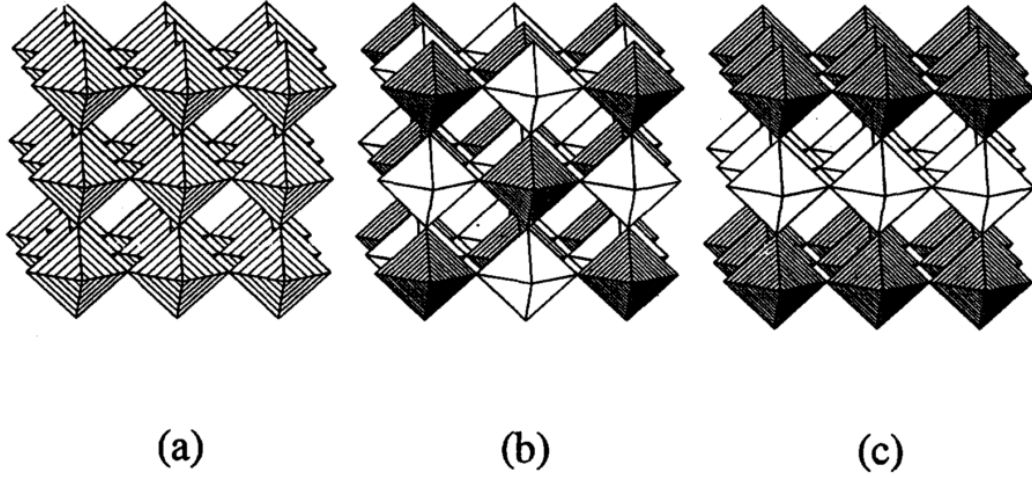


Figure 1.9: Representation of the different B-cations arrangements [17]. The different B-site elements are represented by O-octahedra of different colors.
 (a) random (b) rock-salt (c) layered

The various B cations arrangements can be discriminated unambiguously based on the presence of different superlattice reflections.

Since the layered arrangements is particular to $\text{La}(\text{Cu}_{1/2}\text{Sn}_{1/2})\text{O}_3$, we will, in the following, focus only on the random and rock-salt arrangements.

1.2.1.1 Quantification of Chemical Ordering

Double Perovskites

As in all but one double perovskites, B-site cations arrange randomly or with a rock-salt order, these two states are referred to in the literature as disordered and ordered. Accordingly, the degree of ordering s in a perovskite is the percentage of the material presenting a rock-salt arrangement.

In practice, the degree of ordering is calculated using the intensity of superstructure reflections (I_{SSR}) associated with chemical order (e.g. $(h/2 \ h/2 \ h/2)$) normalized by the intensity of a Bragg reflection (I_{Bragg}) applying the following formula

$$s^2 = \frac{\left(\frac{I_{SSR}}{I_{Bragg}}\right)_{meas}}{\left(\frac{I_{SSR}}{I_{Bragg}}\right)_{s=1}} \quad (1.2)$$

where $\left(\frac{I_{SSR}}{I_{Bragg}}\right)_{s=1}$ is the value calculated for a perfectly ordered material.

arrangement has never been observed.

Solid Solutions

Solid solutions in which one of its end-member is a double perovskite (mainly $\text{Pb}_2(\text{B}'\text{B}'')\text{O}_6$ - PbTiO_3) have been theoretically predicted to present rock-salt chemical ordering [18] and this chemical ordering has indeed been observed experimentally [19–21]. However, to our knowledge, no attempt at characterizing the degree of chemical ordering in these solid solutions has been carried out.

Starting from the double perovskite, the addition of a third atom on the B site offers several ordering possibilities. One such possibility is that the third atom destroys the order of the double perovskite, resulting in a single perovskite structure with completely random occupancies of the B site by the three B cations (see Fig.1.10(a)). Another possibility is that the B'-B'' order is preserved and that the third B cation substitutes with equal probability for the B' and B'' cations. The resulting structure is therefore still a double perovskite but its chemical formula changes (see Fig.1.10(b)). A third possibility is that the third B cation inserts itself regularly every $(n+1)$ atoms, n being equal to the concentration of double perovskite divided by the concentration of single perovskite. This is presented in Fig.1.10(c).

To characterize the degree of ordering (if any), the most obvious solution is the use of Eq.1.2 adapted to the case of solid solutions. However, the use of this formula in the case of a solid solution between a double perovskite and a simple perovskite raises the question of the choice of a reference state for the perfectly ordered material.

The pure ordered double perovskite cell is a good candidate to be the reference state. But, in this case, the presence of a third chemical element on the B site is not taken into account in the calculation of the structure factor. Thus the computed intensities of the reflections in the reference state do not reflect the chemical composition of the solid solution.

All chemical elements can be included in the calculation by creating a pseudo-double perovskite (Fig.1.10(b)) $\text{A}_2(\text{B}^1\text{B}^2)\text{O}_6$, where B^1 and B^2 would be pseudo-atoms composed of one of the B cations of the pure double perovskite (B' and B'') and half of the disrupting B-site cations (typically Ti).

Nonetheless, when forming a solid solution, the crystallographic structure changes and these changes must be considered when calculating the structure factor for the reference state. In addition, the degree of chemical ordering is also often unknown. These two pieces of information (structure and degree of chemical ordering) are investigated simultaneously whereas one is required to find the other.

To bypass the problem of needing the structure to know the degree of chemical ordering (or vice versa), the real material can be described as a composite of an ordered and disordered phase; the ordered phase being the pseudo-double perovskite aforementioned. In this case, the structure of each component of the composite and their relative percentage can be refined simultaneously. However, the limited number of available reflections due to experimental constraints might require that some parameters (e.g. the cell parameters) be kept identical in both phases.

Alternatively, the solid solution can be described by an average structure with a modulation of

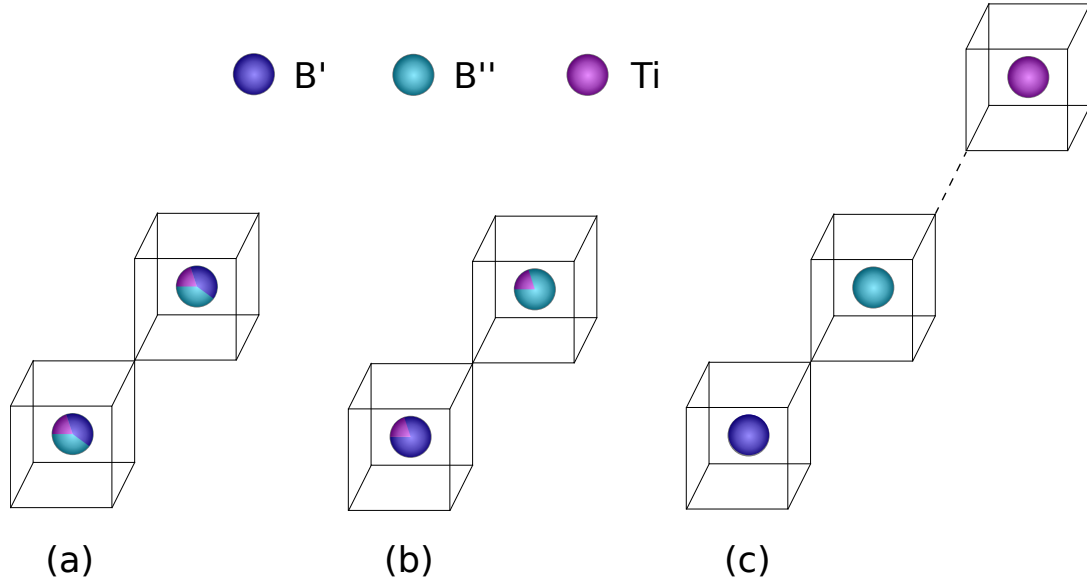


Figure 1.10: Different possibilities for the distributions of the cations on the B-site in the case of a double-perovskite-PT solid solution.

(a) Random distribution

(b) Pseudo double perovskite cell: a double perovskite where B' and B'' are composed of one of the B-cations of the pure double perovskite and of half of the Ti^{4+} cations.

(c) Insertion of Ti^{4+} : the Ti^{4+} inserts between the double perovskite cells in a repetitive fashion. For example, $\text{B}'\text{B}''\text{B}'\text{B}''\text{Ti}^{4+}\text{B}'\text{B}''\text{B}'\text{B}''\text{Ti}^{4+}\text{B}''$. This arrangement leads to SSRs that are not in $(h/2\ h/2\ h/2)$ and that depends on the repetition. In this case, the equation (1.2) can be directly applied using the perfect repetition state as the reference state.

the B-site occupancy. But because of the presence of three different chemical elements on the B site, solving the structure requires at least two sets of data obtained with different radiation type (e.g. X-ray and neutron diffraction patterns). Indeed the ratio of cross sections of the atoms is usually different depending on the radiation type and therefore two sets of data might be sufficient to solve the occupancy modulation.

All these possibilities of measuring the degree of ordering can be applied in the same way to double perovskites for which the structure is unknown.

1.2.1.2 What Influences the Chemical Ordering

It was thought for a long time that the differences of ionic radii and of charges between the B-sites cations were the driving forces for the chemical ordering in double perovskites [17]. However, these differences could not account for the B-site arrangement in all double perovskites (Fig.1.11(a)).

In 1998, Bellaiche and Vanderbilt [18] explained the arrangement of B cations in double perovskites based on a model taking into account only the electrostatic interactions. Later, Bokov

and Ye [22] confirmed the prevailing influence of the electrostatic interactions by proposing that chemical ordering in double perovskites is driven by the sum of the “ionization potentials” (nowadays named ionization energy) ($I_3 + I_5$) of the two B-site cations (Fig.1.11(b)).

The n -th ionization energy refers to the energy required to remove an electron from an ion with the charge $(n - 1)$. I_3 and I_5 correspond to the third and fifth ionization energy, respectively. Hence the ionization energy can be seen as a measure of “how much a cation wants to share its electrons” and therefore the sum of ionization energies describes “how much electrons are shared in the bond”, i.e. the type of chemical bonds: ionic or covalent.

Because, in general, the decrease of ionic radius leads to an increase of ionization energies, the difference in ionic radii was a good approximation for the driving mechanism for ordering in double perovskites. However, because the ionization energies do not correlate exactly with atomic radii, only taking into account difference in sizes could not explain chemical arrangements in all perovskites.

In the same paper, Bokov and Ye [22] support theoretically their model based on the sum of the ionization energies by calculations of effective ionic charges and ordering energies using the semiempirical density functional electronegativity equalization method.

This model explains well a large part of the literature available on double perovskites, however it still cannot explain the B-sites arrangement in every perovskites. Bokov and Ye [22] suggested that the rock-salt ordering present in some perovskites predicted to have a random arrangement is due to an ordering mechanism during a slow cooling after the formation of the perovskite phase. This explanation is rather surprising since their model is based on thermodynamic equilibrium and slow cooling should favor this equilibrium rather than higher energy phases.

1.2.2 Effect of Chemical Ordering on the Macroscopic Properties

In the attempt of tailoring the material to meet the needed macroscopic properties, chemical substitution, i.e. forming solid solutions, is the most common method used. However chemical ordering provides a new degree of freedom to tailor macroscopic properties to one’s needs.

Indeed studies on some perovskites have shown that a change in chemical ordering induces a change in macroscopic properties, however only limited systematic tendency between the macroscopic properties and the chemical order has been found yet. Indeed $\text{Pb}(\text{Sc}_{1/2}\text{Nb}_{1/2})\text{O}_3$ [23] presents a relaxor behavior when disordered and a ferroelectric behavior when ordered whereas $\text{Pb}(\text{In}_{1/2}\text{Nb}_{1/2})\text{O}_3$ [24] presents also a relaxor behavior when disordered and when ordered the behavior is now *antiferroelectric*. All perovskites for which the effect of chemical ordering has been studied² present the same behavior: relaxor when disordered and FE or AFE when ordered. Hence it appears that disorder always leads to a relaxor behavior but that ordering may have greatly different effects on the macroscopic properties.

To try to understand the effect of chemical ordering on the properties, I have reported in Ta-

² $\text{Pb}(\text{Sc}_{1/2}\text{Nb}_{1/2})\text{O}_3$, $\text{Pb}(\text{Sc}_{1/2}\text{Ta}_{1/2})\text{O}_3$, $\text{Pb}(\text{In}_{1/2}\text{Nb}_{1/2})\text{O}_3$ and $\text{Pb}(\text{Yb}_{1/2}\text{Nb}_{1/2})\text{O}_3$

Double perovskite	Chemical order	Polar order	Transition temperature	Ref
$\text{Pb}(\text{Fe}_{1/2}^{2+}\text{W}_{1/2}^{6+})\text{O}_3$	yes	RFE	178	[25]
$\text{Pb}(\text{Co}_{1/2}^{2+}\text{W}_{1/2}^{6+})\text{O}_3$	yes	AFE/FE	298/9	[26]
$\text{Pb}(\text{Mg}_{1/2}^{2+}\text{W}_{1/2}^{6+})\text{O}_3$	yes	AFE	311	[26]
$\text{Pb}(\text{Ni}_{1/2}^{2+}\text{W}_{1/2}^{6+})\text{O}_3$	yes	AFE	311	[25]
$\text{Pb}(\text{Mg}_{1/2}^{2+}\text{Te}_{1/2}^{6+})\text{O}_3$	yes	AFE		[26]
$\text{Pb}(\text{Fe}_{1/2}^{3+}\text{Nb}_{1/2}^{5+})\text{O}_3$	yes	FE/FE	376/355	[27]
$\text{Pb}(\text{Mn}_{1/2}^{2+}\text{Nb}_{1/2}^{6+})\text{O}_3$	yes	AFE	311	[25]
$\text{Pb}(\text{Y}_{1/2}^{3+}\text{Nb}_{1/2}^{5+})\text{O}_3$	yes	AFE	615	[28]
$\text{Pb}(\text{Yb}_{1/2}^{3+}\text{Ta}_{1/2}^{5+})\text{O}_3^*$	yes	AFE/FE	558/450	[21]
$\text{Pb}(\text{Yb}_{1/2}^{3+}\text{Nb}_{1/2}^{5+})\text{O}_3^*$	yes	AFE	565	[29]
$\text{Pb}(\text{Sc}_{1/2}^{3+}\text{Nb}_{1/2}^{5+})\text{O}_3^*$	yes	FE	385	[30]
$\text{Pb}(\text{Sc}_{1/2}^{3+}\text{Ta}_{1/2}^{5+})\text{O}_3^*$	yes	AFE/FE	313/298	[31]
$\text{Pb}(\text{In}_{1/2}^{3+}\text{Nb}_{1/2}^{5+})\text{O}_3^*$	yes	AFE	465	[32]
$\text{Pb}(\text{Dy}_{1/2}^{3+}\text{Nb}_{1/2}^{5+})\text{O}_3$	no	AFE	630	Ref in [33]
$\text{Pb}(\text{Er}_{1/2}^{3+}\text{Nb}_{1/2}^{5+})\text{O}_3$	no	AFE	610	[33]
$\text{Pb}(\text{Yb}_{1/2}^{3+}\text{Nb}_{1/2}^{5+})\text{O}_3^*$	no	RFE	373	[29]
$\text{Pb}(\text{Sc}_{1/2}^{3+}\text{Nb}_{1/2}^{5+})\text{O}_3^*$	no	RFE	390	[30]
$\text{Pb}(\text{Sc}_{1/2}^{3+}\text{Ta}_{1/2}^{5+})\text{O}_3^*$	no	AFE/FE	263/233	[34]
$\text{Pb}(\text{In}_{1/2}^{3+}\text{Nb}_{1/2}^{5+})\text{O}_3^*$	no	AFE	326	[32]
$\text{Pb}(\text{In}_{1/2}^{3+}\text{Ta}_{1/2}^{5+})\text{O}_3$	no	RFE	521	[35]
$\text{Pb}(\text{Fe}_{1/2}^{3+}\text{Ta}_{1/2}^{5+})\text{O}_3$	no	RFE	243	[36]
$\text{Pb}(\text{Tm}_{1/2}^{3+}\text{Nb}_{1/2}^{5+})\text{O}_3$	unknown	AFE	575	Ref in [28]
$\text{Pb}(\text{Cr}_{1/2}^{3+}\text{Nb}_{1/2}^{5+})\text{O}_3$	unknown	FE		[37]
$\text{Pb}(\text{Ni}_{1/2}^{3+}\text{Nb}_{1/2}^{5+})\text{O}_3$	unknown	FE	173	[36]
$\text{Pb}(\text{Mn}_{1/2}^{3+}\text{Ta}_{1/2}^{5+})\text{O}_3$	unknown	FE	373	[36]
$\text{Pb}(\text{Co}_{1/2}^{3+}\text{Ta}_{1/2}^{5+})\text{O}_3$	unknown	FE	203	[36]

Table 1.1: Chemical order, Polar order and Transition temperature of Pb-based double perovskites found in literature. * marks double perovskites that can be ordered or disordered. When the double perovskite undergoes two transitions from high temperature, the two polar states and transition temperatures are reported.

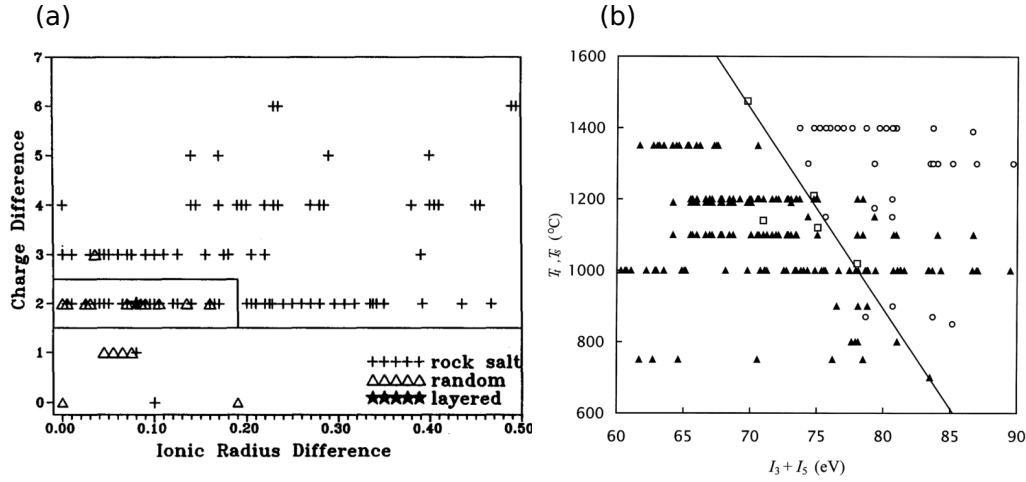


Figure 1.11: (a) Effect of the ionic radii difference and the charge difference on the chemical ordering [17].
 (b) Temperatures of order-disorder phase transition (T_t) for $\text{Pb}(\text{B}^{3+}\text{B}^{5+})\text{O}_3$ complex perovskite (squares) and synthesis temperatures (T_s) for all other ordered (triangles) and disordered (circles) $\text{A}(\text{B}^{3+}\text{B}^{5+})\text{O}_3$ complex perovskite versus sum of ionization potentials of B-site cations ($I_3 + I_5$) [22]

ble1.1 the properties and ordering state of Pb-based double perovskites found in the literature. The number of ordered and disordered Pb-based perovskites presenting antiferroelectric (AFE), ferroelectric (FE), relaxor (RFE) and paraelectric (PE) behavior at room temperature is presented in Fig.1.12. The B-site arrangement of some perovskites has not been clarified in the literature (labeled “unknown” in Fig.1.12). It is probable that these perovskites present a random arrangement, i.e. a disordered structure since authors tend to mention chemical ordering when superstructure peaks related to chemical order are observed.

It appears that most of the ordered double perovskites are AFE at room temperature. Moreover all spontaneously ordered perovskites but one (see below) present a transition from a paraelectric state to an AFE state. Indeed the perovskites that are not AFE at room temperature present either a second transition from an AFE to a FE or RFE phase above room temperature or the transition from the PE to the AFE state occurs at a temperature lower than room temperature. Ordered $\text{Pb}(\text{Sc}_{1/2}\text{Nb}_{1/2})\text{O}_3$ is the only reported double perovskite that transforms directly from the high-temperature PE phase to the low temperature FE phase whereas its counterpart $\text{Pb}(\text{Sc}_{1/2}\text{Ta}_{1/2})\text{O}_3$ transforms first into an AFE state that itself turns into a FE phase. Furthermore, among the perovskites that can be prepared ordered and disordered, $\text{Pb}(\text{Sc}_{1/2}\text{Nb}_{1/2})\text{O}_3$ is the only one for which the transition temperature is higher when disordered. The limited number (4) of perovskites that can be stabilized either in an ordered or a disordered state prevents us from concluding but it seems that $\text{Pb}(\text{Sc}_{1/2}\text{Nb}_{1/2})\text{O}_3$ has a behavior different from the other double perovskites.

On the other hand, most of the disordered perovskites present a RFE behavior. This is unsurprising because disorder is long known to favor relaxor behavior (see Sec.1.1.4). However,

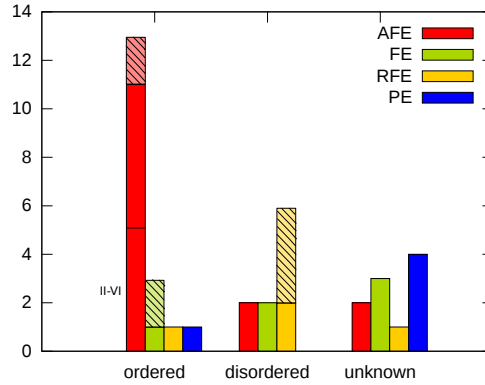


Figure 1.12: Polar orders at room temperature for ordered, disordered Pb-based double perovskites and perovskites of unknown B-site arrangement. The hatched blocks represent double perovskites that can be either ordered or disordered based on the thermal treatment. The double perovskites $\text{Pb}(\text{B}_{1/2}^{2+}\text{B}_{1/2}^{6+})\text{O}_3$ are labeled II-VI, the rest of the data is for $\text{Pb}(\text{B}_{1/2}^{5+}\text{B}_{1/2}^{3+})\text{O}_3$.

because of limited data, no global trend for disordered complex perovskites can be established.

Because the B-cations sizes, charges and ionization energies play a great role in the chemical ordering of perovskite, I have investigated the influence of these parameters on the polar ordering.

The polar order as a function of the charge and the size differences of the B cations is plotted in Fig.1.13. As expected, the perovskites that have larger difference of charges and ionic radii, i.e. that tend to be ordered, present an AFE behavior at room temperature. Besides perovskites for which the B^{3+} is smaller than the B^{5+} (negative values of difference of ionic radii) present a PE behavior at room temperature. Finally perovskites with intermediate differences of charges (2) and ionic radii ($\sim 0.2 \text{ \AA}$) can be either RFE or FE but no evident link between the difference of ionic radii and RFE or FE behavior appears.

The effect of the sum of the ionization energies on the macroscopic properties has been addressed by looking at the transition temperature from the paraelectric phase to a polar phase (Fig.1.14). As in the case of the influence of the charges and ionic radii differences, no link between sum of ionization energies and polar orders is evident. Ferroelectric materials have sums of ionization energies comparatively large ($\gtrsim 75 \text{ eV}$) whereas antiferroelectrics and relaxors have smaller sum of ionization energies ($\lesssim 78 \text{ eV}$).

1.3 HIGH TEMPERATURE PIEZOELECTRIC MATERIALS

Piezoelectric materials have attracted a considerable amount of work in the last 80 years due to the variety of possible applications such as accelerometers, gyroscopes or transducers. Some of these applications take place at temperatures higher than room temperature or over a large temperature range. Materials for such applications must have a depolarization temperature larger

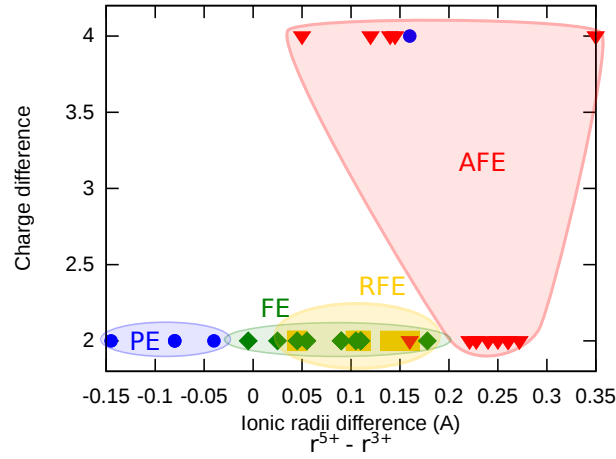


Figure 1.13: Polar ordering at room temperature of Pb-based double perovskites as a function of the differences of charge and of ionic radii between the two B-sites cations. Red triangles represent antiferroelectrics (AFE), yellow squares relaxors (RFE), green diamond ferroelectrics (FE) and blue circles paraelectrics (PE).

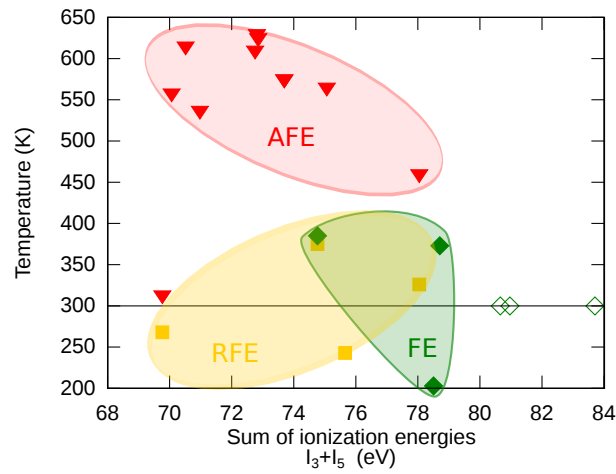


Figure 1.14: Transition temperature from the paraelectric state to an antiferroelectric state (red triangles), to a relaxor state (yellow squares) and to a ferroelectric state (green diamond). When the transition temperature is unknown the room temperature state is displayed in open symbols.

than the targeted highest temperature of operation and must be as temperature independent as possible on the operating temperature range. Thus, in these cases, materials with high Curie temperature (T_c) are required.

Piezoelectric materials with high Curie temperature were less investigated than their counterparts for room temperature applications because the properties are usually lower and the corresponding market smaller. Moreover, these materials are usually more challenging to process than room temperature materials because high Curie temperature is associated with a Goldschmidt factor far from unity [38]. Indeed we have seen in Sec.1.2 that a Goldschmidt factor far from unity leads to strongly distorted perovskites making the material more difficult to synthesize.

To find the most appropriate materials, the Curie temperature and the piezoelectric coefficient d_{33} of some piezoelectric materials found in the literature are compared in Fig.1.15. It appears that the piezoelectric properties tend to decrease when the Curie temperature increases. Thus compromise between large properties and temperature usage range has to be made. Despite potential high T_c , lead free materials tend to present piezoelectric properties disqualifying them for applications. On the other hand, relaxor-PT materials may present extremely large properties but with a limited operating temperature range. The classical piezoelectric material PZT may present various Curie temperatures and piezoelectric properties depending on the doping level and the type of impurities.

In the case of this PhD work, a material with a Curie temperature above 570 K is required. Solid solutions in which one of the end-member is $\text{Pb}(\text{Yb}_{1/2}\text{Nb}_{1/2})\text{O}_3$ have the highest reported piezoelectric properties and a high enough Curie temperature. We have chosen to focus on its simplest solid solution: $\text{Pb}(\text{Yb}_{1/2}\text{Nb}_{1/2})\text{O}_3\text{-PbTiO}_3$ (PYN-PT).

Besides, single crystals processing of PYN-PT is possible. And these single crystals have been reported to have piezoelectric properties comparable to the best relaxor-PT single crystals.

In this study, higher piezoelectric coefficients d_{33} than what was reported in the literature were obtained (open symbols in Fig.1.15) because of the use of a more efficient processing method (mechanosynthesis). The solid solution PYN-PT will be described in the following section.

1.4 $\text{Pb}(\text{Yb}_{1/2}\text{Nb}_{1/2})\text{O}_3\text{-PbTiO}_3$ (PYN PT)

After an exhaustive literature survey of $\text{Pb}(\text{Yb}_{1/2}\text{Nb}_{1/2})\text{O}_3$ (PYN), its solid solution with the classical ferroelectric (FE) PbTiO_3 (PT) will be introduced.

1.4.1 $\text{Pb}(\text{Yb}_{1/2}\text{Nb}_{1/2})\text{O}_3$ (PYN)

$\text{Pb}(\text{Yb}_{1/2}\text{Nb}_{1/2})\text{O}_3$ was first synthesized in the Soviet Union in 1958 and it was characterized as antiferroelectric (AFE) (Ref.[1] in [19]). After that, several groups have attempted to characterize the number and type of transitions as well as the crystallographic structure. All the studies are summarized in Table.1.3 (page 44) and described hereafter.

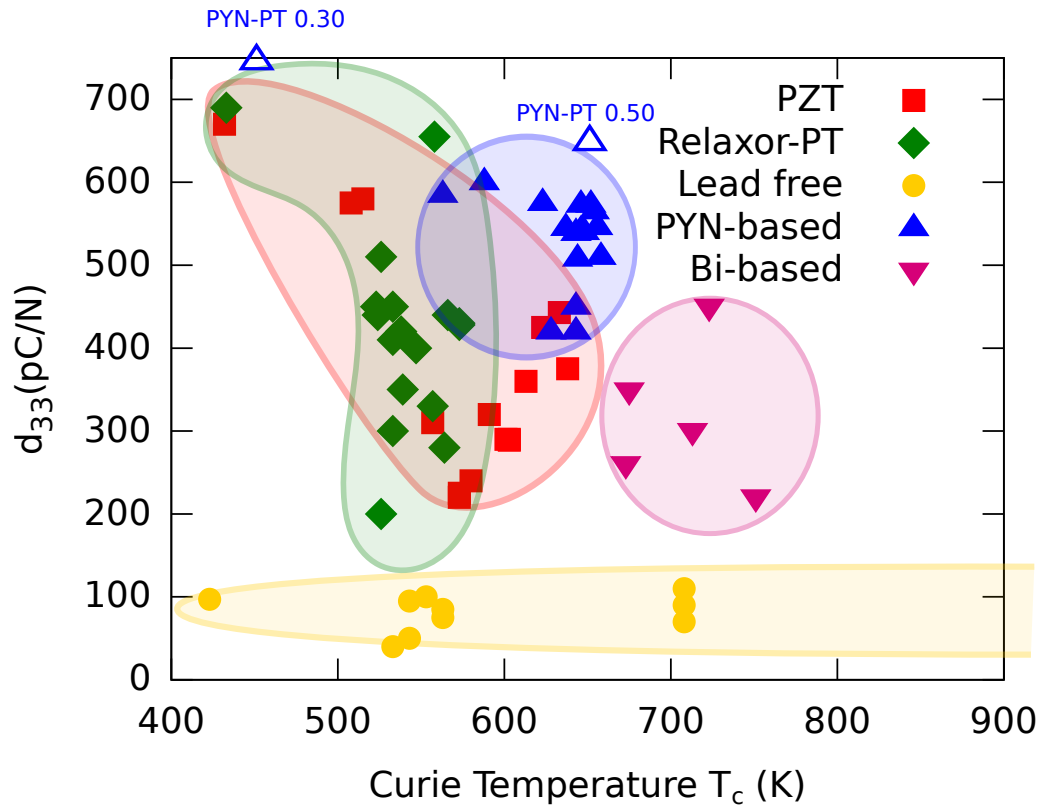


Figure 1.15: Piezoelectric coefficient d_{33} as a function of the Curie temperature for ceramics. The data are grouped together by material type: red squares represent the classical piezoelectric material PZT with various doping, green diamonds represent solid-solutions of PbTiO_3 (PT) and relaxors materials such as $\text{Pb}(\text{Mg}_{1/3}\text{Nb}_{2/3})\text{O}_3$, $\text{Pb}(\text{Zn}_{1/3}\text{Nb}_{2/3})\text{O}_3$ or $\text{Pb}(\text{Sc}_{1/2}\text{Nb}_{1/2})\text{O}_3$, yellow circles represent lead-free materials, pink triangles pointing downwards represent solid solutions in which one of the end-members has bismuth on the A-site of the perovskite and blue triangles pointing upward represent solid solutions in which one of the end-members is $\text{Pb}(\text{Yb}_{1/2}\text{Nb}_{1/2})\text{O}_3$ (the open triangles represent the data obtained in this work for PYN-PT 0.30 and PYN-PT 0.50).

Structure

Much effort has been put into characterizing the crystallographic structure of PYN. Tomashpol'skii and Venevtsev [39] were the first to attempt to describe the crystallographic structure. They have described the structure as a monoclinic cell with $Z=1$ (referred to hereafter as pseudocubic and denoted $(hkl)_{pc}$) and observed superstructure reflections (SSRs) due to both chemical ordering and antiparallel displacements. The structure proposed however does not explain every observed reflections.

Later Kwon and Choo [40] were the first to propose a structure describing all observed reflections. They found that the pseudo-cubic structure is monoclinic, in agreement with Tomashpol'skii's study, in addition, they proposed a $(3/8, 3/8, 0)_{pc}$ modulation vector for the Pb²⁺ cations displacements and a $(1/2, 1/2, 1/2)_{pc}$ modulation vector for the chemical ordering of Yb³⁺ and Nb⁵⁺. These modulations led them to propose an orthorhombic cell describing all observed reflections. The monoclinic cell and the orthorhombic cell are represented in Fig.1.16. The lattice parameters of the two cells are related as follows

$$\begin{pmatrix} a_o \\ b_o \\ c_o \end{pmatrix} = \begin{pmatrix} 1 & 1 & 0 \\ 4 & -4 & 0 \\ 0 & 0 & 2 \end{pmatrix} \cdot \begin{pmatrix} a_m \\ b_m \\ c_m \end{pmatrix} \quad \begin{pmatrix} a_m \\ b_m \\ c_m \end{pmatrix} = \begin{pmatrix} 1/2 & 1/8 & 0 \\ 1/2 & -1/8 & 0 \\ 0 & 0 & 1/2 \end{pmatrix} \cdot \begin{pmatrix} a_o \\ b_o \\ c_o \end{pmatrix}$$

The Miller indices are linked by the same relationships.

Kwon and Choo [40] proposed a $Pbnm$ space group to describe this orthorhombic structure and found that the displacements of Pb²⁺ are along the a_o direction and their amplitudes is of about 0.24 Å (for comparison, displacements of Pb in PbZrO₃ \sim 0.20 Å, in PbTiO₃ \sim 0.16 Å and of Ba in BaTiO₃ \sim 0.07 Å). These displacements lead to the antiferroelectric polarization arrangement described in Fig.1.17. Kania [41], using single crystals, found an orthorhombic structure with cell parameters close to the ones obtained by Kwon and Choo [40].

Finally, Demidova et al. [42] conducted a structural analysis on single crystals and proposed also an orthorhombic cell with the same relationship between the orthorhombic cell and the monoclinic cell. They also came to the conclusion that Pb atoms are displaced only along the a_o -direction. Unlike Kwon and Choo [40], they took into account the chemical ordering and refined the positions of the B cations, Yb and Nb. They found that the B cations are not in the positions expected from the perovskite structure (but displaced within (001) planes) leading to the space group $Pcm2_1$.

The results of Demidova et al. [42] are in agreement with the results of Kwon and Choo [40] since $Pcm2_1$ is a subgroup of $Pbnm$. Only looking at the direction of the Pb²⁺ displacements, the structure found by Kwon and Choo [40] and Demidova et al. [42] are extremely similar, except for the origin of the orthorhombic cell (see Fig.1.17) and the antiparallel displacement pattern of lead atoms can be schematically represented as $\uparrow\uparrow\downarrow\downarrow\uparrow\downarrow$.

However, the polar order derived from the structure proposed by Demidova et al. [42] is much more complex than what is displayed in Fig.1.17. Indeed, all Pb-atoms are not displaced by the same amount and the displacements of the B cations are not negligible. The positions of the cations and their relative displacements are given in Table.1.2 and they are represented in Fig.1.18. As for Pb²⁺, all displacements are along the same direction (imposed by the authors). However the amplitude of the displacement are remarkably different. For example, the smallest

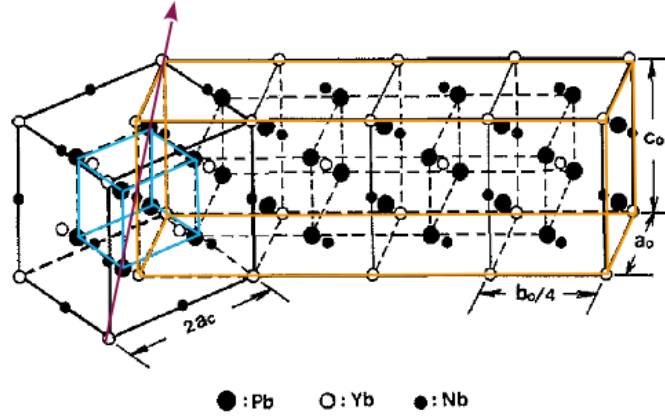


Figure 1.16: Lattice relationship between the high-temperature prototype and low temperature orthorhombic phases (adapted from [40]). The monoclinic cell (light blue cell) with cell parameter $a_{pc} \sim 4 \text{ \AA}$ corresponds to the usual simple perovskite cell. Chemical ordering on the B site along $\langle 111 \rangle_{pc}$ (red arrow) leads to a doubling of the cell parameters. The antiparallel displacements induce a rotation and a quadrupling of the cell leading to the orthorhombic unit cell (orange cell)

amplitude of displacements is about 0.145 \AA whereas the largest one is about 0.398 \AA . Moreover symmetry imposes the amplitude of displacements to be the same in the $z = 1/4$ and $z = 3/4$ layers.

The displacements of B cations are comparable to the one of the Pb cations: Yb^{3+} displacements $\sim 0.181 \text{ \AA}$ and Nb^{5+} displacements $\sim 0.200 \text{ \AA}$.

The influence of these displacements on the polar ordering was evaluated by looking at the dipole moment created by the displacements of all the cations off their ideal position (Table.1.2). The formal charges of each atom were used. The dipole moments are represented on Fig.1.19. In this figure, it clearly appears that the dipole moments created by the B cations are comparable to the ones created Pb^{2+} . However, since the dipole moments were calculated using the formal charges and not the effective charges, the estimated values of the dipole moments have strong uncertainties and therefore no definite conclusion can be drawn. However it is worth noting that the polar ordering in PYN might not only come from the displacements of Pb^{2+} as it is usually thought in Pb-based AFE, but that displacements of B-site cations might have a strong influence on the polar ordering.

Our study of the structure of PYN in Sec.3.4.1 shows that, in first approximation, the modulation vector proposed by Kwon and Choo [40] and Demidova et al. [42] to account for the antiparallel displacements of the Pb^{2+} cations may be used to describe most of the superstructure reflections in the diffractograms of PYN. However, I will show that the structure is more complex and I will propose to describe it with two modulation vectors: the one proposed by Kwon and Choo [40] to describe the displacements of Pb cations and a second one to describe the displacements of the B-site cations (an extension of the structure proposed by Demidova et al.

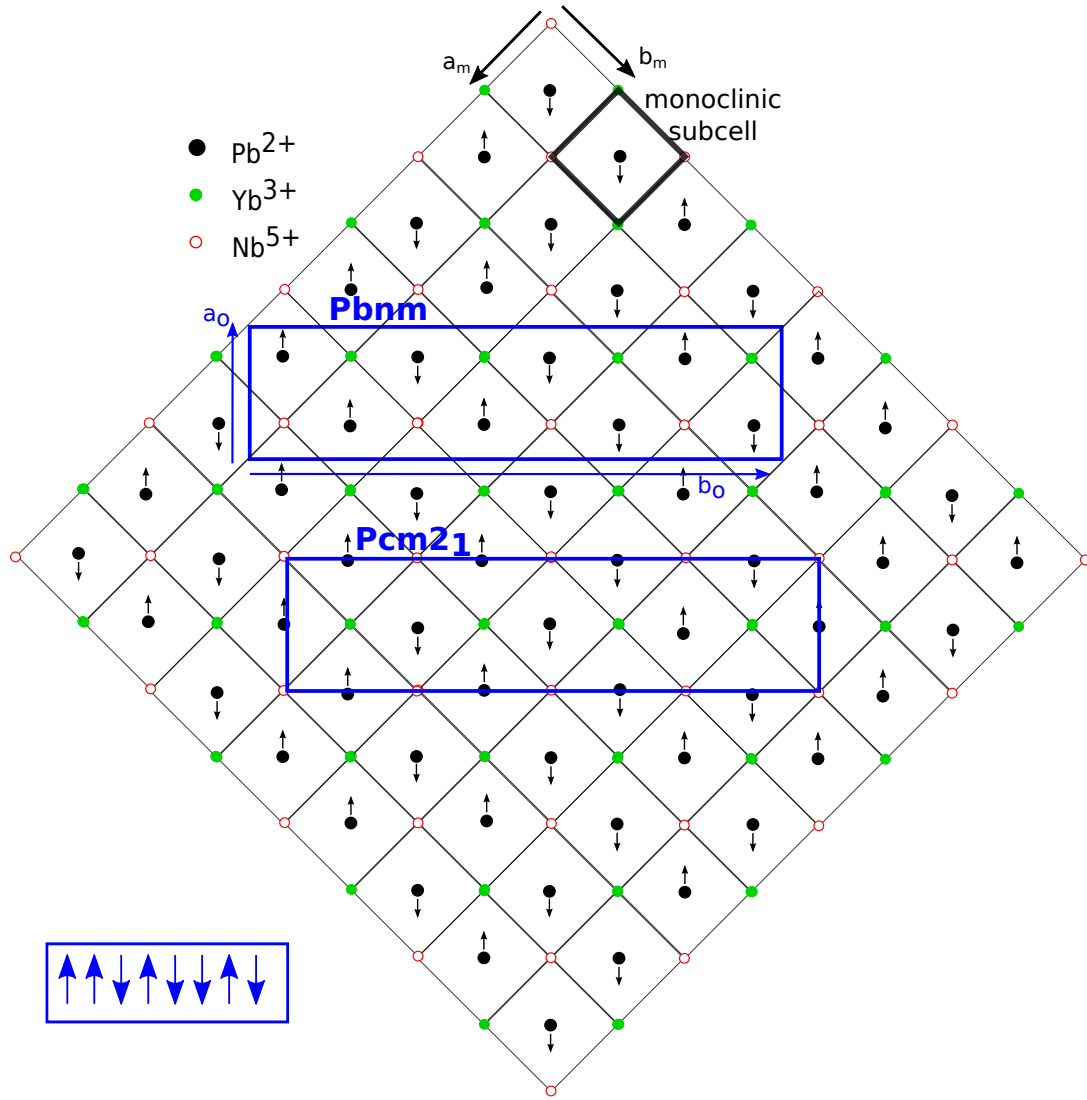


Figure 1.17: Schematic projection of the Pb-displacements in PYN. Thin black lines demarcate the monoclinic cell. Thick blue lines define the orthorhombic cells *Pbnm* (defined by Kwon and Choo [40]) and *Pcm2₁* (defined by Demidova et al. [42]). Arrows represent the shifts of Pb cations. Yb and Nb are alternatively located at the corners of the squares. The oxygens have been omitted for clarity. The polar order inside one orthorhombic unit cell is plotted in the bottom left corner.

Atoms	x (Å)	y (Å)	shift (Å)	dipole moment (C.m)
Pb1	0.145		0.145	0.46
Pb2	0.257		0.257	0.82
Pb3	0.398		0.398	1.28
Pb4	0.157		0.157	0.50
Nb1	0.109	0.024	0.111	0.89
Nb2	0.109	0.204	0.231	1.85
Nb3	0.077	0.024	0.080	0.64
Nb4	0.077	0.204	0.218	1.74
Yb1	0.165	0.118	0.203	0.98
Yb2	0.165	0.163	0.232	1.11
Yb3	0.029	0.118	0.122	0.59
Yb4	0.029	0.163	0.166	0.80

Table 1.2: Displacements and dipole moments of the Pb^{2+} , Nb^{5+} and Yb^{3+} cations calculated from the atomic positions found by Demidova et al. [42].

The axes were rotated compared to the paper to match the convention used in this work.

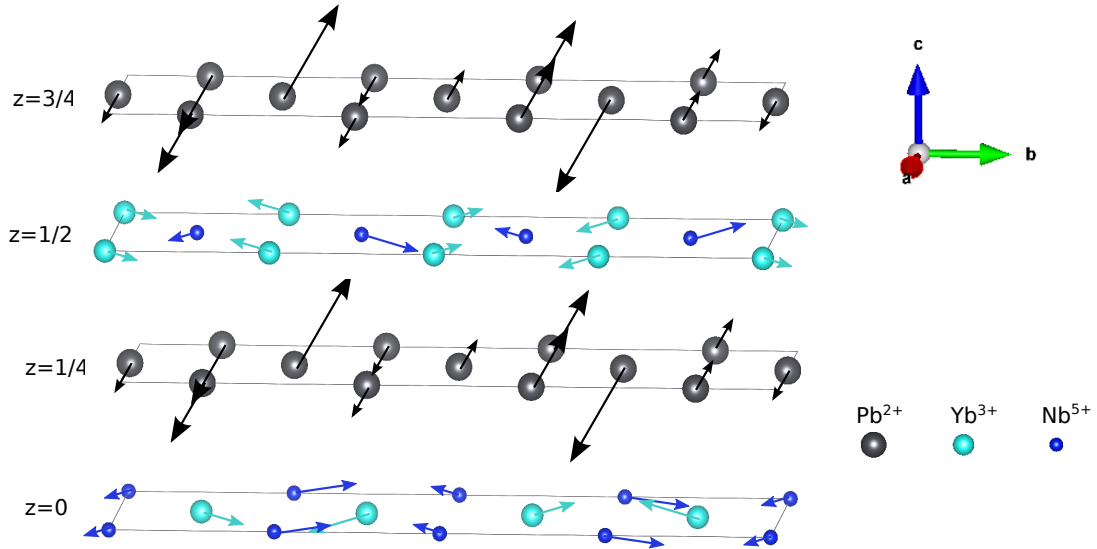


Figure 1.18: Atoms position in the orthorhombic cell as described by Demidova et al. [42]. The arrows indicate the direction of the displacements and their relative amplitudes (not with respect to the cell). For clarity the displacements in the $z = 1/2$ layer are multiplied by 3 and the oxygen atoms are omitted.

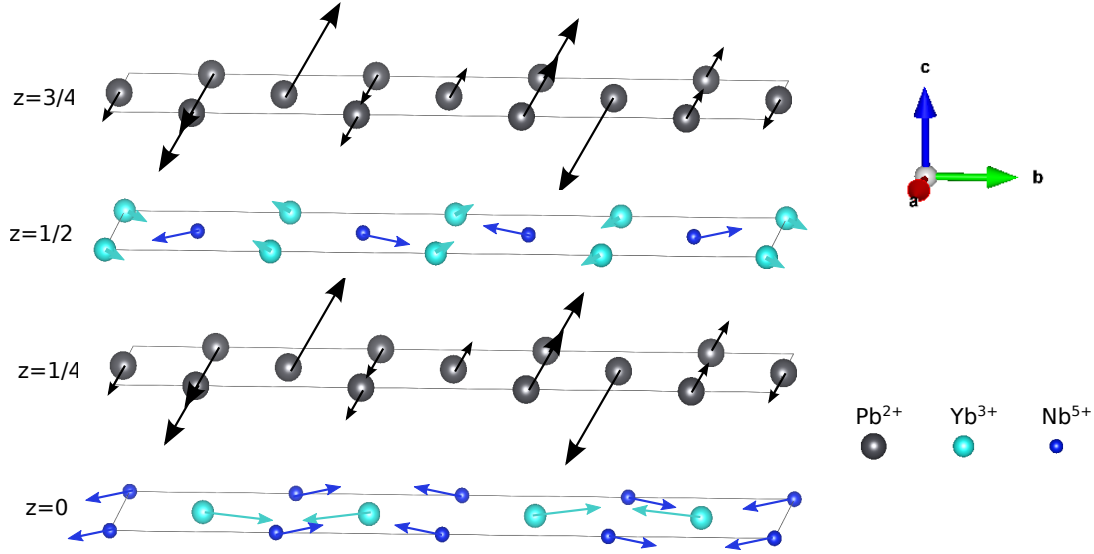


Figure 1.19: Dipole moments created by the displacements of the cations. The dipole moments are calculated from the positions proposed by Demidova et al. [42] and the formal charges.

[42]). Furthermore, I will demonstrate that the Pb^{2+} cations are displaced along the modulation vector and not perpendicularly to it as in most AFE, and as proposed by Kwon and Choo [40] and Demidova et al. [42].

Phase sequence

Whereas there is a general consensus on the structure of PYN, the sequence of phase transformation from the high temperature $Fm\bar{3}m$ structure to the room temperature orthorhombic phase remains controversial in the literature.

Tomashpol'skii and Venetsev [39] and Demidova et al. [42] found that the AFE orthorhombic phase is not directly formed from the high-temperature PE cubic phase but through the formation of an intermediate FE phase of monoclinic symmetry. However, the two groups found transition temperatures to the AFE phase that are 90K apart, raising questions on the sample quality.

On the other hand, Kwon et al. [44] and Kania [41] found that the high-temperature PE cubic phase is converted directly into the AFE orthorhombic phase, both at the same temperature (~ 575 K).

In PbZrO_3 , the model AFE, it was suggested that the intermediate FE phase might be ascribed to PbO vacancies [45]. However, the temperature range of existence of the intermediate phase in PYN is much larger than in PbZrO_3 suggesting that the origin of the intermediate phase might be different.

For the sake of completeness, Yasuda and Inagaki [43] have reported PYN to be FE at room temperature. Our observations and the aforementioned articles disagree with this result that

year	structure	monoclinic cell parameters	orthorhombic cell parameters	Transitions (K)	Ref
1965	monoclinic chemical ordering antiparallel displacements	$a = c = 4.168 \text{ \AA}$ $b = 4.107 \text{ \AA}$ $\beta = 90.45^\circ$		433/583 AFE/FE/PE	[39]
1991	monoclinic chemical ordering	$a = c = 4.161 \text{ \AA}$ $b = 4.110 \text{ \AA}$ $\beta = 90.3^\circ$		466/573 FE/AFE/PE	[43]
1991	orthorhombic	$a = c = 4.077 \text{ \AA}$ $b = 4.111 \text{ \AA}$ $\beta = 90.53^\circ$	$a = 5.918 \text{ \AA}$ $b = 23.453 \text{ \AA}$ $c = 8.221 \text{ \AA}$	573 AFE/PE	[40]
1994	orthorhombic	$a = c = 4.165 \text{ \AA}$ $b = 4.112 \text{ \AA}$ $\beta = 90.49^\circ$	$a = 5.865 \text{ \AA}$ $b = 23.663 \text{ \AA}^*$ $c = 8.224 \text{ \AA}$	523/563 AFE/FE/PE	[42]
2008	orthorhombic	$a = c = 4.161 \text{ \AA}$ $b = 4.116 \text{ \AA}$ $\beta = 90.53^\circ$	$a = 5.857 \text{ \AA}$ $b = 23.644 \text{ \AA}$ $c = 8.232 \text{ \AA}$	573 AFE/PE	[41]

Table 1.3: Timeline of the structure and polar ordering in PYN. The monoclinic cell parameters were calculated from the orthorhombic cell parameters for [41, 42]. For all structures, when the values of the monoclinic angle were lower than 90° , the monoclinic angles were changed to be larger than 90° in order to be in accordance with the standards of the International Union on Crystallography.

* The cell parameter b reported by Demidova is 22.663 \AA and would lead to a highly unstable perovskite phase. I assumed that there was a typo in the original article since changing this value of the b parameter to 23.663 \AA makes the perovskite stable.

we shall hereafter disregard it.

My studies of the evolution of the dielectric constant, hysteresis cycles (Sec.2.4.1) and cell parameters (Sec.3.5.1) as a function of temperature are in agreement with those of Kwon et al. [44] and Kania [41]. The paraelectric phase transforms directly into the antiferroelectric phase upon cooling.

Effect of the Chemical Ordering in PYN

Bokov et al. [29] have been the only ones studying the effect of the chemical ordering on PYN. They found that no thermal treatment is able to alter the chemical ordering of Yb^{3+} and Nb^{5+} without transforming the structure into pyrochlore and that addition of Li^+ on the A site of the perovskite is needed to disrupt the chemical ordering on the B site. They ascertained that when disorder increases in $\text{PYN}+2\text{wt}\%\text{Li}^+$ the material transforms from AFE to diffuse FE (definition in Sec.1.1.4) when the order parameter s drops below a critical value of $s_c \sim 0.6$.

They also found that this change of electric behavior in $\text{PYN}+2\text{wt}\%\text{Li}^+$ is accompanied by a change of the structure. The intensities of the SSRs due to the antiparallel displacements decrease when the chemical ordering decreases. Moreover, the splitting of fundamental Bragg

reflections (with respect to the pseudocubic cell) first decreases when the chemical ordering decreases down to the threshold value s_c . When the chemical ordering decreases even more, the splitting starts to increase again. However, the distortions do not remain purely monoclinic but becomes a mixture of rhombohedral and monoclinic.

Since doping with lithium was necessary to study the effect of chemical ordering, the role of the Li-doping and the associated oxygen vacancies cannot be ruled out as the origin of the diffuse FE behavior. Especially, considering that, in the solid solution $(\text{Pb},\text{La})(\text{Zr},\text{Ti})\text{O}_3$, even at extremely low content of PT, La^+ -doping leads to the appearance of relaxor behavior.

The influence of Li-doping on the relaxor properties has not been addressed in the paper. Yet, it is possible to evaluate it by looking at the evolution of the dielectric constant with temperature for pure PYN and $\text{PYN}+2\text{wt}\%\text{Li}^+$ with similar chemical ordering and percentage of perovskite phase: in pure PYN, only one transition is observed, whereas two are observed in $\text{PYN}+2\text{wt}\%\text{Li}^+$. The synthesis parameters being similar, this second transition can be attributed to the presence of Li^+ (and the associated oxygen vacancies). The temperature at which the second transition happens corresponds within 10 K to the second transition temperature observed by Tomashpol'skii and Venevtsev [39] in pure PYN. I have suspected above that the presence of the second transition in pure PYN may be ascribed to Pb- and O-vacancies. Since, in PYN, as in PbZrO_3 , no influence of the presence of the intermediate phase on the room temperature behavior may be observed, doping with 2wt% lithium probably does not modify the effect of the chemical ordering on the properties. This is further supported by the fact that the room temperature X-ray diagram of pure PYN and $\text{PYN}+2\text{wt}\%\text{Li}^+$ are similar.

Furthermore the transition to the diffuse FE phase can be clearly distinguished from the two transitions related to a potential intermediate phase because it occurs at a temperature about 60 K lower than the intermediate transition. Indeed, some samples, depending on the thermal treatment, present three anomalies in the dielectric constant indicating three transitions from high temperature: the transition from the PE phase, the second transition (due to Li-doping/O-vacancies) and the diffuse transition. The diffuse transition becomes stronger when the chemical ordering decreases and while the other two transitions become weaker. Therefore, the diffuse transition seems to be linked to the alteration of the chemical ordering and not only due to the Li-doping.

However, the decrease of the chemical ordering in the study of Bokov et al. [29] is associated with a decrease of the phase purity, therefore the diffuse FE behavior could be associated with a secondary phase in the samples.

In conclusion, even though some caution is required regarding the conclusion of this study, it appears plausible that PYN, when chemically disordered, presents a relaxor behavior. This is also supported by the analogy with all other complex perovskites that present a FE or AFE behavior when ordered and relaxors when disordered (see Sec.1.2.2).

1.4.2 The Solid-Solution $(1-x)\text{Pb}(\text{Yb}_{1/2}\text{Nb}_{1/2})\text{O}_3$ - $x\text{PbTiO}_3$ ($(1-x)\text{PYN}$ - $x\text{PT}$)

Phase diagram

Only three articles reporting a thorough study of the entire phase diagram of $(1-x)\text{PYN}$ - $x\text{PT}$ have been published. One of the articles reports a study on single crystals, thus fewer compositions were examined. All articles agree that all polar orders (AFE, relaxors, classical FE) are present in the system at room temperature. However, there are discrepancies on the composition range over which each polar order exists (see Fig.1.20).

Lim et al. [46] found that $(1-x)\text{PYN}$ - $x\text{PT}$ is AFE for $x \leq 0.10$, relaxor for $0.10 < x < 0.25$ and FE for $x \gtrsim 0.30$ with a morphotropic phase boundary (MPB) at 0.50. On the other hand, Yamamoto and Ohashi [19] found that $(1-x)\text{PYN}$ - $x\text{PT}$ is AFE for $x \leq 0.10$, FE for $0.10 \leq x \leq 0.18$, relaxor for $0.20 \leq x \leq 0.49$ and FE for larger PT content and that the system presents a MPB at $x = 0.49$.

Both groups agree that the solid solution at low PT content ($x \leq 0.10$) is AFE and that above the MPB (for which they agree on the composition: $x \sim 0.50$) the solid solution presents a FE behavior. In between ($0.10 < x < 0.50$), there is no consensus as to whether the solid solution is relaxor or FE.

Because these two articles agreed on the composition of the MPB, later studies have focused their attention on compositions close to the MPB due to the potential industrial applications. The articles focusing on the MPB show that compositions on the lower PT content side present a relaxor behavior (see for example Lim et al. [47] for a study of the diffuseness or Zhang et al. [48] for a study of the frequency-dependence of the polarization using a Random-Field model). These studies support the polar ordering proposed by Yamamoto and Ohashi [19]: when increasing the PT content, the solid solution $(1-x)\text{PYN}$ - $x\text{PT}$ is successively AFE, FE, relaxor and FE again.

High-Temperature Piezoelectric properties

$(1-x)\text{PYN}$ - $x\text{PT}$ has been mostly studied because of its high piezoelectric properties associated with a high Curie temperature. The published values of the dielectric constant, remnant polarization, coercive field are reported in Table.1.4 with $\text{Pb}(\text{Zr,Ti})\text{O}_3$ (PZT) and $\text{Pb}(\text{Mg}_{1/3}\text{Nb}_{1/3})\text{O}_3$ - PbTiO_3 (PMN-PT) as reference materials since they are respectively the most common ceramic and single-crystal materials used in industrial applications. It appears that the piezoelectric coefficient d_{33} for $(1-x)\text{PYN}$ - $x\text{PT}$ ceramics is much larger than the one of commercial PZT with comparable T_c and dielectric constant. Moreover, in single crystal form and for compositions close enough to the MPB the piezoelectric coefficient of $(1-x)\text{PYN}$ - $x\text{PT}$ is comparable to the one obtained for PMN-PT but the T_c of $(1-x)\text{PYN}$ - $x\text{PT}$ is much higher.

Besides, ternary solid solutions such as PYN - PZ - PT [56] or PYN - PMN - PT [57] have been studied aiming to improve the properties. Piezoelectric coefficient d_{33} has reached about 600 pC/N for ceramics with no variation of the Curie temperature making $(1-x)\text{PYN}$ - $x\text{PT}$ an equivalent of PMN-PT regarding the piezoelectric properties but with a larger operating temperature range. Piezoelectric coefficient values larger than 1200 pC/N [56] have been measured on ceramics using

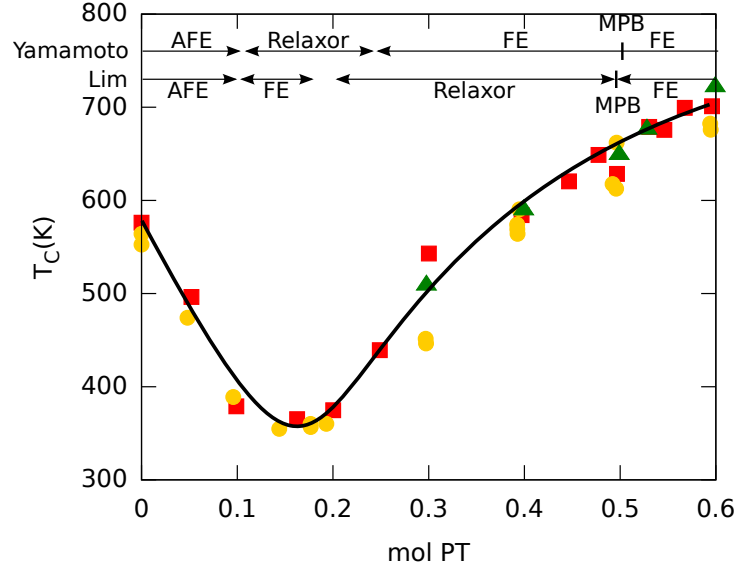


Figure 1.20: Phase diagram of $(1-x)\text{PYN}-x\text{PT}$ obtained from literature data. Red squares represent the data from Yamamoto and Ohashi [19]. Yellow circles represent the data from Lim et al. [46]. Green triangles represent the data from Yasuda et al. [49]. The polar orders proposed by Yamamoto [19] and by Lim [46] are presented on the top of the diagram

unipolar strain measurements, but this value has been attributed to domain wall motions and such high values have not been observed on bipolar measurements.

Crystallographic Structure

The structure of PYN has been described as a large orthorhombic cell with $a \sim 5.8 \text{ \AA}$, $b \sim 23.4 \text{ \AA}$ and $c \sim 8.2 \text{ \AA}$ (see Sec.1.4.1 for details). Lim et al. [46] and Yamamoto and Ohashi [19] have observed that when PT is added to PYN the structure remains the same for $x \leq 0.05$.

At the other end of the phase diagram, PT has a tetragonal structure with a $P4mm$ space group with $a \sim 3.89 \text{ \AA}$ and $c \sim 4.14 \text{ \AA}$, at room temperature [58]. Based on the observation of the splitting of the main Bragg peaks by different groups, it appears that the structure of $(1-x)\text{PYN}-x\text{PT}$ remains mainly tetragonal for compositions down to $x \sim 0.50$ (the MPB). For compositions with $0.10 \leq x < 0.50$, there is no agreement in the literature regarding the crystal structure. Yamamoto and Ohashi [19] proposed a monoclinic phase whereas Lim et al. [46] proposed a pseudo-cubic phase. The studies focusing on the MPB suggest a rhombohedral phase on the PYN side of the MPB [47]. No proper structure determination using Rietveld refinement (or at least profile matching analysis) were conducted in the study of the MPB and the crystal structure was mainly determined by analogy with the PZT solid solution.

However since no thorough study of the crystal structure in the $(1-x)\text{PYN}-x\text{PT}$ solid solution has been conducted so far, a clear understanding of the structure is missing.

Furthermore Lim et al. [46] and Yamamoto and Ohashi [19] have observed SSRs due to chemical ordering of the B cations for pure PYN as well as for the solid solution. The SSRs disappear for

Material	d_{33} (pC/N)	Pr ($\mu\text{C}/\text{cm}^2$)	Ec (kV/cm)	ε	ε_m	Ref
(1- x)PYN- x PT 0.50		32.8	27.5	1646	18000	[19]
(1- x)PYN- x PT 0.495	510	33	16.2	2800	27300	[47]
(1- x)PYN- x PT 0.50	500	36	21	1900	30000	[50]
(1- x)PYN- x PT 0.50	624	22.5	16.7	1500	21000	This work
(1- x)PYN- x PT 0.30	727	14.5	8.5	2500	10000	This work
PZT (Navy II)	425	34	15.5	1800		[51]
(1- x)PYN- x PT 0.40 $\langle 001 \rangle$	1200	26.5	10.1	2100		[52]
(1- x)PYN- x PT 0.40 $\langle 011 \rangle$	900	27.6	9.4	2463		[52]
(1- x)PYN- x PT 0.40 $\langle 111 \rangle$	1730	41.6	11.5	1628		[52]
(1- x)PYN- x PT 0.46 $\langle 001 \rangle$	2500	26.5	10.7	2500	13000	[53]
PMN-PT $\langle 001 \rangle$	1600-3000			4400		[54, 55]

Table 1.4: Electric properties of (1- x)PYN- x PT close to the MPB in ceramics (upper part) and in single crystals (lower part). The results obtained in this work (in Chapter 5) are also added for comparison. These results are compared with commercial PZT ceramics and PMN-PT single crystals for references.

$x > 0.30$ for Yamamoto and Ohashi [19]. Lim et al. [46] have not addressed the topic of chemical ordering. From their figures, the chemical ordering disappear at the same composition as for Yamamoto and Ohashi.

In conclusion, (1- x)PYN- x PT has attracted attention mainly because of its high temperature piezoelectric properties. However, the whole phase diagram is not yet clearly established. What is clear is that for $x \leq 0.05$ an orthorhombic structure associated with AFE is observed. A MPB at $x \sim 0.50$ was observed and for larger PT content the solid solution is FE with a tetragonal phase. Between $0.05 < x < 0.50$ lie relaxor and FE phases, however their respective compositional ranges of existence remain to be clarified.

My study of the phase diagram agrees mainly with the various studies of the phase diagram of PYN-PT already conducted. I will however show that there is no rhombohedral phase on the Ti-poor side of the MPB. Furthermore, in an attempt to precise the compositional range of the existence of the various polar orders, I will demonstrate that several polar orders may coexist at a given composition and temperature explaining why there are some disagreements regarding the respective compositional range of existence of the various polar orders.

1.4.3 System Similar to (1- x)PYN- x PT: $\text{Pb}(\text{Yb}_{1/2}\text{Ta}_{1/2})\text{O}_3$ - PbTiO_3

Insight on the PYN-PT solid solution may be gained through the comparison of other solid solutions based on a double perovskite and PbTiO_3 . $\text{Pb}(\text{Yb}_{1/2}\text{Ta}_{1/2})\text{O}_3$ (PYT) is a material extremely similar to PYN since Ta^{5+} and Nb^{5+} have the same formal charges and the same ionic radii. Like PYN, PYT presents a transition at 570K from a AFE phase to a PE phase.

Moreover, the room temperature X-ray diagrams of PYN and PYT are similar and in particular SSRs due to the antiparallel displacements appear at the same 2θ angles.

However, when decreasing temperature, PYT undergoes a second transition. This transition is diffuse. Dielectric measurements performed on single crystals have shown that the diffuse transition only occurs along the $\langle 111 \rangle_{pc}$ axis of the crystal. When the crystals are oriented along the $\langle 100 \rangle_{pc}$ and $\langle 110 \rangle_{pc}$ axes only the high-temperature transition (the one similar to PYN) occurs [59]. Even though FE hysteresis cycles can be observed along the $\langle 111 \rangle_{pc}$ at room temperature, the remnant polarization is small ($P_r = 0.15 \mu\text{C.cm}^{-2}$ for applied electric field as high as 30 kV/cm). Hence, at room temperature, PYT is believed to be AFE or weakly FE depending on the crystallographic orientation.

In the temperature range 470-570 K, when purely AFE, PYT has an orthorhombic structure with cell parameters close to the ones of PYN ($a \sim 5.9 \text{ \AA}$, $b \sim 23.5 \text{ \AA}$, $c \sim 8.2 \text{ \AA}$). This orthorhombic structure is described using the space group $Pbnm$ [60], the one proposed by Kwon and Choo [40] for PYN.

In the low temperature state, the structure remains orthorhombic with the same cell parameters, but a different space group ($Pbn2_1$) was proposed. However, the atomic positions in the two orthorhombic states are extremely similar and $Pbnm$ is a good approximation to describe the lattice at room temperature [60], especially when a limited number of reflections is available for the study.

The solid solution $(1-x)\text{PYT}-x\text{PT}$ presents a phase diagram with a lot of similarities with the one of $(1-x)\text{PYN}-x\text{PT}$ (Fig.1.21). Indeed both solid solutions present all polar orders at room temperature. Moreover, when increasing the PT content, the solid-solution $(1-x)\text{PYT}-x\text{PT}$ is successively AFE, relaxor and FE, i.e. the same polar order sequence as was proposed for $(1-x)\text{PYN}-x\text{PT}$ by Yamamoto and Ohashi [19]. The major difference between the two solid solutions appears at low PT content ($x < 0.02$). Indeed in this compositional range, $(1-x)\text{PYT}-x\text{PT}$ presents, at room temperature, weak ferroelectricity that has never been reported in $(1-x)\text{PYN}-x\text{PT}$.

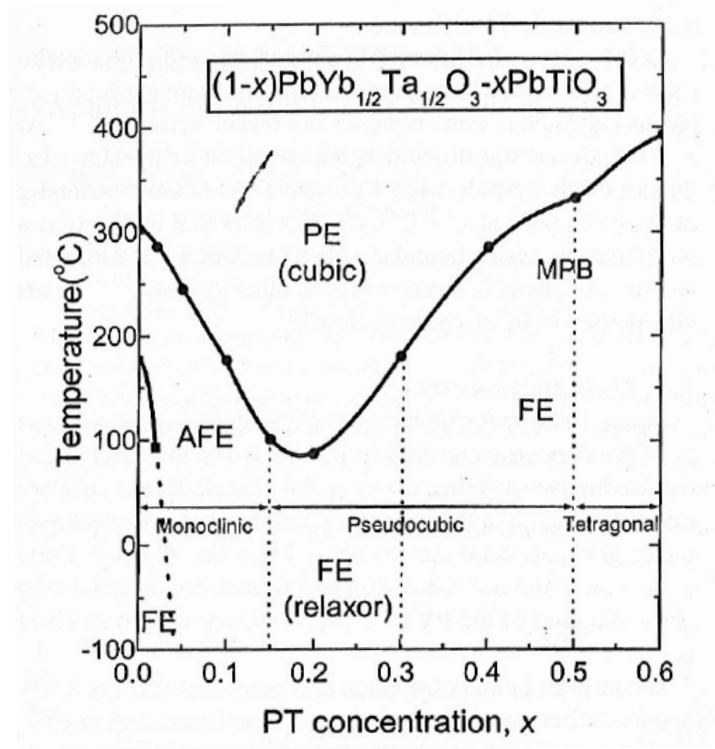


Figure 1.21: Phase diagram of $(1-x)\text{PYT}-x\text{PT}$ proposed by Park and Choo [21]

- CHAPTER 2 -

PROPERTIES

This Chapter focuses on the study of the dielectric, ferroelectric and piezoelectric properties in the $\text{Pb}(\text{Yb}_{1/2}\text{Nb}_{1/2})\text{O}_3\text{-PbTiO}_3$ (PYN-PT) solid solution.

The main dielectric and piezoelectric properties of the different polar orders: antiferroelectricity, relaxor and ferroelectricity will be reviewed first (Sec.2.1).

In Sec.2.2, the overview of the dielectric measurements will enable us to separate the various compositions depending on the value of the maximum of the dielectric constant and its frequency dependence.

In Sec.2.3, the ferroelectric and piezoelectric properties of the various compositions will be presented.

The evolution of the dielectric constant, ferroelectric and piezoelectric properties of the compositions divided in this way will be examined in more details in Sec.2.4.

Finally, in the conclusion (Sec.2.5), a phase diagram based only on the properties measurements will be proposed (Fig.2.23, page 95). This phase diagram will be compared to the one based on the structural studies (Fig.3.28, page 169) in Chapter 4.

2.1 INTRODUCTION

We shall review briefly hereafter the characteristic features of the antiferroelectric, relaxor and ferroelectric polar orders that allow their identification (Fig.2.1), starting with ferroelectrics.

2.1.1 Ferroelectrics

Ferroelectric (FE) materials usually present a strong dielectric constant ($\epsilon' \sim 1000$ at room temperature) that peaks at the Curie temperature (T_c) ($\epsilon' \sim 10\,000$). The evolution of dielectric constant with temperature above and below T_c follows the Curie-Weiss law

$$\begin{aligned} \text{for } T > T_c \quad \epsilon' &= \frac{C^{HT}}{T - T_c} \\ \text{for } T < T_c \quad \epsilon' &= \frac{C^{LT}}{T_c - T} \end{aligned} \tag{2.1}$$

where C is the Curie constant ($C \sim 10^3 \text{ K}^{-1}$ for order-disorder transitions and $C \sim 10^5 \text{ K}^{-1}$ for displacive transitions).

Landau theory can be used to determine a link between the values of the Curie constant above and below T_c in the case of ferroelectrics. For a first order phase transition (e.g. BaTiO_3), the Curie constant below T_c is eight time larger than the one above T_c , whereas for a second order phase transition (e.g. PbTiO_3), the Curie constant below T_c is only twice larger than the one above T_c .

These exact ratios of slopes have never been observed practically even on single crystals of model FE materials such as BaTiO_3 and LiTaO_3 [61].

In ferroelectrics, because of the possibility to switch the polarization by the application of an electric field, the polarization as a function of the electric field show an hysteretic behavior. At low electric field, the polarization of the material varies linearly with the dielectric susceptibility χ , so that

$$P = \epsilon_0 \chi E + P_s \quad \text{with } \chi = \epsilon' + 1 \simeq \epsilon' \quad \text{for FE materials}$$

with P is the measured polarization, E the electric field and P_s the spontaneous polarization. At large electric fields, domains reversal plays a non-negligible role in the polarization and the above formula is no longer valid.

Besides, as ferroelectrics are necessarily piezoelectrics, the strain-electric field relation also shows an hysteretic behavior. At low electric field, the strain (S) is proportional to the electric field ($S = dE$) with d the piezoelectric constant introduced in Sec.1.1.1. At larger fields, domains reversal leads to the occurrence of a so-called “butterfly loops” typical of FE.

From a property point of view, in the solid solutions with PbTiO_3 as an end-members (to

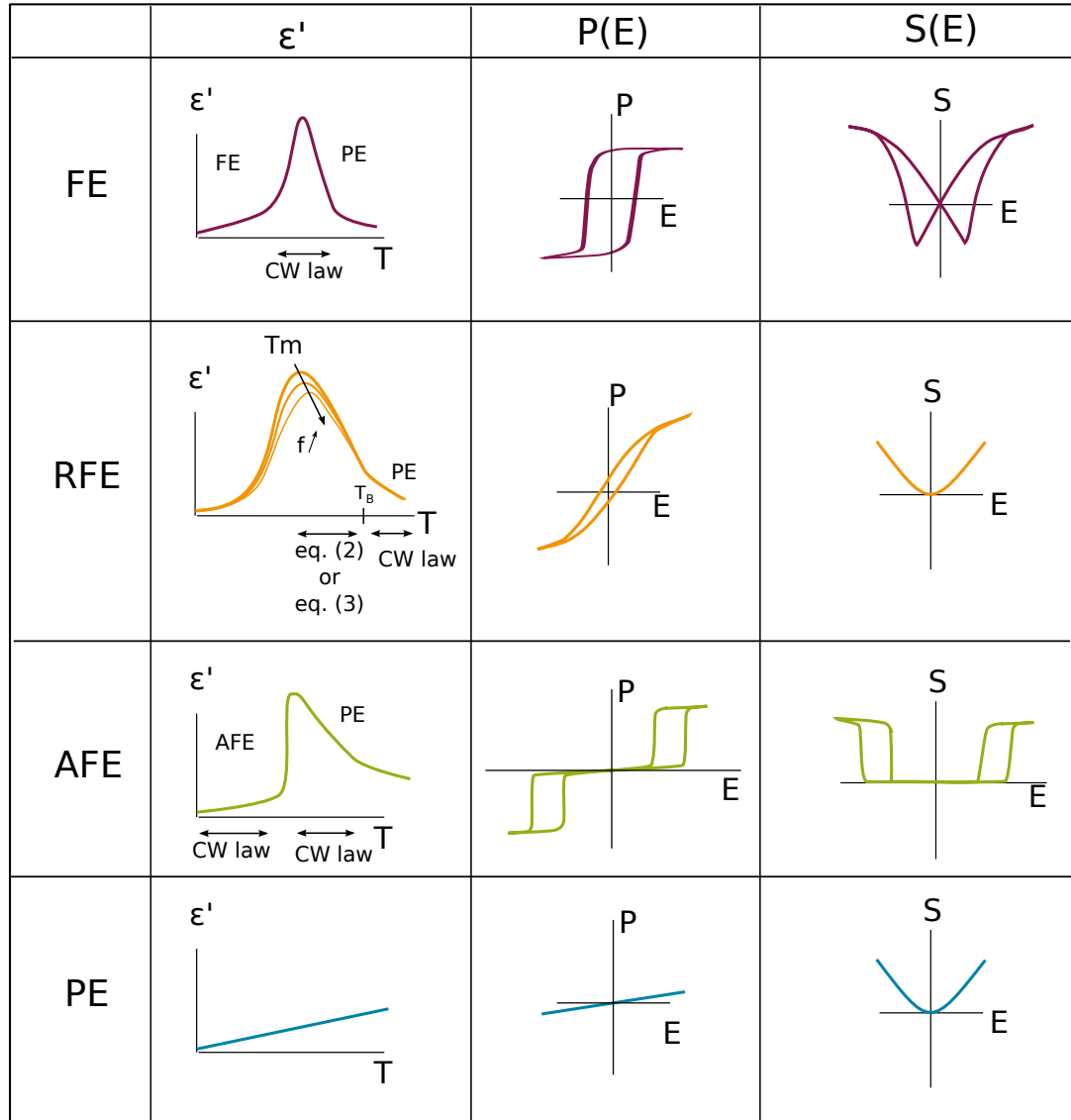


Figure 2.1: Evolution of the dielectric constant (ϵ') with temperature and of the polarization (P) and strain (S) with electric field (E) for ferroelectric (FE), relaxor (RFE), antiferroelectric (AFE) and paraelectric (PE) materials.

FE, AFE and PE material have a dielectric constant that follows Curie-Weiss (CW) law. RFE have a dielectric constant that depends on frequency and that follows Curie-Weiss law only above Burns temperature (T_B).

The evolution of the polarization as a function of the electric field for FE is hysteretic. The hysteresis cycle is slim and slanted for RFE. In AFE materials, the polarization exhibits a double loop cycle as a function of the electric field. In PE materials, a linear relation holds between polarization and electric field.

RFE and PE are only electrostrictive: the strain depends quadratically on the electric field. FE materials have a strong piezoelectric response in addition to the electrostrictive one, the strain-electric field relationship is usually dominated by piezoelectricity and therefore the cycle is the typical butterfly loop. As for polarization, the strain in AFE is a double loop.

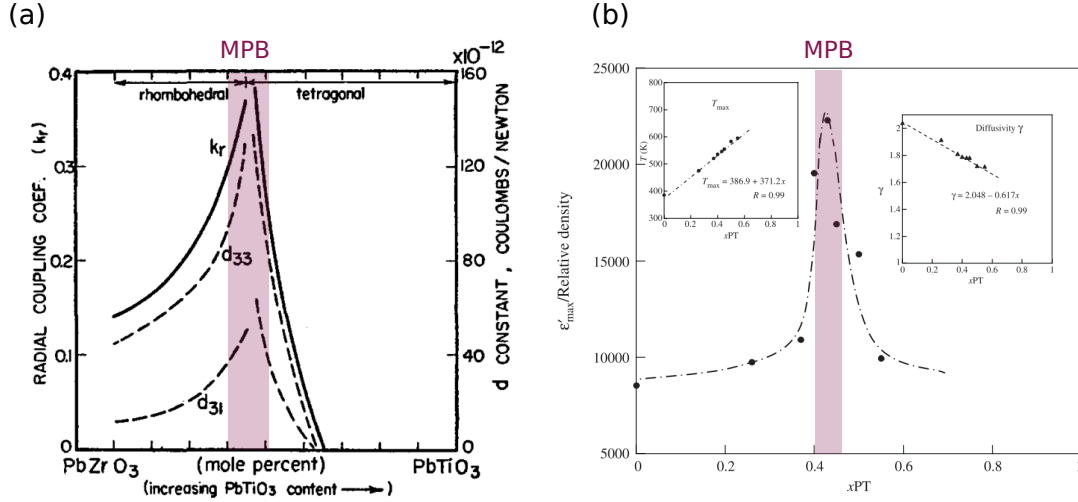


Figure 2.2: Increase of (a) the piezoelectric properties in $\text{PbZrO}_3\text{-PbTiO}_3$ [1] solid solution and (b) the dielectric properties in $\text{Pb}(\text{Sc}_{1/2}\text{Nb}_{1/2})\text{O}_3\text{-PbTiO}_3$ [62]

which PYN-PT belongs), properties such as polarization and piezoelectricity exhibit a maximum in a compositional range. This range is referred to as the “morphotropic phase boundary” (MPB) (Fig.2.2: MPB of $\text{PbZrO}_3\text{-PbTiO}_3$ and $\text{Pb}(\text{Sc}_{1/2}\text{Nb}_{1/2})\text{O}_3\text{-PbTiO}_3$).

2.1.2 Relaxors

The maximum of the dielectric constant of relaxors is extremely high ($\epsilon' \sim 20\,000$ at T_m) and comparable to the values found for the best ferroelectric materials.

The main differences in the dielectric behavior of relaxors and ferroelectrics lie in the frequency dependence and in the width of the dielectric peak at T_m or T_c . Indeed, in relaxors, the dielectric constant is strongly dependent on the frequency of the measuring AC electric field. This behavior is attributed to the presence of polar nanoregions (PNRs) with different dynamics (see Sec.1.1.4 (page 19) for details concerning the polar features in relaxors). The broadening of the dielectric peak at T_m , on the other hand, is linked to local disorder.

By analogy with spin-glass, the frequency-dependence of the dielectric constant in relaxors has been found to follow a Vogel-Fulcher law [9]:

$$f = f_0 \exp \left[\frac{-E_a}{k_B(T_m - T_f)} \right] \quad (2.2)$$

The freezing temperature T_f is the temperature at which the non-ergodic relaxor state transforms into the ergodic state. The activation energy E_a is believed to represent the energy for polarization fluctuations of an isolated PNR. The Debye frequency f_0 relates to the frequency of vibration of the PNRs, and k_B is the Boltzmann constant ($1.38 \cdot 10^{-23} \text{ m}^2 \cdot \text{kg} \cdot \text{s}^{-2} \cdot \text{K}^{-1} = 8.62 \cdot 10^{-5} \text{ eV} \cdot \text{K}^{-1}$).

The evolution of the dielectric constant with temperature, in relaxors, depends strongly on the temperature range considered.

Above Burns temperature T_B , the dielectric constant follows the Curie-Weiss law, similarly to the ferroelectric case.

Below T_B , the dielectric constant follows a different law. Several models have been proposed to describe this behavior. The model proposed first describes the evolution of the dielectric constant with temperature using a modified Curie-Weiss law, with the addition of a critical exponent γ

$$\frac{\varepsilon_m}{\varepsilon'} = 1 + B(T - T_m)^\gamma \quad (2.3)$$

where B and γ are fitting parameters and ε_m is the maximum of the dielectric constant. In this case, the critical exponent γ describes the “degree” of relaxation in the material and is usually comprised between 1 and 2 with classical values closer to 2.

Later, Bokov and Ye [22] proposed a Lorentz-type relation

$$\frac{\varepsilon_A}{\varepsilon'} - 1 = \frac{(T - T_A)^2}{2\delta^2} \quad (2.4)$$

where T_A and ε_A are fitting parameters defining the temperature and magnitude of the static dielectric peak. δ is a measure of the degree of diffuseness of the peak and hence describes the “degree” of relaxation, in this case. Experimentally, equation (2.4) has been shown to hold for temperatures even a few degrees below T_m whereas the modified Curie-Weiss law (2.3) does not describe the behavior below T_m [22]. I will show in Sec.2.4.2.2 that Eq.(2.4) cannot be used to describe the thermal evolution of the dielectric constant in the case of PYN-PT.

Below T_m , no simple expression has been found to model the thermal behavior of the dielectric constant. However more elaborate models to fit the dielectric constant in this temperature range have been developed (see for example [6]).

Relaxors present a slightly hysteretic behavior under the application of an electric field. Indeed relaxors have, on average, a cubic structure and therefore no polar axis. The polarization-electric field curves usually show a slanted, slim cycle. Also because of the centrosymmetric cubic structure no piezoelectricity can be observed and the electric-field induced strain is simply due to electrostriction.

2.1.3 Antiferroelectrics

Antiferroelectric (AFE) materials usually have a low dielectric constant even at the Curie temperature ($\varepsilon' \sim 500$ -1000 at the Curie temperature). All reported antiferroelectrics undergo a first order phase transition from the paraelectric (PE) phase to the AFE phase.

Using Landau theory, it can be shown that the evolution of the dielectric constant with temperature follows the same law as in ferroelectrics: the Curie-Weiss law (2.1). This model however assumes that antiferroelectrics can be described by the superimposition of two polar sublattices (see Sec.1.1.3). No simple derivation of the Landau theory can predict the ratio of Curie constants below and above the transition temperature in the case of a first-order PE-AFE phase

transition [61].

Antiferroelectric materials do not present a spontaneous polarization. Thus under the application of a reasonable electric-field, the observed polarization is simply due to the dielectric behavior, i.e. the polarization is proportional to the electric field such as: $\mathbf{P} = \epsilon_0 \chi \cdot \mathbf{E}$. Furthermore, because the antiferroelectric and the ferroelectric states are close in energy, it is possible to induce an AFE-FE transition with an electric field. This AFE-FE transition leads to the appearance of an hysteretic behavior at large electric fields. Hence the AFE hysteresis loop is dielectric at low field and hysteretic when the FE phase is induced.

Two types of responses depending on the electric-field strength are also observed in the strain response: at low electric field, no strain is induced whereas strain is induced for fields large enough to induce the AFE-FE transition. Indeed, assuming the model with the superimposition of two oppositely directed polar sublattices for antiferroelectrics, the sublattice with polarization along the application of the electric field elongates whereas the other sublattice, with antiparallel polarization, shrinks leading to zero net strain. At large fields, the antiferroelectric phase transforms into a ferroelectric, hence piezoelectric phase in which electric-field induces a large linear strain. However, because this FE phase is metastable, when the electric field is removed the FE transforms back into the AFE phase and therefore no butterfly loop typical for piezoelectric materials is observed.

Double-Hysteresis Loops not due to Antiferroelectricity

It is generally accepted that double hysteresis loops are fingerprints of antiferroelectricity. However, double hysteresis loops have been observed in the doped classical FE material $\text{Pb}(\text{Zr},\text{Ti})\text{O}_3$. In this case, the double loop comes from the pinning of domains/domain walls by dipoles created by the doping atoms. Indeed, the applied electric field can bring enough energy to overcome this pinning and induce a macroscopic net polarization, but when the electric field is removed the restoring forces created by the coupling of defects dipoles and domains switch the polarization back to its initial state.

The main difference between antiferroelectric and doped-FE double loops is that the remnant polarization does not have to be zero in doped FE (Fig.2.3). Moreover, the double loops can be unpinched either by the application of large electric fields or by an appropriate thermal treatment (see for example [63]). Double-loops are mostly observed in ferroelectric materials when they are doped with acceptors such as Fe^{3+} or Sc^{3+} ("hard" doping). (On the contrary doping a ferroelectric with donors, such as Nb^{5+} or Ta^{5+} , is referred to as "hard" doping.)

Finally, double loops have been observed in the classical ferroelectric BaTiO_3 close to the Curie temperature. In this case, the double-loop is due to the energetical proximity of the paraelectric and ferroelectric phases. Indeed, at such temperature, BaTiO_3 is in the paraelectric phase, however the application of a strong-enough electric field induces the paraelectric-ferroelectric phase transition and, as in the case of antiferroelectrics, at large electric field, the ferroelectric phase leads to the appearance of strong polarization and strain[64].

Doping the PZT material with donor or acceptor ions changes its properties dramatically. Donor

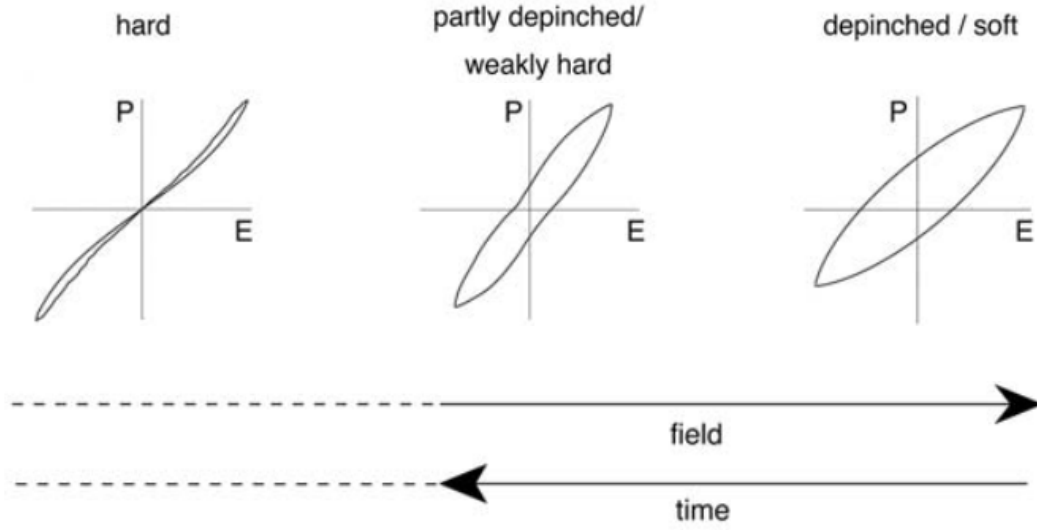


Figure 2.3: Polarization-electric field hysteresis loops for materials with (left) strongly pinched domain wall or hard material, (middle) with partly depinched domain walls or weakly hard material, and (right) for a soft material. Experiments have shown transition from (middle) to (right) after relaxing with field, and from (right) to (middle) after aging. Adapted from [63]

doping with ions such as Nb^{5+} or Ta^{5+} provides “soft” PZTs, like PZT-5, because of the easing of domain motion due to the resulting Pb-vacancies. On the other hand, acceptor doping with Fe^{3+} or Sc^{3+} leads to “hard” PZTs, such as PZT-8, because the oxygen vacancies will pin the domain wall motion.

Conclusion

Ferroelectrics and relaxors have larger dielectric constants compared to antiferroelectrics and paraelectrics. Ferroelectrics and antiferroelectrics follow Curie-Weiss law above and below the Curie temperature whereas relaxors follow the Curie-Weiss law only above T_B . Below T_B , the evolution of dielectric constant of relaxors is still under debate today. Moreover only in relaxors is the dielectric constant dependent on the frequency.

2.1.4 Use of the derivative of the inverse of the dielectric constant:

$$\xi = \frac{\partial(1/\epsilon')}{\partial T}$$

Despite the above mentioned characteristic features of FE, RFE, AFE and PE, it is sometimes difficult experimentally to determine the polar order, as illustrated by the multiple possible origins of double hysteresis loops described above. Therefore, to determine the polar order of a material, it may be useful to plot the derivative of the inverse of the dielectric constant with respect to temperature (ξ) to determine if the dielectric constant follows a Curie-Weiss law, a

modified Curie-Weiss law or a more complex law. Indeed fitting the various laws to the dielectric constant to find the one actually describing the data can be very challenging because in addition to the fitting of the various parameters of the law, the temperature range over which the law applies usually has to be fitted as well. ξ is calculated regardless of the temperature range and it can be used to characterize the type of dielectric behavior (Fig.2.4). Moreover, the number of parameters to fit when using ξ is reduced.

In the case of the Curie-Weiss law, ξ is inversely proportional to the Curie constant since

$$\text{Curie-Weiss law} \quad \xi = \frac{\partial(1/\varepsilon')}{\partial T} = \frac{\partial}{\partial T} \left[\frac{T - T_c}{C} \right] = \frac{1}{C} \quad (2.5)$$

In the case of relaxors, the two laws described previously Eq.(2.3) and Eq.(2.4) (page 57) lead to behavior that are similar in practical cases ($\gamma \sim 2$).

$$\begin{aligned} \text{Eq.(2.3): modified Curie-Weiss law} \quad \xi = \frac{\partial(1/\varepsilon')}{\partial T} &= \frac{1}{\varepsilon_m} \cdot \frac{\partial}{\partial T} [1 + B(T - T_m)^\gamma] \\ &= \underbrace{\frac{1}{\varepsilon_m} \cdot B \cdot \gamma}_{\alpha} \cdot (T - T_m)^{\gamma-1} \end{aligned} \quad (2.6)$$

$$\begin{aligned} \text{Eq.(2.4):proposed by Bokov et al. [65]} \quad \xi = \frac{\partial(1/\varepsilon')}{\partial T} &= \frac{1}{\varepsilon_A} \frac{\partial}{\partial T} \left[\frac{(T - T_A)^2}{2\delta^2} - 1 \right] \\ &= \underbrace{\frac{1}{\varepsilon_A} \cdot \frac{1}{2\delta^2} \cdot 2}_{\alpha} \cdot (T - T_A) \end{aligned} \quad (2.7)$$

Thus regardless of the model chosen to fit the data, in relaxors, ξ depends strongly on temperature, whether this dependence is linear ($\gamma \sim 2$) or not.

Besides, in cases where interfaces play a non-negligible role (e.g. thin films), using ξ allows to study only the intrinsic behavior of the material because the dielectric response of the defects/interfaces is rather temperature independent. Thus,

$$\xi(T) = \frac{\partial}{\partial T} \left(\frac{1}{\varepsilon(T)} \right) = \frac{\partial}{\partial T} \left(\frac{1}{\varepsilon_{Mat}(T)} + \frac{1}{\varepsilon_{Inter}} \right) \approx \frac{\partial}{\partial T} \left(\frac{1}{\varepsilon_{Mat}(T)} \right)$$

where ε_{Mat} and ε_{Inter} are respectively the dielectric constant of the material and of the interfaces (see Ref.[66] for more details).

The method used to calculate the derivative of the inverse of the dielectric constant for this work is given in Appendix.B

2.2 DIELECTRIC MEASUREMENTS

Dielectric constant measurements were carried out using an HP4294A and an Agilent 4192 impedance analyzer on ceramics sputtered with gold electrodes from 80K to 800K (using a

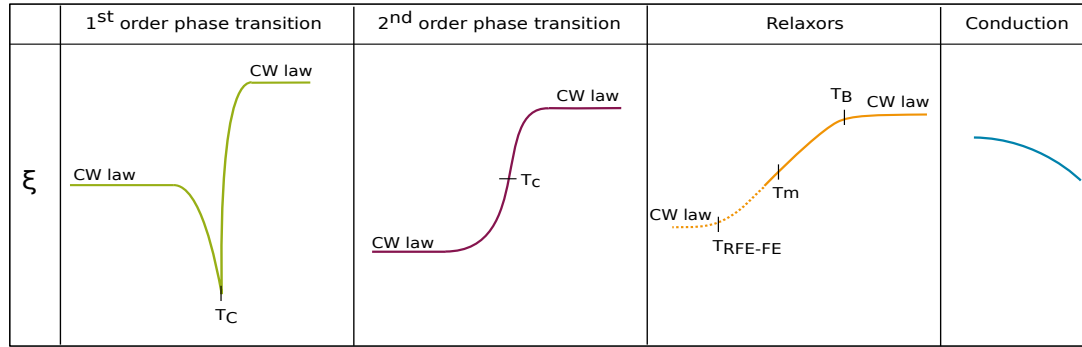


Figure 2.4: Temperature evolution of ξ for various types of transitions.

FE and AFE materials may undergo first or second order phase transitions. Relaxors have a diffuse phase transition characterized by a linear dependence of ξ with temperature. Relaxors may undergo a phase transition toward a FE phase, in this case ξ , as in classical FE materials, follows a Curie-Weiss (CW) law. Conduction mechanisms usually taking place at high temperature may lead to a decrease of ξ with temperature.

cryofurnace and a furnace) in the 1kHz to 1MHz range under an applied AC voltage of 400mV peak-to-peak.

Fig.2.5 shows the evolution of the dielectric constant ε' as a function of temperature measured for several frequencies and compositions.

In the following, the influence of the composition on the value of the dielectric constant and on the peak width will be first discussed. Then, the influence of the frequency will be studied in more detail using the Vogel-Fulcher law. Finally, a sequence of phase transitions will be proposed for each composition.

2.2.1 Influence of composition

In Fig.2.5, the dielectric constants of PYN and PYN-PT 0.05 appear to be extremely small, especially in comparison with the other compositions. The difference of magnitude in the dielectric constant can be seen more easily when looking only at the maximum of the dielectric constant as a function of the composition (Fig.2.6). From this figure, three composition regions can be singled out:

- Very small maximum of the dielectric constant (few hundreds): PYN and PYN-PT 0.05
- Intermediate maximum of dielectric constant (4 000-5 000): from $x=0.10$ to 0.25
- High maximum of the dielectric constant ($>12\,000$): from $x=0.30$ to 0.60

The very small values of the dielectric constant are compatible with the values expected for AFE materials. In the intermediate and high dielectric constant regions, the values are consistent with values of RFE or FE materials.

The value of the maximum dielectric constant peaks within the compositional range $0.45\text{-}0.50$

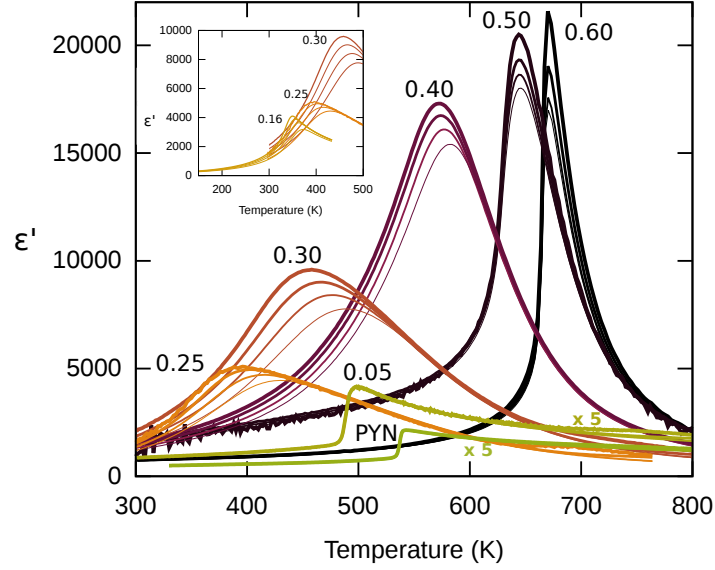


Figure 2.5: Temperature dependence of the dielectric constant ϵ' of PYN-PT ceramics of various selected compositions. The dielectric constant is plotted for 1kHz, 10kHz, 100kHz and 1MHz with decreasing line thickness. Inset: low-temperature measurements

(Fig.2.6) indicating the presence of the MPB in this region, in agreement with literature [19, 47]. However, the peak of the maximum of the dielectric constant at the MPB is *not* as sharp as in other $\text{Pb}(\text{B}'_{1/2}, \text{B}''_{1/2})\text{O}_3\text{-PbTiO}_3$ systems such as $\text{Pb}(\text{Sc}_{1/2}\text{Nb}_{1/2})\text{O}_3\text{-PbTiO}_3$ or $\text{PbZrO}_3\text{-PbTiO}_3$ (Fig.2.2, page 56), i.e. the maximum value of the dielectric constant spreads over a larger compositional range in the PYN-PT solid solution than in the other reported $\text{Pb}(\text{B}'_{1/2}, \text{B}''_{1/2})\text{O}_3\text{-PbTiO}_3$ systems.

I have not synthesized any compositions with PT content larger than 0.60 but it can be inferred from the results reported in literature for the PYN-PT solid solution that the maximum of the dielectric constant will further decrease for composition with $x > 0.60$ as PbTiO_3 has a dielectric constant of 5000.

Moreover the maximum of the dielectric constant evolves little with the composition inside each of the previously categorized regions suggesting that each region corresponds to a polar order.

Despite the obvious change of evolution between the regions of intermediate and high values of the dielectric constant, there is a convergence in these two evolutions for compositions in the 0.25-0.30 range. On the contrary such convergence is absent between the low- and intermediate-regions of dielectric constant.

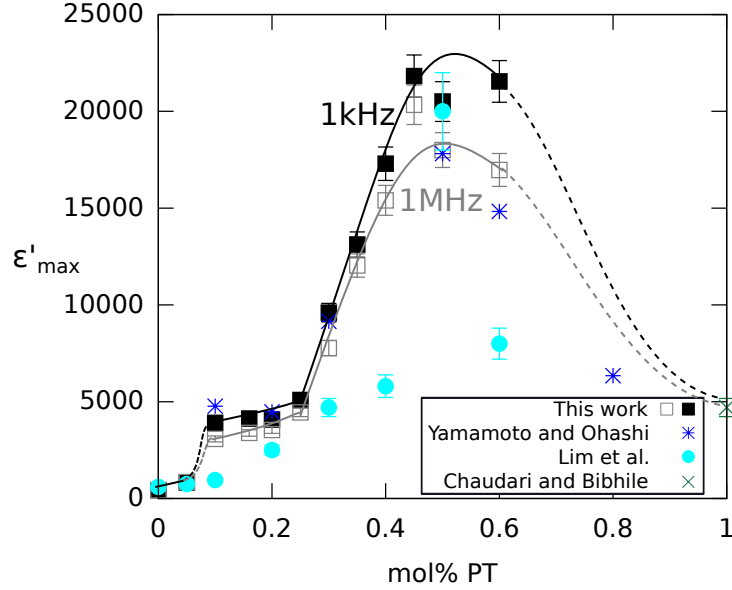


Figure 2.6: Maximum of the dielectric constant for a measuring frequency of 1kHz (solid black squares) and 1MHz (open gray squares) extracted from Fig.2.5. For comparison, the values reported by Yamamoto and Ohashi [19], Lim et al. [46] and Chaudari and Bichile [67]

Peak width

Fig.2.7 displays the width of the dielectric peak as a function of the composition. The width was calculated at several ϵ'_m/n values ($n=1.5$ and 2) and for several frequencies. Even though the actual value of the width depends on the n value, the tendency with the composition remains the same: when increasing the amount of PT, the width decreases up to $x = 0.10$, with larger addition of PT, the width increases, goes through a maximum at $x = 0.25$ and decreases again for higher PT content.

In the case of pure PYN, the large width of the dielectric peak comes from the slow decrease of the dielectric constant above the Curie temperature due to the first-order nature of the phase transition (see Sec.2.4 for details). When PT is added to PYN, the first-order character of the transition decreases causing the width of the dielectric peak to decrease.

However, when large amount of PT is added, the width of the dielectric peak increases indicating that the solid solution present a more and more diffuse character, which is consistent with relaxor behavior. Moreover, the width of the dielectric peak goes through a maximum at $x = 0.25$ indicating that the “maximum of diffuseness” is reached for this composition.

For even larger amount of PT, the width of the dielectric peak decreases signaling that the behavior evolves away from relaxor and toward ferroelectricity based on the large values of the dielectric constant observed for these compositions.

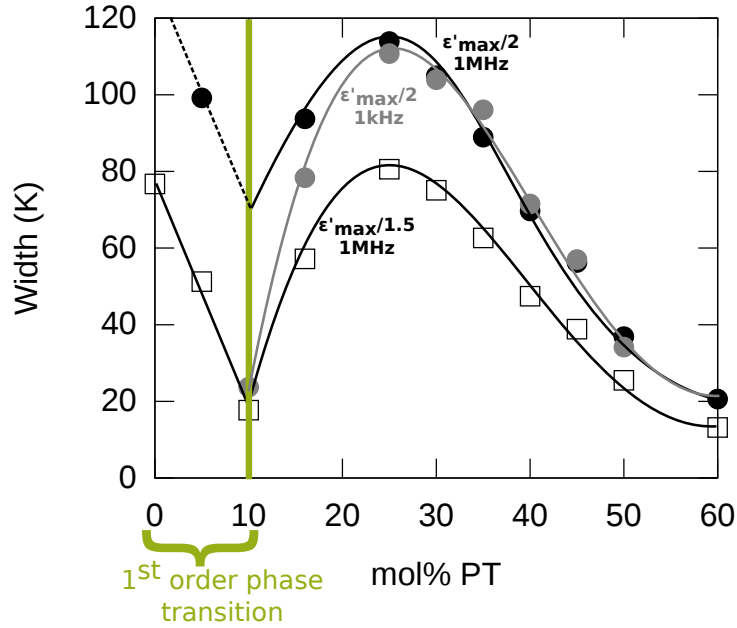


Figure 2.7: Width of the dielectric peak as a function of composition. The width of the peak is taken at $\epsilon'/2$ (fill circles) for 1kHz (grey) and 1MHz (black). The width is taken at $\epsilon'/1.5$ at 1MHz (black open squares)

2.2.2 Influence of frequency

Fig.2.5 shows that for some compositions the measured dielectric constant depends strongly on the measuring frequency (e.g. for PYN-PT 0.30 the maximum of the dielectric constant occurs at different temperatures depending on the measuring frequency).

The dependence of the dielectric constant on frequency is shown in Fig.2.8 where the difference between the temperatures of the maximum of the dielectric constant for frequencies of 1MHz and 1kHz is plotted. The difference between the two maxima is the largest for PYN-PT 0.25. When the composition deviates from this value, the difference decreases smoothly down to almost zero for $x \leq 0.05$ and $x \geq 0.50$.

This maximum of the frequency-dependence at $x = 0.25$ is coherent with the maximum of the width of the dielectric peak (observed in Fig.2.7) for the same composition. This correlation indicates that the diffusivity of the transition at any given frequency is associated with the dependence of T_m on the measuring frequency, supporting the assignment to a relaxor behavior. Thus, for $x = 0.25$, the relaxor behavior is maximal. For $x > 0.25$, the relaxor behavior decreases toward a FE behavior. On the other hand, for $x < 0.25$, the relaxor behavior decreases also, but toward an AFE state (cf Sec.2.4.1, page 71).

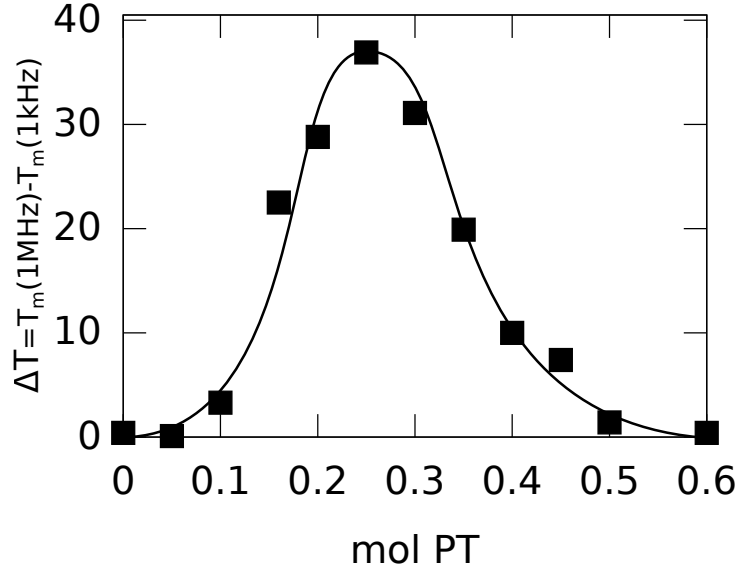


Figure 2.8: Difference between the temperature for which the dielectric constant is maximal when measured at 1MHz and 1kHz corresponding to the thinnest and thickest line respectively in Fig.2.5

Vogel-Fulcher Fitting

Methodology

The Vogel-Fulcher equation (eq.2.2) relates the frequency of the measuring electric field to the temperature of the maximum of the dielectric constant in a relaxor. Fitting this equation enables to determine the activation energy E_a , the freezing temperature T_f and the Debye frequency f_0 . All these parameters describe the dynamic of the polar nanoregions (PNRs) of a relaxor material.

For simplicity, I carried out the fitting procedure using the logarithmic form of the Vogel-Fulcher equation

$$\begin{aligned}
 \text{Vogel-Fulcher law} \quad f &= f_0 \exp \left[\frac{-E_a}{k_B(T_m - T_f)} \right] \\
 \ln f &= \ln f_0 - \frac{E_a}{k_B(T_m - T_f)} \\
 \ln f &= A - \frac{U}{T_m - T_f}
 \end{aligned}$$

Hence the logarithm of the frequency is inversely proportional to T_m and in this case the fitting parameters are $A = \ln f_0$, $U = E_a/k_B$ and T_f .

To ensure that the estimation of A , U and T_f is robust in the resulting fit, the influence of the A parameter was evaluated separately since this fitting parameter is the logarithm of one of the

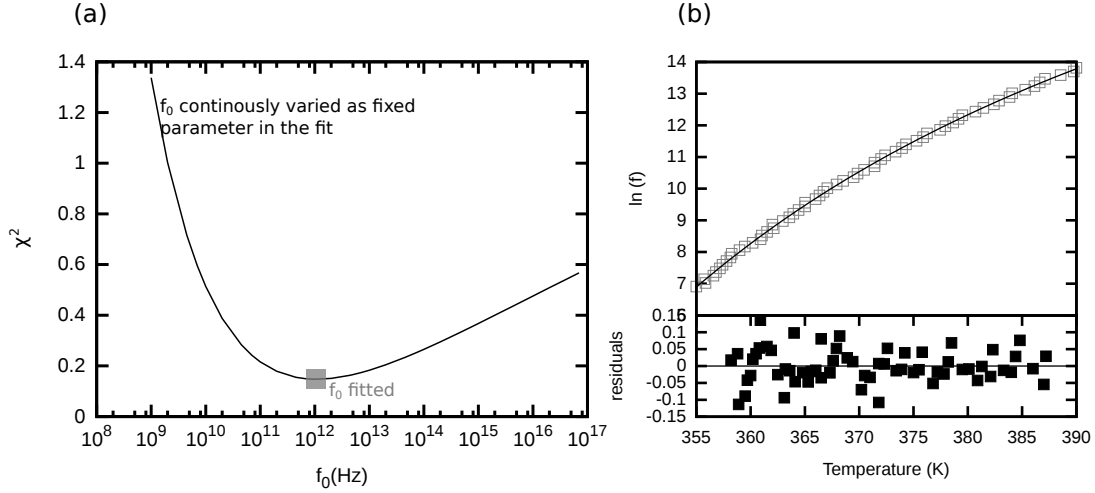


Figure 2.9: Relevance of Vogel-Fulcher for PYN-PT: example of PYN-PT 0.20.

- (a) Influence of f_0 on the quality of the Vogel-Fulcher fit (evaluated using the “least-squares” parameter χ^2).
- (b) Result of Vogel-Fulcher fitting. Residuals are the difference between the fit and the data points.

physically-interesting parameters f_0 and therefore an error on the fit of A leads to major error on the actual f_0 value. Moreover, I observed that a small variation on the f_0 value leads to drastic changes in the E_a and T_f values, whereas varying E_a or T_f have a comparatively smaller influence on the two other parameters.

The influence of the A parameter on the fit was examined by fixing f_0 to a given value (within a physically reasonable frequency range) and conducting the fit with only E_a and T_f as fitting parameters. The quality of the fit for f_0 values between 10^9 and 10^{17} was evaluated using the “least-squares” parameter χ^2 (Fig.2.9).

The error in the fit is minimized for a unique value of f_0 that corresponds to the value obtained when A ($= \ln f_0$) is taken as fitting parameter together with E_a and T_f . Thus A can be taken as a free parameter in the fitting procedure.

I ascertained that the Vogel-Fulcher law was suitable to describe the data by verifying that the residuals of the fit are random (bottom of Fig.2.9(b)). Hence the Vogel-Fulcher law can be used with confidence to describe the data.

Results

The influence of the frequency on T_m was fitted using the same procedure for all compositions showing a frequency-dependence of the dielectric constant: $0.10 \leq x \leq 0.40$.

The activation energy (Fig.2.10(a)) exhibits a maximum of $E_a \sim 0.10$ - 0.15 eV for composition in the range $0.16 \leq x \leq 0.30$. For smaller or larger amount of PT, the activation energy decreases. The freezing temperature T_f has a behavior confirming that compositions in the range $x=0.16$ - 0.30 exhibit relaxor properties. Indeed, the difference between the temperature of the maximum of

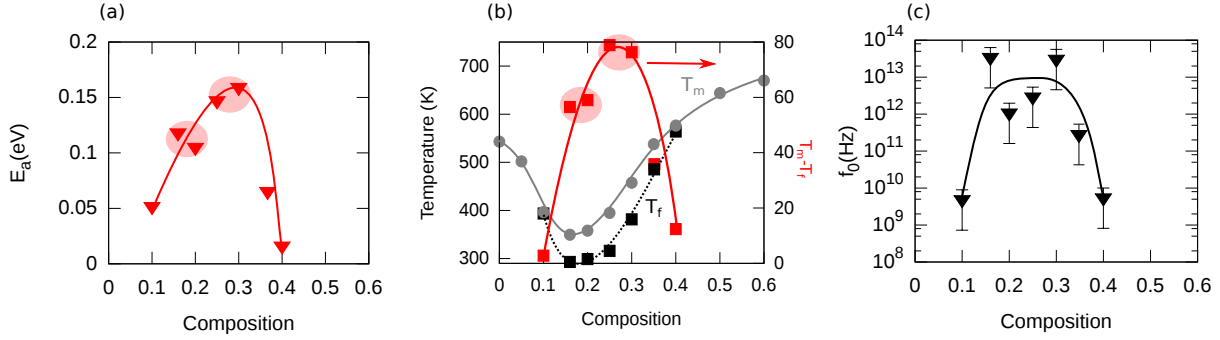


Figure 2.10: Results of the Vogel-Fulcher analysis for different compositions

- (a) Activation energy when f_0 is fitted at the same time as E_a and T_f (solid red triangles)
- (b) Freezing temperature T_f (black squares) and temperature of the maximum of the dielectric constant T_m (gray circles). The difference for each composition is represented by red squares.
- (c) Debye frequency

the dielectric constant and the freezing temperature (Fig.2.10(b)) is large for compositions in this compositional range. Finally this strong relaxor behavior for the compositions $0.16 \leq x \leq 0.30$ is also observed when examining the influence of the composition on the Debye frequency (Fig.2.10(c)): f_0 is large for $0.16 \leq x \leq 0.30$ and small otherwise.

In conclusion, for all compositions displaying frequency-dependent dielectric constant, the frequency and T_m are related by the Vogel-Fulcher law. Furthermore compositions in the range $0.16 \leq x \leq 0.30$ display the strongest relaxor behavior

In the strong relaxation region, the compositions might be divided into two categories: $x = 0.16$ and 0.20 , on the one hand, and $x = 0.25$ and 0.30 on the other hand. Indeed inside a category the values of E_a , $T_m - T_f$ are similar whereas the values are more different between the two categories.

2.2.3 Conclusion about dielectric measurements

From the analysis of the dielectric constant, several conclusions regarding the solid solution PYN-PT can be drawn:

Compositions with $x \leq 0.05$ present a low maximum of the dielectric constant consistent with AFE properties.

The morphotropic phase boundary (MPB) is in the compositional range $0.45 - 0.50$ since these compositions correspond to the maximum of the dielectric constant as a function of composition curve (Fig.2.5).

A dielectric relaxation is observed in the compositional range $0.10 \leq x \leq 0.40$ indicating a re-

laxor behavior. The dielectric relaxation is maximal for $x = 0.25$. A careful Vogel-Fulcher analysis ascertains that the relaxor properties are strong in the range $0.16 \leq x \leq 0.30$.

In conclusion, it appears that the PYN-PT solid solution present an AFE behavior for $x \leq 0.05$ and that compositions with PT content larger than the one of the MPB ($\sim 0.45 - 0.50$) are FE. In the intermediate range the properties change continuously from AFE to relaxor to FE.

2.3 INFLUENCE OF LARGE ELECTRIC FIELD ON THE POLARIZATION AND STRAIN AT ROOM TEMPERATURE

Measurements of polarization and strain as a function of electric field were carried out simultaneously using the commercial piezoelectric evaluation system Aixacct 2000 equipment in association with a so-called “thick-film” sample holder for room temperature measurements and cryofurnace sample holder for measurements between 180 K and 880 K. The measurements were carried out on ceramics sputtered with gold electrodes using a sine function with a 1 Hz frequency.

In contrast to the dielectric measurements reported thus far which were carried out under small electric fields (400 mVpp), the measurements reported hereafter are carried out under much larger electric fields. For the sake of simplicity, measurements of the polarization as a function of electric field will be referred as to “hysteresis” measurements and strain as a function of electric field will be referred to as “strain”.

Fig.2.11 presents the hysteresis and strain measurements for every compositions prepared in this study.

For PYN and PYN-PT 0.05, the polarization is directly proportional to the electric field and no measurable strain is induced by the electric field indicating a dielectric behavior; that is compatible with the low electric-field part of the antiferroelectric behavior. Practically, no larger electric field could be applied because the thickness (~ 0.5 mm) of the samples could not be decreased (thinner samples are extremely fragile) and larger voltage could not be applied because the top electrode burns due to the “imperfect/real” contact with the top contact of the equipment.

PYN-PT 0.10 presents a FE hysteresis loop and a butterfly piezoelectric loop. The measured strain though small ($\sim 0.1 \cdot 10^{-3}$) compared to the strain induced in PYN-PT 0.30-0.50 ($0.5 - 1.5 \cdot 10^{-3}$) was reproducibly measured on several samples.

PYN-PT 0.16 shows a double hysteresis loop that is not perfectly linear at low fields. Likewise, the piezoelectric measurement also presents a double hysteresis loop. These double loops can be due to pinning of a FE cycle by defaults (see Sec.2.1 page 54 for the possible origins of double loops in ferroelectrics) or due to AFE behavior associated with either conduction mechanism or relaxor behavior as the remnant polarization is non-zero.

PYN-PT 0.20 and PYN-PT 0.25 exhibit thin slanted hysteresis loops and electrostrictive be-

havior that are typical of relaxors.

Finally, compositions with $0.30 \leq x \leq 0.60$ show FE hysteresis loops and butterfly-shape piezoelectric loops indicating a FE behavior. In PYN-PT 0.30, the FE hysteresis loop is tilted and the butterfly piezoelectric cycle is strongly influenced by electrostriction probably because this composition appears at the interface between the relaxor and FE compositions.

These hysteresis measurements are in agreement with those of Yamamoto and Ohashi [19] who conducted hysteresis measurements on a more limited set of samples ($x = 0.10, 0.20, 0.30, 0.40, 0.50$ and 0.60). Hence, it would be natural to come to the same conclusion that the PYN-PT solid solution is successively AFE, FE, AFE, RFE and FE again when increasing the PT content. However, I have noted in this section and in Sec.2.1 that double-loops are not always characteristic of antiferroelectricity and that it is possible that PYN-PT 0.16 is not antiferroelectric.

Nonetheless, the careful analysis of the hysteresis and strain measurements as a function of temperature in Sec.2.4.2.3 will show that PYN-PT 0.10 and PYN-PT 0.16 have similar behaviors as a function of temperature and that both compositions undergo a transition from a high-temperature double-loop state (AFE or pinched FE) to a low-temperature FE state. Hence, the FE hysteresis cycle observed for PYN-PT 0.10 and the double loop for PYN-PT 0.16 are related to the same phase sequence, but because of different transition temperatures (above or below room temperature), the two compositions exhibit different behaviors.

Furthermore, the FE hysteresis cycle for PYN-PT 0.10 will be attributed to the effect of the application of a large measuring electric field during the study of the thermal evolution of the hysteresis and strain measurements. Hence, no conclusion regarding the polar state of PYN-PT 0.10 and PYN-PT 0.16 can be drawn based on the room-temperature hysteresis and strain measurements alone.

Finally, the hysteresis and strain measurements reveal that, at room temperature, compositions with $x = 0.20$ and 0.25 exhibit a relaxor behavior and that compositions with $x > 0.30$ show FE properties under strong electric field whereas the FE properties appear for composition with $x \geq 0.45$ under low electric field conditions (dielectric measurements). Therefore, the application of a strong electric field shifts the composition lying on the RFE-FE boundary to lower PT content. Regarding PYN and PYN-PT 0.05, it is only possible to conclude that these compositions exhibit a dielectric behavior that is consistent with non-saturated AFE double loops.

The ferroelectric and piezoelectric properties of PYN-PT within the range $0.30 \leq x \leq 0.60$ will be discussed in Chapter 5.

2.4 PHASE TRANSITIONS

To this point, I have discussed the polar orders present in the solid-solution PYN-PT based on the dielectric properties and polarization-/strain-electric-field relation at room temperature. In

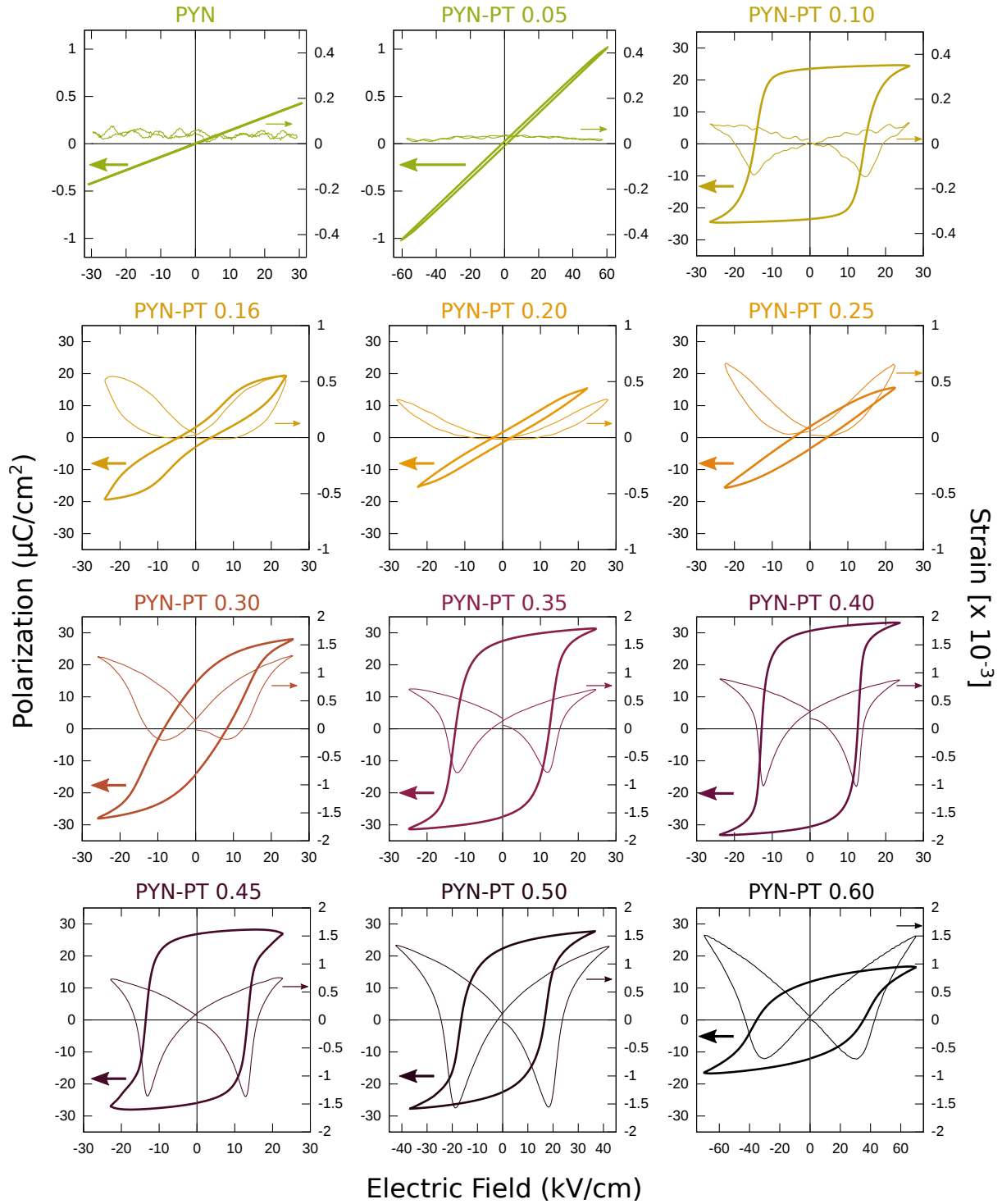


Figure 2.11: Polarization and Strain as a function of Electric Field for all investigated compositions.

For $x \leq 0.10$, the scales for the polarization and the strain are different from the scales for $x \geq 0.16$. For $0.16 \leq x \leq 0.25$ the scale for strain is different from the scale for $x \geq 0.30$.

this section, I will identify the various types of phase transition leading to these polar orders. For that purpose, I will mainly focus on ξ , the derivative of the inverse of the dielectric constant (introduced in Sec.2.1), and on the temperature-dependence of the polarization/strain-electric-field relationships.

2.4.1 AFE

Based on the small values and frequency independence of their dielectric constants, PYN and PYN-PT 0.05 have been established as AFE at room temperature.

These two compositions present a unique maximum in the evolution of the dielectric constant with temperature associated with the transition from the AFE to PE phase. This maximum is reached by a sudden increase of the dielectric constant at the transition (Fig.2.12(a)) indicating a first-order phase transition. The hypothesis of a first-order phase transition is supported by the divergence of ξ at the phase transition (Fig.2.12(b)). Furthermore both PYN and PYN-PT 0.05 show thermal hysteresis (6 K and 3 K, respectively, when the temperature rate is 0.5 K/min) in the dielectric constant confirming again the first-order nature of the phase transition.

Moreover ξ is temperature independent above and below the transition suggesting that the dielectric constant follows the Curie-Weiss law above and below the phase transition, in agreement with the proposed AFE-PE phase transition. Because the transition is of first-order nature, the high-temperature and low-temperature phases should coexist within a temperature region satisfying the following relationship

$$\frac{T_c - T_0}{T_1 - T_0} = \frac{3}{4} \quad (2.8)$$

with T_c the Curie temperature and T_0 and T_1 the low- and high-temperature boundaries of the range of phase coexistence.

In PYN and PYN-PT 0.05, the difference of dielectric constant upon heating or cooling shows a distinct peak (Fig.2.12(c)) indicating the temperature range of coexistence of the high-temperature and low-temperature phases: ~ 25 K for PYN and PYN-PT 0.05.

The Curie temperatures obtained from Eq.(2.8) are in agreement with the ones measured from the maximum of the dielectric constant (Table 2.1) confirming that the thermal hysteresis is due to phase coexistence linked to a first-order phase transition.

Therefore the study of the evolution of the dielectric constant with temperature show a single first-order phase transition between the low temperature AFE phase and the high temperature PE phase.

Existence of an Intermediate Phase?

In the literature, the sequence of phase transition from the high temperature paraelectric phase to the low temperature antiferroelectric phase is still under debate (see Sec.1.4.1). Since in the model AFE material, PbZrO_3 (PZO), the intermediate phase is characterized (among other

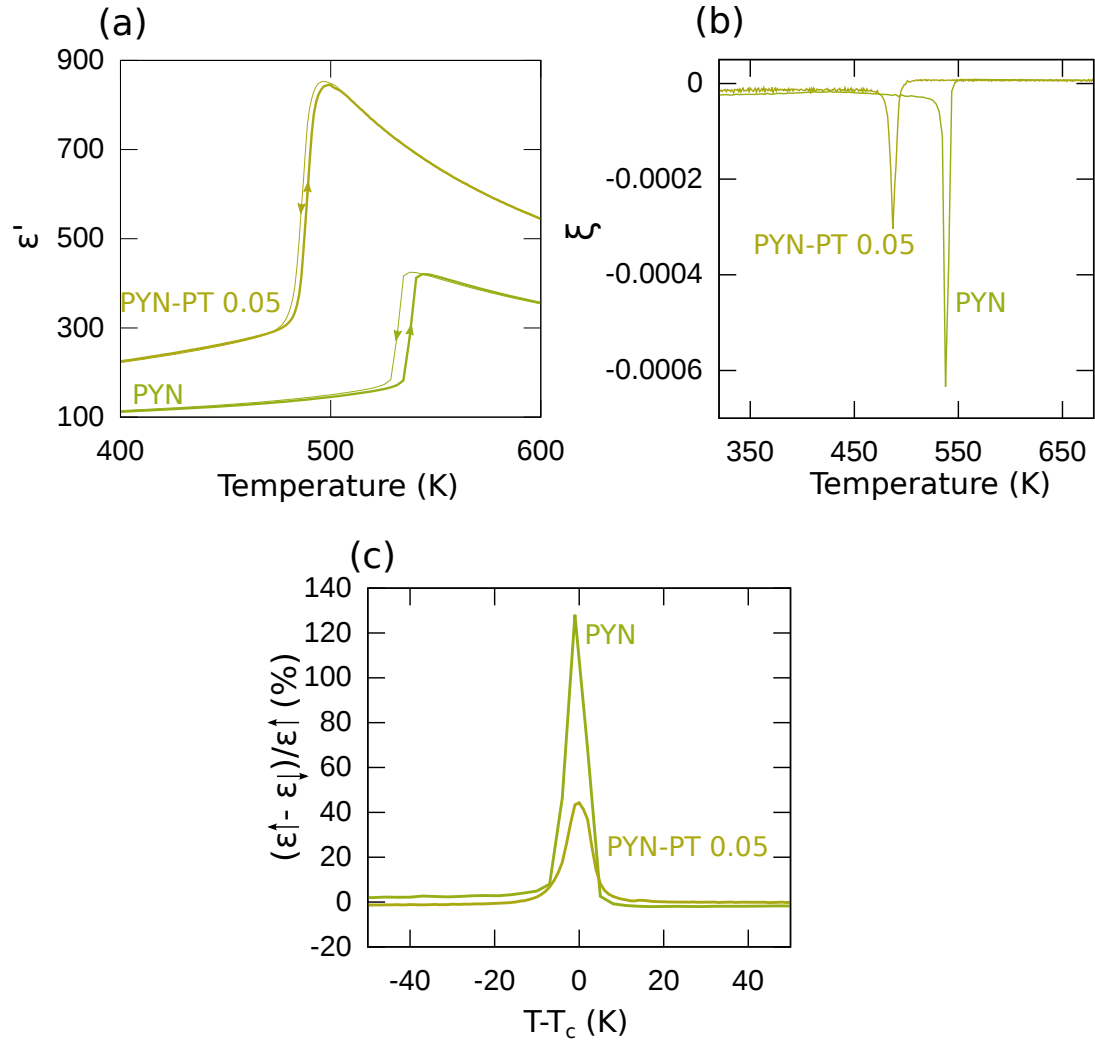


Figure 2.12: (a) Dielectric constant for PYN and PYN-PT 0.05 measured upon heating (thick line) and cooling (thin line).
 (b) ξ for PYN and PYN-PT 0.05 measured upon heating.
 (c) Difference between the dielectric constant measured upon heating and cooling normalized to the dielectric measured upon heating. To facilitate the reading the temperature scale has been shifted by subtracting the value of the T_c measured upon heating.

	T_0	T_1	T_c based on Eq.(2.8)	T_c based on ε'_m
PYN	522±8 K	544±4 K	538.5±17 K	544 K
PYN-PT 0.05	477±3 K	506±2 K	499±7 K	498 K

Table 2.1: Curie temperatures measured from the maximum of the dielectric constant on heating and from the temperature range of phases coexistence for PYN and PYN-PT 0.05. The lower (T_0) and upper (T_1) limits of the difference of dielectric constants are also reported. The measure of T_0 and T_1 is strongly influenced by the percentage of variation taken to consider that the difference between the dielectric constant upon heating and cooling is significant leading to a strong incertitude on the actual values of T_0 and T_1 .

things) by FE hysteresis loops, I have conducted large-field polarization and strain hysteresis measurements as a function of temperature. I have started with measurements on PYN-PT 0.05 since we have seen that PYN-PT 0.05 is extremely similar to PYN and the presence of Ti^{4+} are supposed to help stabilize the FE phase. Hence the would-be-induced-FE phase should exist over a larger temperature range in PYN-PT 0.05 than in PYN making the FE phase easier to find experimentally in PYN-PT 0.05 than in PYN.

No change in the hysteresis behavior with temperature has been evidenced in PYN-PT 0.05: the polarization-electric field hysteresis cycles are dielectric from room temperature to 50 K above T_c (Fig.2.13) suggesting that PYN-PT 0.05 remains AFE up to the PE phase transition for electric field up to 20 kV/cm.

The opening of the hysteresis loops at high temperature may be due to conduction mechanisms since the I-V curves are no longer symmetrical with respect to the X-axis at high temperature and since no current peak that would indicate domain reversal is observed on the I-V curves and since the dielectric losses ($\tan \delta$) are large. However, the possibility that the opening of the loops may be due to the onset of ferroelectricity induced by the large measuring field should not be neglected since it was observed in the archetypal antiferroelectric PbZrO_3 that ferroelectricity can be induced by strong electric fields above Curie temperature [68].

The present hysteresis data do not enable to conclude regarding the existence of a ferroelectric phase above the Curie temperature in PYN-PT 0.05 and further investigations in order to gain better understanding of the opening of the hysteresis loop at high temperature are needed. However, these measurements do not reveal the existence of a ferroelectric phase below the Curie temperature as was reported by Tomashpol'skii and Venevtsev [39] and Demidova et al. [42].

This absence of ferroelectric phase below the Curie temperature is further confirmed by the similarity in the dielectric constants calculated from the polarization-electric field measurements (using eq.(2.1.1) $\varepsilon' \propto \frac{\partial P}{\partial E}$) and the one obtained by the classical impedance measurement method (Fig.2.13). This means that the so-called "high-field" dielectric constant is equal to the "low-field" one. However, as previously mentioned the dielectric losses ($\tan \delta$) become large, at high temperature, and their influence on the dielectric constant calculated from hysteresis measurements can no longer be neglected. Indeed the exacerbation of the dielectric losses by the application of a strong electric field needed for the measurement lead to the opening of the

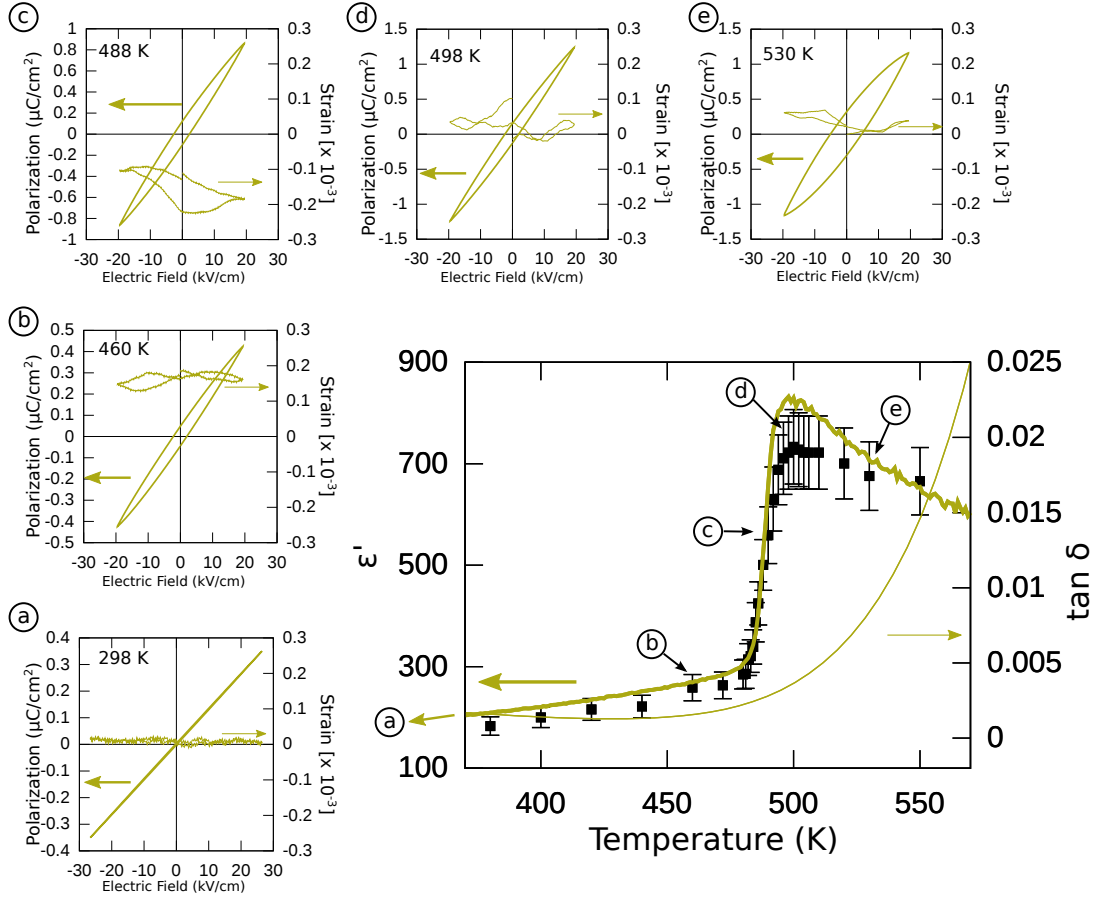


Figure 2.13: Evolution of the real part of the dielectric constant (ϵ') for PYN-PT 0.05 with temperature measured using the impedance method (thick line) and calculated from the hysteresis measurements (black squares) as well as the dielectric losses ($\tan \delta$) (thin line) measured by the impedance method both taken at increasing temperature. A smoothing procedure was used for the plot of $\tan \delta$ to improve the readability of the figure. The significance of the smoothing compared to the raw data was checked. To take into account the difference between the temperature setups, the dielectric constant calculated from the hysteresis measurements are shifted by 20 K.

(a-e) Polarization and strain electric-field dependence at various temperature.

From polarization-electric field measurements, the dielectric constant is calculated by taking the derivative $\frac{\partial P}{\partial E}$ since $P = \epsilon_0 \chi \cdot E$ with $\chi = 1 + \epsilon'$ at small electric field (see Sec.2.1)

hysteresis cycle (at least part of it) and therefore to errors in the calculation of the dielectric constant.

The AFE-PE transition can be unambiguously observed in the thermal evolution of the dielectric constant obtained by the two methods. No intermediate phase is observed even under high electric-field proving that there is only one phase transition in PYN-PT 0.05 even under an electric field up to 20 kV/cm.

Since no intermediate phase was found in PYN-PT 0.05, no hysteresis measurements as a function of temperature were conducted for PYN as I assumed that, if the intermediate phase existed in PYN, its temperature range of existence would be reduced compared to the one of PYN-PT 0.05.

In conclusion, using dielectric and hysteresis measurements as a function of temperature, I observed a single first-order phase transition between the AFE and PE phases in PYN and PYN-PT 0.05. These results are in agreement with the results of Kwon and Choo [40] and Kania [41] and in contradiction of those of Tomashpol'skii and Venevtsev [39] and Demidova et al. [42].

I have suggested in Sec.1.4.1 that the intermediate phase observed by some groups might be due to Pb/O-vacancies. In the present case, the samples were prepared by mechanosynthesis (see Appendix A) that limits the number of Pb/O-vacancies. Thus it is possible that my samples have comparatively lower vacancy densities and that no intermediate phase is to be observed. To confirm the hypothesis of an intermediate phase induced by Pb/O-vacancies, samples with larger amount of vacancies should be prepared possibly by subsequent calcination in lead-free atmosphere or under partial vacuum.

2.4.2 Relaxors

In this section, I will discuss the change of behavior for compositions in the range $0.10 \leq x \leq 0.40$ that were identified as relaxors in Sec.2.2.2 on the basis of their frequency-dependence of the dielectric constant and which appeared RFE (PYN-PT 0.20 and 0.25 and possibly PYN-PT 0.16), FE (PYN-PT 0.10 and PYN-PT with $x \geq 0.30$) in the large-field hysteresis measurements in Sec.2.3.

For that, I will, in a first step, describe the thermal evolution of the dielectric constant, on the one hand, and, on the other hand, the thermal evolution of the hysteresis and strain measurements. Finally, I will review the similarities and differences observed in the thermal evolutions of the low electric field properties (dielectric constant) and the large electric field properties (hysteresis and strain measurements).

Relaxors have been characterized for a long time using three temperatures: the Burns temperature T_B , the maximum of the dielectric constant T_m and the freezing temperature T_f that were introduced in Sec.1.1.4.

In 2008, another critical temperature T^* was proposed to characterized the behavior of relaxors [69]. This temperature corresponds to a nanoscale phase transition of associated with random fields and is independent of the material ($T^* \sim 500$ K). This critical temperature T^* will not be discussed in this Chapter as the dielectric and hysteresis data have not revealed any critical that

could be associated with T^* . T^* will, however, be evidenced when studying the temperature-dependent structural studies (Sec.3.5.2).

In the case of a relaxor-FE phase transition, the Curie temperature T_c is also a characteristic temperature.

T_m and T_f were already discussed in Sec.2.2.2 therefore this section aims to characterize T_B and to find a possible relaxor-ferroelectric phase transition.

Every temperature at which there is a change in behavior in the dielectric constant or in the hysteresis and strain measurements will be summarized in Fig.2.21.

2.4.2.1 Evolution of dielectric constant as a function of temperature

Despite different large-electric-field properties, all compositions with x in the range [0.10:0.40] exhibit a strong relaxation of the dielectric constant that can be fitted with a Vogel-Fulcher law (Sec.2.2.2). Therefore, in this section focusing solely on the study of the thermal evolution of the dielectric constant, all of these compositions will be regarded as relaxors. The possible disparity between the results obtained in this section (i.e. low electric field results) and the ones of the next section (i.e. large electric field properties) will be addressed in Sec.2.4.2.4.

The dielectric constant of relaxors follows the Curie-Weiss law above T_B , but not below T_B . This change of behavior in dielectric constant translates into a change of slope in the derivative of the inverse of the dielectric constant ξ with respect to temperature (see Sec.2.1): above T_B , ξ is temperature independent whereas it depends strongly on temperature below T_B .

Only for compositions with $x < 0.25$ is it possible to see a plateau in the evolution of ξ (Fig.2.14-2.15) and therefore to determine T_B , even though the temperature range investigated goes up to 850 K.

However, in the case of PYN-PT 0.16 and PYN-PT 0.20, ξ does not remain temperature independent at high temperature (it can be inferred from Fig.2.14 and more clearly seen in Fig.2.18 for PYN-PT 0.16). This different high-temperature behavior of ξ is probably not due to conduction mechanisms, since ξ increases with temperature at high temperature, whereas ξ tends to decrease with temperature when the dielectric constant is dominated by conduction. Thus, the low temperature at which ξ deviates from the plateau for PYN-PT 0.16 and PYN-PT 0.20 may not be the "usual" Burns temperature, T_B .

The change of behavior of the dielectric constant at T_B is due to the appearance of polar nanoregions (PNRs) that induce frequency dependence in the dielectric constant. Thus in order to have a lower limit for T_B , we resorted to study the appearance of frequency dependence in the dielectric constant by calculating the difference between the dielectric constant values measured at two frequencies.

The evolution of the dispersion of the dielectric constant with frequency as a function of temperature (Fig.2.16) reveals two regions where the dispersion is large. The dispersion at high temperature is believed to be due to conduction since for these compositions the dielectric losses $\tan \delta$ are large. On the other hand, the dispersion that appears at lower temperature (~ 400 -

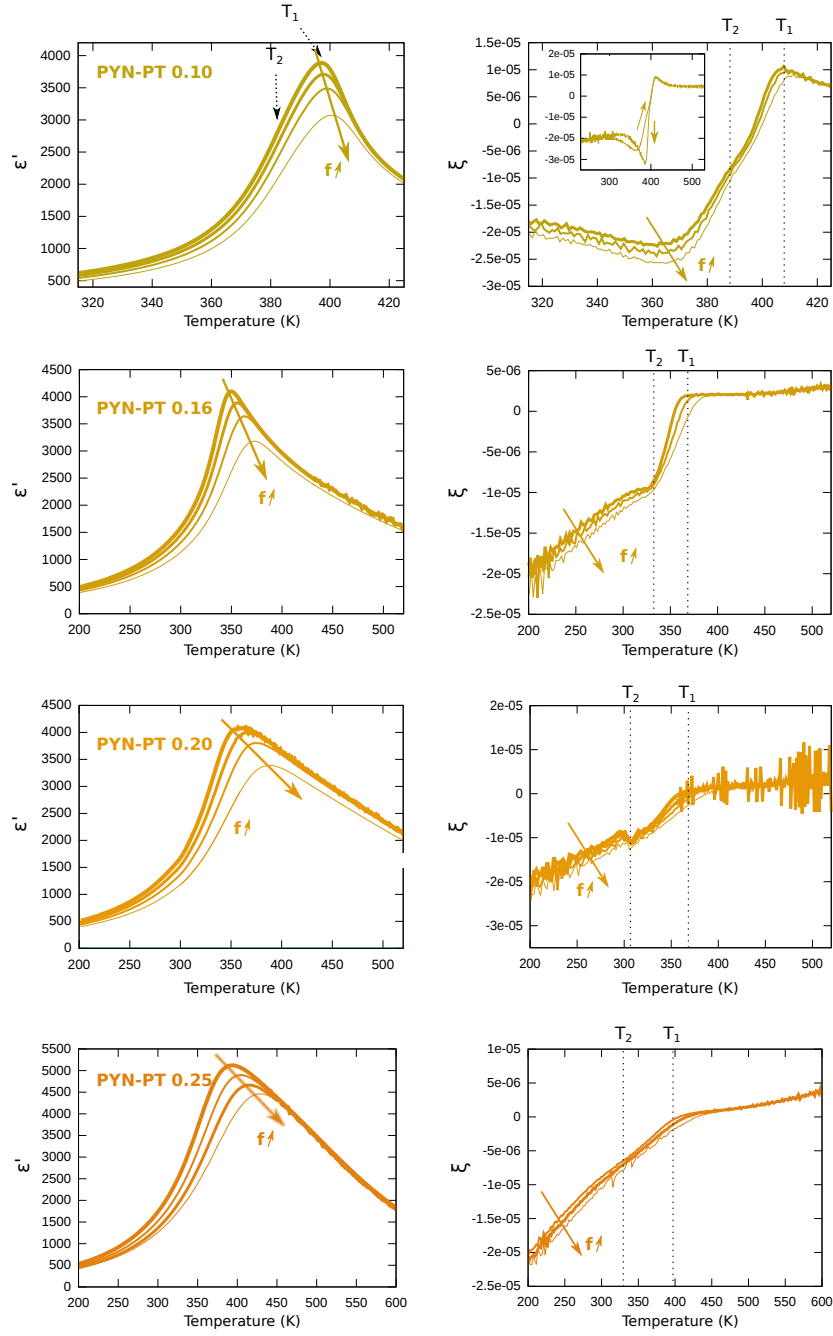


Figure 2.14: Evolution of the dielectric constant ϵ' and the derivative of the inverse of the dielectric constant ξ with temperature for PYN-PT $x = 0.10-0.25$ for 1 kHz, 10 kHz, 100 kHz and 1 MHz (decreasing line thickness).

The inset for PYN-PT 0.10 display the thermal evolution of ξ upon heating (thin line) and cooling (thick line). For the other compositions, the thermal evolution of both ϵ' and ξ do not show any difference.

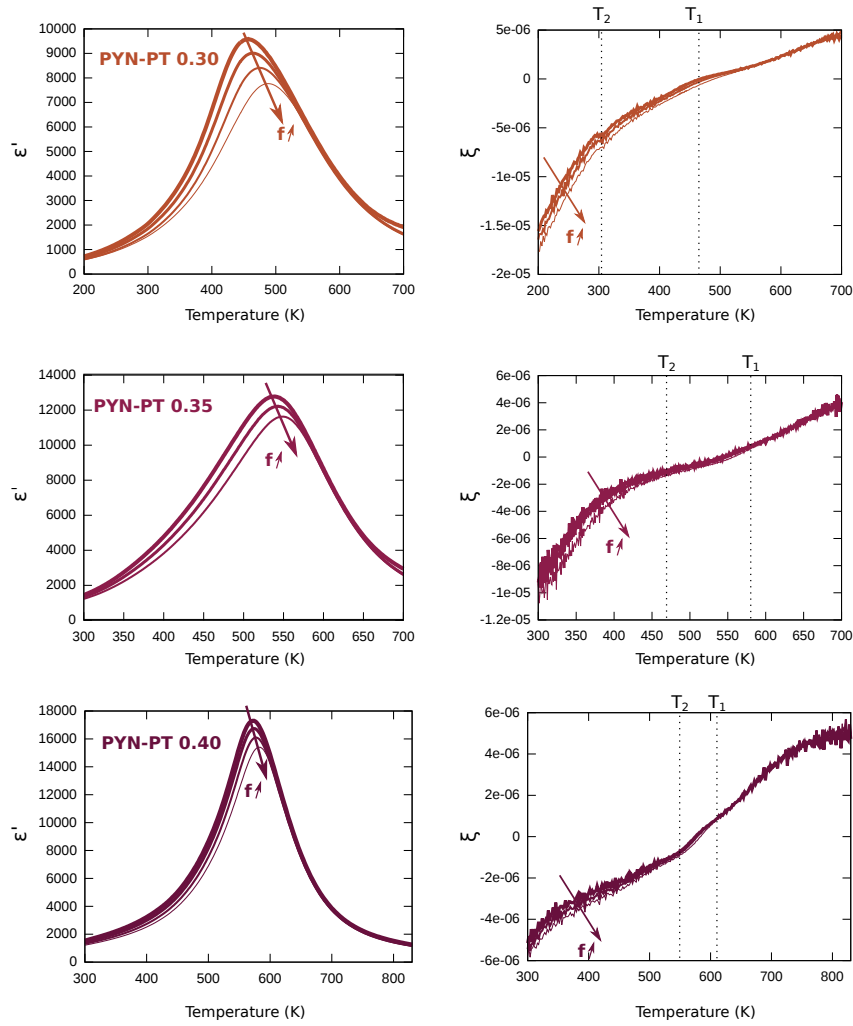


Figure 2.15: Evolution of the dielectric constant ϵ' and the derivative of the inverse of the dielectric constant ξ with temperature for PYN-PT $x = 0.30-0.40$

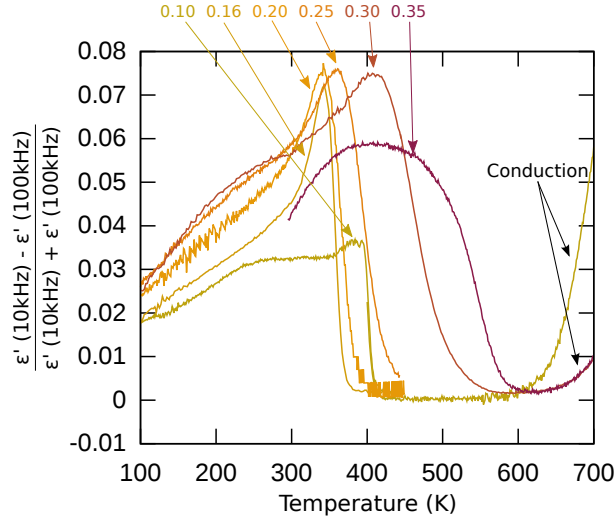


Figure 2.16: Normalized difference of the dielectric constant ϵ' for 10 kHz and 100 kHz for compositions in the range $0.10 \leq x \leq 0.35$.

600 K depending on the composition) is believed to be due to PNRs. Hence, it is possible to measure the temperature at which the PNRs have a dielectric response that is strong enough to be measured. This temperature is lower than T_B and strongly depends on the composition, whereas, in other Pb-based solid solutions, T_B was found to be rather composition independent. Thus, the temperature at which the PNRs have a dielectric response strong enough to be measured increases with Ti content indicating that the size of PNRs increase with the Ti amount at a given temperature, considering that PNRs with comparable sizes give comparable dielectric response. This increase of the size of the PNRs with the amount of Ti will be confirmed by the high-temperature diffraction measurements of Sec.3.5

In conclusion, the present dielectric measurements do not enable the determination of the Burns temperature T_B (or the temperature of the deviation from the Curie-Weiss behavior) but for compositions in the range $0.10 \leq x \leq 0.20$. For compositions in the range $0.25 \leq x \leq 0.40$, studying the appearance of dielectric dispersion has not shed any light on the value of T_B in this compositional range, but it appeared that the size of PNRs increase with increasing the Ti content.

In the thermal evolution of ξ , two significant changes of behavior can be identified at temperatures T_1 and T_2 in Fig.2.14-2.15. The change of behavior at the highest temperature, T_1 , is strongly frequency dependent and corresponds well to T_m .

The second change of behavior at T_2 is more intriguing since the behavior below T_2 is not the same for all compositions. Indeed, ξ does not follow the Curie-Weiss law below T_2 (i.e. $\xi \neq \text{constant}$) for every relaxor compositions, except for $x=0.10$. Hence it seems that *only in the case of PYN-PT 0.10*, T_2 would correspond to a Curie temperature T_c toward a low temperature FE phase (based on the high-field measurements Sec.2.3) or AFE phase (based on

the observation of SSRs in the X-ray pattern Sec.3.5.2). Actually, the temperature-dependent diffraction experiments will show a change in the local structure at about 370 K (labeled T_2^*) that correspond to the minimum of ξ . This difference between the critical temperatures will be discussed and reconciled in Chapter 4.

For the other compositions, no such low temperature AFE or FE phase is observed as ξ does not follow the Curie-Weiss law below T_2 .

Another difference in the change of behavior at T_2 between PYN-PT 0.10 and the other relaxor compositions is that the temperature T_2 is different upon cooling and heating for PYN-PT 0.10 (inset of Fig.2.14) whereas T_2 is the same upon cooling and heating for the other compositions. Furthermore, in the compositional range $x = 0.25-0.40$, the change of behavior at T_2 is not as marked as in the compositional range $x = 0.10-0.20$ since in the compositional range $x = 0.25-0.40$, T_2 is associated only with a diminution of the frequency dependence of ξ and not anymore with a change of slope.

In conclusion, there is a change of behavior at a temperature T_2 for compositions in the range $0.10 \leq x \leq 0.20$ and possibly for compositions in the range $0.25 \leq x \leq 0.40$.

For $x = 0.10$, the low temperature phase follows the Curie-Weiss law.

For PYN-PT 0.16 and PYN-PT 0.20, T_2 is only associated with a change of slope of ξ indicating a potential change of behavior of the dynamics of the PNRs.

For PYN-PT 0.10, PYN-PT 0.35 and PYN-PT 0.40, the temperature T_2 corresponds well to the freezing temperature T_f measured using the Vogel-Fulcher equation in Sec.2.2.2. Therefore, it is likely, that the change of dynamics of the PNRs at T_2 is related to the freezing of the PNRs for these compositions.

For the other compositions, the change of behavior is not related to the freezing of the PNRs and an attempt at explaining this change of behavior will be given in Chapter 4.

2.4.2.2 Critical exponent

In Sec.2.1 were described the different models proposed in literature to explain the evolution of dielectric constant with temperature. In this section, I will try to fit the various model to our data to characterize the degree of relaxation in the PYN-PT solid solution.

Model proposed by Bokov and Ye

The model developed by Bokov and Ye [22] (Eq.(2.4) page 57) has been shown to hold for a larger temperature range than the modified Curie-Weiss one and for a large number of compositions [6]. The model is fitted to the data using the following transformation of the equation

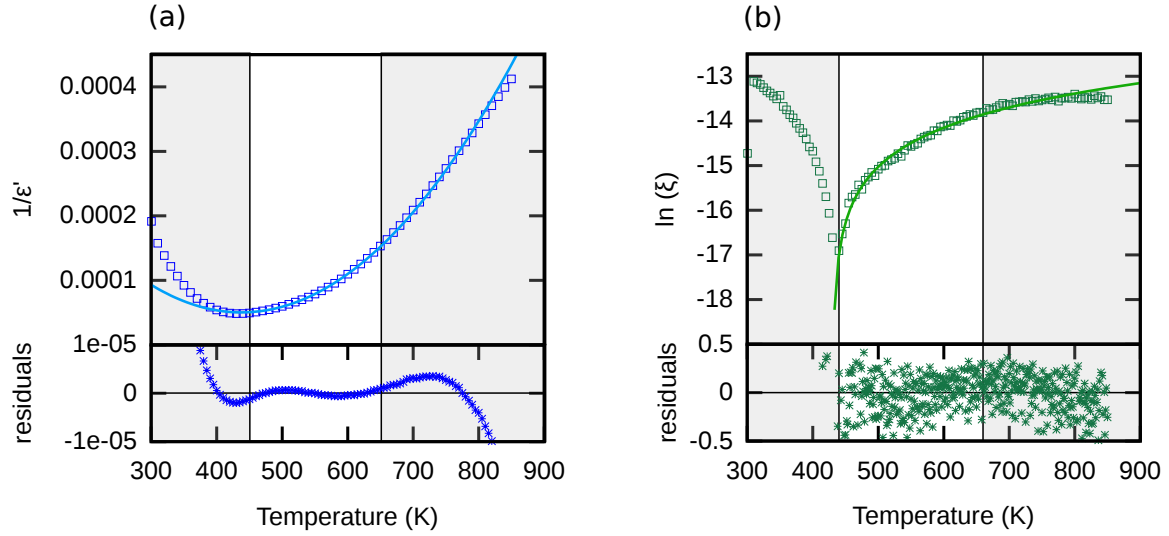


Figure 2.17: Fit of PYN-PT 0.25 to the different models proposed to described the behavior of relaxors. The regions excluded from the fit are darkened.

(a) Eq.(2.4): model proposed by Bokov and Ye [22]

(b) Eq.(2.3): modified Curie-Weiss law

proposed

$$\begin{aligned}
 \text{Eq.(2.4)} \quad \frac{\epsilon_A}{\epsilon'} - 1 &= \frac{(T - T_A)^2}{2\delta^2} \\
 \frac{\epsilon_A}{\epsilon'} &= \frac{(T - T_A)^2}{2\delta^2} + 1 \\
 \frac{1}{\epsilon'} &= \underbrace{\frac{1}{\epsilon_A}}_B \cdot \underbrace{\frac{1}{2\delta^2}}_A \cdot (T - T_A)^2 + \underbrace{\frac{1}{\epsilon_A}}_B
 \end{aligned}$$

In this case, the fitting parameters are A , B and T_A . The fit was conducted on various temperature ranges in order to find the best agreement.

For PYN-PT 0.10, 0.16 and 0.20 it is not possible to fit such law to the measured dielectric constant. For compositions with $0.25 \leq x \leq 0.40$, the fit using the model proposed by Bokov and Ye is not completely satisfactory since the residuals are not randomly distributed. However, the values obtained for δ are not too far from the one reported in the literature (Table 2.2).

Bokov and Ye underlined in their paper that when applying this model to other systems “it is necessary to keep in mind that any additional nonrelaxor polarization process giving rise to a significant contribution to the dielectric constant can disturb the scaling”[22]. Thus, it is possible that in PYN-PT additional contributions come in addition to the relaxor one such as conduction or another type of relaxor behavior.

In Sec.3.3.2 (page 113), we will see that compositions with $x \leq 0.35$ exhibit chemical ordering. In

Material	$T_m(\text{kHz})$	T_A	δ	$10^{-2}\varepsilon_A$	Ref
PYN-PT 0.10	399	x	x	x	This work
PYN-PT 0.16	396	x	x	x	This work
PYN-PT 0.20	358	x	x	x	This work
PYN-PT 0.25	395	437	106	199	This work
PYN-PT 0.30	458	471	79	91	This work
PYN-PT 0.35	538	554	56	114	This work
PYN-PT 0.40	576	581	48	153	This work
$\text{Pb}(\text{Mg}_{1/3}\text{Nb}_{2/3})\text{O}_3$	276	262	41	206	[65]
$\text{Pb}(\text{Sc}_{1/2}\text{Nb}_{1/2})\text{O}_3$	380	348	36	567	[65]
$\text{Pb}(\text{Zn}_{1/3}\text{Nb}_{2/3})\text{O}_3$	424	416	28	419	[65]
$\text{Pb}(\text{In}_{1/2}\text{Nb}_{1/2})\text{O}_3$	370	338	109	77	[65]
0.42 $\text{Pb}(\text{Sc}_{1/2}\text{Nb}_{1/2})\text{O}_3$ -0.58 $\text{Ba}(\text{Sc}_{1/2}\text{Nb}_{1/2})\text{O}_3$	92	39	332	3.8	[65]
0.92 $\text{Pb}(\text{Sc}_{1/2}\text{Nb}_{1/2})\text{O}_3$ -0.08 $\text{Ba}(\text{Sc}_{1/2}\text{Nb}_{1/2})\text{O}_3$	321	294	81	115	[65]

Table 2.2: Fitted parameters obtained from the model proposed by Bokov and Ye for PYN-PT compared to the values they reported.

x indicates that it is not possible to fit the dielectric constant using this model.

this case, it is possible that PYN-PT is the siege of two relaxation mechanisms: one associated with chemically ordered regions and one with chemically disordered regions. The possibility of having different polar orders due to different chemical orders will be detailed in Chapter 4

In particular, compositions for which the chemical order is low or non-existent (PYN-PT 0.35 and PYN-PT 0.40), δ is comparatively small (~ 50) and close to the value obtained for classical relaxor materials such as $\text{Pb}(\text{Mg}_{1/3}\text{Nb}_{2/3})\text{O}_3$ or disordered $\text{Pb}(\text{Sc}_{1/2}\text{Nb}_{1/2})\text{O}_3$, whereas in the case of compositions for which the chemical order is strong (PYN-PT 0.25 and PYN-PT 0.30), δ is large (~ 90) and close to the value obtained for non-classical relaxor materials such as $\text{Pb}(\text{Sc}_{1/2}\text{Nb}_{1/2})\text{O}_3$ - $\text{Ba}(\text{Sc}_{1/2}\text{Nb}_{1/2})\text{O}_3$ or $\text{Pb}(\text{In}_{1/2}\text{Nb}_{1/2})\text{O}_3$.

“Classical” relaxors (e.g. $\text{Pb}(\text{Mg}_{1/3}\text{Nb}_{2/3})\text{O}_3$ or $\text{Pb}(\text{Zn}_{1/3}\text{Nb}_{2/3})\text{O}_3$) have surprisingly lower values of δ compared to the “non-classical” relaxors (e.g. $\text{Pb}(\text{In}_{1/2}\text{Nb}_{1/2})\text{O}_3$) whereas, for fixed values of ε_A and T_A , larger δ values lead to wider dielectric peak and therefore larger diffusivity.

The thermal evolution of the dielectric constant of PYN-PT with $0.25 \leq x \leq 0.40$ cannot be completely explained by the model proposed by Bokov and Ye and therefore a model with a critical exponent different from 2 will be investigated.

x	0.10	0.16	0.20	0.25	0.30	0.35	0.40
γ	1.00	1.75	1.94	2.12	1.98	2.08	1.95

Table 2.3: Critical exponent for various compositions.

The value reported is the one obtained for the fitting range leading to the lowest χ^2 (best agreement factor). Depending on the fitting range and for comparable values of χ^2 , γ can vary by ± 0.05 (except for 0.10 for which the value of γ does not depend on the fitting range). The value reported for $x = 0.16-0.20$ is the one fitted only at high temperature.

Critical exponent different from 2

The other model proposed to describe the dielectric behavior of relaxor materials is the modified Curie-Weiss law. For simplicity, the fitting procedure was conducted using the logarithm of the derivative of the inverse of the dielectric constant.

$$\begin{aligned}
 \text{Eq.(2.3)} \quad \xi &= \frac{1}{\varepsilon_m} \cdot B \cdot \gamma \cdot (T - T_m)^{\gamma-1} \\
 \ln \xi &= \underbrace{\ln\left(\frac{1}{\varepsilon_m} \cdot B \cdot \gamma\right)}_C + \underbrace{(\gamma - 1)}_D \ln(T - T_m) \\
 \ln \xi &= C + D \ln(T - T_m)
 \end{aligned}$$

Also deriving the model proposed by Bokov and Ye [22] leads to similar results the only difference being the definition of $C(= \frac{1}{\varepsilon_A \cdot 2\delta^2} \cdot \gamma)$ and $D(= \gamma - 1$ with $\gamma = 2)$. Hence, using this methodology, fitting the modified Curie-Weiss law leads to the exact same result, in terms of fitting parameters, as fitting the model proposed by Bokov and Ye allowing the critical exponent γ to differ from 2 (as it was proposed in their first paper proposing this model). The physical meaning of the underlying physical constant nevertheless remains different. As in the previous case, the fit will be conducted on various temperature ranges to find the best possible agreement factor.

For PYN-PT with $x=0.25-0.40$, the fit with a critical exponent different from 2 is more satisfactory since the difference between the fit and the data is completely random (see an example in Fig.2.17(b)).

The value of the critical exponent obtained for the various compositions (Table 2.3) when refined are closed to 2. Hence, the thermal evolution of the dielectric constant can be interpreted with both the modified Curie-Weiss law and the model proposed by Bokov and Ye if the critical exponent is allowed to differ slightly from 2.

For PYN-PT 0.10, the fitting of the critical exponent leads to a value of 1 with very low uncertainty since this value does not depend on the temperature fitting range. Hence, for this composition, the dielectric constant can be described by a Curie-Weiss law (as was observed in Sec.2.4.2.1). It therefore seems to indicate that this composition is not really a relaxor despite the frequency-dependency of T_m that can be modeled with a Vogel-Fulcher law.

For PYN-PT 0.16 and PYN-PT 0.20, it is not possible to conduct a satisfying fitting procedure on a temperature range including the temperature just above T_m , but a satisfactory fit can be obtained over a temperature range starting higher than 500 K (Fig.2.18). Thus, these composi-

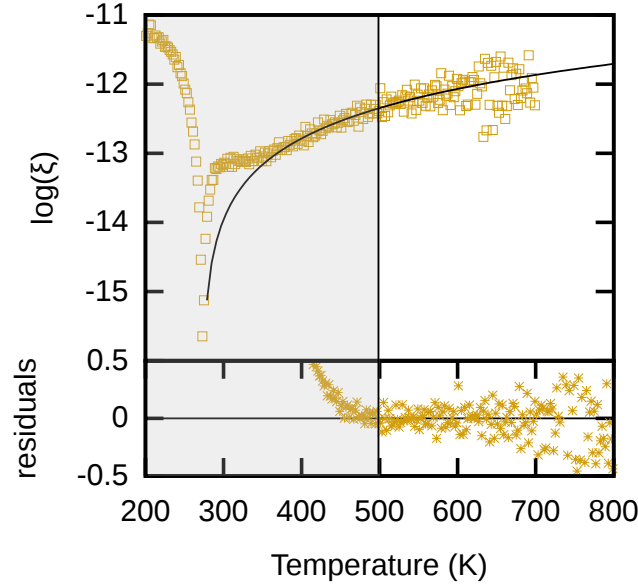


Figure 2.18: Fit of PYN-PT 0.16 with the critical exponent different from 2.

tions follow a modified Curie-Weiss law at high temperature and a Curie-Weiss law close to T_m (as indicated by the temperature-independent value of ξ in Fig.2.14 page 77). The high temperature behavior may not be ascribed to conduction mechanisms since, at high-temperature, ξ increases with temperature whereas if conduction was responsible for the thermal dependency of ξ , it would decrease with increasing temperature. Thus, the dielectric constant of PYN-PT 0.16 and PYN-PT 0.20 behaves as if the material displayed a relaxor behavior at high temperature and underwent, upon cooling, a phase transition toward a paraelectric, ferroelectric or antiferroelectric state at a temperature above T_m .

In conclusion, several behaviors have been observed in the compositional range of the PYN-PT solid solution that have been shown in Sec.2.2.2 to present a dielectric relaxation ($0.10 \leq x \leq 0.40$):

PYN-PT 0.10 follows the Curie-Weiss law above T_m even though the dielectric constant shows a distinct relaxation at T_m

PYN-PT $x=0.16-0.20$ follows the Curie-Weiss law on a temperature interval above the maximum of the dielectric constant ($T < T_m + 100$), but for larger temperatures, the dielectric constant may be described using the modified Curie-Weiss law that has been developed for relaxors.

PYN-PT $x=0.25-0.40$ follows a modified Curie-Weiss law or the model proposed by Bokov and Ye provided a critical exponent slightly different from 2.

The intrinsic error (± 0.05) of the fitting of a critical exponent makes it difficult to compare the values obtained for the various relaxor compositions. It is clear that, in the case of PYN-PT, the

value of the critical exponent is not precisely 2 since the fit conducted with the model derived by Bokov and Ye is not satisfactory, but the critical exponent remains close to 2 in agreement with what is expected for relaxors.

2.4.2.3 Evolution of the large electric field properties as a function of temperature

In Sec.2.3, for all synthesized compositions in the PYN-PT phase diagram, the room-temperature hysteresis and strain measurements carried out simultaneously using the LASER-interferometer based a commercial evaluation system were discussed. Hereafter, I will present the evolution of the hysteresis and strain measurements with temperature. The evolution of the piezoelectric coefficient d_{33} with temperature will be examined in Sec.5.2.2 (page 205).

PYN-PT 0.10 has been shown in Sec.2.3 to have a FE behavior at room temperature. This FE behavior persists up to 400K. Above 405K, the FE cycle becomes pinched and the pinching becomes stronger and stronger with increasing temperature. No hysteresis cycles are observed above ~ 420 K.

PYN-PT 0.16 has a thermal behavior similar to PYN-PT 0.10: FE cycle below 263 K, a pinched FE cycle between 263 K and 338 K and no hysteresis cycle above 338 K.

For these two compositions, the pinching of the FE hysteresis loops is associated with a maximum of the piezoelectric coefficient d_{33} (see Fig.5.4 page 206). Moreover, these compositions show surprisingly low piezoelectric coefficient d_{33} (~ 40 -80 pC/N) even when the FE cycles are well saturated.

PYN-PT 0.20-0.25-0.30 do not show hard square FE cycles but soft tilted FE cycles (see Fig.2.11 page 70). The cycles become softer and softer (i.e. the coercive field lowers) when the temperature increases and the cycles disappear completely at $T=322, 323, 423$ K respectively for 0.20-0.25-0.30.

Moreover, for these compositions, there is a maximum of d_{33} at a temperature 50 to 100 degrees lower than T_f (see Fig.5.4)

PYN-PT 0.35-0.40 exhibit a hard FE cycle at room temperature that persists up to T_m . A maximum of the piezoelectric constant d_{33} can be observed at 420 K and 490 K for $x = 0.35$ and $x = 0.40$, respectively (Fig.5.4).

Therefore, in all compositions presenting a frequency-dependence of the maximum of the dielectric constant ($0.10 \leq x \leq 0.40$), a maximum of the piezoelectric coefficient d_{33} can be observed. This maximum of d_{33} is related to a phase transition induced by the application of the strong electric field required to carry out the hysteresis and strain measurements.

Indeed the thermal evolution of the dielectric constant measured from the slope of the polarization-electric field cycles differs from the one of the dielectric constant measured using the impedance method shows the presence of a phase transition for PYN-PT 0.30 (Fig.2.19). The evolution of the large-field dielectric constant below the phase transition can be fitted to the Curie-Weiss

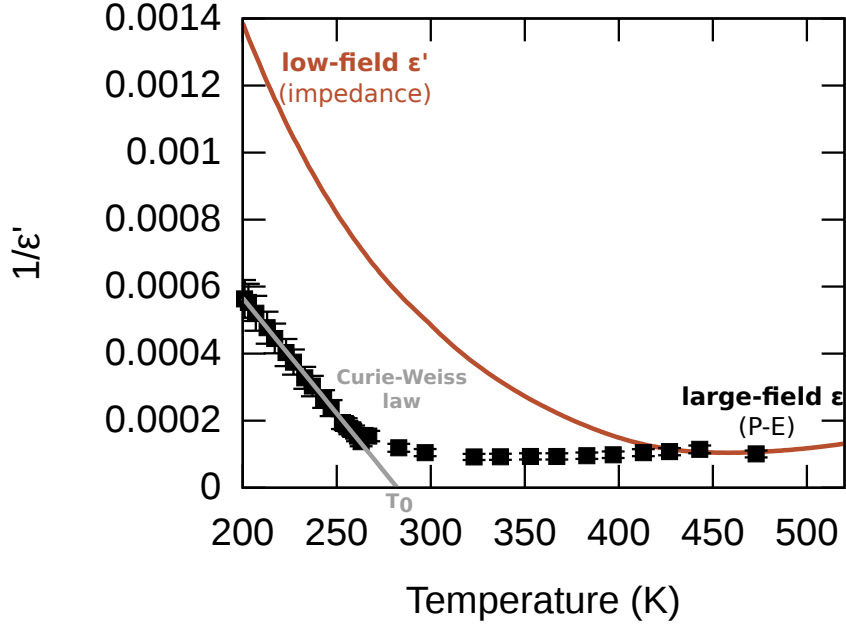


Figure 2.19: Evolution of the real part of the dielectric constant (ϵ') for PYN-PT 0.30 with temperature measured using the impedance method (line) and calculated from the hysteresis measurements (black squares)

From polarization-electric field measurements, the dielectric constant is calculated by taking the derivative $\frac{\partial P}{\partial E}$ since $P = \epsilon_0 \chi \cdot E$ with $\chi = 1 + \epsilon'$ at small electric field (see Sec.2.1) The low-temperature large-field dielectric constant is fitted using the Curie-Weiss law $\frac{1}{\epsilon'} = \frac{T - T_0}{C}$.

law and the fitted critical temperature (labeled T_0 in Fig.2.19) corresponds to the maximum of the piezoelectric coefficient d_{33} .

For compositions in the range $0.16 \leq x \leq 0.25$ and PYN-PT 0.35, similar analysis may be conducted, but the limited number of data points available does not allow clear conclusions. For PYN-PT 0.40, the large-field dielectric constant was not determined, but the poled dielectric constant was measured and the maximum of the piezoelectric coefficient d_{33} can be undoubtedly ascribed to a change induced by the poling (See Sec.5.2.2 for details).

Therefore, the maximum of the piezoelectric coefficient d_{33} observed using large field polarization and strain measurements is electric-field induced.

Nevertheless, the effect of the electric field is different depending on the composition. Indeed, in the case of PYN-PT with $0.30 \leq x \leq 0.40$, the maximum of d_{33} is related to a transition between two ferroelectric phases (detailed in Chapter 5), whereas in the case of PYN-PT with $0.10 \leq x \leq 0.25$, the transition is related to the presence of a second current peak in the I-V measurements. The change of behavior of this second current peak will be associated to an AFE-FE relationship, in the following.

For relaxor compositions in the range $0.10 \leq x \leq 0.25$, in the I-V measurements, a second current

peak (labeled (2)) exists in addition to the current peak due to domains reversal (labeled (1)) as illustrated in Fig.2.20. The presence of the second peak is surprising since, for FE and RFE samples, only one current peak is expected when monotonically changing the voltage. Indeed the current is the time derivative of the polarization and one expect the current to peak when the change of polarization with the voltage is the largest, i.e. at the coercive field when the polarization rotates to align with the applied electric field. Thus, a second current peak in the I-V curves is a peculiar behavior for the relaxor compositions present in the PYN-PT solid solution and the evolution of this current peak will be detailed hereafter.

At low temperature, this second current peak is close to the peak due to domains reversal. When temperature increases, the critical voltage of the second peak decreases linearly. Actually, the critical voltage decreases so much with temperature that its value becomes negative inducing the pinching of the hysteresis loops observed for PYN-PT 0.10 and PYN-PT 0.16. For the other compositions ($x = 0.20 - 0.25$), the critical voltage of the second peak also becomes negative for high enough temperatures, but the current of this peak is so small that its influence on the polarization is negligible.

For all compositions, when the critical voltage of the second peak is zero the piezoelectric coefficient d_{33} goes through a maximum. The temperature of this maximum will be referred to as T_3 hereafter. (An explanation of the increase of the piezoelectric coefficient d_{33} at T_3 associated with the change in the I-V measurements is provided in Chapter 5 page 205.)

In the I-V curves, the presence of a second peak with the sign of its critical voltage opposite to the one of the classical FE domain switching peak usually leads to a double-loop P-E hysteresis cycle. This double loop can be due either to an AFE phase or to a FE phase with defects pinning the domain motion (see Sec.2.1.3). On the other hand, the presence of a second peak with the same sign of critical voltage as the classical FE domain switching peak can be simply due to the presence of two phases that have different, but close, coercive fields, i.e. the material is analogous to a composite.

Thus, below T_3 , PYN-PT can be seen as a composite of two ferroelectric phases and, above T_3 PYN-PT can be seen either as a FE phase with defects leading to the pinning of the hysteresis loops or as an AFE (with possibly a secondary phase, that is not observed in the large-field measurements).

In Chapter 4, coexistence of several local polar orders for compositions in the range $0.10 \leq x \leq 0.25$ will be proposed. Furthermore, the change of behavior of the I-V curves at T_3 will be ascribed to a change in the type of phases that coexist. Above T_3 , phases with antipolar, polar and relaxor orders coexist, whereas below T_3 the antipolar phase has disappeared. From a macroscopic point of view, this corresponds to the scenario of a transition between an AFE and a FE state introduced above, but it will be proposed that the low-temperature FE phase is induced by the large electric-field applied for the measurements and that without the application of an electric field the phase is more relaxor-like.

Therefore, in the range of compositions presenting frequency-dependent dielectric constant ($0.10 \leq x \leq 0.40$), a maximum of the piezoelectric coefficient d_{33} has been observed. This maximum has been ascribed to the influence of the large electric field applied to conduct the hysteresis

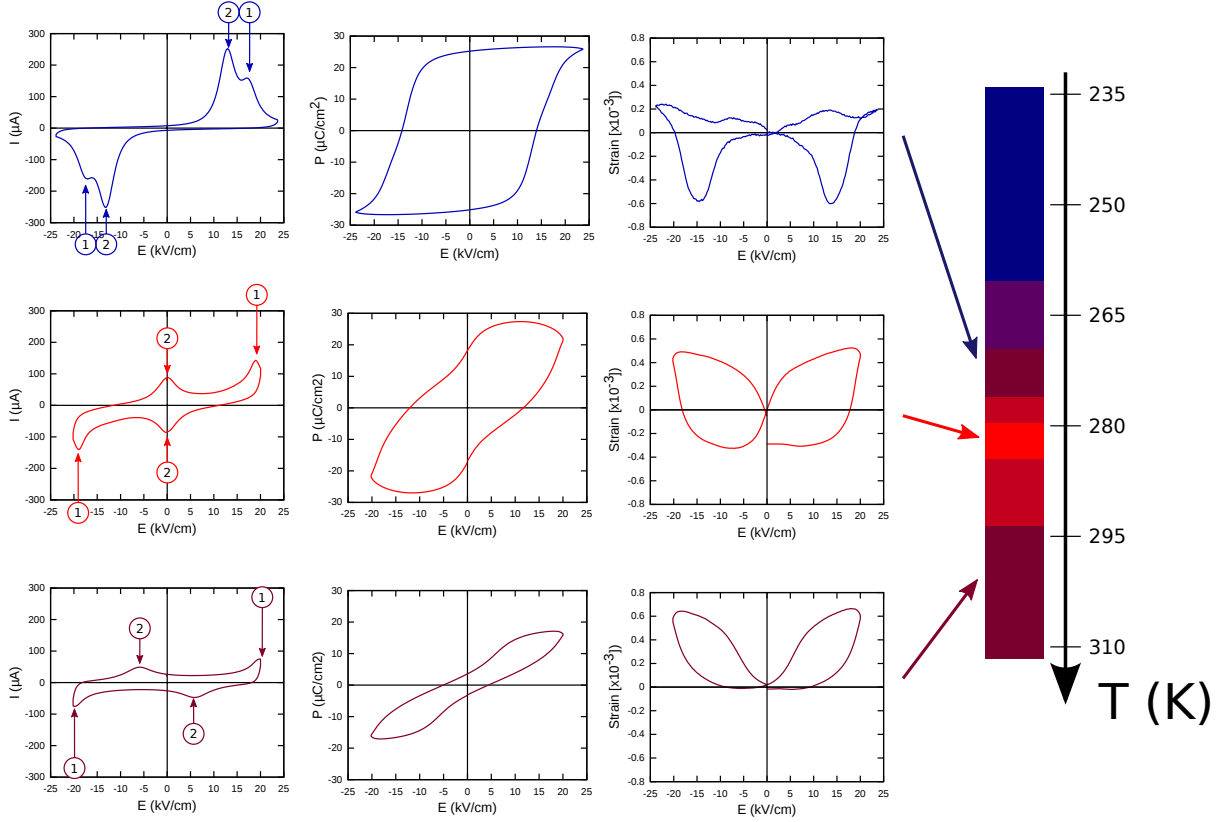


Figure 2.20: Example (PYN-PT 0.16) of evolution of the I-V curves, hysteresis measurements and strain measurements as a function of temperature.

and strain measurements. However, two different thermal behaviors of the large electric-field properties have been observed: a transition from an AFE to a FE state has been proposed for $0.10 \leq x \leq 0.25$, and a transition between two FE states has been identified for $0.30 \leq x \leq 0.40$.

2.4.2.4 Summary and conclusions on the thermal behavior of the relaxor compositions

In summary, in this section, the evolution of the dielectric constant, the polarization-electric field loops as well as the strain-electric field loops have been studied for compositions that have been observed in Sec.2.2.2 to present a frequency-dependence of the temperature of the maximum of the dielectric constant: $0.10 \leq x \leq 0.40$. All characteristic temperatures and transition temperatures have been summarized in Fig.2.21.

The study of the derivative of the inverse of the dielectric constant ξ has enabled to determine the Burns temperature T_B for composition in the range $0.10 \leq x \leq 0.20$.

The measured Burns temperatures, for PYN-PT $0.10 \leq x \leq 0.20$, are surprisingly close to the maximum temperature. Indeed for $\text{Pb}(\text{Mg}_{1/3}\text{Nb}_{1/3})\text{O}_3$ or $\text{Pb}(\text{Zn}_{1/3}\text{Nb}_{1/3})\text{O}_3$, T_B is about 300 K higher than T_m ($T_B = 630$ K and 740 K with $T_m = 260$ K and 450 K respectively [70]) whereas T_B is only about 60 K higher than T_m in PYN-PT. This supports the idea that the temperature referred to as the Burns temperature, in this work, may not be the Burns temperature of classical relaxors (as suggested by the relaxor-like behavior of the dielectric constant at high temperatures for PYN-PT 0.16 and PYN-PT 0.20). This difference between the temperature of the deviation from the Curie-Weiss behavior and the Burns temperature will be discussed in Chapter 4.

For compositions in the range $0.25 \leq x \leq 0.40$, it was only possible to determine the temperature at which the dielectric response of the polar nanoregions is strong enough to be experimentally observed using the dielectric constant measurements. The study of the evolution of the cell parameters (Sec.3.5.2) will show that, in this compositional range the Burns temperature is about 690 K.

Two models to describe the thermal dielectric behavior of the different compositions have been investigated: the model proposed by Bokov and Ye [22] and the modified Curie-Weiss model.

The model proposed by Bokov and Ye cannot be satisfactorily used to describe our data for compositions in the range $0.25 \leq x \leq 0.40$, however the fitting parameters are in good agreement with the ones reported in the literature. In this compositional range, using a critical exponent different from 2 allows a better modeling of the experimental data.

For PYN-PT 0.10, it appeared that even though a dielectric relaxation is observed the dielectric constant follows the Curie-Weiss law down to T_m .

For PYN-PT 0.16 and PYN-PT 0.20, the dielectric constant can be modeled using a modified Curie-Weiss law with a critical exponent close to 2 at high temperatures and with a Curie-Weiss law in a temperature range hundred degrees above T_m .

A change of behavior of the dielectric constant at a temperature T_2 lower or equal to T_f has also been discovered due to a change of slope in the derivative of the inverse of the dielectric constant. The change of slope is well marked for compositions with $x=0.10-0.20$, for the other relaxor compositions, only the frequency-dependence of ξ is different at T_2 .

The large electric-field measurements of the polarization and strain have shown a decrease of the remnant polarizations and coercive fields with increasing temperature. Moreover, for all compositions, an electric-field induced phase transition has been associated with the maximum of the piezoelectric coefficient d_{33} . This phase transition has been shown to be between an AFE and FE phases for $0.10 \leq x \leq 0.25$ and between two FE phases for $0.30 \leq x \leq 0.40$. The AFE-FE transition happens at the temperature T_3 that is close to T_2 for compositions in the range $0.10 \leq x \leq 0.16$. For the other compositions the temperatures T_2 and T_3 are different enough to be sure that the difference is not due to an experimental artifact. Hence, for compositions with $0.20 \leq x \leq 0.40$, no changes of behavior for the large-field properties have been observed at T_2 , however changes in the thermal evolution of the cell parameters at T_2 for PYN-PT with $0.16 \leq x \leq 0.25$ were observed indicating that there is indeed a change in the polar order at T_2 . For PYN-PT $0.30 \leq x \leq 0.40$, no conclusion regarding the existence of T_2 can be drawn from

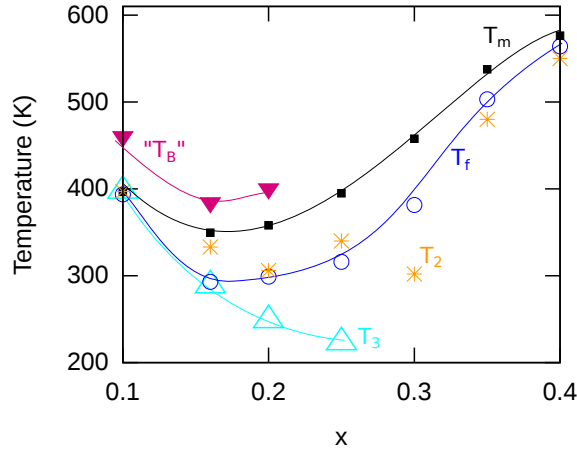


Figure 2.21: All critical temperature found using dielectric, hysteresis and strain measurements for compositions in the range $0.10 \leq x \leq 0.40$.

T_m is the temperature of the maximum of the dielectric constant measured at 1 kHz (black squares).

T_B is the Burns temperature (or the temperature of the deviation from the Curie-Weiss behavior) (pink triangles).

T_f is the freezing temperature determined using the Vogel-Fulcher law in Sec.2.2.2 (open blue circles).

T_2 correspond to the change of behavior observed in the thermal evolution of ξ (yellow stars).

T_3 is the temperature of the maximum of the piezoelectric coefficient d_{33} associated with the changing of sign of the second peak in the I-V curves (light blue open triangles).

the temperature-dependent diffraction experiments due to the limited amount (and quality) of data. Comparing the values of T_2 and T_f , it seems reasonable that the change in the dielectric response observed at T_2 for PYN-PT 0.35 and PYN-PT 0.40 is related to the freezing of the PNRs.

From all these measurements and analysis several conclusions will be drawn, regarding the different behaviors of the relaxor phase in PYN-PT solid solution.

Even though PYN-PT 0.10 displays a dielectric relaxation that can be fitted using a Vogel-Fulcher law, its dielectric constant evolves more as if the material was FE or AFE, i.e. the dielectric constant follows the Curie-Weiss law above and below T_m . It is possible that even if PNRs appear at T_B the relaxor phase cannot establish itself throughout the sample and the material undergoes a transition toward a low-temperature AFE/FE state at $T_2 \sim T_3 \sim T_f$.

Compositions in the range $0.25 \leq x \leq 0.40$ appear to be relaxor since the dielectric constant can be fitted with classical models derived for such kind of materials.

Finally, PYN-PT 0.16 and PYN-PT 0.20 exhibit extremely peculiar behaviors since they seem

to be relaxors at high-temperature and to undergo a transition toward a ferroelectric or antiferroelectric phase at a temperature hundred degrees above T_m . Hence, the temperature reported previously as the Burns temperature may have a different meaning and may be the onset temperature of a phase transition.

Also the dielectric constant of this composition suggests two changes of behaviors a frequency-dependent one at T_m and a frequency-independent one at T_2 . Hence, in the absence of a large electric-field, this composition seems to be oscillating between the behavior of a relaxor and the one of a ferroelectric or antiferroelectric.

Under a large electric field, these compositions undergo an additional change of behavior at T_3 as mentioned in the above paragraph.

2.4.3 FE

In previous sections, I have shown that PYN-PT $x=0.45-0.60$ have large values of dielectric constant and that the temperature of the maximum of the dielectric constant is frequency-independent and exhibit FE hysteresis cycles and butterfly-shape strain cycles.

The evolution of the dielectric constant with temperature (Top of Fig.2.22) shows a unique maximum corresponding to the transition from the high-temperature to the low-temperature phases.

A small thermal hysteresis is observed for $0.45 \leq x \leq 0.60$: 1.5 K, 6 K and 8 K for 0.45, 0.50 and 0.60, respectively. This thermal hysteresis indicates a first-order phase transition. The first-order type of transition is confirmed by the divergence of ξ at T_c for PYN-PT 0.50 and 0.60 (Bottom of Fig.2.22). For PYN-PT 0.45, the first order nature of the transition is not as pronounced as for the other compositions, as evidenced by the much smaller thermal hysteresis, and therefore the divergence of ξ at T_c is not as clear as for the other compositions.

However the evolution of ξ with temperature reveals that the dielectric constant follows the Curie-Weiss law only below the transition for $x=0.45-0.60$. For all compositions, above the phase transition, the dielectric constant exhibits the behavior of a relaxor material. Hence compositions with $0.45 \leq x \leq 0.60$ do not undergo a PE-FE transition, at $T_c=T_m$, but a non-ergodic RFE-FE transition (as described in Fig.1.3 page 21).

At even higher temperature, it is possible to find a temperature interval for which ξ is temperature independent ($\lesssim 700$ K), i.e. the dielectric constant follows the Curie-Weiss law. The ratio between the Curie constant C above and below the phase transition: $1.5 \pm 0.32 \text{ K}^{-1}$, $3.6 \pm 0.52 \text{ K}^{-1}$ and $1.7 \pm 0.27 \text{ K}^{-1}$ for PYN-PT 0.45, 0.50 and 0.60 respectively (Center of Fig.2.22) is different from the value (8) expected for a first-order PE-FE phase transition (see Sec.2.1). Usually, the ratio of the Curie constants measured experimentally is close to 8 but can strongly deviates from this value [61]. Moreover, in the compositional range $0.45 \leq x \leq 0.60$, PYN-PT does not undergo a PE-FE phase transition but a RFE-FE transition. Therefore, the theory may not apply to the case of PYN-PT.

Finally, based only on the dielectric data, the Curie-Weiss behavior of the dielectric constant at high temperature may be questioned since at such temperatures the conduction in the samples is no more negligible ($\tan \delta$ diverges for $T > 700$ K). However, a distinct changes in the temperature-dependent diffraction experiments indicate that the plateau observed in ξ at high

temperature is indeed due to a Curie-Weiss dependency and not due to conduction. Therefore, upon cooling PYN-PT with $0.45 \leq x \leq 0.60$ is successively PE, RFE and FE.

The hysteresis and strain measurements as a function of temperature have the classical behavior of FE materials and these measurements will be detailed in Sec.5.2.2. FE hystereses and piezoelectric loops can be observed for temperatures above T_m (that will be attributed to the presence of large PNRs). Furthermore, these measurements also show that there is a phase transition between two ferroelectric phases at a temperature lower than T_m . This transition will be undoubtedly attributed to the influence of the large electric field applied to carry out the measurements.

Finally, for $x=0.45$, below the phase transition the dielectric constant does not follow the Curie-Weiss law since ξ increases slightly with temperature. Because there is a phase transition this composition is assumed not to be RFE but FE at low temperature, even though the FE order may not establish itself on a long range and therefore causes the deviation from the Curie-Weiss law.

2.5 SUMMARY AND CONCLUSION ON THE PHASE DIAGRAM

In this chapter, the solid solution PYN-PT with $x=0-0.60$ has been studied using dielectric measurements, polarization-electric field and strain-electric field relationships as a function of temperature.

Using only dielectric measurements, it was found that compositions with $x \leq 0.05$ are antiferroelectrics and that the MPB is situated in the range $x=0.45-0.50$. Furthermore, the strong frequency dependence in the intermediate range ($0.10 \leq x \leq 0.40$) have lead me to classify these compositions as relaxors.

The study of the evolution of the low-electric-field and large-electric-field dielectric constants with temperature for pure PYN and PYN-PT 0.05 has shown that these two compositions undergo only one phase transition, of first-order nature, at the Curie temperature T_c between a high-temperature paraelectric phase and a low-temperature AFE phase.

PYN-PT 0.10 follows the Curie-Weiss law above and below the frequency-dependent temperature of the maximum of the dielectric constant, T_m .

The evolution of the dielectric constant with temperature of PYN-PT 0.16 and PYN-PT 0.20 follows the Curie-Weiss law over a limited temperature range above and below the frequency-dependent T_m . Apart from this temperature range, the thermal evolution of the dielectric constant is more consistent with a relaxor behavior.

For PYN-PT with $x=0.25-0.40$, the evolution of the dielectric constant with temperature is the one expected of a relaxor material.

The solid solution PYN-PT with $x=0.45-0.60$ exhibits a relaxor behavior at high temperature and it undergoes a spontaneous relaxor-ferroelectric phase transition at $T_m = T_c$.

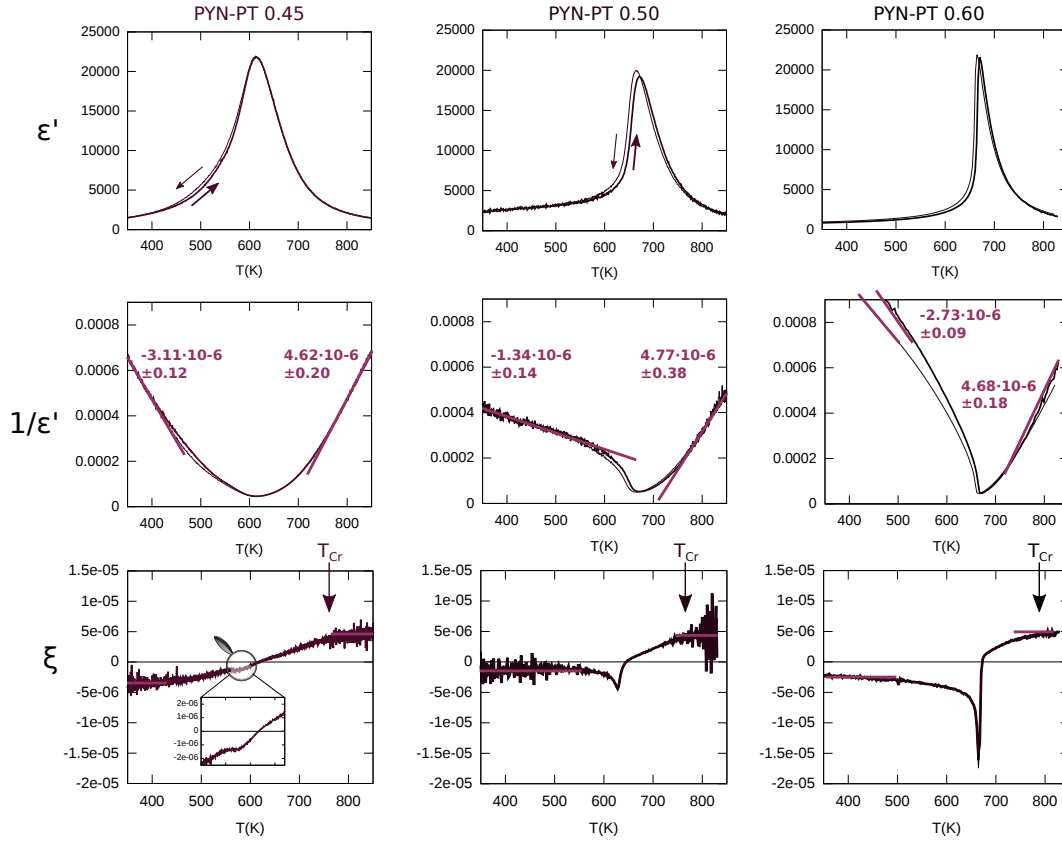


Figure 2.22: (*Top*) Dielectric constant (ϵ') at 1kHz for $x=0.45-0.60$ measured under increasing temperature (thick line) and decreasing temperature (thin line) (*Center*) Inverse of the dielectric constant at 1kHz for $x=0.45-0.60$ measured under increasing temperature (thick line) and decreasing temperature (thin line). The slopes are measured using the temperature-independent part of ξ . (*Bottom*) Derivative of the inverse of the dielectric constant ξ at 10kHz, 100kHz and 1MHz (decreasing line thickness). The difference between the various frequencies is not visible because the various curves are almost perfectly superimposed.

Moreover, compositions in the range $0.10 \leq x \leq 0.40$ undergo an additional transition at a temperature lower than T_m , under the application of a large alternating electric-field. This transition has been evidenced by a maximum of the piezoelectric coefficient d_{33} . This transition is of different nature depending on the composition: a transition between an AFE and a FE state, for compositions in the range $0.10 \leq x \leq 0.25$ and between two FE states for compositions in the range $0.30 \leq x \leq 0.40$.

Thus, upon cooling, PYN undergoes a first-order phase transition from the high-temperature paraelectric state toward the low-temperature AFE state (Fig.2.23). Its solid solution with PT presents the same behavior for a small amount of substitution ($x \leq 0.05$). For PYN-PT with larger amount of PT substitution, the transition becomes more diffuse, as evidenced by the frequency-dependence of T_m . This diffuse character of the transition is usually associated with the appearance of nanoregions in a matrix.

In the case of PYN-PT 0.10, the dielectric constant of the low-temperature state can be described by the Curie-Weiss law indicating either an AFE or a FE state. We suggest this state to be AFE based on the presence of superstructure reflections in the X-ray diffraction pattern (described in Sec.3.3.2) and on the compositional proximity with the AFE state of PYN. The frequency-dependent maximum of the dielectric constant indicates the presence of a relaxor behavior. Hence, it is possible that, in PYN-PT 0.10, there are nanoregions, that are responsible for the dielectric relaxation, are AFE in nature distributed in a paraelectric matrix and that the increase in their sizes and correlations leads to the apparent macroscopic AFE behavior at low temperature. This idea will be further detailed in Chapter 4. Therefore, PYN-PT 0.10 would be a new kind a relaxor in which nanoregions of antiferroelectric nature.

The cases of PYN-PT 0.16 and 0.20 are similar to the case of PYN-PT 0.10, in the sense that, over a certain temperature range, the dielectric constant of these compositions behaves as if the material was relaxor and follows the Curie-Weiss law for other temperatures. However, in the case of PYN-PT 0.16 and PYN-PT 0.20, the high-temperature and the low-temperature states are relaxor-like, whereas, in the intermediate temperature range (hundred degrees above the transition to thirty degrees below), the material behaves has AFE or FE. Therefore, the thermal evolution of the dielectric constant of these compositions is the one of a relaxor superimposed with the evolution of an AFE or FE material undergoing a phase transition. This phase is most likely AFE by analogy with PYN-PT 0.10. Thus, PYN-PT 0.16 and 0.20 would belong, as PYN-PT 0.10, to this new class of relaxors with nanoregions of antiferroelectric nature. However, the frequency-dependence of the maximum of the dielectric constant is already strong for these compositions and therefore it is possible that "classical" PNRs coexist with these antiferroelectric nanoregions.

Compositions in the range $0.25 \leq x \leq 0.40$ behave as relaxors. The large-electric-field polarization and strain measurements indicate that the more PT there is in the solid solution, the more FE-like it behaves indicating that the size and correlation of PNRs increase with the addition of PT leading in the extreme case ($x \geq 0.45$) to a purely FE phase. Moreover compositions

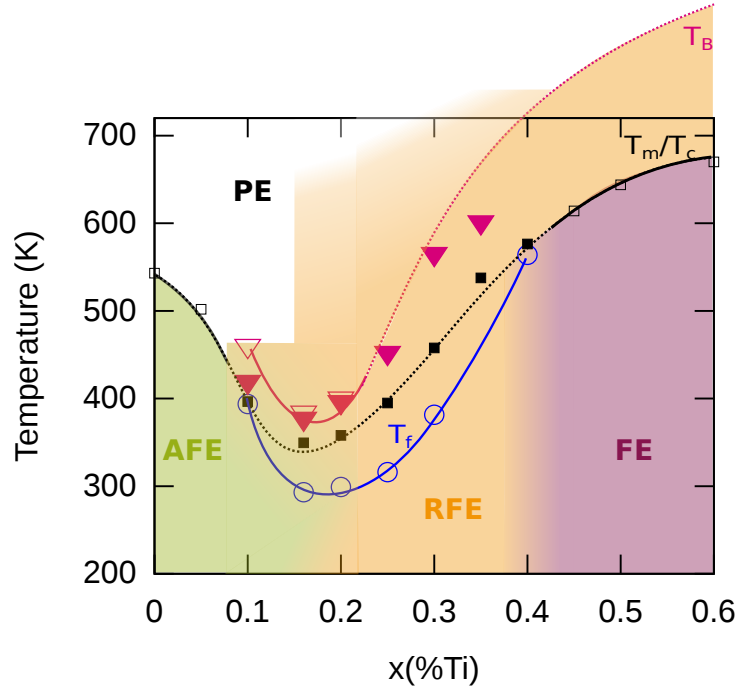


Figure 2.23: Phase diagram produced from the study of the dielectric constant, hysteresis and strain measurements as a function of temperature. Lines are guides for the eyes. Solid and open black squares refer to T_m and T_c respectively. Open blue circles are T_f calculated from the Vogel-Fulcher equation. Open and solid circles are the measured and estimated values of the Burns temperature, respectively. Green area refers to antiferroelectric (AFE) properties, yellow area refers to relaxor (RFE) properties, purple area refers to ferroelectric (FE) properties.

in the range $0.25 \leq x \leq 0.30$ are proposed to have two types of PNRs due to different chemical environment based on the incompatibility of the model proposed by Bokov and Ye [22] with our data and the presence of chemical ordering.

In conclusion, PYN and PYN-PT 0.05 exhibit the behavior of antiferroelectric materials. At the other end of the investigated compositional range, PYN-PT $x = 0.45-0.60$ exhibit at room temperature a ferroelectric state. In between, the solid solution exhibits a relaxor behavior that is strongly influenced by the low PT content AFE phase (for $x \leq 0.20$) and the large PT content FE phase for ($x \geq 0.25$) (Fig.2.23).

- CHAPTER 3 -

STRUCTURE

In Chapter 2, we showed that the PYN-PT solid solution presents antiferroelectric, relaxor and ferroelectric properties. In this chapter, we shall investigate, the structures this solid solution presents.

I shall introduce this chapter with the characteristic features related to the observed properties (Sec.3.1). An overview of the methodology I used will follow (Sec.3.2) before moving to the description of the results.

In Section 3.3, I will start with the results on the long-range distortions and superstructures reflections due to Pb displacements, chemical ordering on the B-site and oxygen-octahedra rotations.

In Section 3.4, the room-temperature structure of the various studied compositions will be presented in details, and in Section 3.5, their evolution with temperature. This will enable me, in the conclusion (Sec.3.6), to propose a new phase diagram based on the structural features.

The next Chapter will be devoted to the comparison of the phase diagrams obtained from the properties measurements (Fig.2.23, page 95) and from the determination of the structures (Fig.3.28, 169)

3.1 STRUCTURAL FEATURES RELATED TO DIFFERENT POLAR ORDERS

Different polar orders are associated with different crystallographic structures, e.g. ferroelectricity exists only in non-centrosymmetric crystals and the unit cell is elongated along the polarization direction. Antiferroelectricity, on the contrary, requires a center of symmetry. These structures are commonly studied using various diffraction techniques on single crystals or powders.

Hereafter, we will only review the structural fingerprints of the various properties studied in Chapter 2.

3.1.1 Ferroelectrics

All ferroelectrics (FE) are also piezoelectrics and the appearance of piezoelectricity requires a non-centrosymmetric crystal as pointed out in Sec.1.1.1.

The structures of Pb-based ferroelectric materials have been intensively studied for the last fifty years. Based on all work to date, it appears that the Pb-based ferroelectric materials form in a rather limited number of crystallographic space groups: $R3m$, Pm , Cm , $P4mm$. For all structures devoid of oxygen-octahedra (O-octahedra) tilts, space groups observed in Pb-based complex perovskites, the positions of the atoms and the refinable parameters are listed in Table 3.1. In addition, the appearance of O-octahedra tilts in Pb-based FE perovskites adds to the possible space groups: $R3c$ and Cc which corresponds to the $a^-a^-a^-$ and $a^-a^-c^-$ tilt systems, respectively (among all possible tilt systems listed in Ref.[71]).

In the case of PYN-PT, taking into account rock-salt chemical ordering on the B-site changes the symmetry of the space groups proposed for all yet reported Pb-based FE perovskites. The new set of space groups taking into account chemical ordering is given in Table 3.2.

Because of the enhancement of the properties at the morphotropic phase boundary (MPB), a lot of crystallographic studies have focused on this compositional range in order to comprehend the structure leading to those fascinating high properties.

In 1999, Noheda et al. [13] discovered the presence of a monoclinic phase at the MPB of PbZrO_3 - PbTiO_3 (PZT) solid solution. Later, a monoclinic phase has been found at the MPB in many other Pb-based solid solutions such as $\text{Pb}(\text{Sc}_{1/2}\text{Nb}_{1/2})\text{O}_3$ - PbTiO_3 (PSN-PT) [72] or $\text{Pb}(\text{Mg}_{1/3}\text{Nb}_{2/3})\text{O}_3$ - PbTiO_3 (PMN-PT) [73]. This monoclinic phase (with a Pm or Cm space group) has however been shown to coexist with rhombohedral and tetragonal phases over a compositional range larger than the one over which the properties are enhanced (Fig.3.1) [74].

Today, both experimental [72] and theoretical [75] studies have clearly shown that the enhancement of the properties at the MPB is due to the structural bridging of the rhombohedral and tetragonal phases produced by the monoclinic phase allowing an easy rotation of the polarization. Indeed the polarization in the rhombohedral and tetragonal phases is constrained into the $[111]$ and $[001]$ directions respectively due to symmetry, whereas in the monoclinic phases the polarization direction is not constrained into one direction but within a plane, namely (010) and

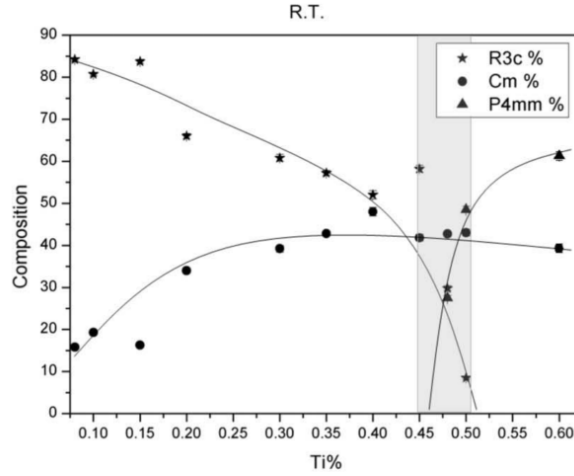


Figure 3.1: Percentage of different crystallographic phases in PZT solid solution [74]. The MPB compositional range where the properties are enhanced is highlighted in light gray.

(110) for Pm and Cm space groups respectively (Fig.1.8, page 28).

3.1.2 Antiferroelectrics

The structure of antiferroelectrics (AFE) is, in the simplest model, described by the superimposition of two polar sublattices with polarization directions opposite to each other, e.g. in one sublattice the polarization points “up” and points “down” in the other sublattice. Hence the lattice actually describing the entire antiferroelectric structure will be larger than each of the sublattices (see Sec.1.1.3).

The simple alternation of dipole pointing “up” and one dipole pointing “down” for antiferroelectrics has never been observed in perovskites, and perovskite antiferroelectrics have a more complex structure in which the lattice is more than twice as large as the sublattice. For example, in the case of the model antiferroelectric $PbZrO_3$, the structure can be described with four pseudo-cubic unit cells with a dipole pattern $\uparrow\uparrow\downarrow\downarrow$.

However, in some antiferroelectrics ($Pb(Co_{1/2}W_{1/2})O_3$ or $Pb(Mg_{1/2}Te_{1/2})O_3$ [26]), the model with two sublattices with opposite directions of polarization does not hold and the antiparallel arrangement of the dipoles is more complex. In these cases the structure is described using an average lattice and a modulation vector describing the displacement of the atoms, i.e. the dipole arrangement.

These two descriptions are not conceptually incompatible as the limit of the description of an antiferroelectric using an average structure with a modulation vector is the simple model with two opposite sublattices in which case the modulation vector is commensurated with the average lattice.

Space group	Chemical ordering	Lattice vectors	Atom	x	y	z
$Pm\bar{3}m$	random	$a_c=a_{pc}$	Pb	0	0	0
		$b_c=a_{pc}$	B _a /B _b	1/2	1/2	1/2
		$c_c=a_{pc}$	O	1/2	1/2	0
$R3m$	random	$a_h=a_{pc} \ b_{pc}$	Pb	0	0	s+1/4
		$b_h=b_{pc} \ c_{pc}$	B _a /B _b	0	0	T
		$c_h=a_{pc}+b_{pc}+c_{pc}$	O	1/6 2e 2d	1/3 4d	1/12
Cm	random	$a_m=a_{pc}+b_{pc}$	Pb	0	0	0
		$b_m=b_{pc} \ a_{pc}$	B _a /B _b	1/2+ δx_B	0	1/2+ δz_B
		$c_m=c_{pc}$	O1	1/2+ δx_{O1}	0	δz_{O1}
			O2	1/4+ δx_{O2}	1/4+ δy_{O2}	1/2+ δz_{O2}
Pm	random	$a_m=a_{pc}$	Pb	0	0	0
		$b_m=b_{pc}$	B _a /B _b	1/2+ δx_B	0.5	1/2+ δz_B
		$c_m=c_{pc}$	O1	1/2+ δx_{O1}	0	1/2+ δz_{O1}
			O2	δx_{O2}	0.5	1/2+ δz_{O2}
			O3	1/2+ δx_{O3}	0.5	δz_{O2}
$P4mm$	random	$a_t=b_t=a_{pc}$	Pb	0	0	0
		$c_t=c_{pc}$	B _a /B _b	1/2	0.5	1/2+ δz_B
			O1	0.5	0	1/2+ δx_{O1}
			O2	0.5	0.5	δz_{O1}

Table 3.1: Space groups observed in Pb(B_a,B_b)O₃ complex perovskites presenting relaxor or ferroelectric properties. Adapted from [74].

For each space group, the lattice vectors are given with respect to the pseudocubic (pc) phase. The s, d, e, T refinable parameters in the rhombohedral $R3m$ structure are the ones described by Megaw and Darlington [76].

Space group	Chemical ordering	Lattice vectors	Atom	x	y	z
$Fm\bar{3}m$	rock salt ($Pm\bar{3}m$)	$a_c=2a_{pc}$	Pb	1/4	1/4	1/4
		$b_c=2a_{pc}$	B _a	0	0	0
		$c_c=2a_{pc}$	B _b	1/2	1/2	1/2
			O	1/4	0	0
$R3m$	rock salt ($R3m$)	$a_h=a_{pc}$ b_{pc}	Pb1	0	0	1/4
		$b_h=b_{pc}$ c_{pc}	Pb2	0	0	3/4
		$c_h=2(a_{pc}+b_{pc}+c_{pc})$	B _a	0	0	0+T
			B _b	1/3	2/3	1/6+T
			O1	1/2 2e 2d	1/2 4d	1/4
			O2	1/6 2e 2d	1/3 4d	1/12
Im	rock salt (Cm)	$a_m=a_{pc}+b_{pc}$	Pb1	1/2	0	1/4
		$b_m=b_{pc}$ a_{pc}	Pb2	0	1/2	1/4
		$c_m=2c_{pc}$	B _a	δx_{B_a}	0	δz_{B_a}
			B _b	$1/2+\delta x_{B_b}$	1/2	$1/2+\delta z_{B_b}$
			O1	$1/4+\delta x_{O1}$	$1/4+\delta y_{O1}$	δz_{O1}
			O2	$3/4+\delta x_{O2}$	$3/4+\delta y_{O2}$	δz_{O2}
			O3	$1/2+\delta x_{O3}$	1/2	$1/4+\delta z_{O3}$
			O4	$1/2+\delta x_{O4}$	1/2	$3/4+\delta z_{O4}$
Cm	rock salt (Pm)	$a_m=2a_{pc}$	Pb1	1/4	1/4	1/4
		$b_m=2b_{pc}$	Pb2	1/4	1/4	3/4
		$c_m=2c_{pc}$	B _{a1}	δx_{B_a1}	0	δz_{B_a1}
			B _{a2}	$1/2+\delta x_{B_a2}$	0	$1/2+\delta z_{B_a2}$
			B _{b1}	$1/2+\delta x_{B_b1}$	0	δz_{B_b1}
			B _{b2}	δx_{B_b2}	0	$1/2+\delta z_{B_b2}$
			O1	$1/4+\delta x_{O1}$	0	δz_{O1}
			O2	$3/4+\delta x_{O2}$	0	δz_{O2}
			O3	$1/4+\delta x_{O3}$	0	$1/2+\delta z_{O3}$
			O4	$3/4+\delta x_{O4}$	0	$1/2+\delta z_{O3}$
			O5	δx_{O5}	0	$1/4+\delta z_{O5}$
			O6	δx_{O6}	0	$3/4+\delta z_{O6}$
$I4mm$	rock salt ($P4mm$)	$a_t=b_t=a_{pc}+b_{pc}$	Pb	1/2	0	1/4
		$c_t=2c_{pc}$	B _a	0	0	δz_{B_a}
			B _b	0	0	$1/2+\delta z_{B_b}$
			O1	0	0	$1/4+\delta z_{O1}$
			O2	0	0	$3/4+\delta z_{O2}$
			O3	1/4	1/4	δz_{O3}

Table 3.2: Space groups determined from the ones commonly observed in Pb(B_a,B_b)O₃ complex perovskites presenting relaxor or ferroelectric properties. The space group without random chemical arrangement on the B-site is given in parenthesis in the “chemical ordering” column.

For each space group, the lattice vectors are given with respect to the disordered $Pm\bar{3}m$ space group.

The s, d, e, T refinable parameters in the rhombohedral $R3m$ structure are the ones described by Megaw and Darlington [76].

Finally, the structure described so far is actually the one of a material with an *antipolar* arrangement. The difference between a material presenting only an antipolar arrangement and an antiferroelectric is the energetic proximity with a FE phase.

3.1.3 Relaxors

Relaxors (RFE) have no global spontaneous polarization and therefore the structure must remain, in average, centrosymmetric which in the case of simple Pb-based perovskite is the cubic $Pm\bar{3}m$ phase.

However relaxors show local distortions due to regions of chemical order (CORs) and polar nanoregions (PNRs). These local distortions lead to the appearance of diffuse scattering that has been described in Sec.1.1.4.

The diffuse scattering has been mainly studied in single crystals but a few attempts at characterizing it have been carried out in powder samples, in particular by conducting Rietveld refinement with two phases: a long-range cubic phase and a short-range rhombohedral phase [77].

In addition to local order, relaxors present strong surface effect (10-50 μm). For example, Xu et al. [78] have shown that the structure of the bulk of $\text{Pb}(\text{Zn}_{1/3}\text{Nb}_{2/3})\text{O}_3$ crystal is different from the structure at their surfaces. Similar results have been obtained on $\text{Pb}(\text{Mg}_{1/3}\text{Nb}_{2/3})\text{O}_3$ [79].

Some relaxors (e.g. $\text{Pb}(\text{Zn}_{1/3}\text{Nb}_{2/3})\text{O}_3$ or $\text{Pb}(\text{Sc}_{1/2}\text{Nb}_{1/2})\text{O}_3$ (PSN)) undergo a spontaneous transition toward a FE phase upon cooling that leads to a non-centrosymmetric structure described previously (Sec.3.1.1). In particular, this spontaneous transition is commonly seen in relaxor- PbTiO_3 solid solutions since the presence of Ti^{4+} cations on the B site of the perovskite favors the appearance of a FE phase.

However, this transition may not always be sudden and the cubic relaxor and the distorted ferroelectric phases may coexist over a large temperature range (~ 60 K in $\text{Pb}(\text{Zn}_{1/3}\text{Nb}_{2/3})\text{O}_3$ [80]).

Furthermore, in materials undergoing spontaneous relaxor-to-FE phase transition, the presence of local chemical order has a major influence on the crystal structure. For example, in the solid solution PSN-PT, a certain degree of local chemical ordering has to be imposed so that effective Hamiltonian calculations reproduce the experimentally observed structure, whereas similar calculations on the PZT solid solution did not require such addition of local order to reproduce the experimental data [81].

Hence, even in the ferroelectric phase, some local features characteristic of the relaxor phase may still be present in addition to the long-range ferroelectric distortions.

Finally, even though the structure of relaxors may remain cubic on average, the change of local structure, e.g. appearance or freezing of the PNRs influences the thermal evolution of the cell parameter (Fig.3.2).

At high temperature, in the paraelectric phase, the cubic cell parameter a decreases linearly with

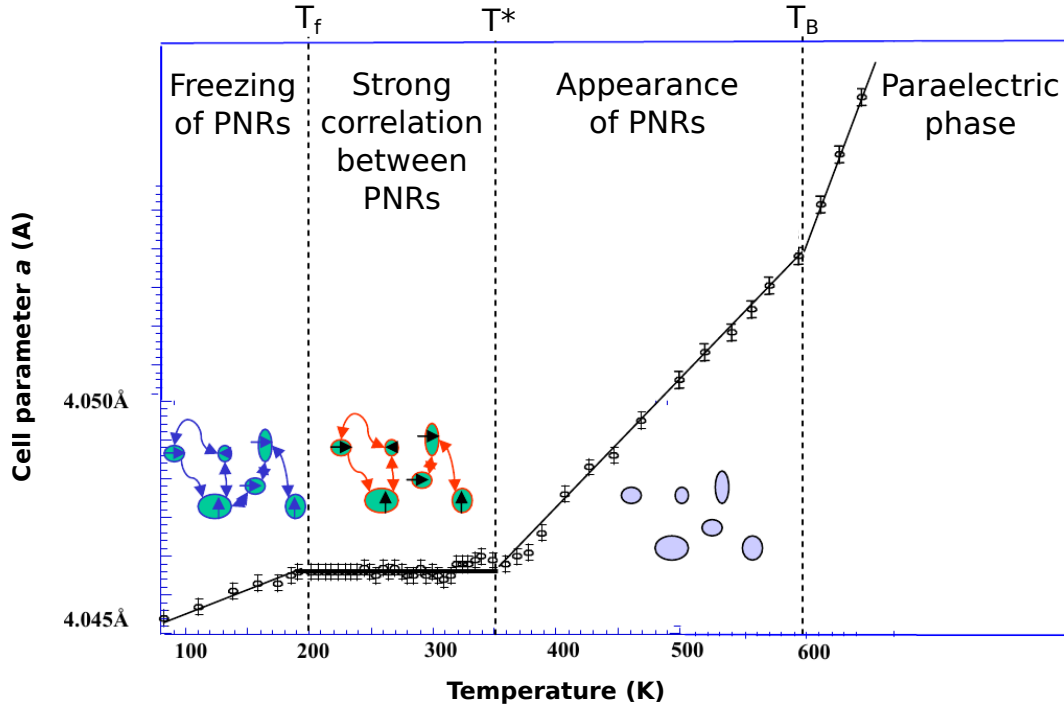


Figure 3.2: Evolution of the pseudo-cubic cell parameters in a $\text{Pb}(\text{Mg}_{1/3}\text{Nb}_{2/3})\text{O}_3$ single crystal. Adapted from [16].

temperature because of thermal contraction. At the Burns temperature T_B , the appearance of PNRs changes the slope of the linear decrease of the cell parameter. At the critical temperature T^* at which the PNRs start to correlate [69], this linear decrease stops. Below T^* , the cell parameter remains constant with temperature down to the freezing temperature T_f . Below the freezing temperature T_f , the cell parameter starts to decrease linearly again with temperature. There is therefore a signature of the local scale phenomena on the global scale structure.

3.1.4 Superstructure Reflections (SSRs)

In perovskites, the structure is commonly described with one chemical formula unit per cell ($Z=1$) making the comparison with the ideal cubic phase easier. In practice, the structure can be more complex and larger units cell may be necessary to describe the structure, as in the case of antiferroelectrics.

These larger unit cells lead to the appearance in the diffraction pattern of extra reflections compared to the unit cell with $Z=1$ that are the so-called “superstructure reflections” (SSRs). The sources of the increase of the unit cell may be diverse, the most common in Pb-based perovskites are due oxygen-octahedra tilting, chemical ordering and correlated antiparallel displacements.

Oxygen octahedra (O-octahedra) tilting is a very common distortion in a perovskite and are com-

monly described using the notation developed by Glazer [82]. In this notation, the O-octahedra tilting is described by specifying the rotations of the octahedra about each of the three Cartesian axes (attached to the $Z=1$ unit cell) using a letter to characterize the magnitude of the rotation and using a superscript indicating whether the rotation in adjacent layers are in the same or opposite directions. O-octahedra tilting usually leads to the appearance of SSRs in $\langle h/2 \ k/2 \ l/2 \rangle$ (all odd) or $\langle h/2 \ k/2 \ l \rangle$ (h, k odd) with different indices in the plane perpendicular to the rotation axis defined in the $Z=1$ pseudo-cubic unit cell.

Different types of chemical order lead to different types of superstructure reflections. The most common chemical ordering in Pb-based perovskite is the rock-salt ordering introduced in Sec.1.2.1.1. This ordering leads to the appearance of SSRs indexed $(h/2 \ k/2 \ l/2)$ with h, k, l all odd.

Correlated antiparallel displacements of Pb^{2+} are common in the case of antiferroelectrics. The type of SSRs observed in this case will depend on the periodicity of the displacements leading to SSRs in $(h/n \ k/n \ l/n)$ with n the number of pseudo-cubic cells ($Z=1$) required to reproduce the pattern of antiparallel displacements. n may be an integer as in the case of PbZrO_3 , the classical AFE, for which $n=4$ [83], but may also be a real number as in the case of $\text{Pb}(\text{Mg}_{1/2}\text{Te}_{1/2})\text{O}_3$ [84], for example.

Finally, several type of SSRs may appear in one material. For example, Woodward [85] pointed that chemical ordering on the B-site is often accompanied by O-octahedra tilting. Furthermore, a recent study by Bellaiche and Íñiguez [86] has shown that O-octahedra tilting and antiparallel displacements (necessary though not sufficient for AFE materials) are coupled.

Therefore, superstructure reflections may originate from various sources in one material, but they can usually be identified unambiguously based on the indexation of the reflections.

Moreover, in the case of Pb-based perovskites, O-octahedra tilting are commonly investigated using neutron or electronic diffraction to take advantage of the related enhancement of the diffracted intensity of the O-octahedra SSRs, since the cross sections of Pb and O are then more similar than in the case of X-rays.

3.2 METHODOLOGY

Before presenting my results about the structure, I shall give hereafter a quick overview of the methodology I used for this study, starting with the experimental conditions.

3.2.1 Experimental Conditions

My study of the evolution of the cell parameters as a function of temperature was performed on a high-accuracy diffractometer in the Bragg-Brentano geometry using $\text{Cu K}\alpha$ wavelength issued from a 18 kW-rotating-anode generator equipped with a cryofurnace (80 K to 450 K) or a furnace

(300 K to 1000 K).

Rietveld refinements were conducted using the Jana2006 software [87] on X-ray diffractograms recorded at the European Synchrotron Radiation Facility (ESRF) and neutron diffractograms at the Laboratoire Léon Brillouin (LLB) and the Institut Laue Langevin (ILL).

X-ray powder diffractograms were recorded at room temperature and 30 ° above the Curie temperature (T_c) or above the temperature of the maximum of the dielectric constant (T_m) in transmission, using quartz capillary of 0.4 mm in diameter, at the ID31 beamline at ESRF using a 0.4 Å wavelength.

The neutron diffractograms were acquired by Dr Florence Porcher on 3T2 on the nuclear reactor Orphée at LLB for PYN-PT 0.40, PYN-PT 0.50 and PYN-PT 0.60 and by Dr Emmanuelle Suard on D2B at ILL for PYN and PYN-PT 0.30.

High resolution Electron microscopy experiments were conducted on the Titan microscope in École Centrale Paris and on Jeol 2100 TEM in Barcelona by Lluís López Conesa.

3.2.2 Rietveld refinement

The introduction of the Rietveld method revolutionized the study of the structure on powder diffraction pattern as it enabled the whole pattern to be analyzed at once sparing the analysis of each individual peak separately. Indeed, in the Rietveld method, the least-squares refinements are carried out until the best fit is obtained between the observed powder diffraction pattern taken as a whole and the entire calculated pattern based for the simultaneously refined models for the crystal structure, instrumental factors and other specimen characteristics (e.g. lattice parameters) [88]. Therefore, this method takes into account all information recorded during the experiment including the absence of intensity on a possible Bragg reflection and is able to deal with possible overlap of reflections.

Nonetheless, the Rietveld method is “only” a least-squares-refinement method and for the structure obtained at the end of the refinement to describe as accurately as possible the actual structure, a reasonably good starting model is required even before starting the refinement.

Practically, before carrying out the proper Rietveld analysis, a “profile matching” analysis is conducted. The profile matching analysis focuses on the determination of the cell parameters, profile of the reflections and some instrumental factors, but neither on atomic positions, nor on thermal agitation parameters. In the case of profile matching analysis the intensity of the Bragg reflections is estimated by the software to fit the diffraction pattern as well as possible and not based on the structure factor (describing the position of the atoms in the structure).

The profile matching analysis is particularly important in the case where very little is known about the structure. Indeed this analysis enables trying a large number of possible structures, since the number of parameters to refine is much lower than in Rietveld refinement and hence allows a fast identification of the “reasonably good starting models” needed for Rietveld refinement. The final choice between these reasonably good models to describe the structure is done using the Rietveld method and based on the quality of the fit.

Several criteria are used to determine the quality of the fit; the most common ones are the R-pattern R_p , the weighted R-pattern R_{wp} and the goodness of fit GOF .

The R-pattern R_p and weighted R-pattern R_{wp} estimate the difference in intensity between the calculated and observed intensity at each data points. In the weighted R-pattern R_{wp} , the weight is estimated based on the uncertainty of the experimental intensity. The goodness of fit GOF is the ratio of the weighted R-pattern R_{wp} to the expected-R R_{exp} (estimation of the highest R_{wp} that can be obtained for a given couple of model and data). Hence, the goodness of fit GOF is a measure of how well the fitted model accounts for the data. A large value of the goodness of fit GOF is a strong indication of an inadequate model or a false (i.e. local) minimum. A value of the goodness of fit GOF lower than 1 shows that more parameters are refined than can be justified by the quality of the data.

A complete definition of the agreement factors R_p , R_{wp} and GOF , as well as their mathematical derivation can be found in Ref.[88] (Chap.1 and Chap.3).

Finally, a visual inspection may be useful to determine if there is inaccuracy between the model and the data and what are the possible sources. For examples, Figures 6-10 in Ref.[74] illustrates the need for visual inspection to determine the presence of a possible phase mixing.

3.2.3 Single peak fitting

In the case where a limited number of reflections are available, e.g. to determine the thermal evolution of the cell parameters, reflections are fitted separately. In this case, the fitting was conducted using the gnuplot software [89] and pseudo-Voigt profile that has been shown in Ref.[90] to be the most appropriate profile to describe diffraction peaks.

The pseudo-Voigt function is defined as a linear combination of the Gaussian and Lorentzian functions and is an approximation of the Voigt function (which is the convolution product of Gaussian and Lorentzian functions).

In the gnuplot software, no functions are defined by default and all profiles must be defined by the user. The Gaussian, $GpV(x)$, Lorentzian, $LpV(x)$, and pseudo-Voigt, $pV(x)$, profiles are defined as follows

```
GpV(x)=exp(-(x-xmax)**2/((2*Wpv)**2))
LpV(x)=1/(1+(x-xmax)**2/(sqrt(log(2))*Wpv)**2)
pV(x)=Impv*((1-abs(sin(eta)))*GpV(x)+abs(sin(eta))*LpV(x))+bg(x)
```

In this case, the mixing parameter, η , i.e. the linear combination factor, is defined as being the absolute value of the sine of an angle ($abs(sin(eta))$) to ensure that the parameter remains in the physically-meaningful interval [0;1].

In this definition of the pseudo-Voigt profile, the Full-Width at Half Maximum, FWHM, is defined as $2*Wpv*(1+log(2))$. Furthermore, the integral breadth β , i.e. the width of a rectangle having the same area as the peak, is defined as

```
beta_pV=(1-abs(sin(eta)))*beta_G+abs(sin(eta))*beta_L
with beta_G=2*Wpv*sqrt(3.14) and beta_L=3.14*2*sqrt(log(2))*Wpv
```

The definition of the different functions and the calculations of the width and integral width were implemented for the gnuplot software by Dr Pierre-Eymeric Janolin in the SPMS laboratory.

3.3 OVERVIEW OF THE PYN PT STRUCTURE

Very few elements of the PYN-PT solid solution structure are known: PYN has a large orthorhombic structure due to the presence of antiparallel displacements (see Sec.1.4.1); the compositions presenting relaxors properties have been proposed to have a pseudo-cubic [46] or a monoclinic symmetry [19]; on each side of the morphotropic phase boundary (MPB), the structure of the solid-solution has been supposed to be rhombohedral and tetragonal by analogy with the PZT solid solution.

However no in-depth analysis of the structure of the whole phase diagram has been carried out and, in particular, no monoclinic phase and phase coexistence, typical of MPB (Sec.3.1) has been proposed.

Therefore, before turning to more detailed analyses (Sec.3.4) of the various structures present in the PYN-PT solid solution, insight will be gained by

- analysing the splitting of some Bragg reflections (Sec.3.3.1)
- looking at the presence and types of superstructure reflections (SSRs) (Sec.3.3.2)
- studying the degree of chemical ordering on the B site for compositions up to $x=0.35$ (Sec.3.3.3)
- investigating the positional disorder on the A site (Sec.3.3.4)

3.3.1 Distortions

Finding reasonable starting points to conduct Rietveld analysis can be challenging when the knowledge on the structure is limited. Hence before trying to resolve the full structure, information regarding the crystal systems will be extracted from the study of the peaks splitting.

We assume the structures in PYN-PT not to be triclinic and we therefore excluded this structure from our analysis. The discrimination between the remaining possible crystal systems was carried out by studying the splitting of $(00l)_{pc}$ and $(hhh)_{pc}$ reflections, since each of the systems leads to a different number of reflections (Table 3.3).

These Bragg reflections are plotted in Fig.3.3-3.5 for all compositions at high temperature and low temperature. The reflections with the largest diffraction angle but with no overlap with other reflections were chosen to reveal possible peak splittings.

Clear splitting of the $(00l)_{pc}$ and $(hhh)_{pc}$ reflections are observed for PYN and PYN-PT 0.05. This splitting is consistent with the monoclinic cell proposed in the literature to describe the pseudo-cubic cell, i.e. the ($Z=1$) cell without taking into account the antiparallel displacements of Pb^{2+} .

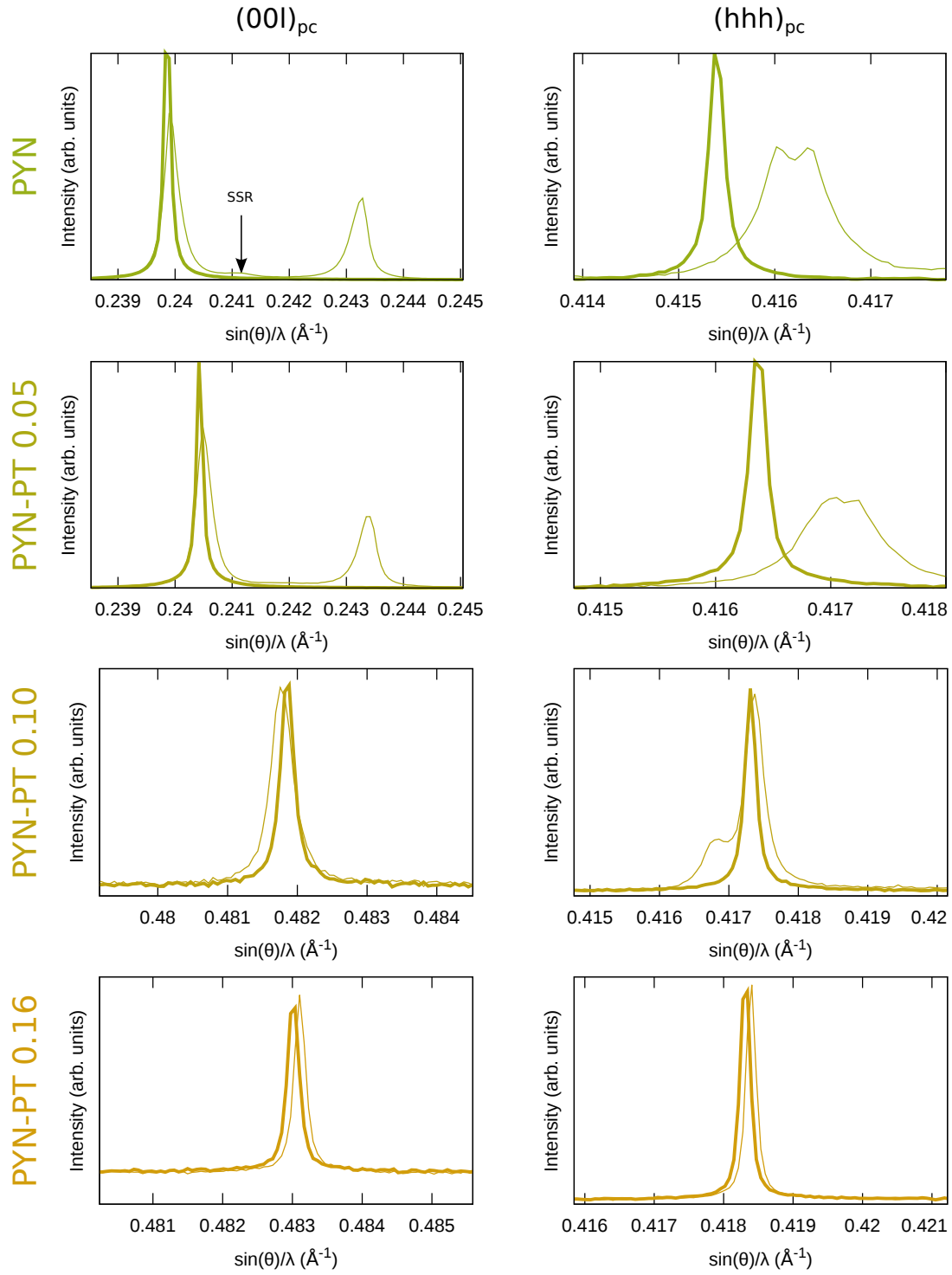


Figure 3.3: $(002)_{pc}$ and $(222)_{pc}$ Bragg reflections of PYN and PYN-PT 0.05 and $(004)_{pc}$ and $(222)_{pc}$ Bragg reflections of PYN-PT 0.10 and PYN-PT 0.16 at high-temperature (thick line and room temperature (thin line)).

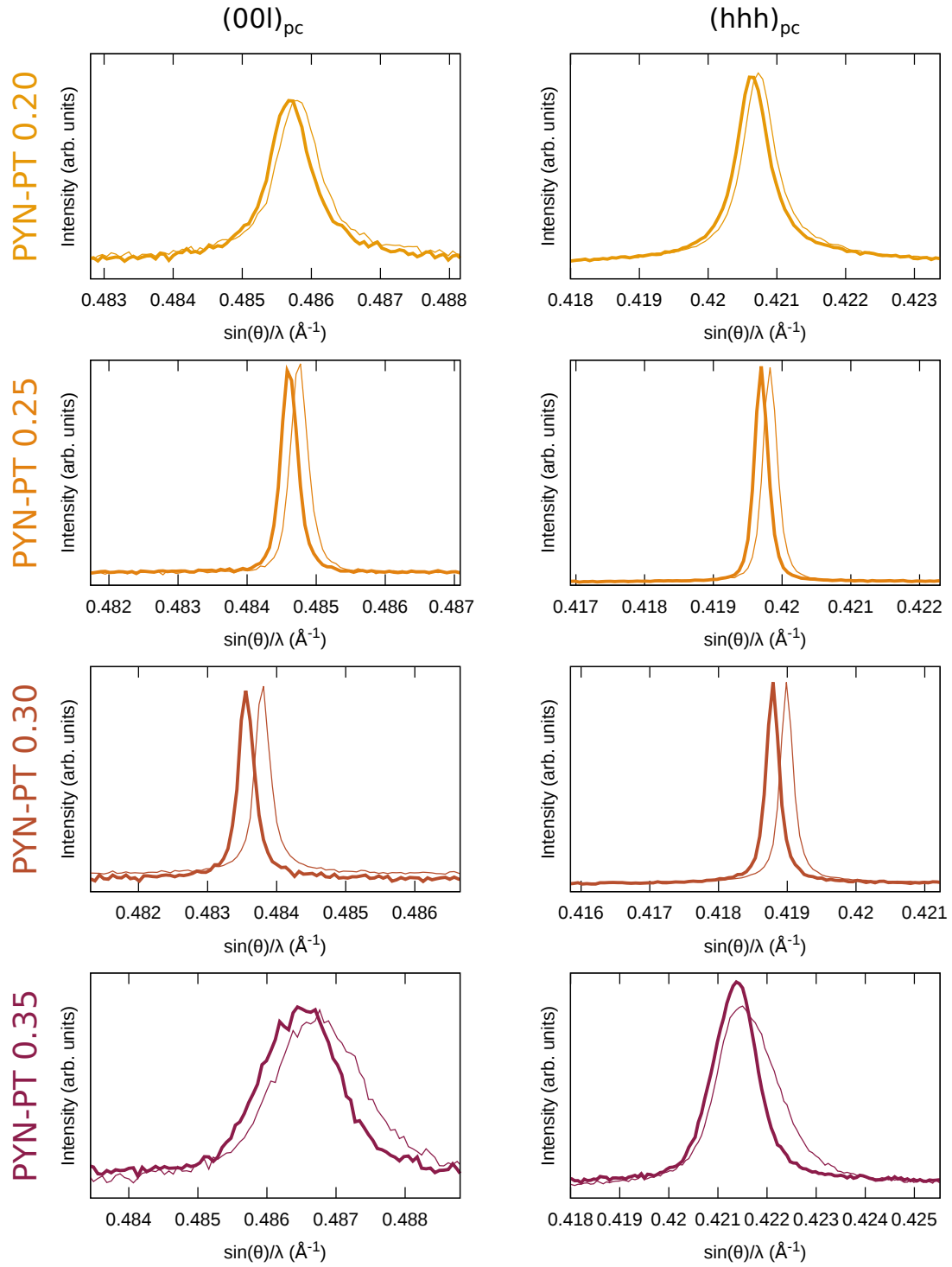


Figure 3.4: Bragg reflections $(004)_{pc}$ and $(222)_{pc}$ of PYN-PT $x = 0.20-0.35$ at high temperature (thick line) and room temperature (thin line)

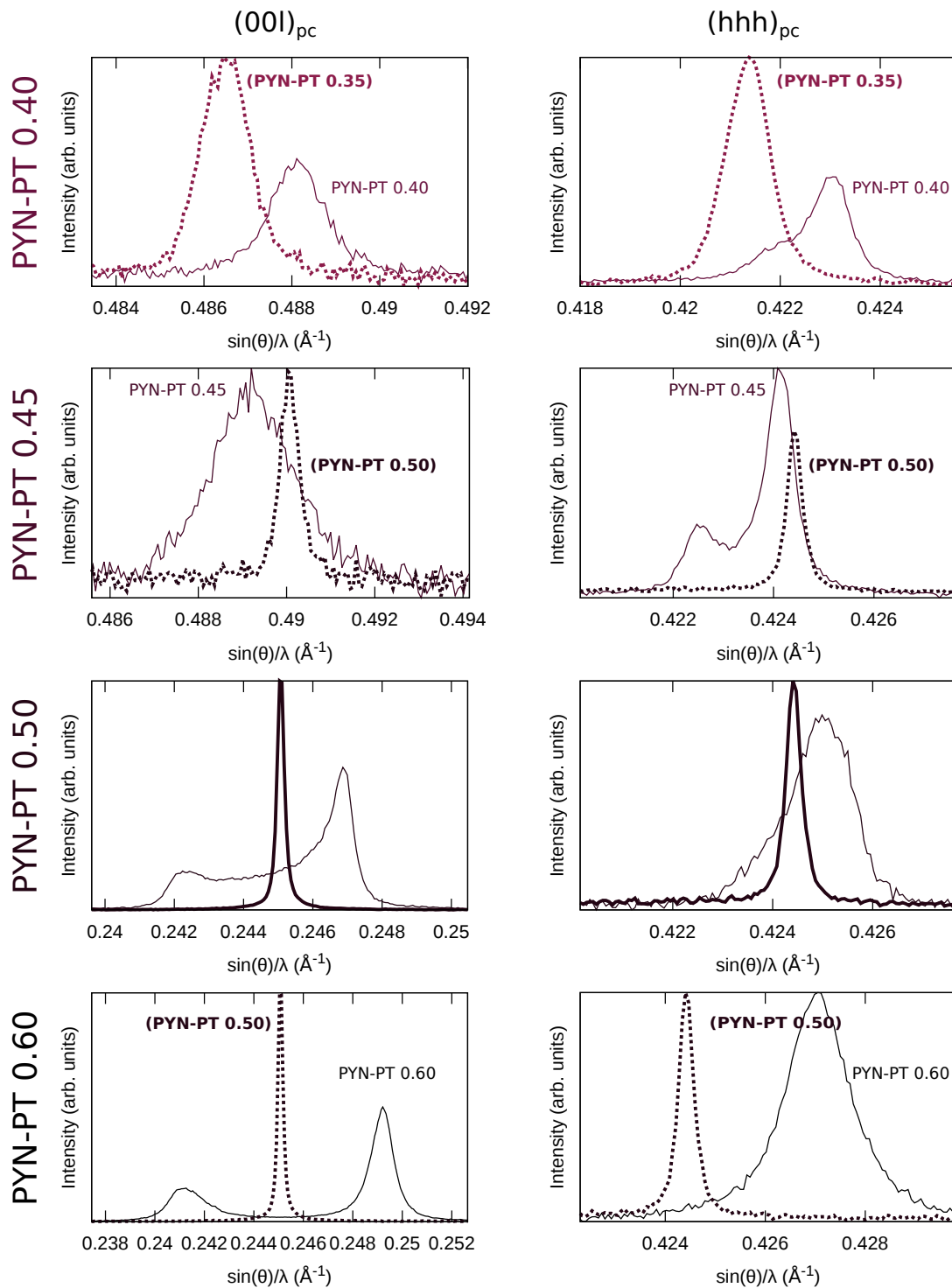


Figure 3.5: $(004)_{pc}$ and $(222)_{pc}$ Bragg reflections of PYN-PT 0.35 and PYN-PT 0.40 and $(002)_{pc}$ and $(222)_{pc}$ Bragg reflections of PYN-PT 0.50 and PYN-PT 0.60 at high-temperature (thick line) and room temperature (thin line).

For the compositions for which the high-temperature X-ray diffraction pattern lacks, the X-ray pattern of the closest composition was used as a reference (in dotted line).

Crystal System	$\langle 00l \rangle_{pc}$	$\langle hhh \rangle_{pc}$
Cubic	$(00l)$	(hhh)
Tetragonal	$(h00) \neq (00l)$	(hhh)
Rhombohedral	$(00l)$	$(hhh) \neq (hh\bar{h})$
Orthorhombic	$(h00) \neq (0k0) \neq (00l)$	(hhh)
Monoclinic	$(h00) \neq (0k0) \neq (00l)$	$(hhh) \neq (hh\bar{h})$

Table 3.3: Splitting of the $(00l)_{pc}$ and $(hhh)_{pc}$ reflections depending on the crystal system.

For PYN-PT 0.10, the splitting of the $(hhh)_{pc}$ reflections indicate a rhombohedral or a monoclinic structure. At room temperature, the $(00l)_{pc}$ reflections is not undoubtedly split but only broadened compared to the high-temperature reflection. This broadening could be due to a subtle splitting of the peak. Hence PYN-PT 0.10 could either have a rhombohedral or a monoclinic structure with $a \approx b \approx c$. The more thorough analysis in Sec.3.4.1.1 (page 130) will show that the structure is rhombohedral.

For PYN-PT with $0.16 \leq x \leq 0.30$, the $(00l)_{pc}$ and $(hhh)_{pc}$ reflections are unique at high temperature and room temperature. For all these compositions, the Full Width at Half Maximum (FWHM) was fitted at high temperature and room temperature (Fig.3.6) using a split pseudo-Voigt profile and the gnuplot software (see Sec.3.2.3). Within the uncertainties, no differences are observed between the high temperature FWHM and the room temperature one, for all compositions. However, for PYN-PT 0.30, the FWHM for the (004) reflections is slightly larger at room temperature compared to high temperature but remains within the limit of the experimental and fitting uncertainties. This increase will be confirmed by the X-ray experiment conducted on PYN-PT 0.30 as a function of temperature (Sec.3.5.2, page 162).

Within this compositional range, PYN-PT 0.20 displays wider diffraction peaks compared to the other compositions. This widening could be due to disorder intrinsic to this composition. However, since PYN-PT 0.20 is the only composition showing this widening, it is assumed that it is rather the lower quality of this particular sample that causes the widening. The study of more samples with compositions equal or close to $x = 0.20$ could confirm this assumption.

Therefore, the compositions in the range $0.16 \leq x \leq 0.30$ do not show any splitting of the $(00l)_{pc}$ and $(hhh)_{pc}$ reflections indicating a cubic phase. The detailed study of these compositions in Sec.3.4.2.1 will reveal that the long-range structure is indeed pseudo-cubic for $0.16 \leq x \leq 0.25$. The systematic study of PYN-PT 0.30 as a function of temperature will show that the slight increase in width observed at low temperature is meaningful and that there are actually monoclinic distortions in PYN-PT 0.30.

For compositions with $0.35 \leq x \leq 0.50$, the $(hhh)_{pc}$ reflection is not unique based either on the distinct splitting of this reflection or on the strong asymmetry of the peak.

Regarding the $(00l)_{pc}$ reflections, there is a distinct splitting for $x \geq 0.50$. For PYN-PT 0.45, the $(00l)_{pc}$ reflection is broad and asymmetric which points toward a non-unicity of this reflec-

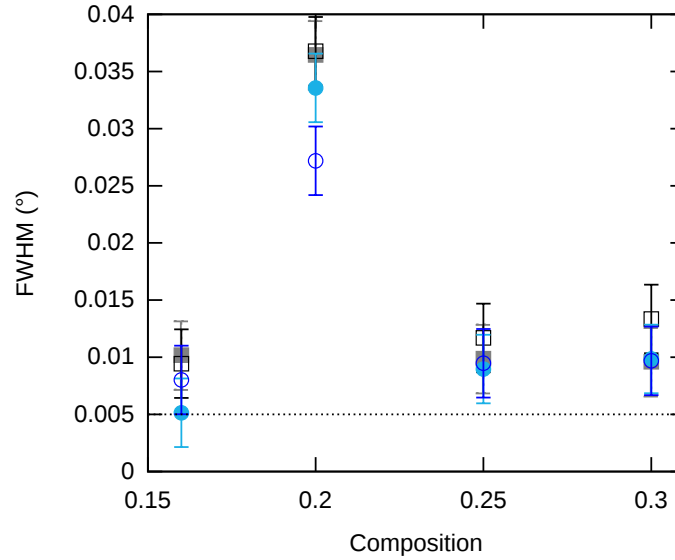


Figure 3.6: Full-Width at Half Maximum (FWHM) for the $(222)_{pc}$ reflection (blue circles) and the $(004)_{pc}$ reflection (squares) for several compositions and temperatures. The high-temperature FWHM is plotted in solid symbols and the room-temperature FWHM is plotted in open symbols.

tion. For PYN-PT 0.35-0.40, the $(00l)_{pc}$ reflections are broad but no asymmetry or splitting can be clearly observed. Hence from these simple observations of two families of Bragg reflections, PYN-PT 0.35-0.40 would appear to be rhombohedral, PYN-PT 0.45-0.50 monoclinic. For PYN-PT 0.60 the $(00l)_{pc}$ is split and the $(hhh)_{pc}$ broad but not necessarily split pointing toward the tetragonal crystal system, in agreement with the literature [47, 52, 53].

However, the more thorough analyses of the structure conducted in Sec.3.4.3 will show that, even in first approximation, the structure of PYN-PT 0.35-0.40 cannot be viewed as rhombohedral and that the broadening is really due to the splitting of the $(00l)_{pc}$ reflection and therefore that the structure of PYN-PT 0.35-0.40 is monoclinic.

Furthermore, these compositions are close to the morphotropic phase boundary ($x \sim 0.50$) for which a coexistence of phases is expected and therefore the observations made here are nothing but good starting points for Rietveld refinement.

These simple observations of the X-ray diffractograms indicate that when increasing the PT content in the PYN-PT solid solution the pseudo-cubic cell (with $Z=1$) is first monoclinic then becomes cubic through a rhombohedral phase, and that, at larger PT content the compositional range close to the morphotropic phase boundary ($x \sim 0.50$), rhombohedral, monoclinic and tetragonal phases are present and probably coexist.

In the more exhaustive analyses of the room-temperature structures (Sec.3.4) and phase transitions (Sec.3.5), the compositions will be separated based on these observations of the splitting

of some reflections and on the presence of SSRs due to antiparallel displacements of Pb^{2+} (evidenced in the next section).

Finally, it is interesting to note that strong distortions from the cubic phase can be observed at room temperature for PYN-PT 0.10, PYN-PT 0.35 and PYN-PT 0.40 whereas these compositions were regarded as relaxors in the chapter dedicated to the study of the dielectric and hysteresis properties (Chapter 2). Relaxors usually have pseudo-cubic structures (see Sec.3.1, page 102) and the splitting of Bragg reflections and the presence of SSRs due to antiparallel displacements of Pb^{2+} for PYN-PT 0.10 (observed in the next section) would rather indicate antiferroelectric (for PYN-PT 0.10) or ferroelectric behaviors (for PYN-PT 0.35 and PYN-PT 0.40). This apparent discrepancy between the structural and properties studies will be discussed in Chapter 4.

3.3.2 Presence and type of SSRs

X-ray diagrams obtained on every compositions at room and high temperatures are plotted in Fig.3.7.

In addition to the Bragg reflections, some additional peaks can be observed for compositions up to $x=0.35$. These additional peaks are superstructure reflections (SSRs) and may come from various sources, such as chemical order, antiparallel displacements or O-octahedra tilting (Sec.3.1.4). Hereafter, we will focus on the determination of the sources of these SSRs. More detailed studies on the antiparallel displacements of Pb^{2+} (Sec.3.4.1.2), chemical ordering (Sec.3.3.3) and O-octahedra tilting (Sec.3.4.4) will be conducted based on the attribution of the SSRs conducted in this section.

All SSRs observed in my X-ray diagrams are considered to be due either to chemical ordering on the B site or to antiparallel displacements of Pb^{2+} on the A site since all SSRs were also observed on fast recorded diagrams using the laboratory Brucker D2 diffractometer. Indeed, even though O-octahedra tilting SSRs have been observed using high-flux X-ray sources (i.e. synchrotron), such SSRs have never been observed using rough-and-ready experiments conducted to check the purity of the material. Hence, the only credible sources for SSRs in X-ray diagrams are B-cations chemical ordering and antiparallel displacements on the A (Pb^{2+}) site. In the X-ray diagrams, the SSRs due to chemical ordering and antiparallel displacements are separated based on their existence at high temperature. Indeed, SSRs due to chemical ordering are considered not to be temperature-dependent in the temperature range investigated for the diffraction experiments (300-600 K) since this temperature is much lower than the typical ordering-disordering temperature ($\sim 1300\text{-}1500\text{ K}$). Therefore, the SSRs remaining at high temperature are attributed to chemical order (open circles in Fig.3.7), whereas the ones that have disappeared at high temperature are attributed to antiparallel displacements of Pb^{2+} (stars and bars in Fig.3.7).

Moreover, to confirm that the SSRs remaining at high temperature are due to chemical ordering, it was checked that their $\sin(\theta)/\lambda$ positions were in agreement with typical reflections expected for rock-salt ordering observed in double-perovskites: $(h/2\ k/2\ l/2)$ with h, k, l all odd integers. Thus, SSRs due to chemical ordering can be observed for compositions up to $x=0.35$ and SSRs

due to antiparallel displacements of Pb^{2+} up to $x = 0.10$.

For both types of SSRs, the compositions with the largest PT content present peculiarities. Indeed, the SSRs due to chemical ordering in PYN-PT 0.35 cannot be indexed with $(h/n\ k/n\ l/n)$ with n precisely equal to 2, but with n slightly larger than 2. This will be discussed in more details in Sec.3.3.3 (page 119).

Furthermore, for PYN-PT 0.10, the SSRs due to antiparallel displacements of Pb^{2+} are of different nature from the ones in PYN and PYN-PT 0.05 since PYN and PYN-PT 0.05 present narrow peaks (stars in Fig.3.7), whereas PYN-PT 0.10 presents broad peaks (bars in Fig.3.7) appearing at diffracting angles different from the ones of the SSRs in PYN and PYN-PT 0.05. The different types of SSRs due to antiparallel displacements of Pb^{2+} will be examined in Sec.3.4.1.2 (page 131).

Despite the fact that O-octahedra tilting is expected to concur with antiparallel displacements of Pb^{2+} [86], no extra reflection is observed in the neutron diffractogram of PYN compared to the X-ray diagram. It is possible that the reflections due to O-octahedra tilting are “hidden” under the numerous peaks due to chemical ordering and antiparallel displacements. Complementary analysis of the structure would be needed to conclude to the presence or absence of O-octahedra tilts in the structure of PYN. Also, the HRTEM images taken on PYN did not unveil any rotation, but a limited number of zone axes were accessible and it is highly possible that O-octahedra SSRs would have been observed in different zone axes.

However, SSRs due to O-octahedra tilting can be observed in the neutron diffractograms for PYN-PT 0.30 and PYN-PT 0.40 as evidenced by the presence of extra reflections compared to the X-ray diffractograms (Fig.3.8). The possible O-octahedra tilt systems associated with these SSRs reflections will be discussed in Sec.3.4.4 (page.153). SSRs due to O-octahedra tilting were not observed in the neutron diffractograms of PYN-PT 0.50 and PYN-PT 0.60.

In summary, chemical ordering is present in PYN-PT for compositions up to $x = 0.35$. Two types of antiparallel displacements are observed for PYN and PYN-PT 0.05, on the one hand and PYN-PT 0.10, on the other hand. Finally, O-octahedra tilting are observed for PYN-PT 0.30 and PYN-PT 0.40.

3.3.3 Quantification of the chemical order on the B-site

As shown in Sec.3.3.2, SSRs due to chemical order are present for compositions up to $x = 0.35$. Hereafter, several methods will be used to examine the chemical order in the PYN-PT solid solution.

For simplicity, the study of the chemical order is conducted on the X-ray diffractograms of the (high-temperature) paraelectric phase in order to eliminate the complications due to distortions and antiparallel displacements.

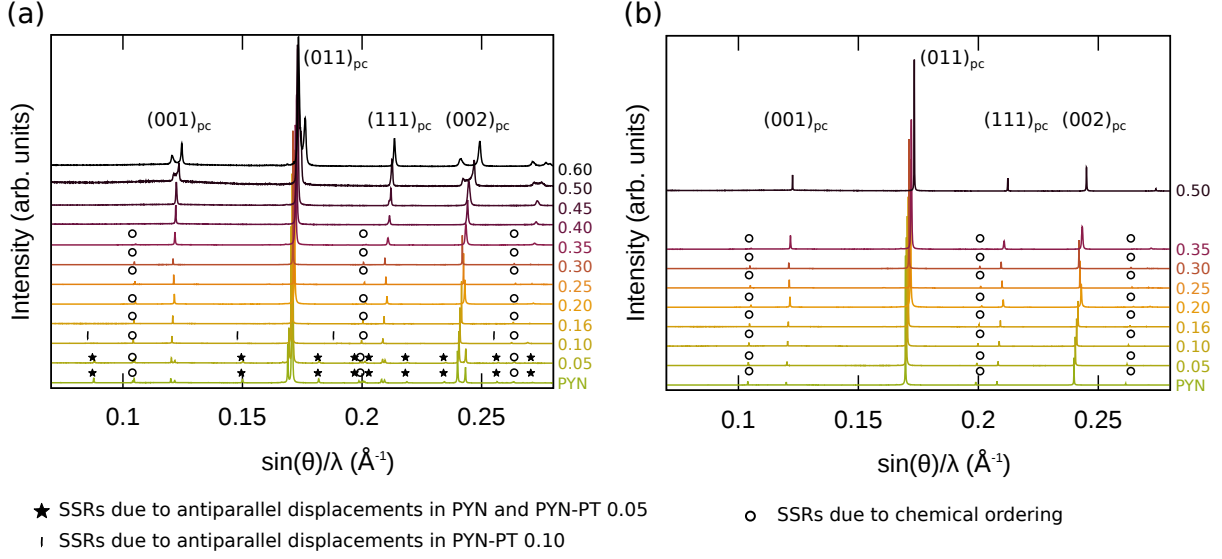


Figure 3.7: X-ray diagram for all compositions recorded at the ID31 beamline at ESRF (a) at room temperature and (b) 30° above the Curie temperature (T_c) or the temperature of the maximum of the dielectric constant (T_m).

Solid stars indicate SSRs due to antiparallel ordering in PYN and PYN-PT 0.05. These SSRs are consistent with the ones reported in the literature.

Vertical lines indicate broad peaks in the PYN-PT 0.10 diagram ascribed to antiparallel displacements.

Open circles indicate SSRs due to chemical ordering. These SSRs are observed both at room and high temperatures.

Chemical order is usually evaluated using the formula introduced in Sec.1.2.1:

$$\text{Eq.(1.2)} \quad s^2 = \frac{\left(\frac{I_{SSR}}{I_{Bragg}}\right)_{meas}}{\left(\frac{I_{SSR}}{I_{Bragg}}\right)_{s=1}}$$

where $\left(\frac{I_{SSR}}{I_{Bragg}}\right)_{s=1}$ and $\left(\frac{I_{SSR}}{I_{Bragg}}\right)_{meas}$ are the ratios of intensity of Bragg reflections to the superstructure reflections due to chemical order for the perfectly ordered perovskite and measured on the real material, respectively. This formula hence requires the knowledge of the structure of the perfectly ordered material.

For B-ordered double perovskites, the standard structure taken as a reference state is the one in which all atoms are in their prototypic positions and the two B cations occupy each different crystallographic sites. For PYN, in the cubic phase, this structure has a $Fm\bar{3}m$ space group with Pb at $(0.25, 0.25, 0.25)$, Yb at $(0, 0, 0)$, Nb at $(0.5, 0.5, 0.5)$, O at $(0.25, 0.25, 0)$.

However the X-ray diagram simulated from this double-perovskite (Fig.3.9(a)) is drastically different from the measured one: the intensities of several Bragg reflections in the simulated diagram strongly deviates from the ones observed experimentally. For example, in the case of

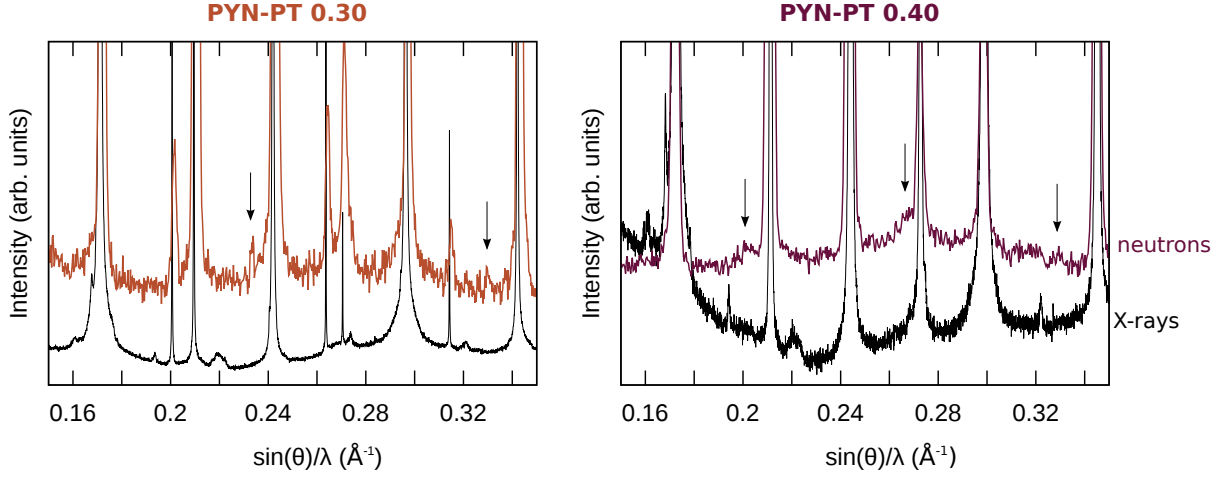


Figure 3.8: Comparison of the X-ray (black) and neutron (color) diffractograms for PYN-PT 0.30 and PYN-PT 0.40.

Additional reflections in the neutron diffraction pattern are indicated by arrows.

the ideal double perovskite $\left(\frac{I_{001}}{I_{011}}\right)_{calc} = 1$ against 0.023 measured in the real material.

Thus, whereas PYN is expected to be highly ordered due to the large difference in ionic radii, valences and large sum of ionization potential between Yb^{3+} and Nb^{5+} (see Sec.1.2.1.2, page 31), the measured X-ray diagram is far from the one simulating a perfectly ordered double perovskite with all atoms in their ideal positions. The difference between the model and our data may come from three sources: PYN is not well ordered or all atoms are not in their ideal position or there is a preferential orientation in our sample.

Because the diffractograms were recorded on powder in rotating capillaries, a preferential orientation is unlikely especially considering such strong changes in the intensity ratios.

If the discrepancy between our model and the data comes from low chemical order in PYN, then the measured X-ray diffractogram would be the superimposition of the patterns of a perfectly ordered and perfectly disordered PYN material. The X-ray diagram of a perfectly disordered PYN perovskite, plotted in Fig.3.9(c), shows intensity ratios for the main Bragg peaks that differ strongly from the measured diagram. In both the disordered and ordered simulated diagrams, the intensity ratios $\left(\frac{I_{001}}{I_{011}}\right)$ are much larger than in the measured one. Therefore, their weighted sum could not match the observed intensity ratio and shows that the discrepancy between the intensity ratios simulated and measured cannot be only explained by a low degree of chemical order. And atomic disorder must then be considered.

To have a better idea of the possible off-centering of atoms in the PYN double perovskite, literature on high-temperature structures was examined using the Crystallography Open Database (COD) [91]. The high-temperature structure of only three Pb-based double perovskites were found: $\text{Pb}(\text{Mg}_{1/2}\text{W}_{1/2})\text{O}_3$, $\text{Pb}(\text{Co}_{1/2}\text{W}_{1/2})\text{O}_3$ and $\text{Pb}(\text{Mg}_{1/2}\text{Te}_{1/2})\text{O}_3$. Only in the cases of the

perfectly-ordered antiferroelectric double-perovskites, $\text{Pb}(\text{Mg}_{1/2}\text{W}_{1/2})\text{O}_3$ and $\text{Pb}(\text{Co}_{1/2}\text{W}_{1/2})\text{O}_3$, is one atom off its ideal position: the Pb^{2+} cation [92]. In both double perovskites, the Pb^{2+} cations is displaced in the $\langle 011 \rangle$ direction of about the same distance. Using this off-centering, a X-ray diagram was simulated for PYN and is plotted in Fig.3.9(b). In this case, the simulated diagram matches better the measured X-ray diagram; in particular, the ratios of the intensity of the Bragg peaks are more correctly described ($\left(\frac{I_{001}}{I_{011}}\right)_{\text{calc}} = 0.026$ against 0.023 measured). Hence, the measured X-ray diagram of PYN can be reproduced fairly well with a perfectly ordered model with Pb^{2+} off-centered.

Finally, the X-ray diagram of a completely disordered PYN perovskite with Pb^{2+} cations off-centered by the same extend as in the ordered case was simulated (Fig.3.9(d)). This diagram does not reproduce well the intensity ratio of the main Bragg peaks ($\left(\frac{I_{001}}{I_{011}}\right) = 1.11$) indicating that a model of chemical disorder with Pb^{2+} -cation off-centered does not seem to suit PYN.

Therefore, despite not enabling a precise determination of the degree of chemical ordering (s), my four different models (ordered/disordered perovskite with Pb^{2+} cation in/off its ideal position) indicate that PYN is mostly chemically ordered and that the Pb^{2+} cation is not in its ideal position even at high temperature.

The off-centering of the Pb^{2+} cation will be studied in the next section and, using this knowledge, a more complex approach describing the system as a composite with an ordered and a disordered phase (introduced in Sec.1.2.1, page 29) will be examined to determine the degree of chemical ordering.

In the PYN-PT solid solution, the degree of ordering in the material could be evaluated using the formula (1.2) (and recalled page 115) but using a pseudo-double perovskite in which the two B-cations are pseudo-atoms (B' and B'') representing Yb/Ti and Nb/Ti respectively (see Sec.1.2.1 for more details). Using this pseudo-double perovskite as reference state for the perfectly ordered material ($s = 1$), the same problem as observed for PYN arises: the intensity ratio of Bragg reflections are not well-described if the Pb^{2+} -cation remains in its ideal position (see Fig.3.9 with the example of PYN-PT 0.25). The same reasoning as for PYN was followed and it also appears that, in PYN-PT, a displacement of the Pb-cation off its ideal position enables a better description of the material.

In conclusion, over the entire compositional range where chemical order is observed in the PYN-PT solid solution, the Pb^{2+} cation does not appear to be in its ideal position requiring the use of a more complex model (e.g. the composite model) to be able to take into account simultaneously the positional disorder of Pb^{2+} cation and the chemical order of B-site cations in the description of the structure.

Coherence length of the chemical order

Before envisioning a more complicated model to evaluate the degree of chemical order, I wanted to check whether the ordered and disordered phases had the same coherence length using a Williamson-Hall approach. Indeed a difference in coherence length may indicate a segregation of Ti imposing to consider another kind of composite model, namely where two PYN-PT phases

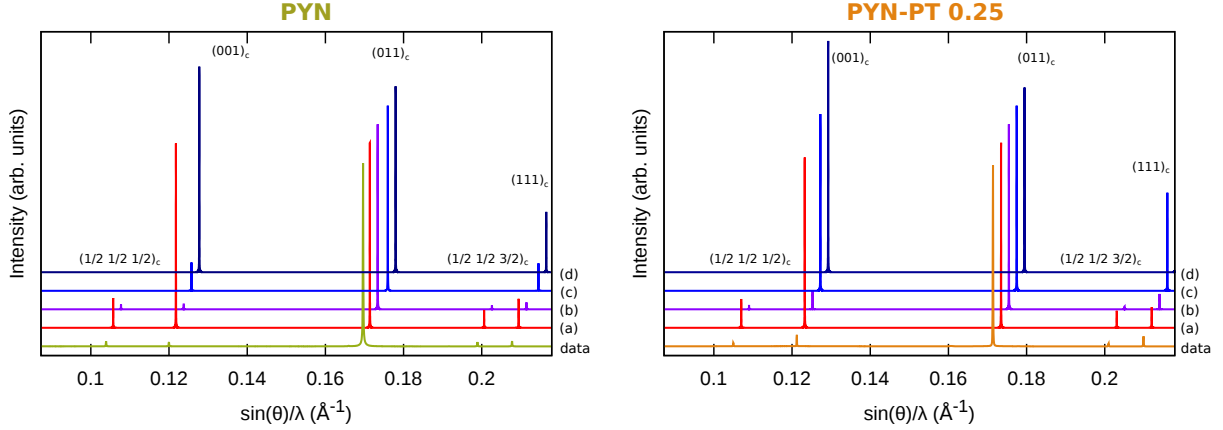


Figure 3.9: Comparison of X-ray diagrams recorded at ESRF ID31 ($\lambda = 0.4 \text{ \AA}$) for PYN and PYN-PT 0.25 with their calculated counterpart. The diagrams are normalized with respect to the $(011)_c$ reflection. All simulated diagrams were created using the Mercury software.

- (a) Ordered perovskite with Pb^{2+} in its ideal position
- (b) Ordered perovskite with Pb^{2+} off its ideal position
- (c) Disordered perovskite with Pb^{2+} in its ideal position
- (d) Disordered perovskite with Pb^{2+} off its ideal position

with different chemical formulae (one rich in PYN and one rich in PT) and degree of chemical order coexist rather than two phases with the same chemical formula but different degree of chemical order (with the extreme case of one phase with ordered B cations and the other one with disordered B cations).

Furthermore, if there is no difference in coherence length, the ordered and disordered phases at the end of the refinement using the latter composite model (described in Chapter 1) should have equivalent profile parameters reducing the number of variables in Rietveld refinements.

The Williamson-Hall analysis relies on the hypothesis that the integral breadth of the peak in the diffraction pattern is only due to size and strain effects. The widening of the peak is then

$$\beta = \beta_{size} + \beta_{strain} = 4\varepsilon \tan \theta + \frac{\lambda}{L \cdot \cos \theta}$$

or

$$\beta \cdot \cos \theta = 4\varepsilon \sin \theta + \frac{\lambda}{L} \quad (3.1)$$

with β the integral breadth of the peak at the diffracting angle θ , λ the wavelength, L the size of the diffracting region, and ε the strain, β_{size} is supposed to be constant with respect to the diffracting angle and β_{strain} to depend linearly on the diffracting angle [93].

Thus, plotting $\beta \cdot \cos \theta$ as a function of $\sin \theta$ enables to separate the broadening due to size effect from the one due to strain effects since the slope will be given by the strain and the intercept by the size (Fig.3.10). The diffraction peak is widened due to size effect only if the size of the diffraction region is below $\sim 100 \text{ nm}$ that is the intrinsic coherence length of X-rays.

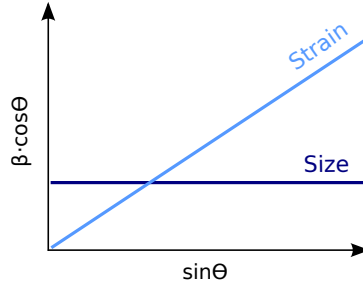


Figure 3.10: Schematic representation of the different contributions of strain and size effect to the integral breadth (β) in a Williamson-Hall analysis.

The Williamson-Hall analysis was conducted on samples with the largest amount of PT and showing SSRs due to chemical order, assuming that the possible change of coherence length will increase with PT content. For each composition, the Williamson-Hall analysis was conducted, using the gnuplot software (see Sec.3.2.3, for details on the fitting procedure) on two subgroups of reflections: the Bragg reflections (which are present regardless of the ordering state prevailing on the B site) and the SSRs due to the chemical order.

The Williamson-Hall plot for PYN-PT $x = 0.25-0.35$ are presented in Fig.3.11. For each composition, the width of the diffraction peak increases linearly with the diffracting angle θ with the same slope for Bragg peaks and SSRs. The diffraction peak of PYN-PT 0.35 are wider than for other compositions, most likely because the material is not completely in its cubic phase as evidenced by splitting of some of the Bragg peaks at large angles and since neither PYN-PT 0.30 nor PYN-PT 0.40 are in their cubic state 30° above the temperature of the maximum of the dielectric constant (Sec.3.5).

Moreover, for Bragg peaks and SSRs, the Williamson-Hall plot does not exhibit a plateau at low $\sin(\theta)$ values indicating that there is no size effect in our samples, i.e. the diffracting region is large compared to the coherence length of X-rays. That is to say that there is either only one phase or that there are two phases both seen as infinite for X-rays. In the case of the presence of two phases, the crystallites of the ordered and disordered phases are larger than 100 nm. The solution with an homogeneous phase seems more appropriate to describe the PYN-PT solid solution based on the change of the chemical ordering of PYN-PT 0.35 discussed in the next paragraph.

Change of the chemical order

In PYN-PT 0.35, the chemical order is slightly different from the one observed in the other ordered compositions. Indeed, the SSRs are no longer in their ideal position ($h/2 \ k/2 \ l/2$), but slightly shifted toward lower $\sin(\theta)/\lambda$ values (Fig.3.12), indicating that the SSRs can no longer be indexed with $(h/n \ k/n \ l/n)$ with n strictly equal to 2. The experimental value determined for n is 2.002 (± 0.002). This value is very close to the exact one, however the comparison of the diffraction pattern obtained from the ideal double perovskite and the actual one (Fig.3.12)

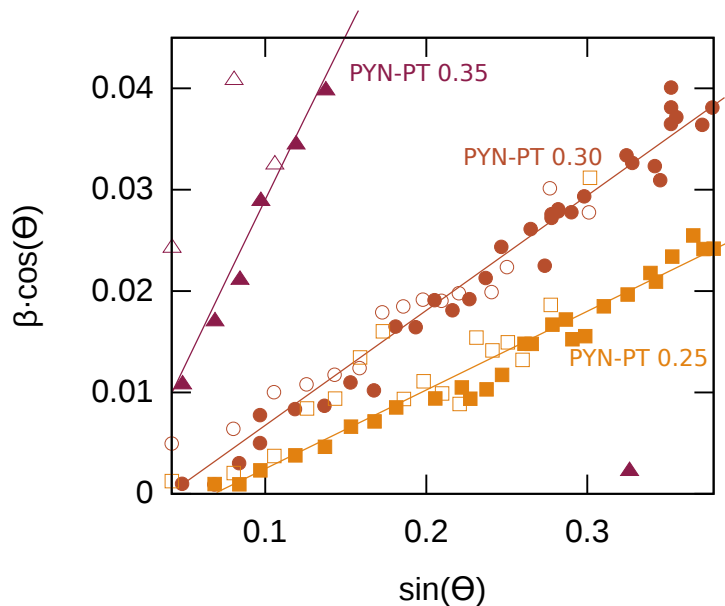


Figure 3.11: Williamson-Hall plot for PYN-PT 0.25 (squares), PYN-PT 0.30 (circles) and PYN-PT 0.35 (triangles). The close symbols represent the main Bragg reflections; whereas the open symbols represent the SSRs reflection due to chemical order. The lines are linear fits.

reveals a distinct mismatch in the diffracting angle for the SSRs related to the chemical order. Since, the corresponding peculiar chemical order occur on the long-range (cf Williamson-Hall study), the structure of PYN-PT 0.35 cannot be described neither as a pseudo-double perovskite nor as a composite of a rock-salt ordered and disordered phases. It may rather be described either as an homogeneous phase with a chemical order different from the classical rock-salt arrangement or by a composite with large clusters of a disordered phase and a phase with chemical order on the B site different from the rock-salt one.

This latter possibility, to create this new type of composite structure, seems dubious since the addition of Ti^{4+} can be easily incorporated in a composite with a rock-salt ordered phase and a disordered one by increasing the number or size of disordered regions.

Hence, for PYN-PT 0.35, it seems more likely that the phase is homogeneous with a different arrangement of the B cations than having an ordered and a disordered phase, with an ordered phase having a chemical arrangement different than the one of the pseudo-double perovskite.

Conclusion

The first attempt at measuring the chemical order in the PYN-PT solid-solution was conducted comparing the measured X-ray patterns with the ones simulated for perfectly ordered (pseudo-)double perovskites. This method was proven not to be adapted to the case of the PYN-PT solid solution because Pb^{2+} cations are displaced from their ideal positions.

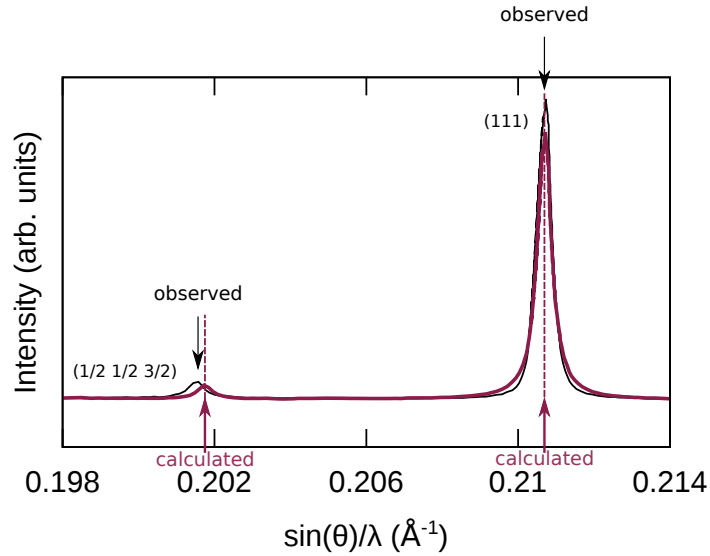


Figure 3.12: Measured (thin black line) and calculated (thick magenta line) diffraction pattern for PYN-PT 0.35 at 300 °C. The calculated diffraction pattern is based on the $Fm\bar{3}m$ space group, i.e. assuming superlattice reflection situated precisely in $(h/2\ k/2\ l/2)$.

Hence a more complex method is required to study the degree of chemical order in the PYN-PT solid solution: a refinement with a composite model with one ordered and one disordered phase or using a modulation of the occupancy of the B site (see details in Sec.1.2.1.1, page 30).

Furthermore the Williamson-Hall analysis has shown that the ordered and disordered regions in the various samples have the same coherence length. Moreover, in PYN-PT 0.35, it appears that the sample is probably homogeneous due to a change of the long-range ordering. Hence, we suppose that compositions with $x < 0.35$ also show a homogeneous phase based on the Williamson-Hall analysis reported above and by analogy with the PYN-PT 0.35 composition. Therefore, in first approximation, the pseudo-double perovskite model might be sufficient to have a better idea of the structure and therefore to study the distortions.

3.3.4 Positional disorder on the A-site

In the previous section, it was shown that the chemical ordering in the PYN-PT solid solution cannot be simply determined from X-ray diagrams because Pb^{2+} is not in its ideal position even at high temperature. In this section, the position of the Pb^{2+} cation will be examined for various compositions.

Methodology

The X-ray diagrams used for this analysis are the ones recorded on the ID31 beamline at ESRF for compositions in the range $0 \leq x \leq 0.35$ and for PYN-PT 0.50. PYN-PT 0.35 has been dis-

carded from this analysis because of the complexity of the chemical ordering in this composition discussed in Sec.3.3.3 (page 119).

In a first step, compositions in the range $0 \leq x \leq 0.30$ will be regarded as perfectly ordered pseudo-double perovskites $\text{Pb}(\text{B}'_{1/2}, \text{B}''_{1/2})\text{O}_3$ with $\text{B}' = \text{Yb}^{3+} + \text{Ti}^{4+}$ and $\text{B}'' = \text{Nb}^{5+} + \text{Ti}^{4+}$ as introduced in Sec.1.2.1.1 (page 29). In a second time, some of the compositions will be examined as perfectly disordered systems, i.e. the B-site of the perovskite structure will be occupied by a unique-pseudo B cation $= \text{Yb}^{3+} + \text{Nb}^{5+} + \text{Ti}^{4+}$ with the occupancy of each atom calculated to match the composition of interest. Hence, the two limiting cases of a perfectly ordered pseudo-double perovskite and a completely disordered perovskite are investigated. For PYN-PT 0.50, only the disordered case was examined as no SSRs reflections due to chemical order can be observed. We will see that both ordered and disordered cases lead to rather similar results proving that this simple approach is a good indicator of the disorder of Pb^{2+} .

The Pb^{2+} off-centering is evaluated by comparing the various agreement factors of the Rietveld refinement (*Rwp*, *Rp* and GOF) introduced in Sec.3.2.2 (page 105) for different positions of the Pb^{2+} cations. The Pb^{2+} cations were displaced at different fixed positions along the cubic $\langle 001 \rangle$, $\langle 011 \rangle$ and $\langle 111 \rangle$ directions.

The agreement factors were taken after the refinement of the thermal agitation parameter *B* for the Pb^{2+} , Yb^{3+} and Nb^{5+} cations. The agitation parameters for the oxygens was kept constant since, when refined, unreasonable values are obtained ($B_{\text{O}} \sim 12 \text{ \AA}^2$). For the sake of comparability of the results, the positions of all atoms were kept constant in the refinement, as well as the cubic cell parameter *a* and the profile parameters that were obtained in a profile matching analysis formerly conducted.

In this analysis, the existence of a minimum in the agreement factors for a non-zero value of a Pb^{2+} displacement would point out the presence of disorder in the structure. This disorder may be of various natures:

- dynamic if the atom “jumps” from one atomic position to another
- static if the atom is “fixed” into one position. This position may vary from one unit cell to the other.

In both cases, the average symmetry may remain cubic.

Results

The agreement factors as a function of the Pb^{2+} off-centering for various compositions are presented in Fig.3.13 for the case of the purely ordered pseudo-double perovskite and in Fig.3.14 for the case of the purely disordered perovskite. The best agreement factors (lower values of the various factors) are obtained for a displacement of about 0.32 \AA for all investigated compositions and regardless of the model chosen: ordered or disordered. This improvement of the modeled structure with Pb^{2+} displacements is also evidenced by a strong decrease of the thermal agitation factor of the Pb^{2+} cation, B_{Pb} : $B_{\text{Pb}} \sim 5.2 \text{ \AA}^2$ when Pb^{2+} is in its ideal position

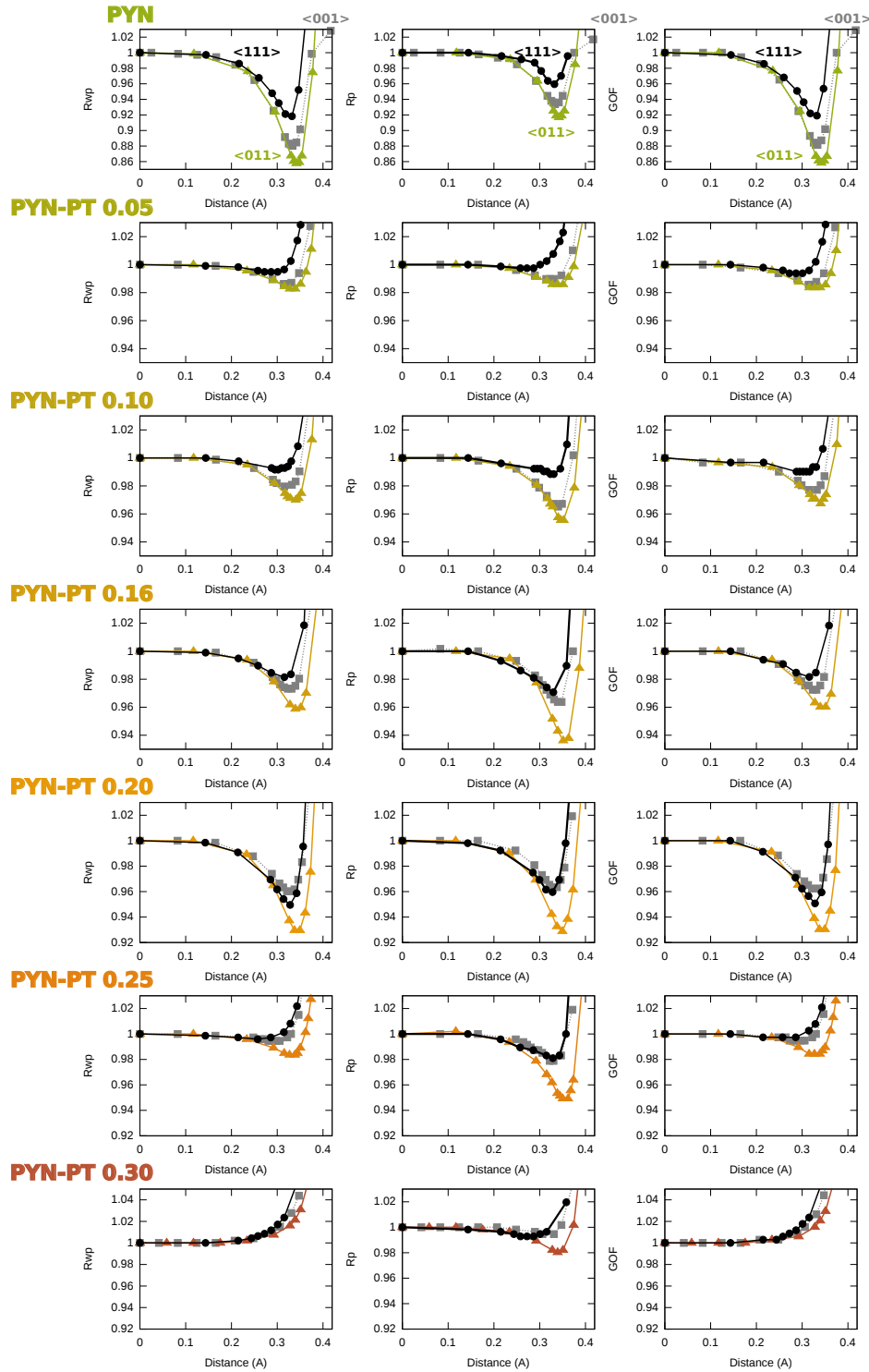


Figure 3.13: Normalized agreement factors for the Rietveld refinement as a function of Pb^{2+} off-centering distance for various compositions assuming a perfectly ordered pseudo-double perovskite. The results for displacements in the $\langle 001 \rangle$ direction are plotted in gray squares, in the $\langle 011 \rangle$ direction in colored triangles and $\langle 111 \rangle$ in black circles. The agreement factors are normalized with respect to the values obtained for a refinement in which Pb^{2+} is in its ideal position (distance = 0).

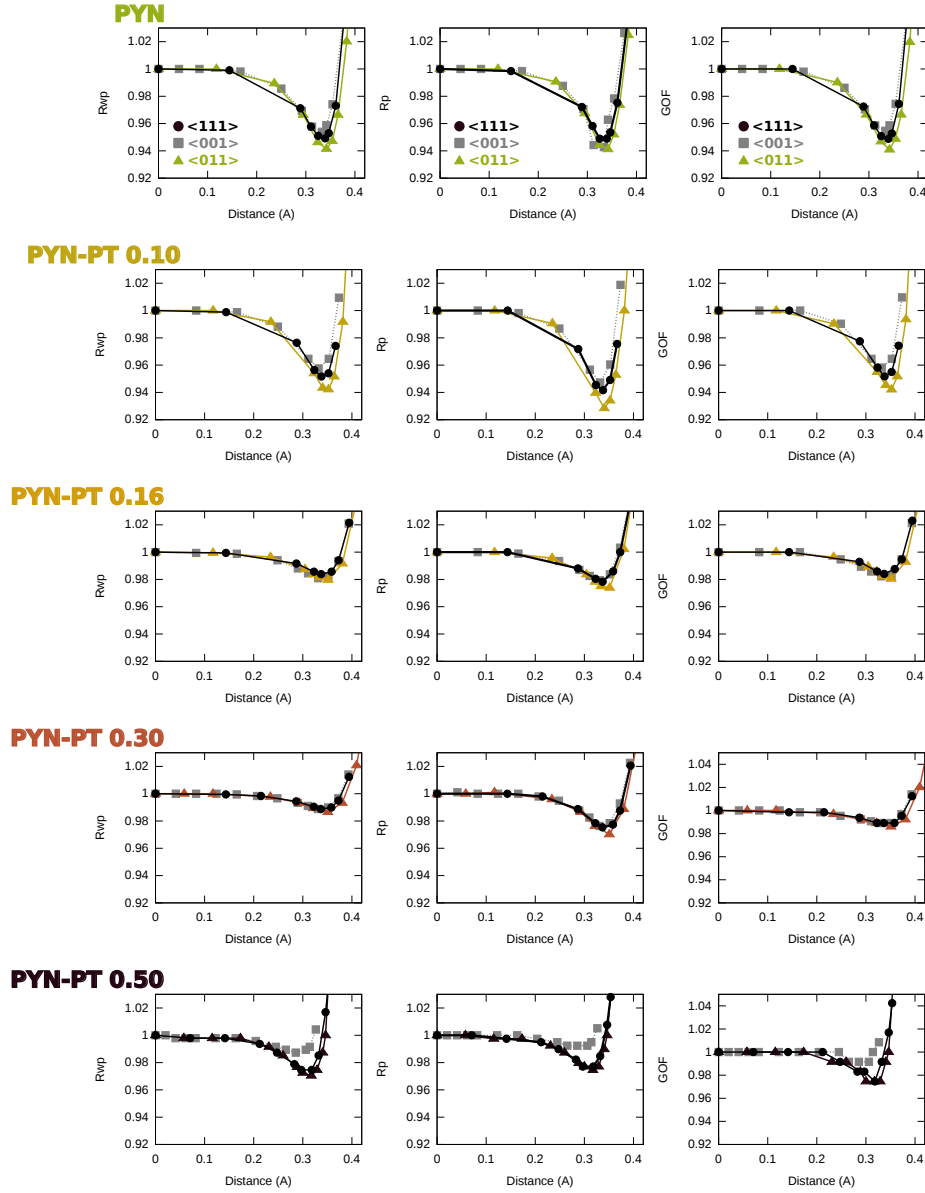


Figure 3.14: Normalized agreement factors for the Rietveld refinement as a function of the Pb^{2+} off-centering distance for various compositions assuming a perfectly disordered perovskite. The results for displacements in the $\langle 001 \rangle$ direction are plotted in gray squares, in the $\langle 011 \rangle$ direction in colored triangles and $\langle 111 \rangle$ in black circles. The agreement factors are normalized with respect to the values obtained for a refinement in which Pb^{2+} is in its ideal position (distance = 0).

and decreases to the more physical value of $B_{Pb} \sim 1.8 \text{ \AA}^2$ for the best agreement factors. For all investigated displacements, the agitation factors for the B-site cations remained physically reasonable $\sim 0.9 \text{ \AA}^2$.

For all compositions, when the solid solution is assumed to be perfectly ordered, the direction $\langle 011 \rangle$ is favored since the minimum of the agreement factors is deeper compared to the other directions, whereas in the disordered case, a more favorable direction of displacement may or may not appear.

Actually, for disordered PYN and PYN-PT 0.10, the Pb^{2+} cation is displaced preferentially along the $\langle 011 \rangle$ direction, as in the ordered case. The difference in agreement factors between the best direction, $\langle 011 \rangle$, and the other directions is smaller in the disordered case than in the ordered case, but undoubtedly present.

For PYN-PT 0.16 and PYN-PT 0.30, in the disordered case, no direction is preferred by the Pb^{2+} for its displacement.

Therefore using the two limiting cases (ordered and disordered) to model the disorder of Pb^{2+} , the amplitude of the displacement of Pb^{2+} off its ideal position can be unequivocally determine. However, only using these two models, it is not possible to ascertain for all compositions whether the displacement of Pb^{2+} is equal in all directions or if the displacement is more likely to occur in one direction.

Discussion

In the case of compositions that exhibit antiparallel displacements of Pb^{2+} at low temperature (as evidenced by the presence of SSRs in the X-ray patterns), i.e. $x \leq 0.10$, Pb^{2+} cations are more favorably displaced along the $\langle 011 \rangle$ direction compared to the other directions. Favorable displacements in the $\langle 011 \rangle$ direction were also observed in the high-temperature cubic phase of the Pb-based double perovskites $\text{Pb}(\text{Co}_{1/2}\text{W}_{1/2})\text{O}_3$ and $\text{Pb}(\text{Mg}_{1/2}\text{W}_{1/2})\text{O}_3$. In these cases, the displacement amplitude was of about 0.27 \AA [26].

In the case of the only studied compositions for which the low temperature phase is ferroelectric, PYN-PT 0.50, it is as energetically favorable, for Pb^{2+} cations, to be displaced along the $\langle 011 \rangle$ direction as along the $\langle 111 \rangle$ direction, the two being more favorable than in the $\langle 001 \rangle$ direction.

In the intermediate compositional range, $0.16 \leq x \leq 0.30$, the direction in which the Pb^{2+} cations is displaced is strongly influenced by the chemical ordering of the B-site cations as mentioned previously. Hence, it seems that if the B site is chemically ordered along $[111]$ the Pb^{2+} cation will displace preferentially along the $\langle 011 \rangle$ direction, whereas if the chemical environment is disordered the Pb^{2+} cation will displace randomly in all directions, i.e. on a sphere.

Therefore, in PYN-PT solid solution, Pb^{2+} is disordered on a sphere centered on its ideal position with a radius of about 0.32 \AA . For some compositions, only certain points of the sphere are occupied along special directions. For other compositions, the occupation of the sphere

	refined distance	ideal distance	Ref
Pb(Yb _{1/2} Nb _{1/2})O ₃	2.60 Å	2.95 Å	This work
0.5Pb(Yb _{1/2} Nb _{1/2})O ₃ -0.5PbTiO ₃	2.58 Å	2.89 Å	This work
Pb(Sc _{1/2} Nb _{1/2})O ₃	2.66 Å	2.80 Å	[30]
PbTiO ₃	2.58 Å	2.80 Å	[30]
Pb(Zn _{1/3} Nb _{2/3})O ₃	2.56-2.58 Å	2.87-2.85 Å	[94]
Pb(Mg _{1/2} W _{1/2})O ₃	2.56 Å	2.83 Å	[26]
Pb(Zr _(1-x) Ti _x)O ₃ with $0 \leq x \leq 0.75$	2.595-2.625 Å	2.85-2.95 Å	[95]

Table 3.4: Pb-O distances for several Pb-based perovskites. The Pb-O distance (refined distance) after Rietveld refinement is compared to the one calculated assuming Pb²⁺ to be in its ideal position (ideal distance).

depends on the chemical arrangement of the B cations in neighboring unit cells.

To my knowledge, in all Pb-based perovskites for which the position of the Pb²⁺ cation was studied in the high-temperature phase, the Pb²⁺ was found to be displaced from its special position. Usually on a sphere, this sphere being eventually unevenly occupied. Some results are recalled in Table 3.4.

It appears that regardless of the B-site cations the distance Pb-O is always close to 2.60 Å. This distance is much smaller than the sum of the two ionic radii (2.89 Å). Therefore, in all of these perovskites there is a strong overlap of the 2*p* orbitals of Pb²⁺ and the 2*s* of O²⁻. This is probably due to the strong ionicity of the chemical bond between Pb²⁺ and O²⁻. Indeed the difference in ionization potential of Pb²⁺ and O²⁻ is equal to 1938 kJ/mol when the same difference is 760 kJ/mol for the model ionic crystal NaCl. Hence it appears that the Pb-O distance in complex Pb-based perovskites is mainly driven by electron interactions and that the B-site cations have little influence on it.

Thus, from the previous simple reasoning on the Pb-O bond, the B-site cations have little influence on the displacement of Pb²⁺¹. However, in PYN-PT, the type of chemical arrangement (ordered or disordered) on the B site plays a significant role in the anisotropy of the displacement on the Pb²⁺ site. I propose that this influence on the anisotropy of the displacement of Pb²⁺ is due to local distortions of the O-octahedra cage due to chemical ordering.

Indeed, the different chemical elements on the B site in complex perovskites would tend to have O-octahedra cages of different size around them, considering only the B-O bonding energy. Hence, in the case of chemical ordering, there would always be a “small” O-octahedra around the small B-cation next to a “large” one around the larger B-cation leading possibly to a distortions of the O-octahedra then inducing a preferential displacement of the neighboring Pb²⁺. In the case of chemical disorder on the B site, there is no reason to have a regular arrangement of large and small O-octahedra that would favor one particular direction for the Pb²⁺ displacement. I therefore suggest that distortions of the O-octahedra cage due to long-range chemical

¹Indeed, the size (i.e. ionic radius) does *not* determine the length of the Pb O bond.

ordering lead to the anisotropy of Pb^{2+} displacement.

This idea that Pb^{2+} is always out of its prototypic position and that the direction of the displacement is related to the environment of the B site will be the starting point of the model proposed in Chapter 4 to explain the link between the structure and the properties of the PYN-PT solid solution.

Application to the measure of chemical ordering

In the previous section (Sec.3.3.3), we showed that it is not possible to determine the degree of chemical ordering in the PYN-PT solid solution from the simple approach of comparing the ratios of intensities of a superstructure reflection to a Bragg reflection in the real case and the case of a perfectly ordered material because of the displacement of the Pb^{2+} cations. I concluded that a more complex model taking into account the Pb^{2+} positional disorder should be used to determine the degree of chemical ordering.

This composite model with two phases with Pb^{2+} off-centered in both phases was implemented to determine the degree of chemical ordering in PYN-PT 0.30. It appeared that this model could not be refined on our data, since the refinement would always converge to either a value of chemical ordering larger than 1 or to unreasonable values of thermal agitation parameters of Pb^{2+} . Refining the position of the Pb^{2+} did not lead to any improvement in the refinement.

Therefore, for the refinement of our data, the composite model does not appear to be suitable to determine the degree of chemical ordering. An alternative model could be to describe the structure with a modulation of the occupancy on the B site. The determination of this occupancy modulation would require at least two sets of data at high temperature with different radiation types (e.g. X-ray and neutron diffraction pattern) to take advantage of the different ratios of cross sections in the two radiation types (see Sec.1.2.1.1, page 30 for details).

3.3.5 New knowledge about the structure in the PYN-PT solid solution

In summary, in this section, the distortions present in the PYN-PT solid solution were determined by studying the splitting of some of the Bragg peaks:

At room temperature, PYN exhibits a monoclinic distortion of the perovskite pseudo-cubic ($Z = 1$) unit cell and this monoclinic distortions persists for PYN-PT 0.05.

For PYN-PT 0.10, the distortion is much lower and it was not possible from this simple analysis to decide between a rhombohedral and a monoclinic cell. The more in-depth study of the distortions using a profile matching analysis in Sec.3.4.1 (page 130) will show that PYN-PT 0.10 has a rhombohedral distortion at room temperature.

For compositions in the intermediate range ($0.16 \leq x \leq 0.30$) no distortion could be observed. The profile matching analysis (Sec.3.4.2, page 139) will not reveal any long-range distortion of the cubic phase for $0.16 \leq x \leq 0.25$ and a monoclinic phase for PYN-PT 0.30

For compositions in the range $0.35 \leq x \leq 0.60$, distinct splitting of peaks could be observed, consistent with possible rhombohedral, monoclinic and tetragonal structures. Because of the proximity of these compositions with the morphotropic phase boundary ($x \sim 0.50$), the more careful analysis of the structure will show a phase coexistence of several symmetries for all these compositions (Sec.3.4.3, page 151).

In addition, the presence and types of various SSRs were identified: SSRs due to chemical order for compositions up to $x = 0.35$, SSRs due to correlated antiparallel displacements of Pb^{2+} for compositions up to $x = 0.10$ and SSRs due to O-octahedra tilting for PYN-PT 0.30 and PYN-PT 0.40.

Furthermore, I tried to evaluate the degree of chemical ordering in the double perovskite PYN and in a double perovskite-PT solid solution. This evaluation was shown to be difficult due to the disorder on the Pb^{2+} site. Even a more advanced model, in which the material is described as a composite of an ordered and disordered phase, was not sufficient to determine the degree of chemical ordering. Hence, the chemical arrangement in the PYN-PT solid solution may only be known describing the material with an average structure and modulating the occupancy on the B site. This analysis would require the use of at least two data sets, preferably at high temperature (i.e. in the cubic phase), with different radiation types in order to be able to solve the modulation.

Finally, we determined that, for all investigated compositions, Pb^{2+} was disordered on a sphere of about 0.32 \AA of radius and that the movement of the Pb^{2+} was strongly influenced by the chemical arrangement on the B site. Besides, we have evidenced that for all Pb-based perovskites, the Pb^{2+} displacement is mainly driven by the Pb-O bond, the B cations having only an indirect influence through the O-octahedra.

In the following, the structure of the various compositions at room temperature will be investigated more closely. The compositions will be separated as follows: distorted structures with SSRs due to antiparallel displacements of Pb^{2+} (PYN-PT $0 \leq x \leq 0.10$), small or no distortions (PYN-PT $0.16 \leq x \leq 0.30$) and structures with strong distortions but no SSRs due to antiparallel displacements of Pb^{2+} (PYN-PT $0.35 \leq x \leq 0.60$).

This separation of compositions based on the different structures does not fully coincide with the separation done in Chapter 2 based on the macroscopic properties. These differences will be discussed in Chapter 4.

3.4 ROOM TEMPERATURE STRUCTURES FOR (1 x)PYN x PT

In this section, the structure at room temperature of all compositions investigated in this work will be discussed. The first three subsections correspond to the distinctions made in the previous section:

The subsection Structure with SSRs due to antiparallel displacements: $x = 0-0.10$ will focus on the compositions presenting splittings of the main Bragg peaks and superstructure reflections due to antiparallel displacements. This section will specifically characterize the antipolar order present in these compositions.

The subsection Structure with small distortions: $x = 0.16-0.30$ will cover the compositions for which no splitting of the main Bragg peaks has been observed and with a special attention on the local-scale structure.

The subsection Structure with large distortions: $x = 0.35-0.60$ will investigate the compositions displaying strong splitting of the main Bragg peaks and will underline the possible phase coexistence in these compositions.

The last subsection will deal with the study of O-octahedra tilting.

3.4.1 Structure with SSRs due to antiparallel displacements: $x = 0-0.10$

This section addresses the room-temperature structure of PYN-PT with $x \leq 0.10$, i.e. the compositions that present SSRs due to antiparallel displacements of Pb^{2+} . The average structure taking into account chemical order (often referred as to the pseudo-cubic cell in the literature) will be discussed first. Then, a study of the SSRs will be conducted in Sec.3.4.1.2.

3.4.1.1 Average Structure

In Sec.3.3.1, the study of the splitting of the $(00l)_{pc}$ and $(hhh)_{pc}$ reflections have shown a strong splitting of $(hhh)_{pc}$ reflections for all compositions examined in this section ($0 \leq x \leq 0.10$) and a distinct splitting of the $(00l)_{pc}$ reflections for pure PYN and PYN-PT 0.05. For PYN-PT 0.10, the $(00l)_{pc}$ reflections is broader at room temperature than at high temperature, but no definite splitting of the peak could be observed. Hence, the pseudo-cubic structure ($Z=1$) of pure PYN and PYN-PT 0.05 is clearly monoclinic, whereas the structure of PYN-PT 0.10 is either rhombohedral or monoclinic.

Hereafter, the average structure of PYN-PT with $x = 0-0.10$ will be investigated using profile matching analysis. I used the lowest symmetry space group for the different crystal systems considered here (rhombohedral and monoclinic) taking into account chemical order to avoid extinctions due to symmetry. A more complete analysis may show that the structure is of higher symmetry, but this method allows a definite determination of the crystal system.

The cell parameters of a monoclinic cell of pure PYN and PYN-PT 0.05 were accurately determined using a profile matching analysis introduced in Sec.3.2.2 (page 105). The results are

	PYN		PYN-PT 0.05	PYN-PT 0.10	
	neutrons	XRD	XRD	XRD	
	monoclinic	monoclinic	monoclinic	monoclinic	rhombohedral
a (Å)	8.3262(28)	8.3346(16)	8.3187(14)	8.3036(17)	8.3036(6)
b (Å)	8.3436(17)	8.3389(10)	8.3162(19)	8.3042(18)	
c (Å)	8.2291(21)	8.2259(9)	8.2207(8)	8.3092(20)	
γ (°)	90.432(19)	90.518(8)	90.447(6)	90.078(13)	90.015(3)

Table 3.5: Cell parameters of pure PYN (monoclinic cell), PYN-PT 0.05 (monoclinic cell) and PYN-PT 0.10 (monoclinic and rhombohedral) refined from the X-ray diffractograms recorded on ID31 at ESRF and neutron diffractogram recorded on D2B at ILL.

reported in Table 3.5. For both PYN and PYN-PT 0.05, the two monoclinic cell parameters a and b are similar and the structure is strongly distorted as the monoclinic angle γ_m is large for perovskites ($\sim 90.5^\circ$).

In my study of the average structure, I took into account the cell doubling due to chemical ordering which is usually not the case in the literature. My results are in agreement with those reported for PYN within a factor 2 accounting for the chemical order, ($a \sim b \sim 2 \cdot 4.166 = 8.322 \text{ Å}$, $c \sim 2 \cdot 4.110 = 8.220 \text{ Å}$ and $\gamma \sim 90.5^\circ$, see Table 1.3, page 44). According to the literature, the structure of PYN-PT 0.05 is similar to the one of PYN, but no cell parameters for PYN-PT 0.05 were ever reported, to the best of my knowledge.

For PYN-PT 0.10, profile matching analyses were conducted for rhombohedral and monoclinic symmetries to identify the average structure of this composition. Both analyses give extremely similar results. Indeed, the agreement factors are $Rwp = 11.21$ and $GOF = 4.37$ for monoclinic and $Rwp = 11.50$ and $GOF = 4.48$ for rhombohedral. Usually, for comparable agreement factors the structure with the highest symmetry is chosen to describe the material; here this would be the rhombohedral structure.

Besides, the monoclinic cell is actually extremely close to a rhombohedral one as the cell parameters a_m , b_m and c_m are extremely similar to each other and to the cell parameter, a_r , of the rhombohedral structure (Table 3.5).

Moreover, the choice of a rhombohedral cell is supported by the evolution of the width of $(00l)_{pc}$ and $(hhh)_{pc}$ that will be detailed in Sec.3.5.1 (page 159).

Therefore, for PYN-PT 0.10, the best description of the average structure is a rhombohedral phase.

Hence, in the PYN-PT solid solution, compositions that present SSRs due to antiparallel displacements of Pb^{2+} exhibit in average two different structures: monoclinic for $x \leq 0.05$ and rhombohedral for PYN-PT 0.10. In the next section, we will focus no longer on the average structure but on the SSRs.

3.4.1.2 Modulation vectors

Chemical ordering accounts only for some of the SSRs observed in the X-ray diagrams of PYN and PYN-PT $x = 0.05$ -0.10. The extra SSRs have been associated with antiparallel displacements of Pb^{2+} leading to the antiferroelectric properties because these SSRs are absent in the paraelectric phase (Sec.3.3.2). SSRs due to O-octahedra rotations have been evidenced neither by neutron nor by electron diffraction. In neutron diffraction, the large number of reflections created by the antiparallel displacements of Pb^{2+} "hide" potential SSRs due to O-octahedra rotations and, in electron diffraction, no zone axis optimally oriented to observe SSRs due to O-octahedra rotations were reachable.

In the PYN-PT solid solution, the SSRs due to antiparallel displacements have been divided into two types based on their diffracting angles: the ones of PYN and PYN-PT 0.05, on the one hand and the ones of PYN-PT 0.10, on the other hand.

In the following, we will focus only on the structure of PYN and PYN-PT 0.10. Because the X-ray diffraction pattern of PYN and PYN-PT 0.05 are extremely similar, the structure of PYN-PT 0.05 will be considered to be the same as the one of PYN.

PYN

In PYN, Kwon and Choo [40] and Demidova et al. [42] identified the SSRs due to antiparallel displacements of Pb^{2+} and have linked these SSRs to a modulation vector $(3/8, 3/8, 0)_{pc}$ leading to the large orthorhombic cell commonly used to describe the cell of PYN (see Fig.1.17, page 41). The X-ray diagrams obtained in the literature and the one I obtained are extremely similar (Fig.3.15(a-b)): the positions and the intensity ratios of the reflections are comparable. Moreover, the scanning transmission electron microscope (STEM) images (Fig.3.16(a-b)) show that the modulation of the structure occurs in the $[110]_{pc}$ direction as evidenced by the satellite spots (arrows in Fig.3.16(b)). These results are in agreement with the TEM experiments already reported [40].

Therefore, our experimental results are in good agreement with those documented and the structure proposed in the literature is a good starting point for further studies.

Nevertheless, the proposed modulation vector $(3/8, 3/8, 0)_{pc}$ refers to a perovskite cell not taking into account the chemical ordering on the B site and with a monoclinic angle lower than 90° , which is not in accordance with the standards of the International Union on Crystallography. In the double-perovskite cell with the monoclinic angle larger than 90° , the modulation vector becomes $(3/4, -3/4, 0)_{pc}$.

A profile matching analysis was conducted with the $(3/4, -3/4, 0)_{pc}$ and the average structure determined in the previous section (Fig.3.17). The average structure is modeled with the $P1$ space group to avoid any systematic extinctions. The profile matching analysis reveals that most of the SSRs may be well described with the $(3/4, -3/4, 0)_{pc}$ modulation vector, but that all reflections cannot be indexed (see Fig.3.17).

Hence, even though, in first approximation, the structure of PYN may be fairly well described with a double monoclinic structure with the $(3/4, -3/4, 0)_{pc}$ modulation vector, our high-quality

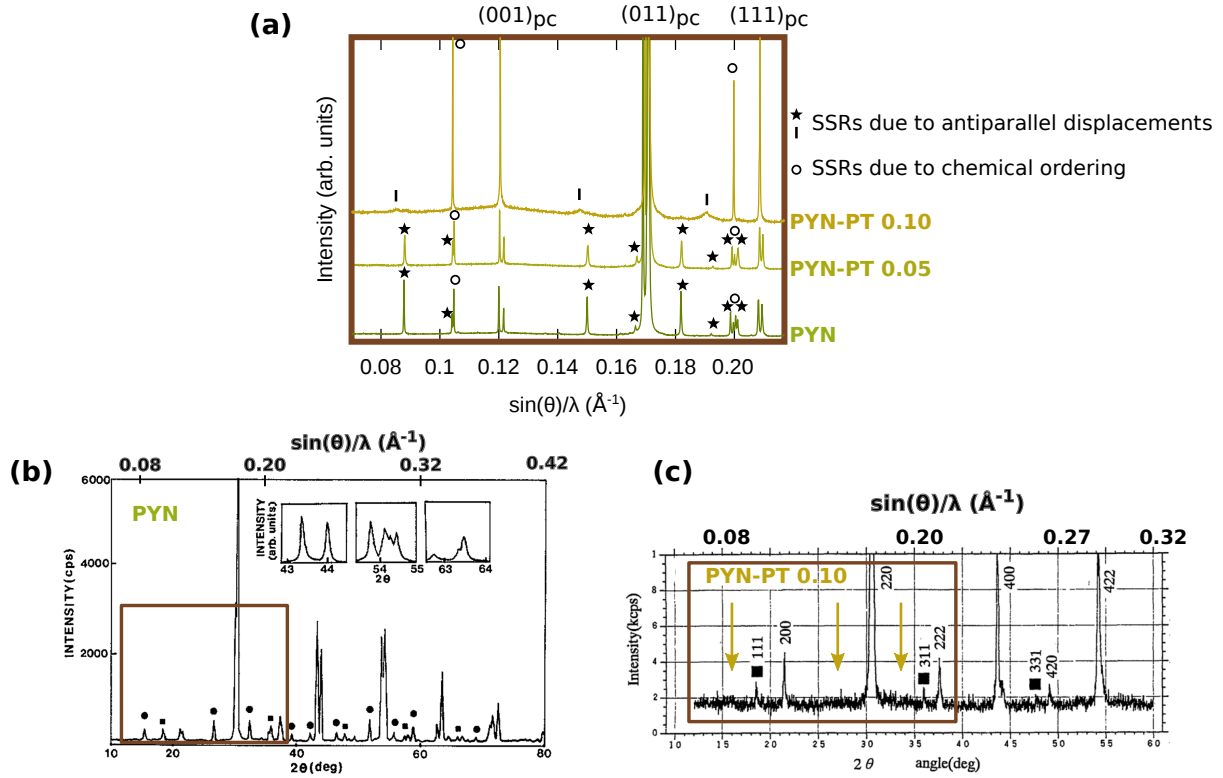


Figure 3.15: (a) X-ray diffraction patterns for PYN and PYN-PT 0.05 and PYN-PT 0.10.

SSRs due to chemical ordering are represented by an empty circle. SSRs due to antiparallel displacements of Pb^{2+} for PYN and PYN-PT 0.05 have extremely similar diffracting angles and are signaled by a solid star. SSRs due to antiparallel displacements in PYN-PT 0.10 are marked with a vertical line. These SSRs are of different nature than the ones in PYN and PYN-PT 0.05 since the diffracting angles and width are different.

(b) X-ray diffraction pattern of PYN. Squares indicate chemical order and circles SSRs due to antiparallel displacements of Pb^{2+} . Adapted from [40].

(c) X-ray diffraction pattern of PYN-PT 0.10. Squares indicate SSRs due to chemical order. Arrows indicate "bumps" in the background located at the same $\sin(\theta)/\lambda$ values as the ones where we observe SSRs. Adapted from [19].

The large brown squares highlight the same $\sin(\theta)/\lambda$ range.

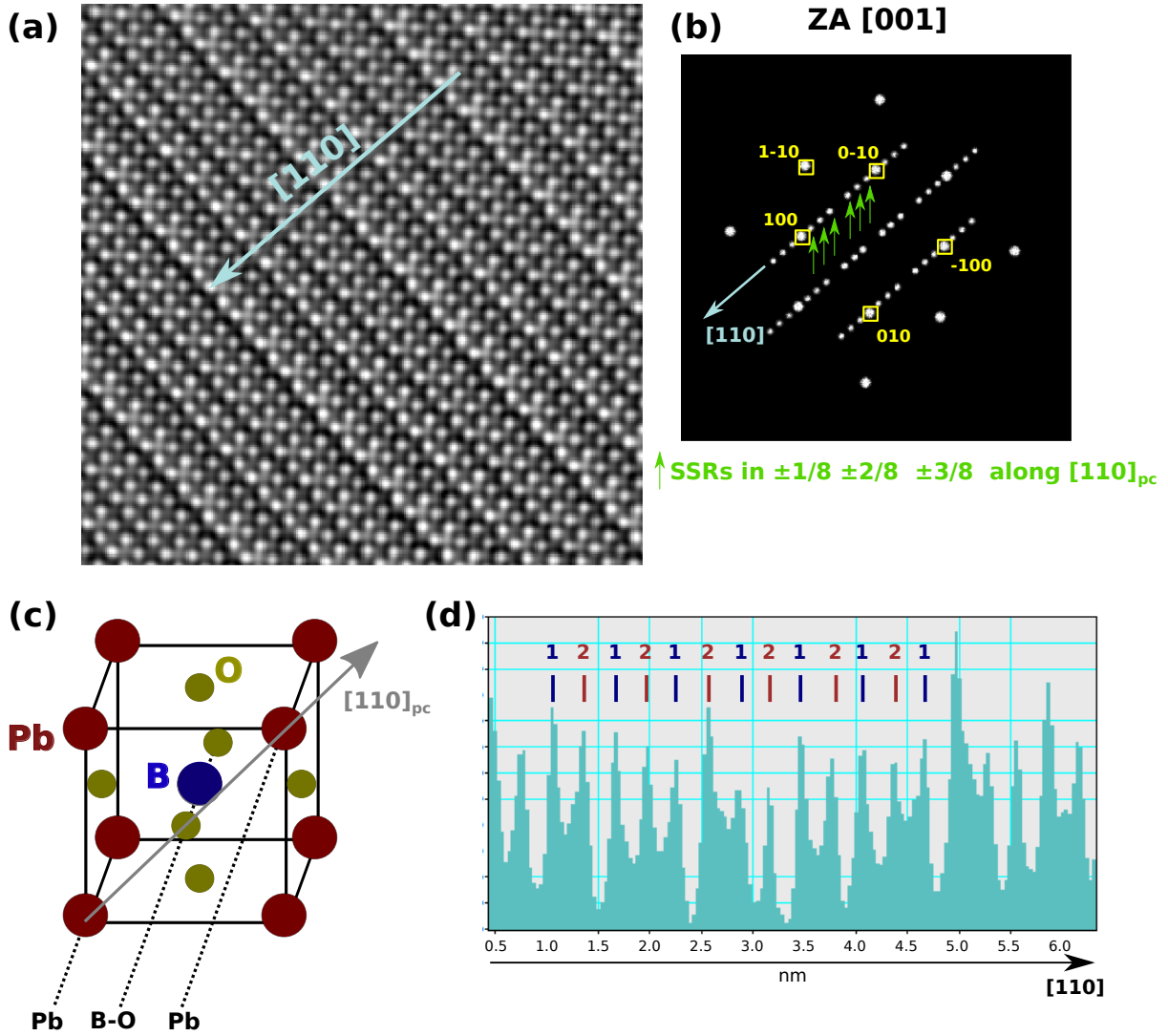


Figure 3.16: (a) STEM images with the $[001]_{pc}$ zone axis, (b) associated filtered Fourier transform and (d) Intensity profile along the $[110]_{pc}$ direction.

In the perovskite cube (c), the $[110]_{pc}$ direction and the column of atoms corresponding to the intensity profile are indicated.

In the filtered Fourier transform (b), the SSRs are indicated with green arrows. The same diffraction pattern is obtained using conventional electron diffraction technique.

In (d), 1 and 2 correspond to the two different types of columns that can be observed along the $[110]_{pc}$ direction, namely Pb^{2+} or B-O columns. The attribution to either Pb^{2+} or B-O columns cannot be done due to similar atomic numbers of Pb and Yb.

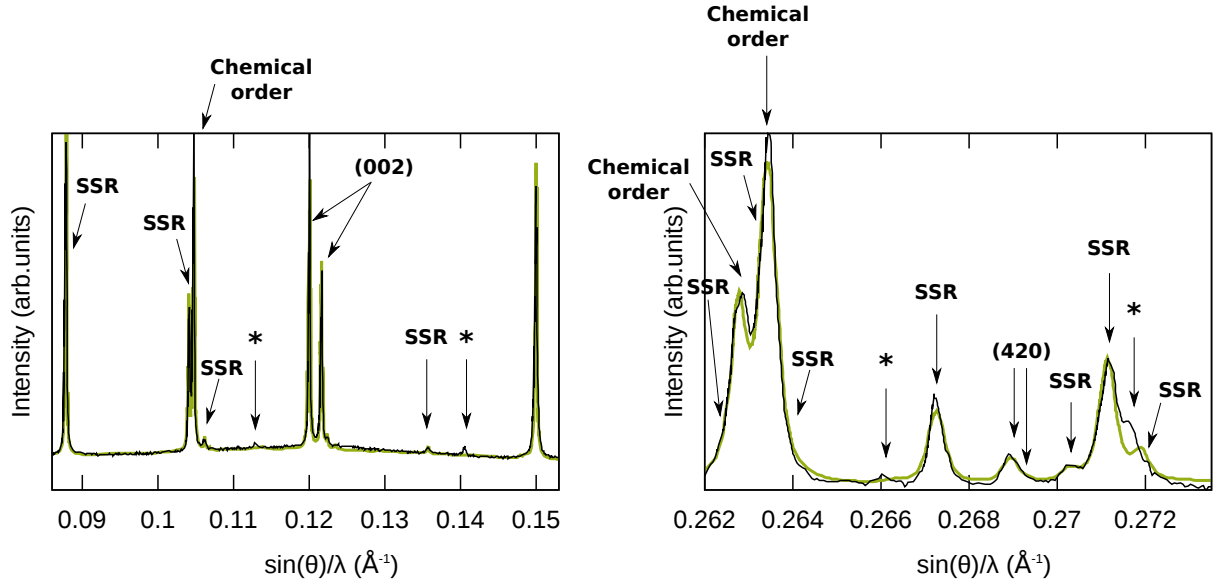


Figure 3.17: Selected area of the X-ray diffractogram observed (black) and calculated (green) for PYN at room temperature. The structure is calculated for a triclinic structure with a modulation vector $(3/4, -3/4, 0)_{pc}$.

In the diagrams, the Bragg reflections are indexed, the SSRs due to chemical order are designated with "Chemical order", SSRs that can be explained by the model are labeled "SSR" and the ones that cannot be explained are indicated with a star.

data show that the structure is more complex. Thus, other modulation vectors were investigated.

Because the TEM images have shown satellite spots along the $[110]_{pc}$ direction, the investigation of modulation vectors were restricted to this direction. However, since the indexation of the TEM images is conducted in the pseudo-cubic cell ($Z = 1$), all six $\langle 110 \rangle_{pc}$ directions (that are symmetrically equivalent to the $[011]_{pc}$ in the cubic phase) should be considered for direction of modulation ($[101]_{pc}$, $[10\bar{1}]_{pc}$, $[011]_{pc}$, $[01\bar{1}]_{pc}$, $[110]_{pc}$ and $[1\bar{1}0]_{pc}$). However, the analysis of the average structure conducted in the previous section has shown that the cell parameters a and b are almost equal. Therefore some directions were assumed to be (almost) symmetrically equivalent leading to a reduced number (4) of directions to be explored.

Thus, the only modulation vectors considered were directed along one of the four non equivalent directions: $[110]_{pc}$, $[101]_{pc}$, $[\bar{1}10]_{pc}$ and $[\bar{1}01]_{pc}$ with various amplitude of modulations: $1/8$, $1/4$, $3/8$, $1/2$, $5/8$ and $3/4$. When the amplitude of the modulation vector investigated matches most of the SSRs, the modulation vector was refined to see if all reflections could be explained with a small variation of the amplitude of the modulation vector.

However, none of these modulation vectors could satisfactorily describe all SSRs.

From this analysis, the only possibility that I have found to explain all SSRs consists in us-

ing two modulation vectors: $(1/2, 0, 1/2)_{pc}$ and $(3/4, -3/4, 0)_{pc}$.

The presence of a second modulation vector seems plausible based on the STEM images, since the intensity profile (Fig.3.16(d)) indicates that both Pb^{2+} and the B cations are not equally spaced along the $[110]_{pc}$ direction.

Indeed, in the STEM images, two types of columns are observed along $[110]_{pc}$ (Fig.3.16(c)): one with only Pb^{2+} atoms and one with B cations and oxygens. In the profile intensity (Fig.3.16(d)), the intensities of both types of columns are similar due to the large atomic numbers of both Pb^{2+} and the Yb^{3+} B cations making the distinction between the two columns in the profile intensity impossible.

Nonetheless, because the Pb^{2+} and B-O columns are observed alternately, it is still possible to distinguish two types of columns, labeled 1 and 2 in Fig.3.16(d), even though the definite attribution of columns 1 and 2 to Pb^{2+} or B-O columns is not possible.

For columns 1 and 2, the distance between successive columns of the same type along the $[110]_{pc}$ direction does not remain constant indicating that both Pb^{2+} and B-O columns have positions that changes along the $[110]_{pc}$ direction. A change in the position of the Pb^{2+} columns can be easily envision since Pb^{2+} displacements are expected to occur in antiferroelectrics, whereas in the common model for the structure of antiferroelectrics, B cations remain in their ideal positions. Hence, the analysis of the STEM images suggests a modulation of the position of both Pb^{2+} and B-cations that supports the possibility of having two modulation vectors to describe the structure of PYN. In this case, the displacement of Pb^{2+} and B cations would be within the same plan $(11v)_{pc}$, but their modulations vectors are not collinear.

However, no STEM images could be obtained with a zone axis allowing the observation of the $(1/2, 0, 1/2)_{pc}$ modulation preventing the definite clarification of the presence of a second modulation vector.

Because, the modulation vector $(3/4, -3/4, 0)_{pc}$ leads to strong SSRs, I propose that this modulation corresponds to the displacements of Pb^{2+} since the modulation is the most common in Pb-based perovskites. Consequently, the displacements of the B-cations would be described by the $(1/2, 0, 1/2)_{pc}$ modulation vector.

In addition, the structure proposed by Demidova et al. [42] presents strong displacements of the B-cations that have been evidenced in Sec.1.4.1 (page 39). The orthogonal projections of these displacements along the $[110]_{pc}$ direction are compatible with the $(1/2, 0, 1/2)_{pc}$ modulation of the structure proposed here. Hence, the presence of a second modulation vector is allowed by their results.

In summary, the X-ray diagrams and STEM images obtained on PYN are consistent with the ones reported in the literature and, in first approximation, the structure of PYN can be described as an average monoclinic structure with a $(3/4, -3/4, 0)_{pc}$ modulation of the position of Pb^{2+} leading to the large orthorhombic cell ($Z = 16$) proposed to describe the structure (Fig.1.16, page 40).

However, the high-accuracy diffractograms and electronic microscopy images that we obtained show that the structure is more complex than the one proposed in the literature: PYN has an

average monoclinic structure with possibly two modulation vectors $(3/4, -3/4, 0)_{pc}$ and $(1/2, 0, 1/2)_{pc}$ describing the positions of Pb^{2+} and the B cations respectively.

Therefore, the polar arrangement for Pb^{2+} would be the one described by Demidova et al. [42] and Kwon and Choo [40]: $\uparrow\uparrow\downarrow\uparrow\downarrow\uparrow\downarrow$ and the one of the B cations would be the one of $PbZrO_3$: $\uparrow\uparrow\downarrow\downarrow$.

Finally, all displacements observed in STEM images are along the $[110]_{pc}$ direction indicating that the displacements of Pb^{2+} induced by the modulation of the structure are parallel to the modulation vector, whereas, to my knowledge, in all other antiferroelectrics, such as $PbZrO_3$, $Pb(Mg_{1/2}W_{1/2})O_3$ and $Pb(Yb_{1/2}Ta_{1/2})O_3$, the displacements are perpendicular to the direction of the modulation vector. Moreover, in the case of PYN, the displacements of the B cations would be in the direction orthogonal to the modulation vector.

In Fig.3.18 is represented the displacement arrangement derived from the two modulation vectors found in the profile matching analysis and the STEM experiments. The displacements are displayed in $(ab)_{pc}$ -planes of the pseudo-cubic unit cell ($Z=1$), then the perovskite structure can be reconstructed by piling Pb^{2+} - and B-cations plan alternatively along the c_{pc} axis.

The polar arrangements within the Pb layer and the B layer are known. However, the polar arrangements between the different layers (i.e along the c_{pc} -axis of the pseudo-cubic cell ($Z=1$)) is unknown.

Taking the Pb layer as reference, there are only four possible polar arrangements along the c-axis, all given in Fig.3.18.

In all cases, within $(ab)_{pc}$ -planes, head-to-head and tail-to-tail arrangements of dipoles are induced by the displacements of the Pb^{2+} and B cations.

Summing the dipoles moments along the c-direction for one Pb layer and one B layer, the polar arrangement (2) and (4) would lead to a lower number of head-to-head and tail-to-tail arrangements within an $(ab)_{pc}$ plane and therefore would appear more physically stable.

However, with the present understanding of the structure, there is no reason to favor one piling of Pb and B layers over the others and further investigations are needed to gain a full understanding of the structure of PYN.

PYN-PT 0.10

Neither the presence of SSRs in PYN-PT 0.10 nor the presence of a second type of SSRs in the PYN-PT solid solution have been reported in the literature. Therefore, the possibility that these extra peaks come from a different source than antiparallel displacements has been checked. The extra peaks in the X-ray pattern do not come from a secondary phase since the positions of the extra peaks do not correspond to any of the precursors used during the processing of the ceramic or to a pyrochlore. Moreover, these extra peaks are also not observed on X-ray patterns obtained at temperatures above the Curie temperature (T_c) indicating that they are linked to the same phase transition. Hence it seems that these extra peaks in the diffractogram are intrinsic to the structure of PYN-PT 0.10.

Furthermore, in the only X-ray pattern reported in the literature for PYN-PT 0.10 [19], small bumps can be observed at the same $\sin(\theta)/\lambda$ value (Fig.3.15(c)). However, in the published diffractogram the intensity of these bumps is so low and their width is so large that the bumps

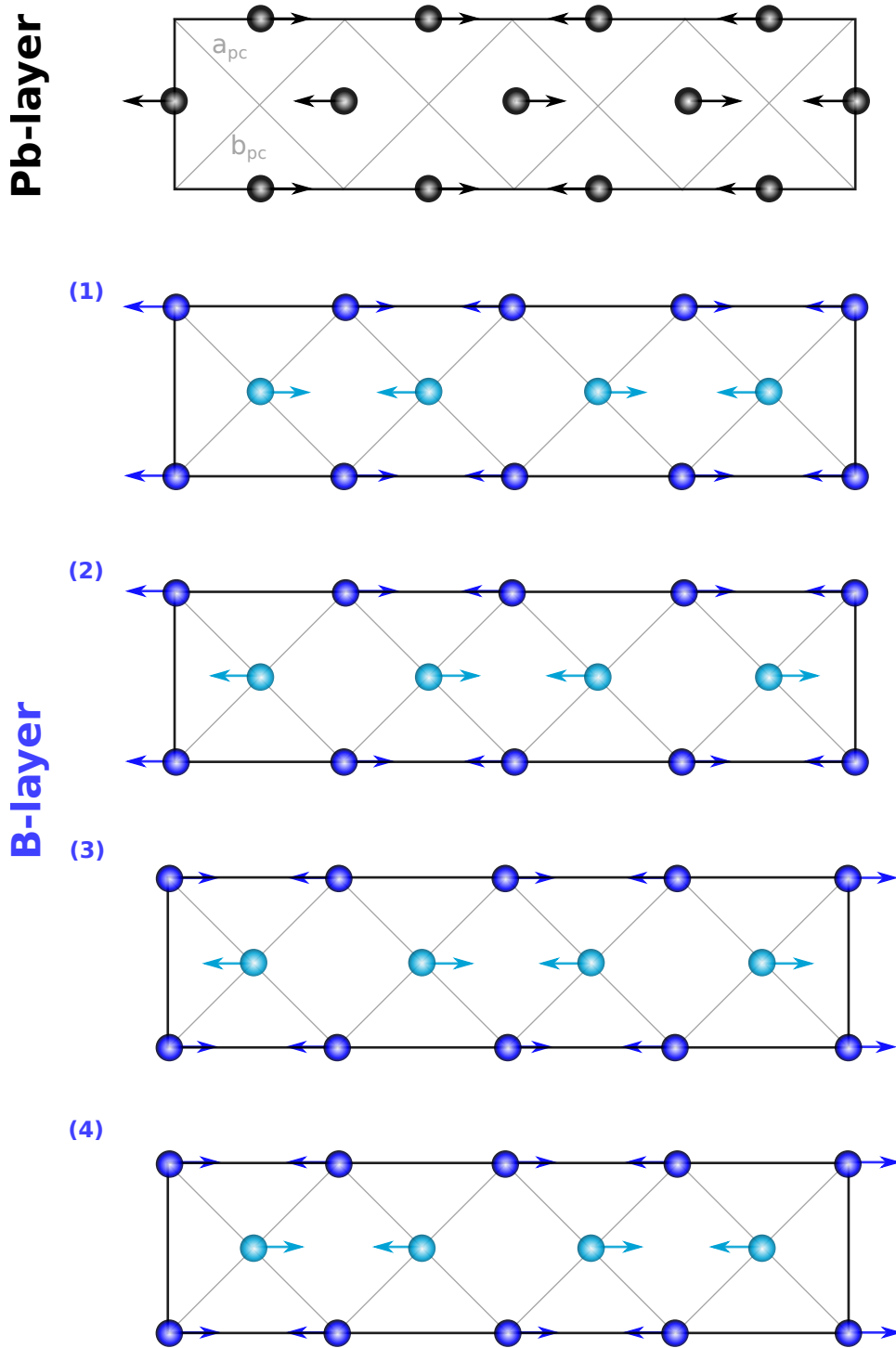


Figure 3.18: Schematic representation of the displacements of Pb^{2+} and B cations. Oxygens have been omitted for clarity.

For a given translation of the Pb layer, the B layer can be organized in four different ways: (1), (2), (3) and (4).

This representation does not account for the actual structure, it only reproduces the different possibility for piling Pb^{2+} and B cations along the c_{pc} direction due to the perovskite structure of PYN.

could be simply due to noise in the measurement.

Therefore, my conclusion is that these additional reflections are due to correlated antiparallel displacements and are therefore intrinsic.

The Williamson-Hall study conducted on the compositions showing small distortions (Sec.3.4.2.2, page 143) and extended to PYN-PT 0.10 will show that the inhomogeneous strain increases slightly in PYN-PT 0.10 when cooling from the high-temperature phase. This rather limited increase of the strain may be due to local strains induced by the local correlation of antiparallel displacements evidenced by the presence of broad SSRs.

As in the case of PYN, various modulation vectors were tried to describe the SSRs in PYN-PT 0.10.

A double rhombohedral structure (taking into account the degree of chemical ordering) with a modulation vector along one of the diagonal of the faces of the rhombohedron (i.e $[\delta \delta 0]$ and $[\bar{\delta} \delta 0]$) with an amplitude δ of $1/2$ can explain all reflections in PYN-PT 0.10. However, because the structure is only slightly distorted ($\alpha_{rhombo}=90.015^\circ$) and the SSRs are broad it is not possible to clarify the direction of the modulation vector.

This change of the modulation vector compared to PYN and PYN-PT 0.05 can be ascribed to two origins: first to a change of the displacement pattern of the Pb^{2+} compared to the one in PYN and PYN-PT 0.05. It is possible that with the addition of titanium in the structure, the polar arrangement of Pb^{2+} changes from the one observed in PYN ($\uparrow\uparrow\downarrow\downarrow\uparrow\downarrow$) to the one observed in PbZrO_3 ($\uparrow\uparrow\downarrow\downarrow$).

And second to the disappearance of the displacements of the Pb^{2+} and only the $(1/2, 1/2, 0)_{pc}$ modulation vector of the B cations introduced in the study of PYN and PYN-PT 0.05 would remain.

My suggestion is that, in PYN-PT 0.10, the introduction of Ti in PYN destabilizes the antipolar order and therefore that the Pb^{2+} antiparallel displacements occur on a shorter scale leading to the appearance of the shorter polar arrangement: $\uparrow\uparrow\downarrow\downarrow$. This destabilization of the antipolar order by the addition of Ti will be detailed in Chapter 4.

Summary

The structure of PYN was reported in the literature to be orthorhombic due to the presence of a commensurate modulation of an average monoclinic structure due to the pattern of the Pb^{2+} displacements [40, 42]. Our experiments show that this structure can explain most of the reflections in PYN, as a first approximation. Nonetheless, the structure appears to be more complicated possibly due to the modulation of both Pb^{2+} and B cations. Moreover, on the contrary to all other reported AFE materials, the displacements of Pb^{2+} appear parallel to the modulation vector and not perpendicular to it.

The structure of PYN-PT 0.05 was not studied in such great details, but because the X-ray diffractograms of PYN and PYN-PT 0.05 are extremely similar, the structure of PYN-PT 0.05 is assumed to be similar to the one of PYN.

Regarding the structure of PYN-PT 0.10, I have determined that the structure was on average rhombohedral with a modulation along the diagonal of the faces of the pseudo-cube with an amplitude of $1/2$. This modulation of the structure must happen at a local scale since the associated SSRs are extremely broad. The exact nature of these displacements requires further investigation, but these displacements appear undoubtedly different from the ones of PYN and PYN-PT 0.05.

3.4.2 Structure with small distortions: $x = 0.16-0.30$

In this section, the structure of the compositions (PYN-PT with $0.16 \leq x \leq 0.30$) that have been shown in Sec.3.3.1 to present slight, if any, distortions will be analyzed in more details. In a first step, the distortions will be investigated using profile matching in order to find the average structure of these compositions. Then, the presence of diffuse scattering at the bottom of the peak will be checked. Finally, the possible positional disorder on the Pb^{2+} site will be investigated.

3.4.2.1 Average structure

Hereafter, the long-range structure of the compositions in the range $0.16 \leq x \leq 0.30$ is investigated by conducting profile matching analysis using all possible space groups proposed in Sec.3.1.1 on the X-ray synchrotron data obtained at ESRF for all compositions and the neutron data obtained for PYN-PT 0.30 at ILL.

The results for each composition and phase are summarized in Table 3.6.

When refining X-ray data, it appears that no significant difference in the agreement factors are observed using the various space groups, for all compositions, and that the distortions from the cubic phase are extremely small in the rhombohedral, monoclinic and tetragonal phases. Only a Rietveld analysis would enable to conclude on the structure.

On the other hand, the profile matching analysis conducted on neutron data (second to last row in Table 3.6) shows a clear improvement when a non-cubic symmetry is considered for PYN-PT 0.30. However, the cell parameters obtained on neutron data are very different from the ones obtained in the X-ray profile matching analysis. Actually, the cell parameters found using the neutron data should lead to a clear splitting of the $(00l)_{pc}$ and $(hhh)_{pc}$ in the X-ray diagrams that is not observed.

This strong difference in the cell parameters depending on the radiation type is believed to be due to diffuse scattering at the base of the neutron diffraction peaks that will be detailed in the next section. Thus, the base of the peak is ill-defined using only the pseudo-Voigt profile, commonly used to describe the profile of diffraction peaks, and the refinement program adjusts the cell parameters in order to take into account the diffuse scattering, artificially increasing the distortions. Therefore, profile matching analysis was conducted on the neutron data setting the cell parameters to the ones refined on X-ray data (last row in Table 3.6).

This new neutron profile matching analysis distinctively shows that the agreement factor for the cubic structure is higher than for the other symmetries; however no significant differences can

x	$Fm\bar{3}m$ ($Pm\bar{3}m$)	$R3m$ ($R3m$)	Im (Cm)	Cm (Fm)	$I4mm$ ($P4mm$)
0.16	8.95 <i>3.13</i>	8.96 <i>3.14</i>	8.96 <i>3.14</i>	8.94 <i>3.13</i>	8.93 <i>3.13</i>
0.20	6.78 <i>4.26</i>	6.75 <i>4.24</i>	6.87 <i>4.32</i>	6.86 <i>4.31</i>	8.61 <i>5.41</i>
0.25	10.5 <i>5.13</i>	10.5 <i>5.13</i>	10.42 <i>5.09</i>	10.45 <i>5.11</i>	10.45 <i>5.11</i>
0.30	5.35 <i>2.61</i>	5.40 <i>2.63</i>	5.36 <i>2.61</i>	5.37 <i>2.61</i>	5.39 <i>2.63</i>
0.30 [*] _(a)	5.63 <i>2.12</i>	4.52 <i>1.71</i>	4.07 <i>1.54</i>	4.29 <i>1.62</i>	4.57 <i>1.72</i>
0.30 [*] _(b)	5.63 <i>2.12</i>	4.52 <i>1.71</i>	4.57 <i>1.73</i>	4.63 <i>1.75</i>	4.57 <i>1.72</i>

Table 3.6: *Rwp* and GOF (in italic) of the profile matching made with different space groups on X-ray and neutron (*) diffractograms. (a) and (b) subscript refers respectively to the neutron refinement conducted with free cell parameters and the one where cell parameters are set to the ones determined using X-ray diffraction.

The space groups without taking into account the chemical order are given in parenthesis.

be seen between the agreement factors of the rhombohedral, monoclinic and tetragonal phases. Actually, as SSRs due to O-octahedra tilting were observed in Sec.3.3.2, the structure of PYN-PT 0.30 has to be lower than cubic.

The distinction between these symmetries can be made by studying the cell parameters as a function of temperature (Sec.3.5.2). A distinct widening of $(00l)_{pc}$ and $(hhh)_{pc}$ at room temperature compared to the high temperature has already been mentioned in Sec.3.3.1 indicating monoclinic distortions.

Therefore, it is the combined study of neutron and X-ray diffractograms that enables to conclude that the structure of PYN-PT 0.30 is of monoclinic symmetry, but definite conclusion regarding the space group could only be obtained with Rietveld refinements.

For the other compositions, neutron diffractograms are not available and no peak widening was observed as a function of temperature in the X-ray diffractograms. Therefore, for compositions in the range $0.16 \leq x \leq 0.25$, the structure remains cubic down to room temperature.

Finally, the possible presence of local features and disorder will be studied in the next section, since diffuse scattering was observed in the neutron diffractogram of PYN-PT 0.30 and the agreement factors obtained in the X-ray refinements are high (especially compared to the results in Table 3.8 (page 147) for compositions with strong distortions) suggesting that there might be some local features also in X-ray diffraction patterns.

In the coming sections, we will look into the presence of diffuse scattering at the base of the peaks and at the evolution of strains using the Williamson-Hall approach.

3.4.2.2 Structure at local scale

The compositions in the range $0.16 \leq x \leq 0.30$ present minute, if any, distortions from the cubic phase. These compositions were characterized as relaxors in Chapter 2 based on the strong frequency dependence of the dielectric constant. Relaxors are known to have a cubic (or pseudo-cubic) structure with local features (Sec.1.1.4, page 24) that are usually evidenced by diffuse scattering. These local features may come from local chemical inhomogeneity or local polarization (leading to the appearance of polar nanoregions). Hence, we will focus first on the observation of diffuse scattering at the base of some reflections in the PYN-PT solid solution. Moreover, the change of the structure at a local scale with temperature may change the strain state and therefore the evolution of the microstrain with temperature will be investigated next using the Williamson-Hall approach.

Diffuse Scattering

The diffuse scattering is evidenced by a widening of the base of diffraction peaks. Therefore, the presence of diffuse scattering has been evaluated from the comparison of the base of several high intensity reflections and of a reference material (LaB_6), at high temperature and room temperature. A difference in the high-temperature and room-temperature bases of the peaks would indicate the presence of local features evolving with temperature. Because the temperature range investigated (300-600 K) is much lower than the temperature required to change the chemical organization (1300-1500 K), the presence of a diffuse scattering that is temperature dependent will be attributed to the presence of PNRs.

The basis of the peak for the (002) and (111) reflections are represented in Fig.3.19. No widening of the basis of the peak compared to the one of LaB_6 is observed, neither at room temperature nor at high temperature.

However, the widening at the basis of the peak is rather strong in the reference material, LaB_6 , and can therefore be attributed to the experimental setup. It would be useful to conduct the same study on diffractograms recorded on a different experimental setup.

In particular, looking at the neutron diffraction data recorded on PYN-PT 0.30, a large diffusion peak can be observed in addition to the Bragg peaks (Fig.3.20). This broadening has not been observed in other samples and is therefore attributed to local variation intrinsic to this sample. These local variations could be due to chemical ordering or local distortions, i.e. PNRs. A high-temperature experiment in the same experimental setup would be necessary to conclude regarding the nature of these local features.

Hence, diffuse scattering is clearly observed only in the *neutron* diffraction pattern. It may be inferred that local features are present over the entire compositions range $0.16 \leq x \leq 0.30$ since the agreement factors of the X-ray profile matching analysis are high and that the macroscopic relaxor properties are associated with local variations.

Since no diffuse scattering could be observed in the X-ray diffractograms due to experimen-

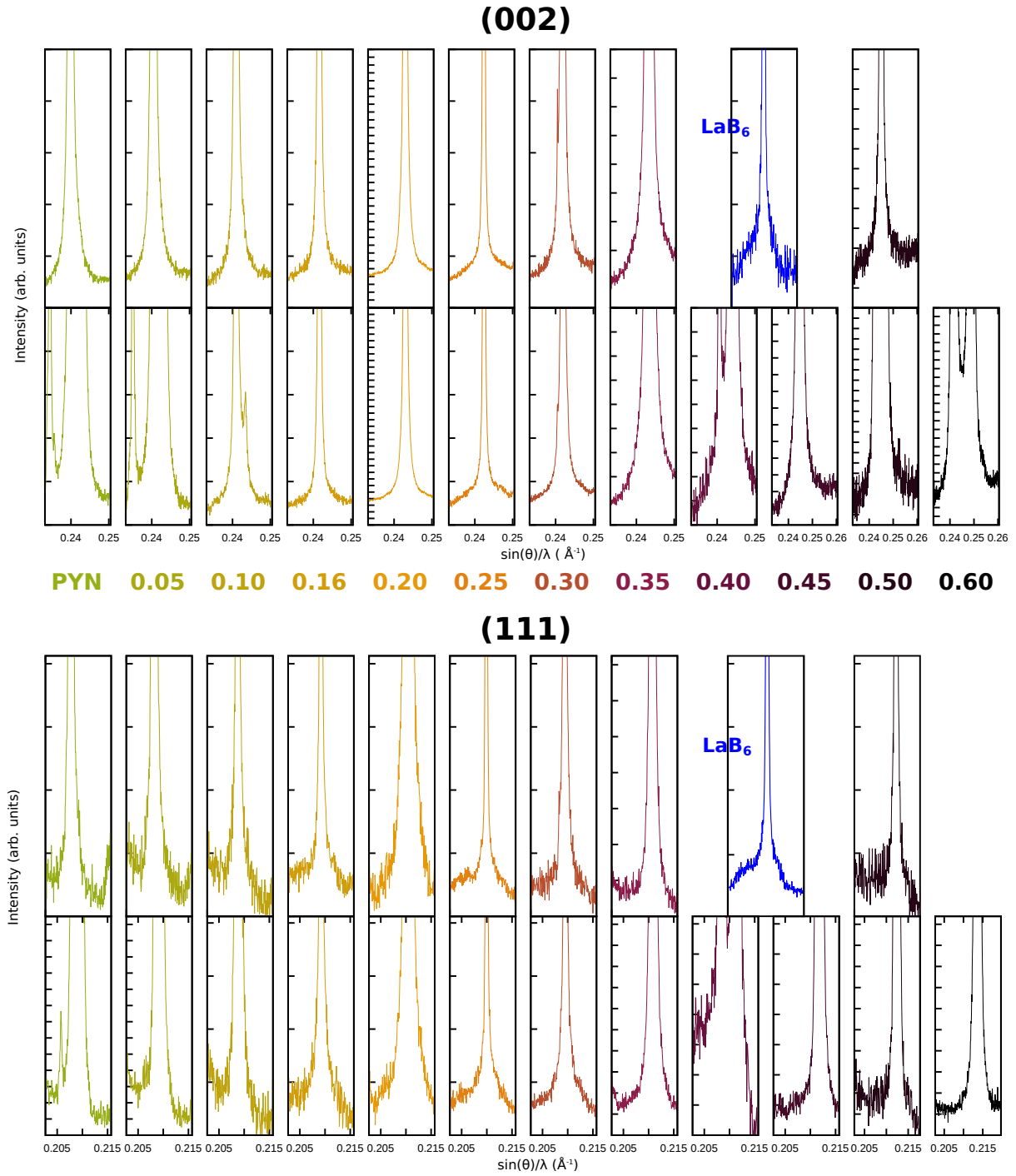


Figure 3.19: Comparison for all compositions of basis of the peak of the (002) and (111) reflections at high temperature (top) and room temperature (bottom). A reflection of LaB_6 with a diffracting angle close to the ones of the PYN-PT solid solution is plotted for reference. Vertical ticks are spaced by the same intensity regardless of the composition.

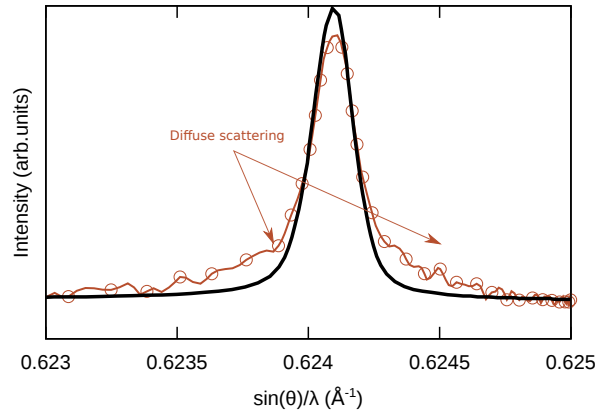


Figure 3.20: Neutron diffractogram (colored points) and refined profile (black line) for PYN-PT 0.30.

tal limitations, complementary neutron experiments are necessary to conclude regarding the presence and type of local features over the entire compositional range.

Strain analysis

To further study the presence of local features, Williamson-Hall analyses were conducted on PYN-PT with $x = 0.10$ - 0.30 . In this study, PYN-PT 0.10 was considered in addition to the compositions exhibiting small distortions, because PYN-PT 0.10 has been shown to have broad SSRs indicating a modulation of the structure at a local scale (Sec.3.4.1.2).

Introduced in Sec.3.3.3 (page 117), let me recall here that the Williamson-Hall approach assumes that the width of the diffraction peaks is only due to size and strain effects, and, in particular, the strain is evaluated based on the slope of the Williamson-Hall plot at large $\sin(\theta)$.

Before studying the evolution of the strain as a function of temperature and composition, the influence of the structural model chosen to describe the structure at room temperature was considered. For that, Williamson-Hall analyses were conducted for all space groups considered in the study of the average structure. Only small differences were observed in the Williamson-Hall plots for different space groups: as illustrated for PYN-PT 0.25 in Fig.3.21(a). The evaluation of the strain, given by the slope at large $\sin(\theta)$, appears to be independent of the model chosen to describe the structure.

Therefore, at room temperature, the value of the slope was evaluated taking the average of the values obtained for different space groups and the error bars represent the dispersion of values. At high temperature, the slope was measured only in the case of a cubic phase.

At high temperature, the strain increases continuously with the addition of PT in PYN for compositions up to $x = 0.50$. Only the value obtained for PYN-PT 0.20 deviates from this trend. During the study of the distortions (in Sec.3.3.1, page 111), the investigation of the evolution of the full width at half-maximum for a selected number of reflections have already revealed that

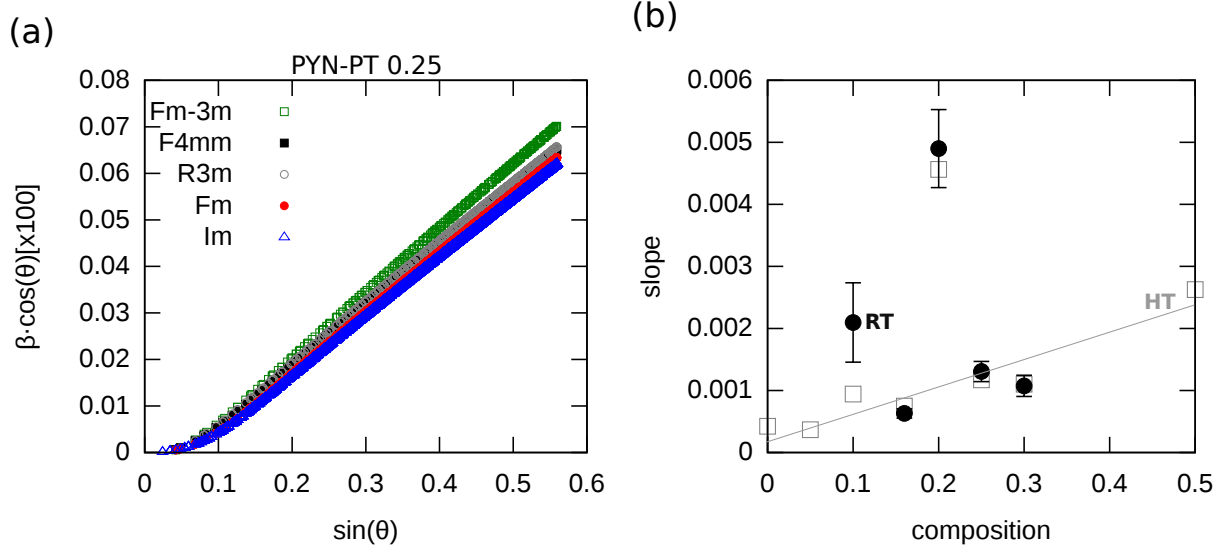


Figure 3.21: (a) Williamson-Hall plot for different structures for PYN-PT 0.25
 (b) Evolution of the inhomogeneous strain as a function of the composition at high temperature (open squares) and room temperature (solid circles). At room temperature, the average of the slopes for profiles refined with different space groups is plotted. The error bars represent the corresponding dispersion of the values at room-temperature.

the width of the diffraction peaks were larger for this composition. This widening of the diffraction peaks was attributed to a lower quality of this particular sample compared to the other ones. I therefore ascribe the same origin to the singular value for PYN-PT 0.20 in Fig.3.21(b).

At room temperature, the compositions showing little or no distortions ($0.16 \leq x \leq 0.30$) have the same strain state as at high temperature, since the value of the slope is the same for both temperatures (see Fig.3.21(b)). Therefore, in this compositional range, the strain does not seem to increase upon cooling.

For PYN-PT 0.10, on the other hand, the strain changes distinctly upon cooling. This increase in the strain state may be related to the apparition of the local modulation of the structure, as discussed in Sec.3.4.1.2. Nonetheless, the change of strain state between high temperature and room temperature is small compared to the effect that unintentional fluctuations in the synthesis may induce (as evidenced by the large values of strain in PYN-PT 0.20).

In conclusion, for all compositions, the examination of the bases of the X-ray diffraction peaks has not evidenced any diffuse scattering. Diffuse scattering was only observed for PYN-PT 0.30 by neutron scattering.

Besides, Williamson-Hall analyses have shown that the strain state remains the same at high temperature and room temperature for compositions with a pseudo-cubic structure ($0.16 \leq x \leq 0.30$).

Therefore, for these compositions, no difference in the strain state was observed between room temperature and high temperature. For PYN-PT 0.30, it is clear that there is a local structure since diffuse scattering was observed on neutron data. Hence, this local structure does not influence strongly enough the strain state to be observed using in the Williamson-Hall analysis in X-rays data.

Finally, information regarding the local structure cannot be obtained from the present data and additional experiments should be conducted to characterize these local features.

3.4.2.3 Positional disorder on the A-site

In Sec.3.3.4, Pb^{2+} positional disorder was evidenced in the high-temperature phase for all compositions investigated. It was shown that the Pb^{2+} is disordered on a sphere and that one direction may be more energetically favorable for Pb^{2+} when chemical ordering was present on the B site.

Relaxors properties, that are exhibited in the compositional range $0.16 \leq x \leq 0.30$, are often attributed to a positional disorder on the Pb^{2+} site, present even at low temperature.

Hereafter, the presence and possible changes in the disorder on the Pb^{2+} site will be examined comparing the high-temperature and room-temperature X-ray diffractograms. In particular, ratios of intensity of several of the main Bragg reflections were studied: I_{002}/I_{011} , I_{111}/I_{011} , and I_{111}/I_{002} .

The differences of intensity ratios between the two temperatures are extremely small ($<10\%$) indicating that disorder on the Pb^{2+} site is still present at room temperature.

The change of intensity ratios with temperature seems more significant for PYN-PT 0.25 and PYN-PT 0.30 (5-10 %) than for PYN-PT 0.16 and PYN-PT 0.20 (0-5 %), but it remains limited. This may indicate that the disorder has changed upon cooling in the cases of PYN-PT 0.25 and PYN-PT 0.30, but the evolution of the intensity ratios are so small that these changes are within the experimental errors.

Therefore, in PYN-PT, in the compositional range showing relaxors properties and a pseudo-cubic symmetry, Pb^{2+} is still disordered at room temperature, in agreement with the literature associating relaxors properties and Pb^{2+} disorder.

Conclusion

The solid solution PYN-PT in the compositional range $0.16 \leq x \leq 0.30$ presents a structure that is mostly cubic on the long range. The different studies conducted here evidenced the presence of local features only for PYN-PT 0.30 because of the extra information gained from neutron diffraction. Therefore, it is possible that local features are also present for the other compositions in the range $0.16 \leq x \leq 0.25$. Further investigations with neutron diffraction were scheduled (proposal accepted) but technical difficulties at the Orphée reactor have prevented them from being carried out.

Hence, the first ever attempt at characterizing the structure of PYN-PT with $x = 0.16-0.30$ shows that the structure is pseudo-cubic on the long-range for compositions in the range $0.16 \leq x \leq 0.25$ and monoclinic for PYN-PT 0.30 with certainly local features and positional disorder of Pb^{2+} .

3.4.3 Structure with large distortions: $x = 0.35-0.60$

In this section, we will give a more precise description of the structure of the compositions that we observed to have strong distortions from the cubic phase in Sec.3.3.1, i.e. PYN-PT within the compositional range 0.35-0.60 using X-ray and neutron (when conducted) diffraction experiments. In particular, the symmetry of the various compositions and possible phase coexistence will be investigated.

The study of the splitting of some of the main reflections in Sec.3.3.1 has shown that in PYN-PT with $0.35 \leq x \leq 0.60$, the structure can be viewed mainly as rhombohedral, monoclinic or tetragonal depending on the PT content. Hence, hereafter, we will focus on these three possible structures. The investigated space groups have been limited to the ones observed in complex Pb-based perovskites, e.g. $\text{Pb}(\text{Zr,Ti})\text{O}_3$ or $\text{Pb}(\text{Sc}_{1/2}\text{Nb}_{1/2})\text{O}_3\text{-PbTiO}_3$. These space groups ($R3m$, Cm , Pm and $P4mm$) have been detailed in Sec.3.1.1 (page 99).

Moreover, the possibility of phase coexistence in the solid solution PYN-PT $0.35 \leq x \leq 0.60$ will be considered because of the compositional proximity with the morphotropic phase boundary ($x \sim 0.50$). Indeed, in all complex Pb-based perovskites, the enhancement of the macroscopic properties at the morphotropic phase boundary (MPB) has been linked to a monoclinic phase allowing a continuous rotation of the polarization between the rhombohedral and tetragonal sides of the MPB (Fig.1.8, page 28). Further studies have shown that this monoclinic phase coexists with other phases, namely rhombohedral, monoclinic or tetragonal over a large compositional range [73, 74].

In Sec.3.3.2 (page 114), it was shown that PYN-PT 0.40 exhibits SSRs due to O-octahedra tilting. The intensity of these SSRs are extremely small and the O-octahedra tilting will be neglected in a first step. We will see in the next section, devoted to the study of the O-octahedra tilting, that this approximation is reasonable.

3.4.3.1 Phase Identification

A profile matching analysis with the different structures considered based on the structures most commonly observed in Pb-based complex perovskites (Table 3.1, page 100) was carried out to identify the most promising phases to conduct Rietveld refinement. The results for each composition and phase are summarized in Table 3.7 for neutron diffraction and Table 3.8 for X-ray diffraction. For simplicity, the possibility of phase coexistence was limited to a maximum of two phases.

The agreement factors, R_{wp} and GOF, obtained for the neutron data on PYN-PT 0.40 are slightly higher than for the other compositions. These larger values are due to the fact that O-octahedra tilting has been neglected here and, therefore, in PYN-PT 0.40, extra reflections cannot be explained by the space groups considered here. Nevertheless, the agreement factors for PYN-PT 0.40 are reasonable.

In the analyses of the X-ray diagrams, the agreement factors are much larger for PYN-PT 0.35

x	$R3m$	Cm	Pm	$P4mm$	$R3m$ + Pm	$R3m$ + Cm	Pm + Cm	$P4mm$ + Cm	$P4mm$ + Pm	$R3m$ + $P4mm$
0.40	3.19	2.99	3.01	3.46	2.61	2.72	2.45	2.59	2.52	2.70
	<i>1.60</i>	<i>1.50</i>	<i>1.51</i>	<i>1.74</i>	1.31	<i>1.37</i>	1.23	1.30	1.26	<i>1.36</i>
0.50	8.98	3.44	2.99	3.75	2.52	2.59	2.38	2.42	2.48	2.74
	<i>4.41</i>	<i>1.69</i>	<i>1.47</i>	<i>1.84</i>	<i>1.24</i>	<i>1.27</i>	1.17	1.19	<i>1.22</i>	<i>1.35</i>
0.60		3.49	3.52	3.49	2.37 ^(a)	2.63	2.34	2.69	2.45	2.72
		<i>1.71</i>	<i>1.72</i>	<i>1.9</i>	<i>1.16</i>	<i>1.29</i>	1.15	<i>1.32</i>	1.20	<i>1.33</i>

Table 3.7: Rwp and GOF (in italic) of the profile matching made with different phases on neutron diffractograms. Bold numbers underline the best fits obtained.

^(a) For PYN-PT 0.60, the refinement of the model using the $R3m$ and Pm gives really good agreement factors, but in this case, the $R3m$ phase is really broad, i.e. would be badly crystalized. We discard these phase mixings from our study.

x	$R3m$	Cm	Pm	$P4mm$	$R3m$ + Pm	$R3m$ + Cm	Pm + Cm	$P4mm$ + Cm	$P4mm$ + Pm	$R3m$ + $P4mm$
0.35	6.47	6.17	6.04	6.43	5.47	4.93 ^(a)	5.46	5.81	5.90	5.50
	<i>3.49</i>	<i>3.33</i>	<i>3.25</i>	<i>3.46</i>	2.95	<i>2.66</i>	2.94	<i>3.14</i>	<i>3.18</i>	<i>2.97</i>
0.40	4.67	3.62	3.82	4.88	3.41	3.28	3.28	3.51	3.33	3.90
	<i>1.96</i>	<i>1.52</i>	<i>1.61</i>	<i>2.05</i>	<i>1.43</i>	<i>1.44</i>	1.38	<i>1.48</i>	1.40	<i>1.64</i>
0.45	7.37	5.57	5.46	7.96	4.47	3.93	3.75	3.75	4.15	3.99
	<i>3.16</i>	<i>2.39</i>	<i>2.34</i>	<i>3.51</i>	<i>1.69</i>	<i>1.68</i>	1.61	1.61	<i>1.78</i>	<i>1.71</i>
0.50		8.20	6.85	8.51	5.14	5.44	4.25	4.16	4.37	5.24
		<i>2.73</i>	<i>2.28</i>	<i>2.83</i>	<i>1.71</i>	<i>1.71</i>	1.41	1.39	<i>1.46</i>	<i>1.74</i>
0.60		7.70	7.65	7.77	5.92	5.89	5.32	4.70	5.09	5.79
		<i>2.64</i>	<i>2.63</i>	<i>2.67</i>	<i>2.03</i>	<i>2.02</i>	<i>1.83</i>	1.61	<i>1.75</i>	<i>1.99</i>

Table 3.8: Rwp and GOF (in italic) of the profile matching made with different phases on X-ray diffractograms. Bold numbers underline the best fits obtained.

^(a) For PYN-PT 0.35, the refinement of the model using the $R3m$ and Cm gives really good agreement factors, but in this case, the $R3m$ phase is really broad, i.e. would be badly crystalized. We discard these phase mixings from our study.

than for the other compositions. These large agreement factors are due to the fact that the chemical ordering was not taken into account here. Indeed in Sec.3.3.3 (page 119), it was shown that the chemical ordering of PYN-PT 0.35 is more complicated than the classical rock-salt arrangement and, therefore, only qualitative results will be obtained for this composition.

For all compositions, the profile matching analysis conducted on both the X-ray and neutron data indicates that the structures are better described by a coexistence of two phases than with a single one.

Moreover, the existence of a rhombohedral phase in the PYN-PT solid solution does not appear clearly from the profile matching analysis (see Table 3.7 and Table 3.8). This absence of a rhombohedral phase in the PYN-PT solid solution would be clearly demonstrated using Rietveld refinements.

When the agreement factors using a rhombohedral phase are low, a visual check of the profiles indicates that this rhombohedral phase describes essentially the base of the diffraction peaks. In such case, the rhombohedral phase would be of extremely low crystallinity which would be surprising considering that all other investigated phases indicate a good crystallinity of the sample. Actually, based on the Rietveld refinements, it will be proposed that some positional disorder of Pb^{2+} persists in the compositional range investigated here ($0.35 \leq x \leq 0.60$). Therefore, the rhombohedral phase describing the base of the peaks describes the widening of the base of the peaks induced by this positional disorder.

In conclusion, the profile matching analysis shows undoubtedly that there are several phases in presence in the compositional range $0.35 \leq x \leq 0.60$ and that the $R3m$ rhombohedral phase is not one of them, except potentially for PYN-PT 0.35 and PYN-PT 0.40.

The difference between the various possibilities of phase mixing will be made by conducting Rietveld refinements.

3.4.3.2 Rietveld Refinements

The profile matching analysis conducted previously has revealed the coexistence of several phases for each investigated compositions in the range $0.35 \leq x \leq 0.60$. To determine what phase mixing would describe best the structures, Rietveld refinements were conducted on the phase mixing that were shown to be the most promising based on the profile matching analysis.

Despite the fact that the agreement factors were not satisfactory in the profile matching analysis, phase mixing with the $R3m$ rhombohedral phase has also been considered for PYN-PT 0.40, since this rhombohedral phase has been observed in the low-PT-content side of the morphotropic phase boundary (MPB) of all studied Pb-based complex perovskite.

The Rietveld refinements were conducted on the neutron diffraction data since neutrons are more sensitive to the atomic positions than X-ray diffraction (due to equivalent scattering factor of Pb and O in neutron diffraction).

For PYN-PT 0.45, neutron diffractograms are not available and therefore Rietveld refinements were carried out on X-ray diffraction data. To ensure that the only structure obtained from

x	$R3m$ $+Pm$	$R3m$ $+Cm$	Pm $+Cm$	$P4mm$ $+Cm$	$P4mm$ $+Pm$
0.40	4.26 <i>2.14</i>	5.73 <i>2.89</i>	2.89 <i>1.46</i>	3.15 <i>1.59</i>	3.22 <i>1.62</i>
0.45*			6.47 <i>2.78</i>	5.86 <i>2.51</i>	5.80 <i>2.49</i>
0.50			4.24 <i>2.08</i>	3.54 <i>1.74</i>	3.61 <i>1.77</i>
0.50*			x	6.19 <i>2.06</i>	7.90 <i>2.63</i>
0.60			4.16 <i>2.03</i>	3.62 <i>1.78</i>	3.26 <i>1.60</i>

Table 3.9: Rwp and GOF (in italic) of the profile matching made with different phases on neutron diffractograms. Bold numbers highlight the best fits obtained.

* denote the fact that the refinement were conducted on X-ray data.

The phase mixing Pm/Cm (marked with x) was refined on the X-ray data, but no convergence with reasonable atomic positions and agitation parameters could be obtained.

the refinement of X-ray data (PYN-PT 0.45) is comparable with the structures obtained from neutron diffraction, Rietveld refinements were conducted on both X-ray and neutron diffraction data for PYN-PT 0.50.

Rietveld refinements were not conducted on PYN-PT 0.35 because of the extra complexity introduced by the complex chemical ordering pattern on the B site evidenced in Sec.3.3.3 (page 119).

The Rwp and GOF obtained at the end of the Rietveld refinements conducted on neutron and X-rays diffraction data are summarized in Table 3.9.

For PYN-PT 0.50, the atomic positions and thermal agitation parameters of the Pb^{2+} and B cations obtained from X-rays diffraction are the same as the ones obtained from neutron diffraction, within experimental errors. The atomic positions and thermal agitation parameters of the oxygen anions are not precisely the same, but they are comparable. X-rays being not really sensitive to oxygen, the information regarding oxygens are less reliable when determined from X-rays diffraction.

Thus, the structure of PYN-PT 0.45, that can only be accessed with X-rays diffraction, can be confidently compared to the other compositions. However, the atomic position and thermal agitation parameters of oxygens should be considered with special care.

For all compositions, in the range $0.40 \leq x \leq 0.60$, the structure is best described by a phase mixing of two phases among the Pm and Cm monoclinic phases and the $P4mm$ tetragonal phase.

Indeed, even for PYN-PT 0.40 for which a rhombohedral phase was expected by analogy with other Pb-based solid solutions, considering a mixing of two phases with one of them being the

rhombohedral $R3m$ phase lead to higher (i.e. worse) agreement factors compared to the ones considering monoclinic and/or tetragonal phases. This absence of a rhombohedral phase on the low-PT content of the MPB is surprising since it has been reported in all previously investigated solid solutions with PT as one end-member.

This absence of rhombohedral phase will be discussed later in this section and will appear more consistent when looking at the structural changes over the entire phase diagram of PYN-PT in Sec.3.6.

For all compositions in the range $0.40 \leq x \leq 0.60$, the agreement factors obtained assuming a mixing of phases Pm/Cm , $P4mm/Cm$ or $P4mm/Pm$ are not extremely different from one another.

However, for PYN-PT 0.40, the mixing of phases Pm/Cm gives better results than the other considered phases.

On the other hand, the mixing of phase $P4mm/Pm$ appears to better describe the structure of PYN-PT 0.60.

For compositions in between, PYN-PT 0.45 and PYN-PT 0.50, assuming a mixing of $P4mm/Cm$ and $P4mm/Pm$ leads to similar agreement factors, but refinement conducted on the X-rays data would point toward a better description of the structure of PYN-PT 0.50 with a mixing of $P4mm$ and Cm phases.

Actually, for PYN-PT 0.45 and PYN-PT 0.50, none of the phase mixing considered gives fully satisfying results. Fig.3.22 shows, for example, some measured and calculated profiles for PYN-PT 0.50 assuming the $Cm/P4mm$ model. Zhang et al. [74] associated a similar poor description of the profile to the presence of a third crystallographic phase. Thus, it is fair to assume that PYN-PT 0.45 and PYN-PT 0.50 cannot be described using only two crystallographic phases, but that a third one is necessary.

Since, it is clear that PYN-PT 0.40 can be described with a mixing of Pm and Cm and that PYN-PT 0.60 can be described with a mixing of Pm and $P4mm$, it is probable that PYN-PT 0.45 and PYN-PT 0.50 can be described with a mixing of the three phases: Pm , Cm and $P4mm$.

These three phases have been reported to be present and coexist close to the morphotropic phase boundary in other Pb-based solid solutions such as $Pb(Sc_{1/2}Nb_{1/2})O_3$ - $PbTiO_3$ [15] or $Pb(Mg_{1/3}Nb_{2/3})O_3$ - $PbTiO_3$ [96] for which one of the end-member is a relaxor. Therefore, it is reasonable to assume that these three phases coexist at the MPB of PYN-PT, i.e. for $x \sim 0.50$. Refining a structure with three phases is an extremely challenging task and higher quality data would be necessary to refine properly these three phases in the PYN-PT solid solution.

In summary, on the low-PT content side of the MPB, the structure can be described with a mixing of two monoclinic phases: Cm and Pm . When increasing the amount of PT, a third phase appears: the tetragonal $P4mm$ phase. On the PT-rich side of the MPB, the structure can be once again described with two phases: the tetragonal $P4mm$ and the monoclinic Pm . Thus, when increasing the PT content, the monoclinic Cm phase disappears and the tetragonal $P4mm$ appears. The monoclinic Pm phase is present on both side of the MPB, and the percentage of the Pm phase probably goes through a maximum close to the MPB.

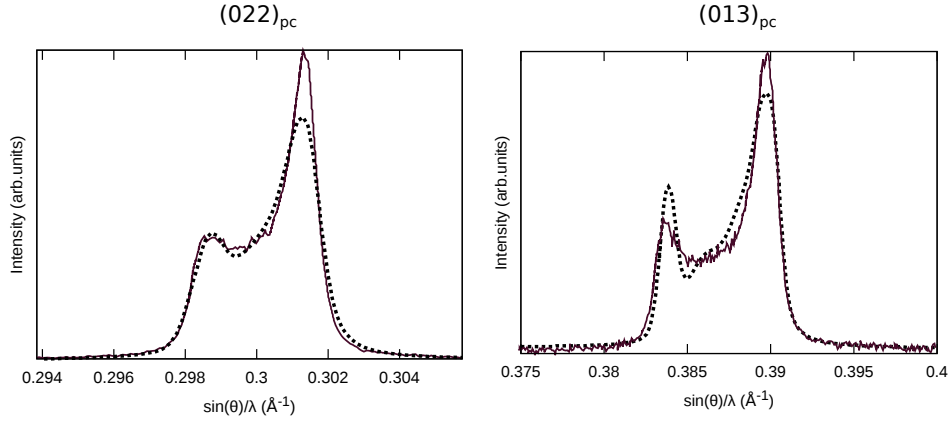


Figure 3.22: X-ray diffractograms (colored thin line) and refined profile (black thick dotted line) of the $(022)_{pc}$ and $(013)_{pc}$ reflections assuming a $Cm/P4mm$ structure.

Assuming that the structure close to the morphotropic phase boundary of PYN-PT may be described with the coexistence of two phases, in first approximation, the refined structural parameters (percentage of phases, cell parameters, atomic positions and thermal agitation parameters) are given for all compositions in Table C.1 (Appendix C, page 249).

The thermal agitation factors of Pb and O are unusually high: $\sim 2\text{-}3 \text{ \AA}$ in comparison with other Pb-based perovskites and, in particular, compared to the thermal agitation parameters of Yb/Nb/Ti ($\sim 0.5 \text{ \AA}$). These high thermal parameters are probably due to positional disorder on the Pb^{2+} site. Indeed, when studying the positional disorder of Pb^{2+} , in Sec.3.3.4, it appeared that when Pb^{2+} was in its ideal position, the thermal agitation parameter was high, whereas it dropped down to more reasonable values when considering an off-centering of Pb^{2+} . Therefore, I propose the sources of the high values of the agitation parameters of Pb^{2+} at room temperature to be the presence of positional disorder on the Pb^{2+} site.

The Pb^{2+} positional disorder observed at high temperature is thought to be due to the strong bonding energy between Pb and O. Hence, the imposition of Pb^{2+} in its ideal position during the Rietveld refinement leads to poor description of the Pb-O bond and therefore to imprecision on the description of the oxygen anions. This imprecision of the description of the atomic position of oxygens leads to the large thermal agitation parameters and large uncertainties on the atomic position of the oxygens.

Therefore, positional disorder of Pb^{2+} seems to be present even at room temperature for PYN-PT with $x = 0.40\text{-}0.60$.

This disorder, rather unusual for classical ferroelectrics, is in complete agreement with the observation of a spontaneous relaxor-FE transition in the dielectric measurements (Sec.2.4.3, page 91). Indeed, in other Pb-based relaxors (e.g. $\text{Pb}(\text{Sc}_{1/2}\text{Nb}_{1/2})\text{O}_3\text{-PbTiO}_3$) undergoing a spontaneous relaxor-ferroelectric phase transition, the local features present in the relaxor phase has been evidenced [81] to persist in the ferroelectric phase.

Hence, in the PYN-PT solid solution, Pb^{2+} disorder present in the high-temperature relaxor phase may persist at room temperature even in compositions presenting strong distortions from the cubic phase, compatible with ferroelectricity: $0.40 \leq x \leq 0.60$.

Hence, for PYN-PT with $0.40 \leq x \leq 0.60$, Rietveld refinements have evidenced that the phases in coexistence are among the monoclinic Pm and Cm and the tetragonal $P4mm$ ones. Rietveld refinements have shown no indication of a rhombohedral phase, contrarily to what was expected based on analogies with all Pb-based perovskites studied up to now. Positional disorder of Pb^{2+} has been demonstrated to be present at room temperature in agreement with previous literature indicating that disorder intrinsic to relaxor properties remains even below the temperature of the spontaneous relaxor-ferroelectric transition.

Discussion

Previously, it was mentioned that in all Pb-based solid solutions, but PYN-PT, a rhombohedral phase was observed on the low-PT-content side of the MPB. Actually, it was recently demonstrated in PZT that the long-range coexistence of the rhombohedral and monoclinic phases derives from a difference in the correlation of displacements of Pb^{2+} in a monoclinic short-range structure [97]. Indeed the analysis of the short-range structure revealed a unique monoclinic structure leading to the appearance of macroscopic monoclinic and rhombohedral regions depending on the correlation of displacements of Pb^{2+} : when all Pb^{2+} atoms are displaced in the same direction the long-range structure appears monoclinic, whereas when Pb^{2+} atoms are displaced randomly (in the allowed monoclinic directions), the long-range structure appears rhombohedral.

Therefore, since in PYN-PT the long-range rhombohedral phase is not observed, there are no regions in which Pb^{2+} is displaced randomly (in the allowed monoclinic directions).

Either the Pb^{2+} are correlated in two different ways leading to the appearance of two macroscopic monoclinic phases (as was proposed for PYN-PT 0.40), or the Pb^{2+} displacements may not be limited to the directions allowed by the monoclinic symmetry, i.e. Pb^{2+} would be positionally disordered on a sphere.

The possibility that the Pb^{2+} may be positionally disordered seems reasonable considering the presence of the high-temperature relaxor phase. Indeed, in relaxors, a positional disorder of the Pb^{2+} on a sphere centered on its prototypic position is commonly admitted.

Thus, in PYN-PT, there would be regions in space, in which the position of Pb^{2+} would be isotropically distributed on a sphere and uncorrelated and others in which Pb^{2+} would be all displaced in the same direction (one that is allowed by the monoclinic symmetry). Hence, in PYN-PT, there would be coexistence of macroscopic monoclinic and a disordered phases, whereas in PZT, there would be coexistence of macroscopic monoclinic and rhombohedral phases. This difference in the long-range macroscopic structures do not account for differences in the short-range structure in PYN-PT and PZT, it is well possible to have for both solid solutions a short-range monoclinic structure, but with different organization of the Pb^{2+} displacements.

This difference would also explain why when using two macroscopic phases in the profile match-

ing analysis, the agreement factors of PYN-PT are not improved as much as it was observed in PZT.

Furthermore, the presence of a disordered phase also explains why the best agreement factors in profile matching analysis were obtained with one phase ($R3m$) presenting broad peaks.

Therefore, the presence of a phase presenting Pb^{2+} positional disorder consistent with the relaxor behavior observed at least at high temperature seems reasonable and should be considered in future investigations of the structure of PYN-PT at the MPB.

In this work, the structure of PYN-PT was examined only in the “classical” way, i.e. considering the coexistence of several macroscopic phases. From this investigation and the previous discussion regarding the presence of a disordered phase, the evolution of the structure across the MPB of PYN-PT can be described in two different ways

- There is coexistence of only macroscopic phases: two monoclinic phases on the PT-poor side of the MPB (PYN-PT 0.35 and PYN-PT 0.40) and monoclinic and tetragonal phases on the PT-rich side (PYN-PT 0.60) with possibly the coexistence of all three macroscopic phases really close to the MPB (PYN-PT 0.45 and PYN-PT 0.50)
- There is coexistence of macroscopic phases and of a disordered phase: one monoclinic phase and the disordered phase on the PT-poor side of the MPB (PYN-PT 0.35 and PYN-PT 0.40) and when the amount of Ti increases the disordered phase and the monoclinic phases disappear in favor to the tetragonal phase with coexistence of the macroscopic monoclinic and tetragonal phases and the disordered phases for PYN-PT 0.45 and PYN-PT 0.50 (and possibly PYN-PT 0.60).

The second hypothesis seems more reasonable in regards to the phase diagram. The reason of the existence of this disordered phase will be detailed in Chapter 4.

3.4.4 O-Octahedra Tilting for $x = 0.30$ and $x = 0.40$

Additional reflections are observed in neutron diffraction compared to X-ray diffraction for PYN-PT 0.30 and 0.40 (see Sec.3.3.2). This additional reflections have been attributed to the presence of O-octahedra tilts due to the higher sensitivity of neutron diffraction to oxygen atoms compared to X-ray diffraction.

For both PYN-PT 0.30 and PYN-PT 0.40, the extra reflections appear at the same diffracting angle and therefore the tilt system is presumed to be the same for the two compositions. The study of the tilt system has been conducted on PYN-PT 0.40 since the SSRs are more intense for this composition.

The notation developed by Glazer [82] will be used here to describe the O-octahedra tilting. In this notation, the O-octahedra tilting is described by specifying the rotations of the octahedra along each of the three pseudo-cubic ($Z = 1$) axes using a letter to characterize the magnitude of the rotation and a superscript indicating whether the rotation in adjacent layer are in the same (+) or opposite (-) direction.

The systems of O-octahedra tilts were limited to the ones belonging to the subgroup of the two

monoclinic phases that were determined in the previous section (Sec.3.4.3) by Rietveld refinement to describe best the untilted structure of PYN-PT 0.40: Pm and Cm . The tilt systems belonging to subgroups of the untilted monoclinic phases were determined using the tables derived from group theory by Stokes et al. [71].

Since the solid solutions PYN-PT and $\text{Pb}(\text{Zr,Ti})\text{O}_3$ have a lot of similarities (e.g. an antiferroelectric and PT as end-members), the tilt systems ($a^-a^-a^-$) observed in $\text{Pb}(\text{Zr,Ti})\text{O}_3$ was also considered, despite the Rietveld refinement results concluding to the absence of rhombohedral symmetry phase.

The list of space groups and tilt systems considered in the examination of the O-octahedra tilting in PYN-PT 0.40 are summarized in Table 3.10.

Because SSRs of the $\langle h \ k/2 \ l/2 \rangle$ type, characteristic of in-phase rotations of the octahedra, are absent of the neutron diffraction pattern, the tilt systems in PYN-PT 0.40 can only have antiphase rotations. Thus, the three tilt systems with in-phase rotations are not considered for further investigations.

With the remaining five possible tilt systems, profile matching analysis were conducted in order to have a simple, fast and reliable way to determine the presence or absence of SSRs associated with these tilt systems. Only three tilt systems induce SSRs that are consistent with the ones observed in PYN-PT 0.40: $a^0b^0c^-$, $a^-a^-c^0$ and $a^-b^-c^0$.

Solely a Rietveld refinement might be able to differentiate between the various tilt systems. However, conducting a Rietveld refinement with the neutron data obtained during this work may not be sufficient to determine the actual tilt system because of the low intensity of the SSRs. Indeed we have observed that Rietveld refinement using the space group $R3c$ inducing the $a^-a^-a^-$ tilt system and explaining partly the SSRs leads to similar results than the Rietveld refinement conducted with the $R3m$ space group not taking into account O-octahedra rotation. Therefore, neutron data with longer counting time are necessary to conclude regarding the tilt system in PYN-PT 0.40.

Nevertheless, from the examination of the type of SSRs present in PYN-PT 0.40, it is clear that the tilt system is different from the two most common tilt systems in the Pb-based FE complex perovskites: $a^-a^-a^-$ and $a^-a^-c^-$.

Indeed, the $a^-a^-a^-$ has been observed in $\text{Pb}(\text{Zr,Ti})\text{O}_3$, the only complex FE Pb-based perovskite that displays O-octahedra tilting in the bulk phase. Moreover, this tilt system has also been identified in some Pb-based relaxors (e.g. $\text{Pb}(\text{Sc}_{1/2}\text{Ta}_{1/2})\text{O}_3$ and $(\text{Pb,Lu})(\text{Zr,Ti})\text{O}_3$) under high-pressure conditions [98–100].

The $a^-a^-c^-$ tilt system has sometimes been considered to be present in $\text{Pb}(\text{Zr,Ti})\text{O}_3$ close to the morphotropic phase boundary, although, today this tilt system is no more considered when investigating $\text{Pb}(\text{Zr,Ti})\text{O}_3$.

Hence, the tilt system observed in PYN-PT appears peculiar in regard of the literature on comparable materials.

The different tilt system is probably not produced by the large strain induced during the synthesis process (mechanosynthesis) of the raw powders. Indeed, even if mechanosynthesis is

Tilt system	Space group	Supergroup	
$a^0 a^0 c^+$	Pc	Cm	in-phase
$a^0 b^0 c^+$	Pm	Pm	in-phase
$a^0 b^0 c^+$	Cm	Pm	in-phase
$a^0 b^0 c^-$	Cm	Pm	antiphase
$a^- a^- c^0$	Cm	Cm	antiphase
$a^- a^- c^-$	Cc	Cm	antiphase
$a^- b^- c^0$	Cm	Pm	antiphase
$a^- a^- a^-$	$R3c$	$R3m$	Pb(Zr,Ti)O ₃

Table 3.10: List of possible O-octahedra tilt systems considered for PYN-PT 0.40.

The notation to describe the O-octahedra tilt system is the one developed by Glazer [82]. In this notation, the O-octahedra tilting is described by specifying the rotations of the octahedra along each of the three axes of the pseudo-cubic cell ($Z=1$) using a letter to characterize the magnitude of the rotation and a superscript indicating whether the rotation in adjacent layer are in the same (+) or opposite (-) directions.

The tilt system $a^0 b^0 c^+$ corresponds to two different space groups. The choice between the two space groups is made based on the displacements of the cations.

The supergroup is the space group without O-octahedra tilting.

well-known to induce large strain in the processed powder, this strain should have been released in the subsequent thermal treatments conducted to obtain the powder used for diffraction experiments (see Appendix A for details regarding the synthesis of the samples).

Moreover, in similar systems, strain induced by application of external pressure leads to the $a^- a^- a^-$ O-octahedra tilt system and not to the one that we observe. Therefore, it would be really surprising that the O-octahedra tilting that we observed for PYN-PT 0.30-0.40 would be due to the processing method.

In conclusion, from the examination of the presence and absence of the SSRs due to O-octahedra rotations, three tilt systems have been found to be possible in PYN-PT: $a^0 b^0 c^-$, $a^- a^- c^0$ and $a^- b^- c^0$.

Further investigations are needed to find the tilt system in this solid solution, but the tilt system in PYN-PT already appears peculiar in regards to similar systems.

3.4.5 Summary and conclusion

In Sec.3.3, the presence, at room temperature, of distortions, chemical order, antiparallel displacements, and O-octahedra tilting were examined by simply looking at the presence of reflections in diffractograms.

The chemical ordering that was already examined extensively in the high-temperature phase in Sec.3.3.3 (page 114) was considered to remain the same at room temperature since the temperature at which the diffraction experiments were conducted are much lower than the ordering/disordering temperature. Therefore, in this section, no further study of the chemical

ordering was conducted.

Here, distortions, antiparallel displacements and O-octahedra tilting at room temperature for the various compositions have been investigated more thoroughly using profile matching analysis and Rietveld refinements. All results obtained in this section are summarized in Fig.3.23.

For PYN-PT with $x \leq 0.05$, the profile matching analysis confirmed that the average structure is indeed monoclinic (M in Fig.3.23) as was reported in the literature [39, 40] and as was determined from the splitting of the peaks in Sec.3.3.1.

Adding PT, the PYN-PT solid solution becomes rhombohedral (R in Fig.3.23) for PYN-PT 0.10 and pseudo-cubic (C in Fig.3.23) in the compositional range $0.16 \leq x \leq 0.25$.

For compositions with larger amount of PT ($0.30 \leq x \leq 0.40$), the structure becomes monoclinic with possibly coexistence of two monoclinic phases: Cm and Pm . Hence, on the low PT-content side of the MPB, no rhombohedral phase was evidenced in this extensive structural study contrarily to what was reported based on more simple analyses relying only on main Bragg reflections splitting and by analogy with other Pb-based solid solutions [47, 52, 53].

Adding even more titanium in the solid solution (PYN-PT $x = 0.45-0.50$), a tetragonal ($P4mm$) phase appears in the structure in coexistence with at least one of the monoclinic phases.

For the composition with the largest amount of titanium considered in this work ($x = 0.60$), the structure is a mixing of the tetragonal $P4mm$ and the monoclinic Pm phases.

Finally, on the right-hand side of the phase diagram, the structure of PT is well established as being tetragonal with a $P4mm$ space group.

In summary, the solid solution PYN-PT with $x \leq 0.05$ displays a monoclinic structure that transforms into a rhombohedral and pseudo-cubic phases with addition of PT. Close to the MPB, the structure goes from a monoclinic to a tetragonal phase through a coexistence of phases.

PYN-PT 0.10 and compositions in the range $0.30 \leq x \leq 0.40$ were demonstrated in this chapter to have a non-cubic structure, whereas these compositions were shown to have a relaxor behavior in Chapter 2 that are usually associated with a pseudo-cubic structure. This apparent discrepancy will be discussed in Chapter 4.

Additionally, no local structure different from the long-range one has been observed for PYN-PT $0.16 \leq x \leq 0.25$ because of experimental limitations of the X-rays diffraction measurements. Indeed local distortions were also not observed in PYN-PT 0.30 in the X-rays experiments, whereas neutrons experiments have clearly revealed diffuse scattering indicating the presence of local distortions.

Thus, further experiments (e.g. neutron diffraction) are necessary to conclude regarding the presence of local features in the compositional range $0.16 \leq x \leq 0.25$.

Furthermore, the study of the local strain using the Williamson-Hall approach has shown that strain may appear upon cooling for PYN-PT 0.10. This strain may be due to the appearance of antipolar order at a local scale. Indeed, in PYN-PT 0.10, the SSRs associated with antipolar ordering are extremely broad indicating a short coherence length for that order.

This antipolar ordering can be explained by a modulation of displacements of cations along $\langle 1/2, 1/2, 0 \rangle$. The atoms involved in this modulation may be Pb^{2+} as commonly seen in Pb-

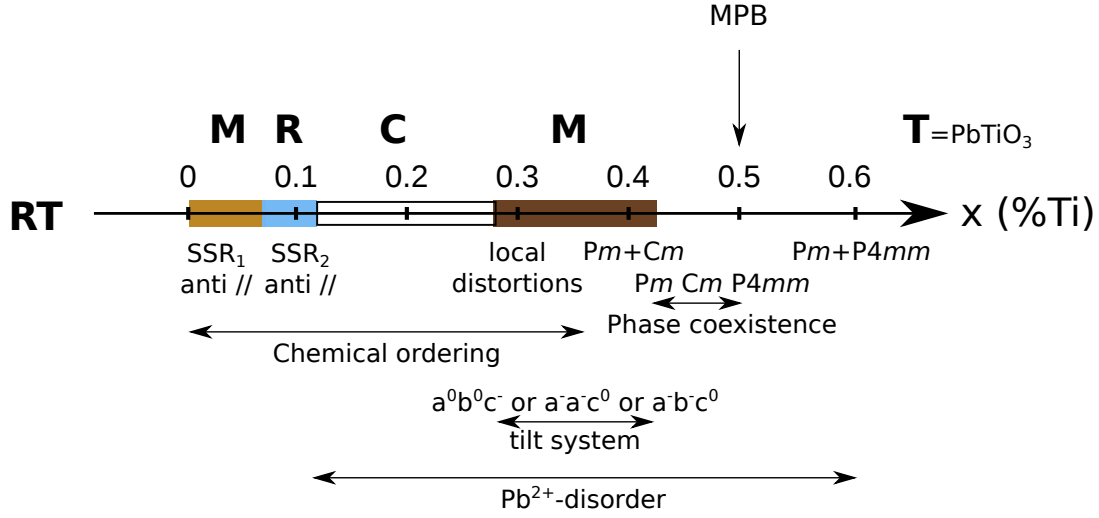


Figure 3.23: Evolution of the room-temperature structure in the PYN-PT solid solution for the $Z=1$ unit cell.

The compositional range with chemical ordering, O-octahedra and Pb^{2+} -disorder are indicated with arrows.

The presence and type of SSRs due to antiparallel displacements are indicated with "SSR_n anti //". n refers to the type of SSRs: $n=1$ corresponds to the sharp SSRs observed for PYN-PT with $x \leq 0.05$ and $n=2$ the broad SSRs observe for PYN-PT 0.10.

based perovskites or B cations by analogy with the modulation proposed in PYN and PYN-PT 0.05. Additional HRTEM images may help lift this uncertainty.

In any case, the antipolar ordering in PYN-PT 0.10 is undoubtedly different from the one observed in PYN-PT with $x \leq 0.05$. Indeed, in first approximation, the antipolar ordering in PYN-PT with $x \leq 0.05$ may be explained by a $(3/4, -3/4, 0)_{pc}$ modulation in the $Z=8$ pseudo-cubic unit cell of the Pb^{2+} positions, in agreement with the literature [40, 42]. But this modulation vector cannot explain all observed SSRs and the structure is more complex than reported in the literature. The only way that I have found to describe the structure is to use a second modulation vector $(1/2, 0, 1/2)_{pc}$ that is proposed to be related to organized displacements of B cations.

Besides, the Pb^{2+} are displaced along the modulation vector and not perpendicular to it as in all other reported Pb-based antiferroelectrics making the antipolar ordering present in PYN-PT $x \leq 0.05$ unique.

Moreover, the comparison of the intensity ratios of some of the main Bragg peaks at high temperature and room temperature in the compositional range $0.16 \leq x \leq 0.30$ and Rietveld refinements conducted on PYN-PT with $0.40 \leq x \leq 0.60$ show that the positional disorder of Pb^{2+} that was evidenced at high temperature persists at room temperature.

This positional disorder of Pb^{2+} for PYN-PT with $x = 0.16-0.60$ has been associated with the relaxor state present at room temperature or only at high temperature as evidenced in Chapter 2.

Finally, O-octahedra tilts observed for PYN-PT 0.30 and PYN-PT 0.40 were studied. The tilt system can be attributed to one of the following tilt systems: $a^0b^0c^-$, $a^-a^-c^0$, or $a^-b^-c^0$. None of these tilt systems were ever reported in Pb-based FE solid solutions, to my knowledge. Therefore, whichever O-octahedra tilting system happens to be describing PYN-PT 0.30 and PYN-PT 0.40, it will be peculiar within the Pb-based solid solutions.

In conclusion, the room-temperature structure of the solid solution PYN-PT was studied using, among other techniques, profile matching analysis and Rietveld refinements.

All these studies prove that the structure of PYN-PT is more complex than what was reported in the literature and in particular, that the MPB is different from all other known ones because of the absence of a rhombohedral phase on the PT-poor side of the MPB.

3.5 PHASE TRANSITIONS

In this section, for a number of selected compositions, the evolution of the cell parameters as a function of temperature will be studied. This will enable to discuss the presence of possible intermediate phases between the high-temperature cubic phases and the room-temperature structures discussed previously. When possible, the type of transition will also be discussed.

The evolutions of the cell parameters as a function of temperature were measured by X-ray diffraction in the SPMS laboratory. Several main Bragg reflections (e.g. (011), (111) and (002)) were recorded at various temperatures between 90 K and 800 K.

As in the previous section, the various compositions are separated, hereafter, based on the presence of distortions and SSRs due to antiparallel displacements.

3.5.1 Structure with SSRs due to antiparallel displacements: $x = 0-0.10$

The room-temperature structure of PYN-PT in the compositional range $0 \leq x \leq 0.10$ has been discussed in Sec.3.4.1. It was shown that, in this compositional range, the solid solution PYN-PT presents a distorted structure with SSRs that have been attributed to antiparallel displacements. The average structures have been determined to be monoclinic with $a \simeq b \neq c$ for PYN and PYN-PT 0.05 and rhombohedral for PYN-PT 0.10 (Table 3.5, page 130).

Moreover, the SSRs in PYN-PT 0.10 have been demonstrated to be different from the ones in PYN or PYN-PT 0.05 (page 131).

The evolution of the average structure with temperature will therefore be investigated separately for PYN-PT with $x = 0-0.05$ and PYN-PT 0.10.

PYN and PYN-PT 0.05

The evolution of the cell parameters for PYN and PYN-PT 0.05 as a function of temperature are presented in Fig.3.24 considering the pseudo-cubic cell ($Z=8$), i.e. the unit cell taking into account the chemical order on the B site but not the antiparallel displacements. In this analysis, the monoclinic cell parameters a and b were considered to be equal since no widening of the $(200)/(020)$ massif was observed down to low temperature.

The change of cell parameters between the high-temperature cubic phase and the low-temperature phase is sudden and happens at 580 K and 495 K for PYN and PYN-PT 0.05 respectively. This abrupt change of cell parameters indicate a first-order nature of the phase transition.

The first-order nature of the cubic-monoclinic transition is also evidenced by the abrupt apparition/disappearance of the SSRs at the Curie temperature T_c .

Furthermore, contrarily to what was found by Demidova et al. [42], we find that the high-temperature cubic phase transforms directly into the low-temperature phase without any intermediate phase, in agreement with the results of Kwon et al. [44].

PYN-PT 0.10

For PYN-PT 0.10, the pseudo-cubic cell considered is the one without taking into account the chemical order ($Z=1$). The splitting of the $(hhh)_{pc}$ reflections observed at room temperature (Sec.3.3.1) is subtle and has only been evidenced due to the extreme high-resolution of the synchrotron X-ray diffractometer. In this study, I considered the structure to be cubic and monitored carefully the evolution of the full width at half-maximum (FWHM) of the peaks.

The evolutions of the pseudo-cubic cell parameter ($Z=1$) as well as the evolution of the FWHM with temperature are plotted in Fig.3.25.

The pseudo-cubic cell parameter presents two changes in its thermal evolution: one at the Curie temperature (T_C) and one at a lower temperature, T_2^* .

The change of slope in the cell parameters at the highest temperature was attributed to the Curie temperature since the width of $(111)_{pc}$ reflection increases rapidly below this critical temperature indicating a splitting of this reflection and therefore the appearance of a different structure. The change in the thermal evolution of the cell parameters at T_2^* , on the other hand, is not accompanied by a drastic change in the FWHM of any of the reflections recorded during this experiment ($(110)_{pc}$, $(111)_{pc}$ and $(002)_{pc}$). Therefore, this change of slope may indicate a transition between two rhombohedral phases or that the rhombohedral phase that appears at the Curie temperature, upon cooling, does not establish itself immediately into its low temperature arrangement, but finishes to settle at T_2^* .

This transition is however not due to the appearance of the SSRs since they appear at T_c (Fig.3.25(c)).

The transition at T_2^* echoes to the one observed in the thermal evolution of the dielectric constant. However, the transition temperature observed in X-ray diffraction is lower than the one observed in the dielectric constant. This raises the question of whether these two temperatures

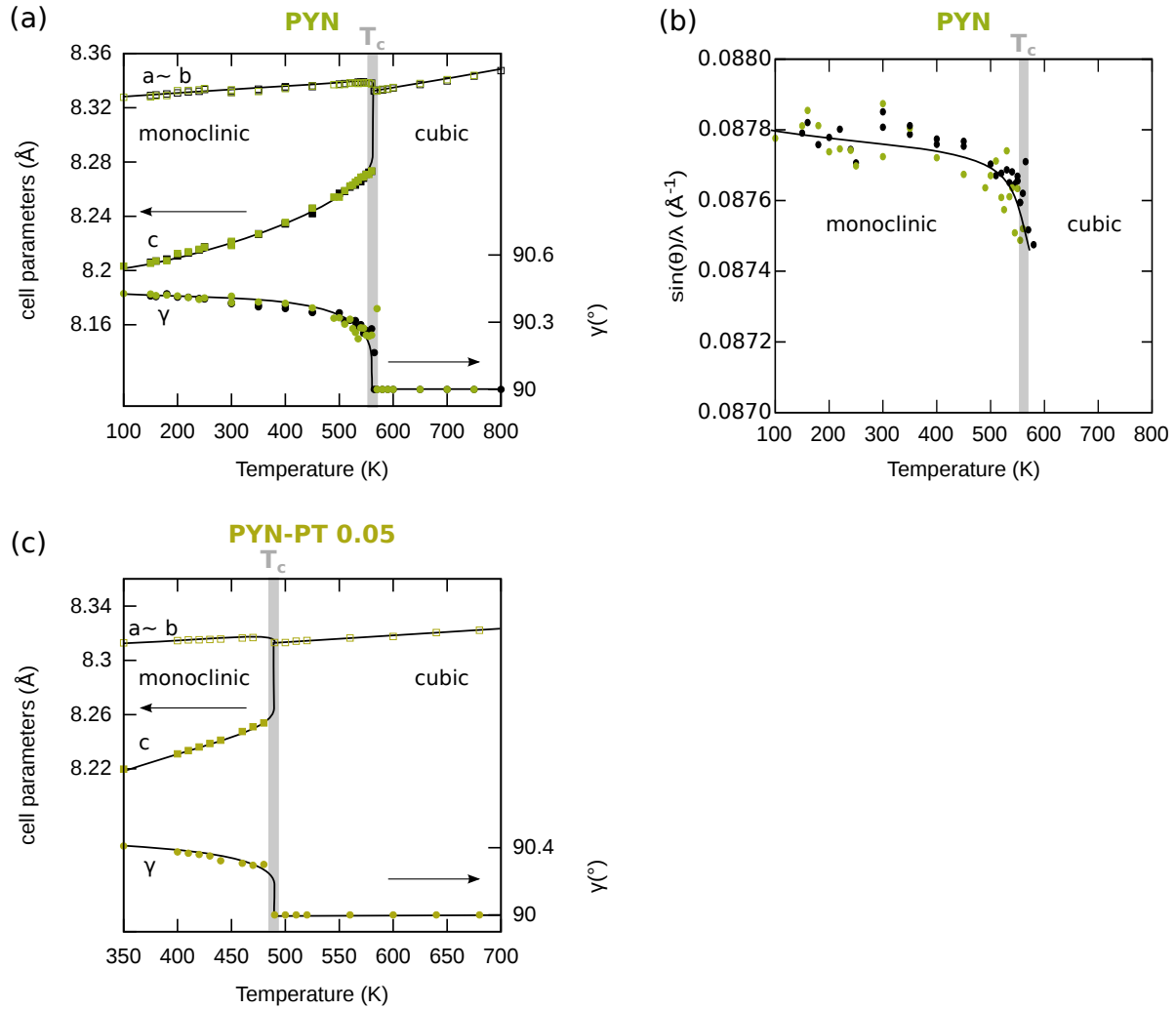


Figure 3.24: In the pseudo-cubic cell ($Z=8$) taking into account chemical order:

- (a) Evolution of the cell parameters, $a \sim b$, c , and γ as a function of temperature for PYN.
- (b) Evolution of the position of a reflection due to antiparallel displacement $(0, -3/4, 5/4)_{pc}$ as a function of temperature.
- (c) Evolution of the cell parameters, $a \sim b$, c , and γ as a function of temperature for PYN-PT 0.05.

The color symbols represent the evolution of the cell parameters upon heating, whereas the black symbols represent the evolution upon cooling. The lines are guides for the eyes.

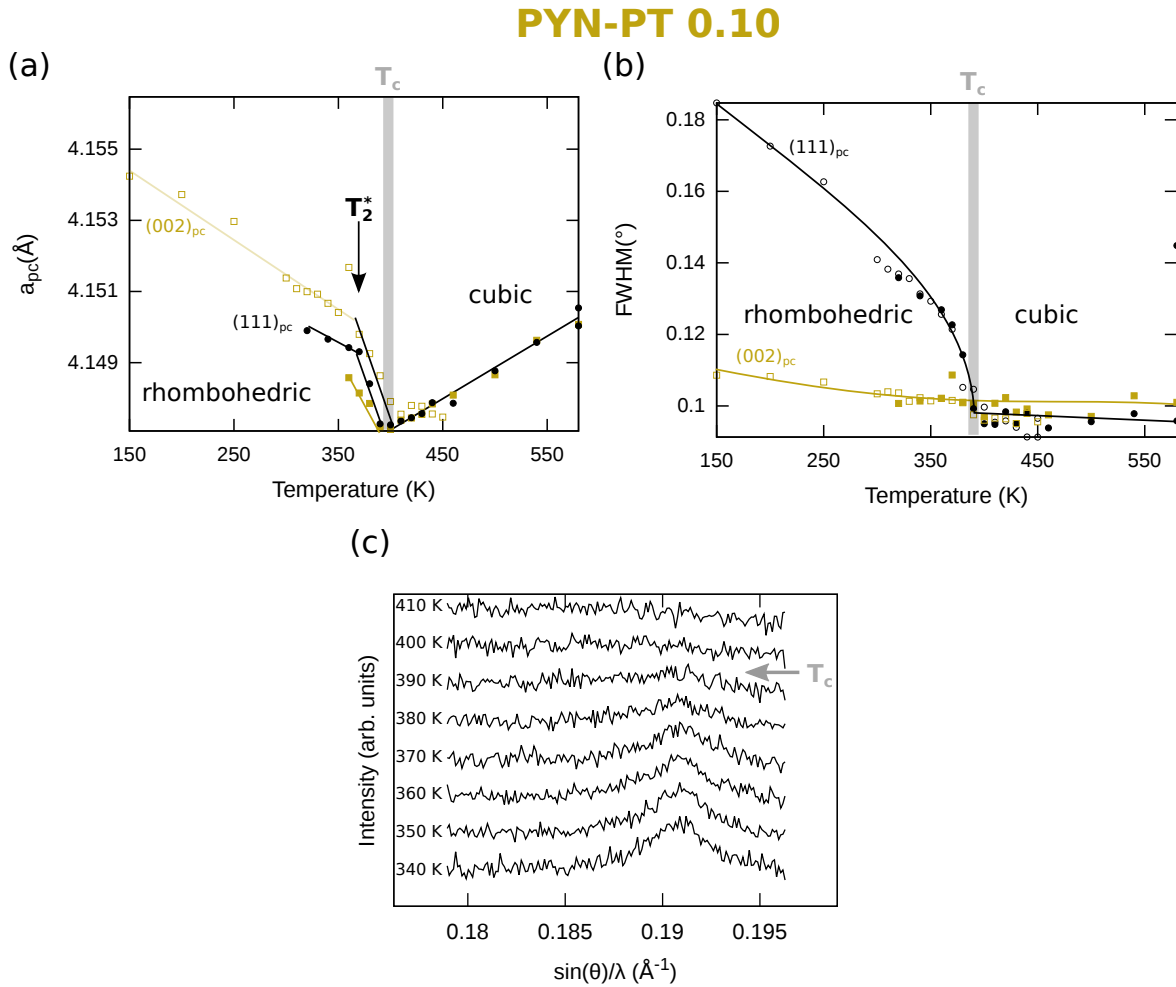


Figure 3.25: In the pseudo-cubic cell ($Z = 1$):

- (a) Evolution of the cell parameters, a_{pc} as a function of temperature for PYN-PT 0.10 .
- (b) Evolution of the full width at half-maximum (FWHM) for the (002)_{pc} and (111)_{pc} reflections.
- (c) X-ray diffraction pattern of a SSRs due to antiparallel displacements as a function of temperature.

The color and the black symbols represent the (002)_{pc} and (111)_{pc} reflections, respectively. The open symbols represent the data collected in the cryofurnace whereas the solid symbols represent the data recorded in the furnace. The lines are guides for the eyes.

are associated to the same change of behavior. This will be discussed in the Chapter 4 devoted to the comparison of the structural and properties results.

3.5.2 Structure with low distortions: $x = 0.16-0.30$

In Sec.3.4.2, we have seen that compositions in the range $0.16 \leq x \leq 0.30$ present no, or minute, long-range distortions. The resulting pseudo-cubic structure is not unexpected for materials presenting the relaxor character evidenced for these compositions in Chapter 2.

In this section, I will discuss the evolution with temperature of the lattice parameter of the pseudo-cubic cell defined without taking into account chemical ordering ($Z = 1$). In particular, changes in the thermal evolution of the cell parameter are often related to changes at the local scale (the relation between the changes in the relaxor behavior and the evolution of the cell parameter as a function of temperature of the archetypal relaxor $\text{Pb}(\text{Mg}_{1/3}\text{Nb}_{2/3})\text{O}_3$ was described in Fig.3.2, page 103).

Moreover, the changes of cell parameter will be put in perspective with the freezing temperature T_f , the temperature associated with a change of the dielectric constant T_2 and the temperature associated with a change in the I-V curves T_3 observed in the Chapter 2 based on the examination of the dielectric and hysteresis measurements as a function of temperature.

The cell parameter was determined by fitting the $(011)_{pc}$, $(002)_{pc}$ and $(111)_{pc}$ reflections as a function of temperature for PYN-PT 0.16, PYN-PT 0.25 and PYN-PT 0.30 and are plotted in Fig.3.26. For PYN-PT 0.30, the evolution of the full width at half maximum (FWHM) is also drawn in the same figure. The FWHM of the two other compositions are not reported since no changes have been observed.

For each composition, changes in the thermal evolution of the cell parameters can be observed. Hereafter, the changes of cell parameters will be discussed, first, composition after composition. The nature of these changes will be discussed in a second time.

For PYN-PT 0.16, there is a clear change of slope in the thermal evolution of the cell parameter at a temperature close to 300 K. This change of slope occurs at a temperature close to any of the temperatures T_f , T_2 or T_3 characterized in Chapter 2.

Moreover a more subtle change of slope can be observed around 430 K. This temperature is denoted T_4 and the change of behavior associated with this change of slope will be discussed shortly after.

For PYN-PT 0.25, there are three distinct changes of slope in the thermal evolution of the cell parameter. All three changes of slope can be related to the characteristic temperatures observed in Chapter 2.

For PYN-PT 0.30, there are two changes of slope in the evolution of the cell parameter as a function of temperature that can be identified: one at the freezing temperature, T_f , and one at ~ 650 K, referred to as T_5 . This change of slope is also associated with an increase of the FWHM of the $(002)_{pc}$ reflection.

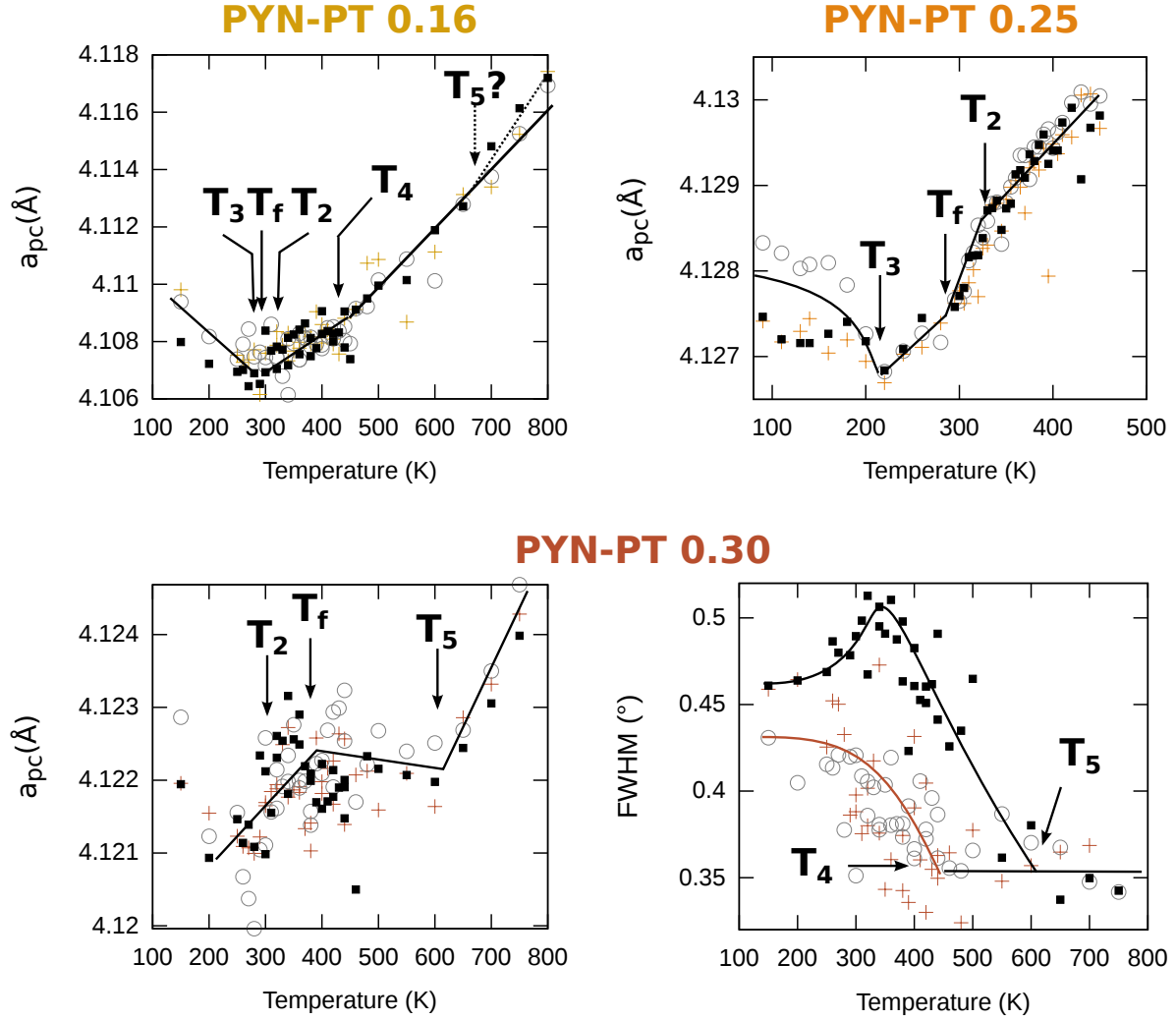


Figure 3.26: Evolution of the pseudo-cubic ($Z=1$) cell parameter for PYN-PT 0.16, PYN-PT 0.25 and PYN-PT 0.30. The pseudo-cubic cell parameter is calculated using the (002) (black squares), (011) (open circles) and (111) (colored crosses) reflections.

The thermal evolution of the FWHM for PYN-PT 0.30 is also reported. No significant changes can be observed in the thermal evolution of PYN-PT 0.16 and PYN-PT 0.30.

T_f , T_2 and T_3 indicate the freezing temperatures and transition temperatures observed in the Chapter 2. T_4 and T_5 indicate changes in the thermal evolution of the cell parameter that do not match the transition temperatures observed in the electric measurements. The lines are guides for the eyes.

Moreover, upon cooling, the FWHM of the $(011)_{pc}$ and $(111)_{pc}$ reflections increases at about 450 K. This change of behavior will be proposed in the next paragraph to be of the same nature as the one observed in PYN-PT 0.16 and therefore is also denoted T_4 .

This increase of the FWHM may appear surprising as no clear widening of the main Bragg reflections has been convincingly observed between the high-temperature and room-temperature data obtained in the high-accuracy diffractometer at ESRF (Sec.3.3.1, page 112). However, a small increase of the FWHM may be observed in the synchrotron data, but the increase is within the experimental and fitting uncertainties and was therefore not firmly established.

Here, the uncertainties remain high (as evidenced by the strong scattering of the FWHM), but because of the large amount of data collected at various temperatures, it is fair to conclude that there is an increase of the FWHM of all reflections upon cooling.

As all considered reflections are widened compared to the high-temperature cubic phase, the room-temperature structure of PYN-PT 0.30 presents monoclinic distortions.

Therefore, for the three investigated compositions, most of the changes in the cell parameter with temperature may be correlated with transition temperatures observed in Chapter 2: T_f , the freezing temperature, T_2 , associated with a change of dielectric behavior and T_3 , characterized by a change in the high electric-field I-V curves.

Moreover, for PYN-PT 0.16 and PYN-PT 0.30, additional changes, at T_4 and T_5 , can be observed in the thermal evolution of the pseudo-cubic cell parameter.

The change at T_4 , close to 430-450 K, can be observed for both PYN-PT 0.16 and PYN-PT 0.30. This temperature is close to the characteristic temperature T^* that has been observed in the literature to be independent of the material [69]. Therefore, I propose that T_4 corresponds to T^* and that the associated change of behavior is related to the appearance of strong correlation between the polar nanoregions.

Finally, the change of behavior at T_5 , observed in PYN-PT 0.30, is proposed to correspond to the Burns temperature, T_B since this temperature (~ 650 K) is comparable to Burns temperatures reported for Pb-based relaxors: 630 K for $\text{Pb}(\text{Mg}_{1/3}\text{Nb}_{2/3})\text{O}_3$ and 740 K for $\text{Pb}(\text{Zn}_{1/3}\text{Nb}_{2/3})\text{O}_3$, for example.

Besides, in PYN-PT 0.16, a change at a similar temperature may also be observed, but the available data are extremely limited and the presence of such temperature remains speculative. Nonetheless, the presence of a change at a temperature close to T_5 , for PYN-PT 0.16, would support the idea that T_5 is T_B since T_B is known to little evolve with PT content. However, at T_5 , there is an increase of the FWHM of the $(002)_{pc}$ reflection that is usually *not* observed at T_B . T_5 corresponds well with the critical temperature T_{Cr} up to which a tetragonal splitting is observed in PYN-PT $0.40 \leq x \leq 0.60$ (Sec.3.5.3). This tetragonal splitting will be associated with the appearance of meso-domains at a "pseudo-Burns temperature". Thus, in the case of PYN-PT 0.30, T_5 may also be related to the appearance of meso-domains, but these meso-domains are smaller than the ones observed for PYN-PT $0.40 \leq x \leq 0.60$ since no tetragonal splitting was noted.

Therefore, the change of behavior at T_5 is associated with a change of behavior similar to the one occurring at the Burns temperature but the polar regions may be larger than "nano".

In summary, many changes with temperature can be observed in the diffractograms of PYN-PT 0.16, PYN-PT 0.25 and PYN-PT 0.30. Some of these changes occur at temperatures that are in good agreement with the characteristic temperatures established while studying the properties: T_f , T_2 and T_3 . Some changes were not observed in the dielectric and hysteresis measurements and are introduced as T_4 and T_5 . These particular temperatures are proposed to correspond to T^* and T_B (or “pseudo-Burns temperature”), respectively, based on the comparison with the literature on relaxors.

A complication, though, arises from the temperature T_4 observed for PYN-PT 0.16 which happens to correspond well with T_B determined from the dielectric measurements. Hence, the deduced change of behavior occurring at T_4 in PYN-PT 0.16 would be different depending on whether it is based on the structural and properties measurements. The reconciliation of this discrepancy of results based on different characterization techniques will be provided in Chapter 4.

3.5.3 Structure with strong distortions: with $x = 0.35$ -0.60

In the compositional range $0.35 \leq x \leq 0.60$, the comparison of the $(00l)_{pc}$ and $(hhh)_{pc}$ reflections at high temperature and room temperature (in Sec.3.3.1) has evidenced the presence of strong distortions of the structures. The more in-depth study of the room-temperature structure (Sec.3.4.3) has demonstrated that in this compositional range, the structure is a mixing of several phases.

Hereafter, the evolution of the cell parameters ($Z=1$ cell) with temperature is reported. In particular, the sequence of phase transitions from the high-temperature cubic phase to the room-temperature structure will be discussed.

$(011)_{pc}$, $(111)_{pc}$ and $(002)_{pc}$ reflections were recorded for PYN-PT 0.40, PYN-PT 0.50 and PYN-PT 0.60 as a function of temperature. Because of the limited number of recorded reflections, the various compositions were described with a single phase. The crystal system of the single phase describing each composition was chosen *a posteriori* based on the number of pseudo-Voigt profiles necessary and sufficient to describe the measured massifs.

For PYN-PT 0.40, the $(002)_{pc}$ reflection was fitted using only two peaks and its splitting can be observed up to 680 K (the corresponding critical temperature is denoted T_{Cr} in Fig.3.25). A distinct splitting of the $(111)_{pc}$ can also be observed at the temperature of the maximum of the dielectric constant T_m (~ 580 K) (Fig.3.27).

For PYN-PT 0.50, a splitting of the $(111)_{pc}$ reflection occurs at the temperature of the maximum of the dielectric constant T_m (Fig.3.27). As in the case of PYN-PT 0.40, the splitting of the $(002)_{pc}$ persists for temperature larger than T_m (up to ~ 690 K). Actually above T_m , it is not possible to decide with my data if the $(002)_{pc}$ reflection is split in two or three reflections. Conducting the same analysis with higher quality data may help lift the uncertainty regarding the symmetry above T_m .

For PYN-PT 0.60, the splitting of the $(002)_{pc}$ reflection is observed for temperatures 20 degrees higher than T_m (Fig.3.27). No splitting or widening of the $(111)_{pc}$ could be observed at any investigated temperature.

In summary, for all compositions a distinct splitting of the $(002)_{pc}$ is observed at a temperature (T_{Cr}) higher than the temperature of the maximum of the dielectric constant T_m . This critical temperature T_{Cr} is independent of the composition and therefore of T_m . Thus, it appears that the high-temperature cubic phase transforms at $T_{Cr} \sim 680-690$ K into a lower symmetry phase, probably tetragonal in regard with the results on PYN-PT 0.40 and PYN-PT 0.60.

For PYN-PT 0.40 and PYN-PT 0.50, the splitting of the $(111)_{pc}$ reflection at T_m indicates a transformation of the proposed tetragonal phase formed at T_{Cr} into a monoclinic phase. This transition has not been observed for PYN-PT 0.60 probably because the room-temperature structure is mainly tetragonal.

I proposed that the critical temperature T_{Cr} would correspond to a “pseudo-Burns temperature” since the value of T_{Cr} is extremely similar to T_5 (associated with the Burns temperature T_B) determined for PYN-PT 0.16 and PYN-PT 0.30 (Fig.3.28, page 169) and that the Burns temperature usually evolves little within a solid solution.

Moreover, for compositions in the range $0.40 \leq x \leq 0.60$, it was established that a relaxor phase exists at temperatures higher than T_m .

However, since strong distortions from the cubic phase can be observed below T_{Cr} , the polar regions that would develop at T_B are not nanoscopic as in the case of “classical” relaxors, but mesoscopic. Therefore, below T_{Cr} , ferroelectric meso-domains with different sizes would form in a paraelectric matrix leading to the appearance of dielectric relaxation and tetragonal distortions.

The coexistence of a paraelectric phase and ferroelectric meso-domains between T_m and T_{Cr} would imply the coexistence of a cubic phase and another phase of lower symmetry (tetragonal) leading to the presence of three peaks in the $(002)_{pc}$ massif. For PYN-PT 0.50, the $(002)_{pc}$ massif was fitted with three peaks up to T_{Cr} but the results are noisy and it is not possible to conclude from them on the presence of two or three reflections. Thus, using our data, it is not possible to fit the $(002)_{pc}$ massif with three peaks in a reliable way and therefore to clarify the coexistence of a cubic and tetragonal phase.

In conclusion, the study of the evolution of the structure with temperature unveiled that PYN-PT with $x = 0.40-0.60$ do not undergo a simple cubic-low temperature phase transition, and that this more complex thermal evolution may be the sign of polar mesoregions.

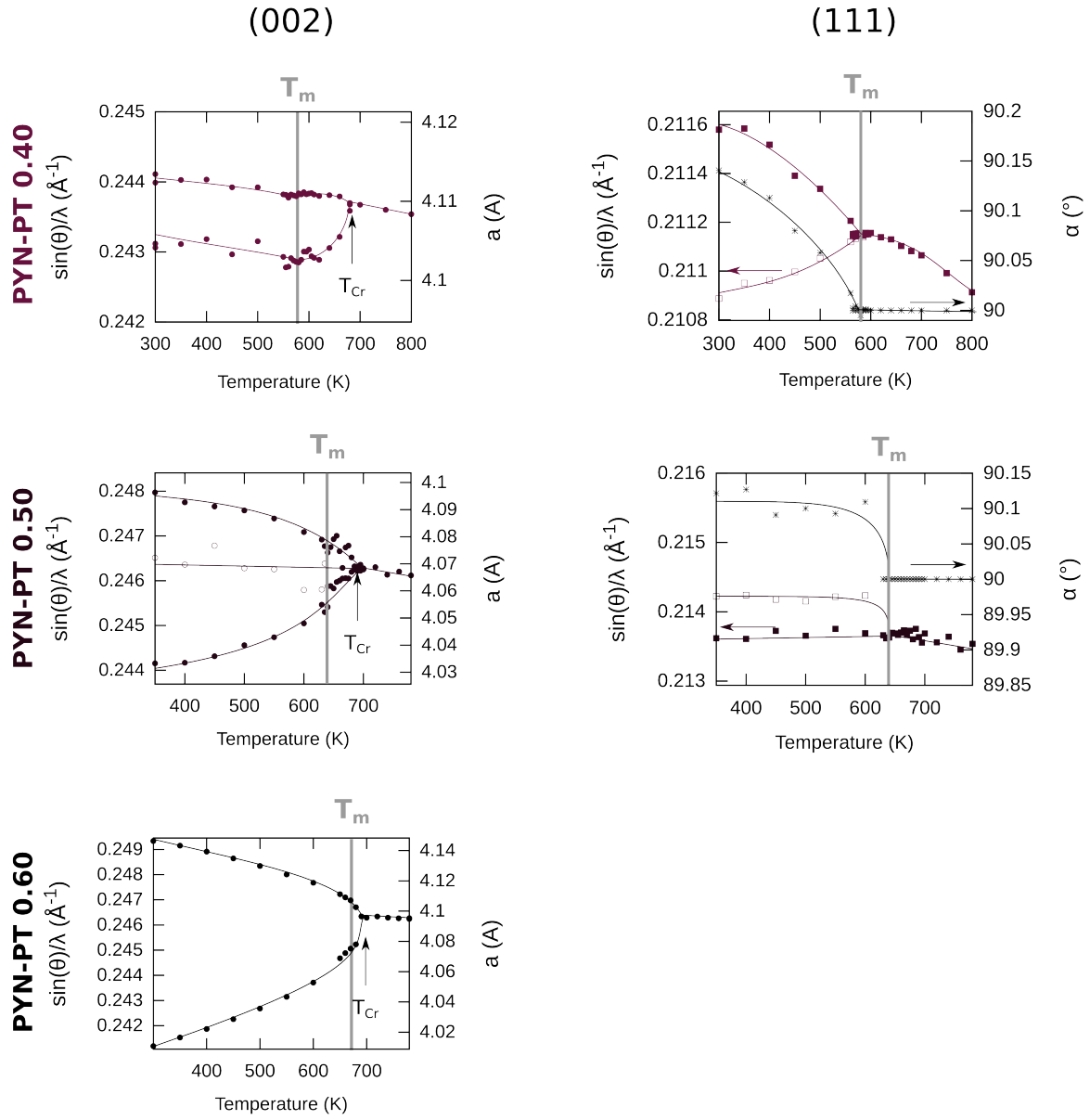


Figure 3.27: Evolution of the $(002)_{pc}$ and $(111)_{pc}$ reflections as a function of temperature for PYN-PT 0.40, PYN-PT 0.50 and PYN-PT 0.60.

The temperature of the maximum of the dielectric constant, T_m , is indicated. The critical temperature (T_{Cr}) of the splitting of the $(002)_{pc}$ reflection is indicated with an arrow.

3.6 SUMMARY AND CONCLUSION ON THE PHASE DIAGRAM

In this chapter, the structure of the solid solution PYN-PT 0-0.60 was studied using neutron and X-ray diffraction.

Because very few things regarding the structure were known, at first, a straightforward approach involving the study of the splitting of some of the main Bragg reflections and presence and type of superstructure reflections (SSRs) was undertaken (in Sec.3.3).

Based on this knowledge, more thorough studies of the average structure, chemical order on the B site, positional disorder of Pb^{2+} , antiparallel displacements and O-octahedra tilting were conducted. In addition, for some compositions, the evolution of the structure with temperature was also examined.

Results obtained regarding the evolution of the structure with temperature and, in particular, the structure at room temperature are summarized hereafter and in Fig.3.28.

The pseudo-cubic ($Z = 8$) unit cell of PYN and PYN-PT 0.05 undergo a unique cubic-monoclinic phase transition at the Curie temperature, upon cooling. This phase transition is associated with appearance of SSRs due to antipolar displacements. These SSRs can be for the largest part explained with a $(3/4, -3/4, 0)_{pc}$ modulation of the position of Pb^{2+} . However, the structure is more complex since some SSRs cannot be explained with this modulation vector. The SSRs that are not related to these Pb^{2+} displacements are proposed to be due to modulated displacements of the B cations with a $(1/2, 0, 1/2)_{pc}$ modulation vector.

Moreover, the displacements of Pb^{2+} cations are along the modulation vector and not perpendicular to it, making this antipolar order unique compared to the other known Pb-based materials.

For PYN-PT 0.10, the structure transforms from the high-temperature cubic phase to a rhombohedral phase at the temperature of the maximum of the dielectric constant, T_m . Concomitantly, broad SSRs due to antiparallel displacements develop.

At lower temperature, a change in the thermal evolution of the cell parameters indicate either a rhombohedral-rhombohedral phase transition or a modification of the structure at a local scale. The SSRs observed up to T_m may be attributed to a modulated displacements of cations along one of the faces of the rhombohedron with a $1/2$ amplitude. However it was not possible to determine which cations were involved in this modulation. Further HRTEM investigations may help answer this question.

These modulated displacements occur on a local scale as evidenced by the large width of the SSRs. Williamson-Hall analyses conducted at high-temperature and room-temperature suggest that this local ordering induce strain in the structure.

The structure remains on average cubic, for PYN-PT $x = 0.16-0.25$, over the investigated temperature range (800 K-100 K). At room-temperature, no evidence of a local structure different from the long-range cubic one was found due to experimental limitations.

However, the study of the thermal evolution of the cell parameters indicate some changes in the local structure despite the fact that on long-range the structure remains cubic. Some of the temperatures at which these changes occur correspond to the temperatures where changes in

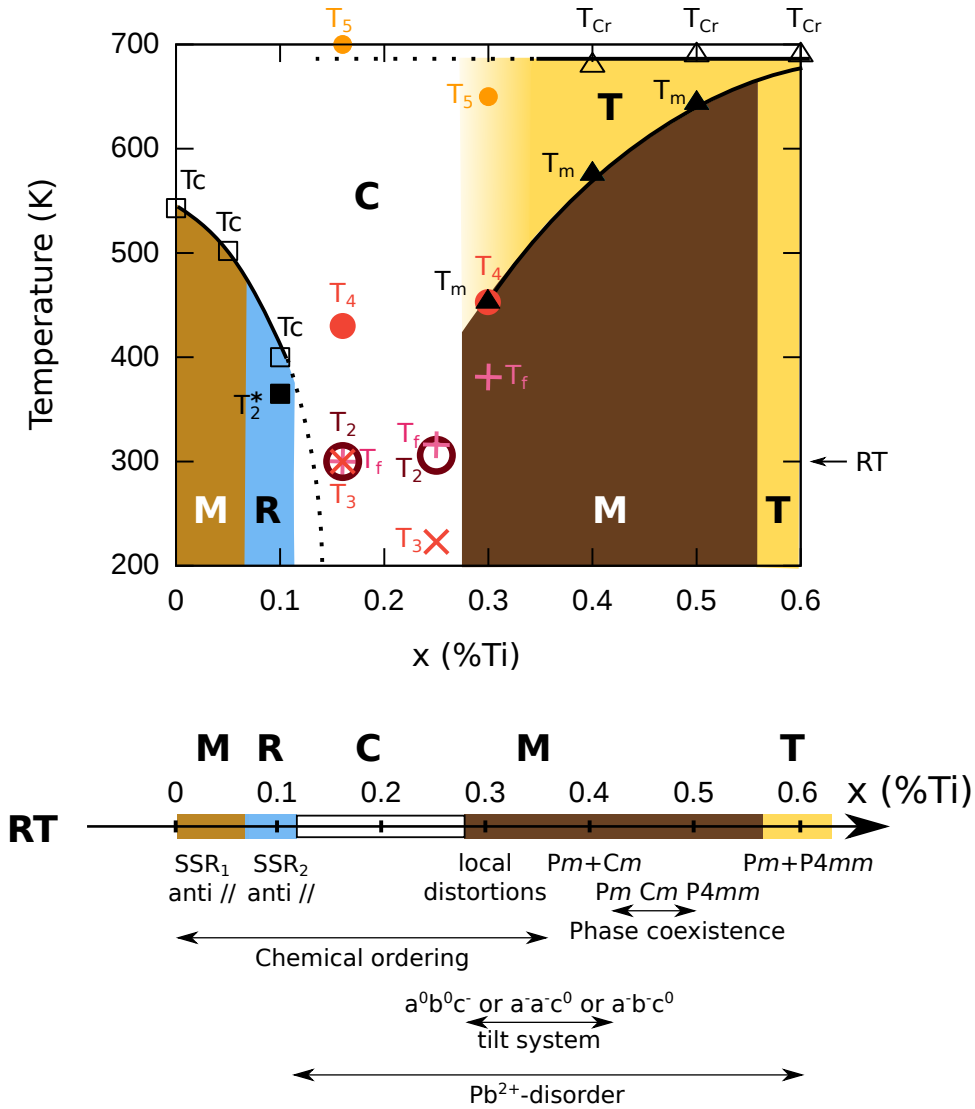


Figure 3.28: Phase diagram produced from the study of the structure using X-ray and neutron diffraction as a function of temperature. The structure at room-temperature for the various compositions is detailed at the bottom (adapted from Fig.3.23). Lines are guides for the eyes.

The crystal systems describing best the average structure of the various compositions are given with bold letters: M, R, C and T referring to monoclinic, rhombohedral, cubic and tetragonal, respectively.

The various temperatures associated with a change of temperature-dependency of the cell parameters are also indicated: open square represent the transformation of the high-temperature cubic phase in the low-temperature monoclinic or rhombohedral phases associated with appearance of SSRs due to antiparallel displacements; solid square indicates the change of slope at T_2^* in the thermal evolution of the cell parameters of PYN-PT 0.10; open circles, x and + indicate changes of slope in the thermal evolution of the cell parameters at temperatures T_2 , T_3 and T_f that were determined in Chapter 2 using dielectric and hysteresis measurements; solid circles represent T_4 and T_5 that have been associated with T^* and T_B ; for PYN-PT with $x \geq 0.40$, the transformation at T_{Cr} from the cubic phase to the tetragonal phase is represented with open triangles and the transformation from the tetragonal phase to the monoclinic phase is represented with solid triangles.

the dielectric and hysteresis behavior were observed in Chapter 2. The temperatures for which no change in the dielectric and hysteresis measurements were observed are labeled T_4 and T_5 . These temperature are supposed to correspond to the critical temperature T^* and the Burns temperature T_B , respectively, based on similarities with other relaxor systems: at T_B , polar nanoregions (PNRs) appear in the paraelectric matrix and these PNRs correlate at T^* .

PYN-PT 0.30 undergoes a cubic-monoclinic phase transition at T_m . In addition, to this long-range transformation of the structure, other changes in the cubic and monoclinic structures were noticed in the evolution of the cell parameters. These changes take place at temperature T_5 (assumed to correspond to the Burns temperature or a pseudo-Burns temperature) and at the freezing temperature, T_f (determined in Chapter 2).

Furthermore, in addition to the long-scale monoclinic structure, a structure at a more local-scale exists as proven by diffuse scattering in neutron experiments.

For PYN-PT with $x=0.40-0.60$, the cubic phase transforms into a tetragonal phase at the T_{Cr} temperature higher than the temperature of the maximum of the dielectric constant that itself turns into the room-temperature structure at T_m .

For all compositions in the range $0.35 \leq x \leq 0.60$, the room-temperature phase is best described by a coexistence of several phases among the monoclinic Cm and Pm phases and the tetragonal $P4mm$ one. Actually, no rhombohedral phases could be observed in the low-PT content side of the MPB making the PYN-PT solid solution uncommon among the Pb-based solid solutions.

In summary, for PYN-PT $x \leq 0.10$, the structure transforms from the high-temperature cubic phase to the low-temperature antipolar one at T_C with a possible change in the local structure of PYN-PT 0.10 at T_2^* . For PYN-PT $0.16 \leq x \leq 0.25$, the structure remains pseudo-cubic in the entire temperature range investigated with changes at a local scale that correlate well with the changes observed in the dielectric and hysteresis measurements as well as with T^* and T_B . For PYN-PT $0.30 \leq x \leq 0.60$, upon cooling, the high-temperature cubic phase transforms at T_5 or T_{Cr} first into a tetragonal structure (or at least into a pseudo-cubic phase with some tetragonal distortion for PYN-PT 0.30). This tetragonal structure transforms then into the low-temperature state at T_m for PYN-PT $0.30 \leq x \leq 0.50$ (such transition is not observed for PYN-PT 0.60 probably because of experimental limitations). The T_5 and T_{Cr} temperatures have been proposed to correspond to a pseudo-Burns temperature at which meso-domains form in a paraelectric matrix similar to the formation of polar nanodomains at T_B .

At room temperature, the structure is monoclinic with antiparallel displacements of Pb^{2+} and possibly of the B cations as well for PYN-PT with $x \leq 0.05$. Adding PT, the PYN-PT solid solution becomes rhombohedral for PYN-PT 0.10 and pseudo-cubic in the compositional range $0.16 \leq x \leq 0.25$. For compositions with larger amount of PT ($0.30 \leq x \leq 0.40$), the structure becomes monoclinic with possibly coexistence of the two monoclinic phases Pm and Cm . Adding even more titanium in the solid solution (PYN-PT $x=0.45-0.50$), a tetragonal phase appears in the structure in coexistence with at least one of the monoclinic phases. For the composition with the largest amount of PT considered in this work ($x=0.60$), the structure is a mixing of

the tetragonal $P4mm$ and the monoclinic Pm phases.

In addition to all these changes of structure with temperature and composition, extra complexity in the study of the structure of the PYN-PT solid solution lies in chemical ordering, positional disorder on the Pb^{2+} site and O-octahedra tilting present for some compositions.

Indeed, rock-salt chemical ordering on the B-site in the solid solution PYN-PT has been observed for $x \leq 0.35$. The degree of chemical ordering could not be determined using simple models (intensity ratios, page 114) or more advanced ones (composite model, 127) because of positional disorder of Pb^{2+} . Therefore, to determine the degree of chemical ordering in PYN-PT more advanced methodologies, for example using at least two sets of diffractograms using different radiations are necessary. Nonetheless, the Williamson-Hall analysis clearly established that chemical ordering happens on a long range.

Positional disorder of Pb^{2+} was observed for all compositions at high temperature and at room temperature in the compositional range $0.16 \leq x \leq 0.60$. At high temperature, the disorder is proposed to be due to the strong bonding between Pb and O. At room temperature, the Pb^{2+} disorder is an expression of the relaxor properties present in the compositional range $0.16 \leq x \leq 0.60$, at least at high temperature.

Finally, O-octahedra tilting is present in PYN-PT with $x = 0.30-0.40$. The tilt system has not been definitely determined: it could be $a^0b^0c^-$, $a^-a^-c^0$, or $a^-b^-c^0$. However, the possible tilt systems in PYN-PT differ from the ones observed in all other Pb-based ferroelectric perovskites.

In conclusion, the PYN-PT solid solution presents many different structures due to the large variety of its macroscopic properties: antiferroelectric, relaxor or ferroelectric. Moreover, chemical ordering, positional disorder of Pb^{2+} and O-octahedra tilting introduce additional complexity in the study of the structure of PYN-PT.

However, this first advanced study of the structure of PYN-PT has shown that the structure is more complex than what was reported in the literature (Ref.[40, 42] for PYN and Ref.[47, 52, 53] for the MPB) and in particular, that the understanding of the structure of the MPB cannot be simply done by analogy with other Pb-based complex perovskites.

- CHAPTER 4 -

STRUCTURE-PROPERTIES RELATIONSHIP

In the two latest chapters, $\text{Pb}(\text{Yb}_{1/2}\text{Nb}_{1/2})\text{O}_3\text{-PbTiO}_3$ (PYN-PT) was investigated using dielectric, piezoelectric and ferroelectric measurements (Chapter 2) and X-rays, neutron and electronic diffraction (Chapter 3).

Hereafter, the phase diagrams proposed from properties measurements (Fig.2.23, page 95), on the one hand, and structural investigations (Fig.3.28, page 169), on the other hand will be recalled first (Sec.4.1). Then the consistency of these two phase diagrams will be examined (Sec.4.2).

Finally, in Sec.4.3, I will present my understanding of the evolution of the properties and structures in the phase diagram and what are the mechanisms leading to the appearance of such complex phase diagram.

4.1 PHASE DIAGRAMS PROPOSED FROM PROPERTIES AND STRUCTURAL INVESTIGATIONS

The phase diagrams proposed after the study of the electric properties and of the structure are recalled in Fig.4.1. Some of the main features of these phases diagrams will be summarized hereafter.

4.1.1 Phase diagram proposed from properties measurements

In the chapter dedicated to the study of the electric properties, the compositions were separated based on the frequency dependence of the dielectric constant and based on the values of the maximum of the dielectric constant:

- Compositions without frequency dependence and low values of the dielectric constant were regarded as antiferroelectrics (AFE): $x \leq 0.05$
- Compositions with frequency dependence of the dielectric were studied as relaxors (RFE): $0.10 \leq x \leq 0.40$
- Compositions without frequency dependence and high values of the dielectric constant were categorized as ferroelectrics (FE): $x \geq 0.45$

The evolution of the maximum of the dielectric constant has also revealed the presence of a morphotropic phase boundary at $x \sim 0.45-0.50$ in agreement with previous works [19, 46].

The examination of the thermal evolution of the dielectric properties and the polarization-electric field and strain-electric field relationships have revealed that PYN-PT $x \leq 0.05$ undergoes a first order phase transition from the low-temperature AFE phase to the high-temperature paraelectric (PE) one without the appearance of an intermediate phase.

For relaxor compositions several changes of behavior were observed as a function of temperature at T_2 (modification of the dielectric behavior) and T_3 (variation in the high electric-field polarization and strain response).

Furthermore, within the relaxor compositions different behaviors were observed for $x = 0.10$, $x = 0.16-0.20$, $x = 0.25-0.30$ and $x = 0.35-0.40$. Indeed, the dielectric constant of PYN-PT 0.10 was found to follow the Curie-Weiss law above and below the temperature of the maximum of the dielectric constant T_m . PYN-PT 0.16 and PYN-PT 0.20 exhibit, right above T_m , a small temperature range where their dielectric constants follow the Curie-Weiss law. At higher temperatures, the dielectric constant follows a more relaxor-like behavior. Finally, the fitting of the thermal evolution of the dielectric constant with the model proposed by Bokov and Ye [22] has indicated two distinct behaviors for compositions with $x = 0.25-0.30$ and $x = 0.35-0.40$ due to strong difference in the values of the degree of diffuseness δ .

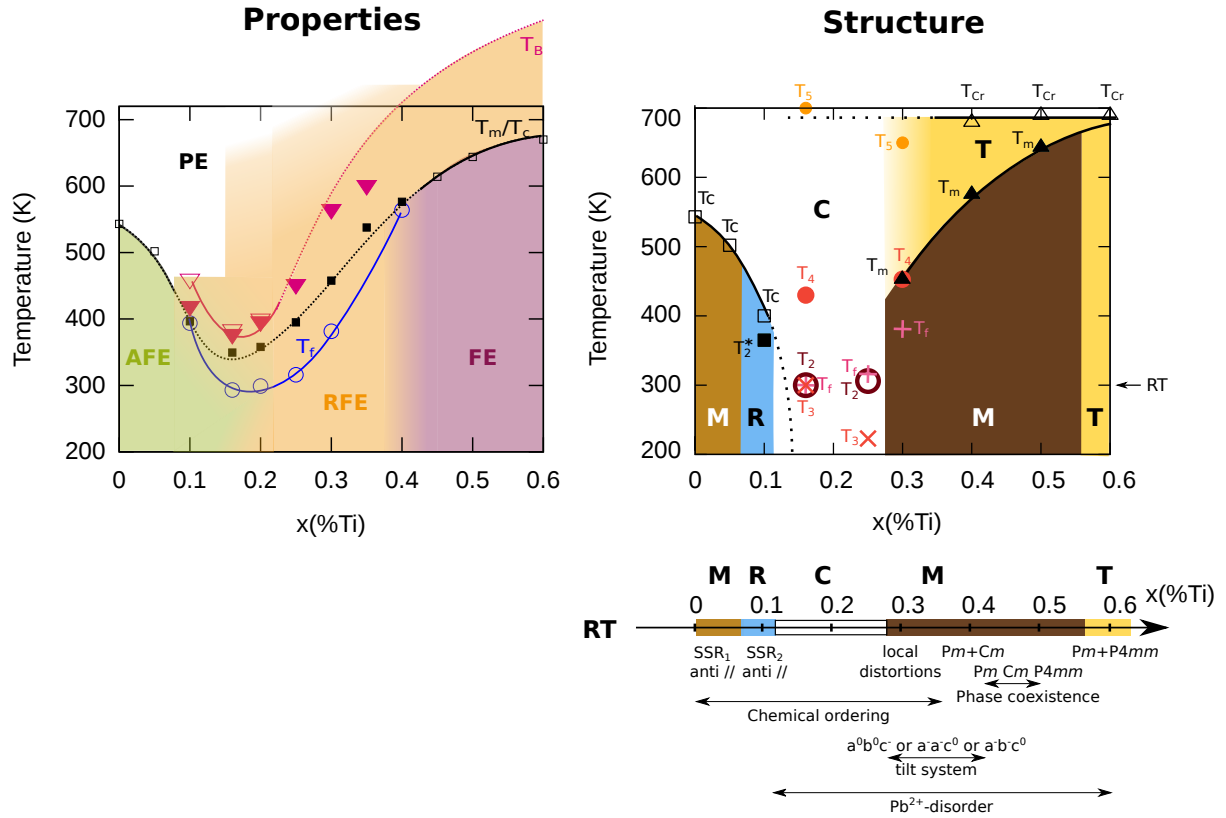


Figure 4.1: Phase diagrams produced from the study of (left) the properties (Fig.2.23) and (right) the structure (Fig.3.28).

(Properties) Green area refers to antiferroelectric (AFE) properties, yellow area refers to relaxor (RFE) properties and purple area refers to ferroelectric (FE) properties.

(Structure) M (monoclinic), R (rhombohedral), C (cubic) and T (tetragonal) refers to the average structure.

The different temperatures indicated on both diagrams are characteristic temperatures observed either during the study of the various properties (Chapter 2) or of the structure (Chapter 3).

For compositions showing FE properties ($0.45 \leq x \leq 0.60$), it was demonstrated that, upon heating, the FE phase transforms into a relaxor phase at the temperature of the maximum of the dielectric constant T_m . This relaxor state was found to possibly transform into a PE phase at about 700 K, but this transformation was not confirmed due to experimental limitations.

4.1.2 Phase diagram proposed from structural investigations

In the chapter devoted to the study of the structure, the compositions were separated depending on the macroscopic distortions of their structure and based on the presence of superstructure reflections (SSRs) due to antiparallel ordering in the diffractograms:

- Compositions with macroscopic distortions and antiparallel order: $x \leq 0.10$
- Compositions with no (or minute) macroscopic distortions: $0.16 \leq x \leq 0.30$
- Compositions with macroscopic distortions and without antiparallel order: $x \geq 0.35$

The study of the structure has revealed that the antipolar ordering is different in the case of PYN-PT $x \leq 0.05$ and PYN-PT 0.10. Moreover, the study of the evolution of the structure with temperature has revealed that the low-temperature structure of PYN-PT $x \leq 0.05$ transforms directly in the high-temperature cubic phase at the Curie temperature. On the other hand, PYN-PT 0.10 undergoes a change in its structure at the local scale at T_2^* before turning in the high-temperature cubic phase at T_m .

For PYN-PT $0.16 \leq x \leq 0.25$, the structure remains cubic down to the lowest investigated temperatures. This cubic phase has been evidenced to display positional disorder of the Pb^{2+} cation. Besides, variations of the structure at the local scale were observed at critical temperatures T_2 , T_3 and T_f evinced in Chapter 2 as well as at temperatures T_4 and T_5 that were proposed to correspond to T^* and the Burns temperature T_B , respectively.

PYN-PT 0.30 presents a monoclinic structure (with minute distortions) at room temperature that undergoes some changes at the local scale at T_f and transforms into a tetragonal phase at T_m that itself undergoes a transition toward the high-temperature cubic phase at T_5 .

The high-temperature cubic structure of the compositions showing distortions and no antipolar ordering ($0.35 \leq x \leq 0.60$), was demonstrated to transform into a tetragonal structure at the critical temperature T_{Cr} and in the low-temperature structure at T_m . At room temperature, the structure was shown to be best described by a coexistence of several phases, namely the monoclinic Cm and Pm and the tetragonal $P4mm$ phases (the ratio between the phases depending on the composition). The room-temperature structure was also demonstrated to present positional disorder of Pb^{2+} cations.

In addition, chemical order was observed for compositions up to $x = 0.35$ and O-octahedra tilts for $0.30 \leq x \leq 0.40$.

4.2 PUTTING IN PERSPECTIVE

In the previous sections, the main features of the phase diagrams developed from the electric properties measurements and the structural investigations were summarized. Hereafter, these two phase diagrams will be compared and, when necessary, the results that do not appear consistent will be discussed.

PYN-PT with $x \leq 0.05$

Both the study of the electrical properties and of the structure have concluded that PYN-PT with $x \leq 0.05$ undergoes, upon heating, a first-order phase transition from a low-temperature antiferroelectric antipolar state toward a high-temperature paraelectric cubic phase.

PYN-PT 0.10

In the chapter dedicated to the study of the electrical properties (Chapter 2), PYN-PT 0.10 was characterized as relaxor because of its frequency-dependence of the dielectric constant despite the fact that the dielectric constant follows the Curie-Weiss law above and below the phase transition. Hence, the dielectric behavior above and below the phase transition are consistent with the structural studies, i.e., at room temperature, an antipolar order (antiferroelectric) following the Curie-Weiss law and a high-temperature cubic paraelectric phase.

In the end, it is only close to the transition that the frequency-dependence of the dielectric constant indicating relaxor behavior is observed. In this temperature range, in addition to the change at the temperature of the maximum of the dielectric constant T_m , a change of the dielectric behavior has been observed at T_2 and a change in the structure at T_2^* , these two temperatures being one hundred degrees apart. The diffraction data are not sufficient to conclude regarding a possible change of the structure at T_2 . However, re-investigating the dielectric results, in particular the evolution with temperature of the derivative of the inverse of the dielectric constant ξ , a change at T_2^* may be noticed: the derivative of the inverse of the dielectric constant goes through a minimum at T_2^* . Below T_2^* , the dielectric constant start to follow the Curie-Weiss law, upon cooling making T_2^* the onset temperature for the antiferroelectric phase.

Finally, the simple picture of the thermal evolution of PYN-PT 0.10 would be that upon cooling, the paraelectric phase undergoes a phase transition toward an antiferroelectric phase, but that this transition does not occur simultaneously throughout the sample, but that different regions transform at different temperatures inducing the relaxation of the dielectric constant.

PYN-PT with $0.16 \leq x \leq 0.25$

Compositions in the range $0.16 \leq x \leq 0.25$ were proposed to be relaxors because their dielectric constant is strongly frequency-dependent. Relaxors usually present a pseudo-cubic structure with a different structure at a local scale. A cubic crystal system was proposed to best describe the long-range structure of these compositions, but no conclusion regarding the structure at the local scale could be drawn because of experimental limitations.

Furthermore, the thermal evolution of the dielectric constant and of the cell parameters have shown changes at the same temperatures. Regarding PYN-PT 0.16, the changes at T_4 observed

in the diffraction experiments were attributed to the critical temperature T^* , whereas this temperature was associated with the Burns temperature while analyzing the dielectric constant. These interpretations of the changes occurring at this temperature are thus different, but the existence of this critical temperature is undeniable.

In conclusion, the electric and structural characterizations are consistent with a relaxor behavior undergoing several changes with temperature. The type of changes taking place at various temperatures are not clarified yet and some propositions regarding them will be made in Sec.4.3.2, but the critical temperatures of these changes are unambiguously established.

PYN-PT with $0.30 \leq x \leq 0.40$

As mentioned above, relaxors are usually described with a pseudo-cubic structure, however it was shown in archetypal relaxor-PT solid solutions such as $\text{Pb}(\text{Mg}_{1/3}\text{Nb}_{1/3})\text{O}_3\text{-PbTiO}_3$ (PMN-PT) or $\text{Pb}(\text{Zn}_{1/3}\text{Nb}_{1/3})\text{O}_3\text{-PbTiO}_3$ (PZN-PT) that long-range distortions appear and increase on the relaxor side when increasing the PT content [14, 101].

Hence, PYN-PT with $x = 0.30\text{-}0.40$, presenting distortions from the cubic phase at room temperature and dielectric relaxation, belongs to the class of relaxors whose structure tends toward the one of classical ferroelectrics.

For PYN-PT 0.30, the structural studies have not confirmed the critical temperature T_2 observed in the dielectric and hysteresis measurements due to experimental limitations raising the question of the existence of T_2 . However, the temperature T_2 is close to the temperature of the maximum of the piezoelectric coefficient d_{33} (that will be evidenced in Chapter 5 to be electric-field induced), supporting the idea that changes may occur at T_2 . Nonetheless, since this critical temperature is not firmly established, it will not be discussed hereafter.

The structural investigations have however confirmed a change of behavior in PYN-PT 0.30 at the freezing temperature T_f determined using a Vogel-Fulcher analysis confirming the strong relationship between structure and properties and the relaxor behavior of this composition.

For PYN-PT 0.35 and PYN-PT 0.40, the changes in the dielectric behavior at T_2 was associated with the freezing of the PNRs. Because of the limited number of temperatures investigated, no changes in the evolution of the cell parameters with temperature could be observed at $T_2 = T_f$. Finally, tetragonal distortions were shown to appear upon cooling at a critical temperature T_5 or T_{Cr} , the re-investigation of the evolution of the dielectric constant with temperature and in particular of the evolution of the derivative of the inverse of the dielectric constant ξ , shows that the dielectric constant follows the Curie-Weiss law above T_5 or T_{Cr} . These tetragonal distortions convert into the low-temperature monoclinic structure at T_m .

In summary, in the compositional range $0.30 \leq x \leq 0.40$, PYN-PT goes from a cubic paraelectric phase to a tetragonally-distorted one below T_5 or T_{Cr} , finally resulting in a monoclinic phase under T_m . These distortions are, as expected, increasing with the addition of PT.

PYN-PT with $0.45 \leq x \leq 0.60$

From the dielectric and hysteresis experiments, PYN-PT was concluded to be ferroelectric at room temperature in the compositional range $0.45 \leq x \leq 0.60$. Ferroelectric behavior at room temperature is supported by the strong distortions from the cubic phase observed in X-ray diffraction experiments.

This ferroelectric phase transforms in a relaxor phase at T_m as was evidenced by the frequency-

dependence of the dielectric constant. This relaxor phase presents tetragonal distortions that induce the persistence of piezoelectric response above T_m (that will be demonstrated in Chapter 5).

At higher temperature, this relaxor phase transforms into a cubic paraelectric phase at T_{Cr} . This transition can be clearly evidenced in the temperature-dependent structural investigations and can be inferred from the dielectric measurements.

Therefore, upon cooling, PYN-PT with $x = 0.45-0.60$ transforms from its high-temperature paraelectric cubic phase in a relaxor phase presenting tetragonal distortions at T_{Cr} that itself transforms into the low-temperature ferroelectric state at T_m .

Summary and Conclusion

PYN-PT with $x \leq 0.05$ undergoes, upon cooling, a first-order phase transition from the high-temperature cubic paraelectric state to the low-temperature antiferroelectric state at the Curie temperature T_C . When adding titanium (PYN-PT 0.10), this first-order phase transition between the antiferroelectric and paraelectric phases becomes relaxor-like with a frequency-dependence of the dielectric constant.

For larger amount of PT ($0.16 \leq x \leq 0.60$), upon cooling from the high-temperature cubic phase, regions with local correlated dipoles appear at the pseudo-Burns temperature T_5 or T_{Cr} . The size of the regions of correlated dipoles increases from nanoscopic (equivalent to PNRs) for PYN-PT 0.16, to mesoscopic for PYN-PT 0.60.

At lower temperatures, this relaxor phase either persists down to the lowest studied temperatures ($x \leq 0.25$) with some changes at the local scale or this relaxor phase transforms in a distorted state at T_m ($x \geq 0.30$). This distorted state being relaxor or ferroelectric depending on the amount of Ti in the solid solution.

In this section, the polar order determined in Chapter 2 based on electric characterization and the structure described in Chapter 3 were compared. The polar order and the associated structures are in good agreement in the compositional range investigated $x \leq 0.60$. Furthermore, the critical temperatures where changes over the polar order and structures concur and are largely understood.

4.3 UNDERSTANDING OF THE PHASE DIAGRAM OF PYN PT

In the previous section, the two phase diagrams proposed based on the study of the electric properties and of the structure were compared. The good agreement between these two phase diagrams have enabled the description of a unified vision of the evolution of the polar order and structure with temperature and composition in the solid solution.

Hereafter, I will propose a model explaining how the polar order and structure evolve with the addition of Ti: in the PT-poor region of the phase diagram, the structure of each unit cell of PYN-PT is monoclinic and the various polar orders and macroscopic structures are the result of different organizations of the Pb^{2+} cations displacements at a local scale. These different organizations are themselves strongly influenced by the chemical nature and the cationic arrangement

of the cations on the B site.

This model relies on several hypotheses:

- Pb^{2+} is always displaced from its prototypic position
- An antiparallel organization of the Pb^{2+} displacements is more energetically favorable if there is rock-salt order on the B site
- A parallel organization of the Pb^{2+} displacements is more energetically favorable if only titanium is present on the B site

The assumption that Pb^{2+} is never in its prototypic position is supported by the high-temperature study of the positional disorder of the Pb^{2+} cation (Sec.3.3.4). This study has shown that the Pb^{2+} cations are never (in PYN-PT solid solution and in other Pb-based solid solutions) in their prototypic position because of the strength of the Pb-O bond. At room temperature, in the two end-members of the solid solution (PYN and PT), Pb^{2+} cations are also not in their prototypic position and it seems reasonable to assume that it is also the case for compositions in between the two end-members.

The fact that the antiparallel organization of the Pb^{2+} displacements would be more energetically favorable with the presence of rock-salt chemical order is based on the literature survey conducted in Sec.1.2.2 regarding double perovskites: all known chemically ordered double perovskites display antiferroelectricity (except $\text{Pb}(\text{Sc}_{1/2}\text{Nb}_{1/2})\text{O}_3$).

The parallel organization of the Pb^{2+} displacements related to the presence of Ti is simply a reformulation of the fact that the perovskite PbTiO_3 is a ferroelectric (and a highly stable one, since it displays a high Curie temperature).

Therefore, the two extreme cases correspond to the respective situations where regions in the sample present a degree of chemical order on the B site large enough to induce antiparallel displacements and where regions present an amount of Ti large enough to induce parallel displacements, both in a monoclinic unit cell.

Actually, Ti may induce *parallel* organization of the Pb^{2+} displacements in a monoclinic unit cell, and larger amounts may even induce tetragonal distortions of the perovskite unit cell. Indeed, in PbTiO_3 , the strongly distorted tetragonal macroscopic structure is the result of the local tetragonal distortions of the perovskite unit cell and the long-range parallel correlation of Pb^{2+} displacements. Hence, in the PYN-PT solid solution, further away from PT, Pb^{2+} displacements may be organized in parallel in either a monoclinic or a tetragonal local unit cell.

However, there are regions (in particular in the compositional range $0.10 \leq x \leq 0.60$) that present neither a degree of chemical ordering sufficient to induce the antiparallel organization of the Pb^{2+} displacements, nor a quantity of Ti sufficient to induce the parallel organization. Thus, in these regions, the displacements of Pb^{2+} are frustrated between these two organizations. This frustration leads to changes in the displacements of Pb^{2+} that lose their organization and eventually their directionality, i.e. the Pb^{2+} displacements become random and eventually isotropic.

Indeed, the high-temperature study of the positional disorder of Pb^{2+} has demonstrated in Sec.3.3.4 that chemical disorder on the B site leads to isotropic displacements of Pb^{2+} . In

addition, the literature survey of double perovskites (Sec.1.2.2) has demonstrated that when disordered these double perovskites (including PYN) display a relaxor behavior. This relaxor behavior is usually associated with isotropic displacements of Pb^{2+} that correlate locally (in the PNRs). Therefore, in the regions in which neither an antiparallel nor a parallel organization of the Pb^{2+} displacements can be achieved, the displacements of Pb^{2+} become isotropic retaining the possibility of local correlations.

Nevertheless, it is also possible that the amount of Ti is not sufficient to induce such frustration leading to isotropic displacements. Indeed, if the amount of Ti is limited, its presence may only prevent the antiparallel organization of the Pb^{2+} displacements, but not the directionality of the displacements, i.e. Pb^{2+} will still be displaced along the $\langle 110 \rangle_{pc}$ direction, but the displacements will not be correlated (hence random and not isotropic).

Despite being preferentially organized in parallel (Pb^{2+} being ferroelectrically active), a different organization of the Pb^{2+} displacements may be energetically favorable depending on the chemical nature and arrangement on the B site. For example, in PYN, the high degree of chemical order on the B site leads to the frustration of the Pb^{2+} displacements into an antiparallel organization.

Therefore, depending on the local chemical arrangement of the B site (degree of chemical ordering along the $[111]_{pc}$) and on the nature of the elements on the B site (amount of Ti), five types of Pb^{2+} organizations can be recognized

- antiparallel organization of the Pb^{2+} displacements along the $[110]_{pc}$ direction: $\text{Pb}_{anti//}$
- no correlation between the Pb^{2+} cations that are displaced along the $[110]_{pc}$ displacements: Pb_{dir}
- the Pb^{2+} cations that are isotropically displaced with possibly local correlations: Pb_{iso}
- parallel organization of the Pb^{2+} displacements along the $[110]_{pc}$ monoclinic direction: $\text{Pb}_{//m}$
- parallel organization of the Pb^{2+} displacements along the $[001]_{pc}$ tetragonal direction: $\text{Pb}_{//t}$

The different organizations of the Pb^{2+} displacements have been related to differences in the chemical arrangement and nature of the B site. However, the chemical arrangement and nature of the B site at a very local scale (several unit cells) may be (slightly) different from the long-range one.

For example, in a sample presenting long-range chemical ordering (inducing thin superstructure reflections in diffraction pattern), regions with higher or lower degrees of local chemical ordering can be observed, as well as regions with more or less Ti (top of Fig.4.2). Similarly, in a sample exhibiting no chemical ordering on the long range (no superstructure reflections due to chemical order), regions with local chemical order can be observed as well as regions with larger amount of Ti (bottom of Fig.4.2).

Thus, inside one sample that appears homogeneous on the long range, at the local scale, the chemical arrangement and nature on the B site may be different from the long range one, leading

to the appearance of regions with higher or lower degree of chemical order, as well as regions with different amount of Ti. These differences in the local B-site environment induce different Pb^{2+} organizations, at the local scale, inside an homogeneous sample.

Finally, the macroscopic polar orders and structures determined in Chapter 2 and Chapter 3 will be an expression of the coexistence of regions with different organizations of Pb^{2+} displacements. These organizations being defined by the local chemical environment of the B site. This model explaining the different macroscopic polar orders by different organization of the Pb^{2+} cation at the local scale is an extension of the model proposed by Zhang et al. [97] in which the different macroscopic structural phases in the morphotropic phase boundary of $\text{Pb}(\text{Zr,Ti})\text{O}_3$ are due to different arrangement of the Pb^{2+} displacements in the local monoclinic unit cell. I “simply” add to this model that the various arrangements of the Pb^{2+} displacements are linked to the nature and arrangement on the B site.

Furthermore, the model presented here to account for the various polar orders in the PYN-PT solid solution differs from the model commonly accepted for relaxor in which polar nanoregions are spread into a paraelectric matrix in the sense that, in my model, there are not only (nano)regions with ferroelectric (parallel) organization, but also regions with antipolar organization. Another difference between the model proposed here and the one of classical relaxors is that, in the case of PYN-PT, the unit cell presents monoclinic distortions and that it is the arrangement of the Pb^{2+} displacements that induces the macroscopic cubic structure in the compositional range $0.16 \leq x \leq 0.25$, whereas in the case of classical relaxors it is the polarization of the PNRs that induce local distortions from the cubic structure. Finally, here I suggested that it is the B-site chemical nature and arrangement that influence the organization of the Pb^{2+} displacements, but the mechanism by which the B site influences the Pb^{2+} organization is not specified: it could be random field, random bond or a combination of the two (as in the Spherical Random Bond Random Field model introduced in Sec.1.1.4).

In the following, the evolution of the room-temperature macroscopic structure and polar order will be examined in the light of local variations of the nature and order on the B site inducing local changes in the organization of the Pb^{2+} displacements. Then, the evolution of the macroscopic polar order and structure with temperature will be discussed in terms of Pb^{2+} organization on the local scale.

4.3.1 Evolution of the structure at room temperature

PYN with $x \leq 0.05$

In PYN, the Yb^{3+} and Nb^{5+} cations are ordered in a rock-salt arrangement on the long range. Therefore, on the local scale all regions are highly chemically ordered. Hence all regions present a $\text{Pb}_{\text{anti}}//$ organization. Since all regions present the same $\text{Pb}_{\text{anti}}//$ organization, the macroscopic structure also present $\text{Pb}_{\text{anti}}//$ organization (the antipolar order described in Sec.3.4.1). This long-range correlation of the Pb^{2+} displacements also induces the appearance of the macroscopic

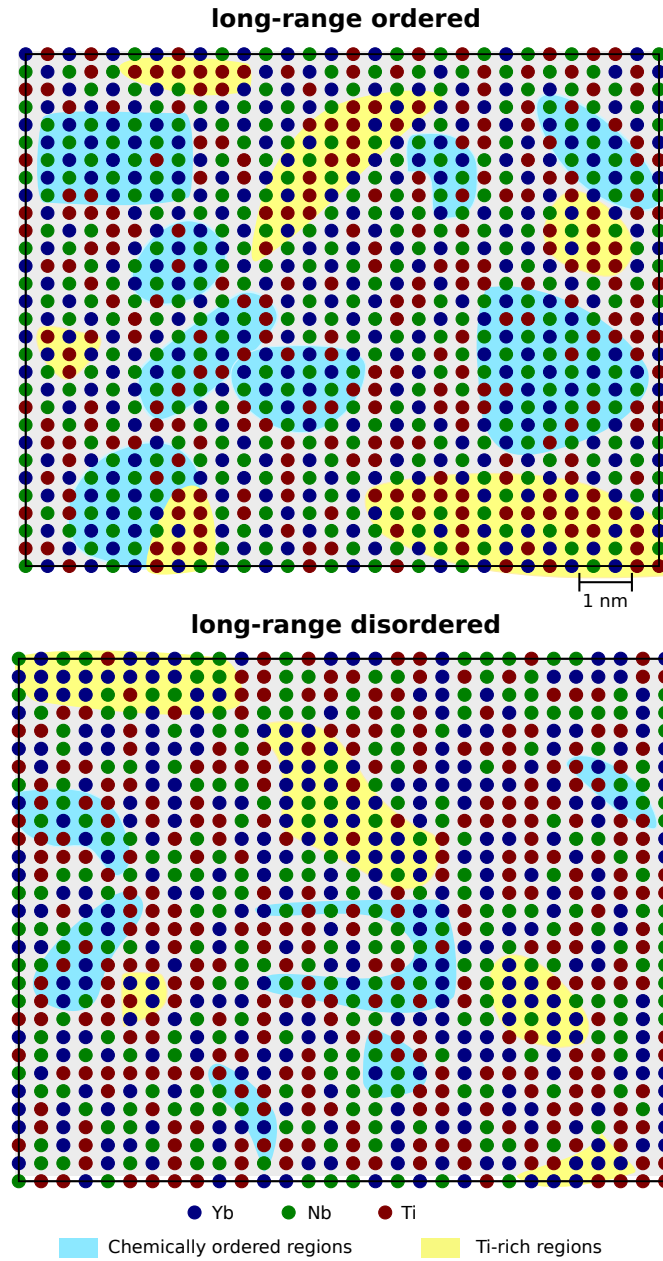


Figure 4.2: Spatial distribution of the B cations in the case of a perfectly ordered double perovskite substituted with Ti (top) and of a completely disordered (simple) perovskite in a $(001)_{pc}$ plane. the chemical order induces alternating lines of Yb and Nb along $[110]$.

In both cases, spatial regions, with high chemical order can be observed (highlighted in blue) as well as Ti-rich regions (in yellow)

The distribution were computer generated (using a python program developed by Charles Paillard in the SPMS laboratory). In the "long-range ordered" case, the Yb and Nb atoms are distributed in perfect rock-salt arrangement and replaced randomly by Ti atoms. This distribution would lead to superstructure reflections due to chemical order in the diffraction patterns. In the "long-range disordered" case, the Yb, Nb and Ti are completely randomly distributed. No superstructure due to chemical order will appear in the diffraction pattern.

monoclinic distortions of the average structure (the pseudo-cubic $Z = 1$ unit cell) of PYN. In PYN-PT 0.05, some titanium is present in the structure, but does not disrupt significantly the long-range chemical order. At the unit cell scale, the number or size of regions presenting a lower degree of chemical order increases, but the degree of chemical order remains high enough to favor the $Pb_{anti//}$ organization. Hence this composition presents the same monoclinic structure and antipolar order as PYN. Nevertheless, the perturbation of the chemical order with Ti leads to the lower stability of the antipolar order of PYN-PT 0.05 compared to PYN expressed by the lower Curie temperature.

PYN-PT 0.10

For PYN-PT 0.10, the quantity of titanium is sufficient to perturb significantly the chemical order on the B site reducing the number or size of the highly chemically ordered regions (similar to the ones of PYN). This reduction of the size and number of the highly chemically ordered regions leads to the breaking of the long-range antiparallel arrangement of the Pb^{2+} cations displacements. However, the amount of titanium is limited and small regions with high degrees of chemical order persist and some antiparallel correlation of the displacements of Pb^{2+} may still persist, inducing the wide superstructure reflections observed in the X-ray diffractograms. Furthermore, at high temperature, it was shown in Sec.3.3.4 that the disorder introduced by the addition of Ti on the B site in PYN-PT 0.10 is not sufficient to lead to isotropic displacements of Pb^{2+} as it is the case for compositions with larger amount of PT. In the case of PYN-PT 0.10, the displacements in the $\langle 110 \rangle_{pc}$ directions are still more energetically favorable even considering the disorder on the B site. Therefore, at room temperature, the regions with lower degree of chemical ordering present a Pb_{dir} organization. Therefore, the displacements of Pb^{2+} are not correlated on the long range, but because of their directionality (along the $\langle 110 \rangle_{pc}$ directions) the average structure appears rhombohedral (same phenomenon as at the MPB of PZT, but with different origins of the displacements of Pb^{2+}).

PYN-PT $0.16 \leq x \leq 0.25$

For PYN-PT in the range $0.16 \leq x \leq 0.25$, the disruption of the chemical order on the B site by Ti is large creating local regions that are chemically mainly ordered and others that are chemically mostly disordered (or local regions that have higher degree of chemical order on the B site than others).

It is worth noting that the compositions in which the local regions are referred to as "chemically ordered" and "disordered" present nevertheless on the long range chemical ordering (as evidenced by the thin superstructure reflections related to chemical order in Sec.3.3.2) and that it is the degree of local ordering that changes.

In the chemically mostly disordered regions, the Pb^{2+} displacements are isotropic (Pb_{iso}) as was shown to happen in chemically disordered perovskite at high temperature (Sec.3.3.4). Whereas, in the chemically mainly ordered regions, the Pb^{2+} displacements are anisotropic and favorably along the $\langle 110 \rangle_{pc}$ directions (Pb_{dir}).

So far, only the disrupting effect of Ti on the chemical order on the B site was considered, but

since rather large amount of Ti is added, its chemical nature favoring the parallel organization of the Pb^{2+} displacements can no longer be neglected. Thus, in the chemically mainly ordered regions, if the amount of Ti is limited the $\text{Pb}_{anti//}$ may be established. But in the regions that are chemically mainly ordered but with a rather large amount of Ti, a frustration of the antiparallel organization (favored by the chemical order) and the parallel organization (favored by Ti) appears. This frustration may lead to isotropic displacements of Pb^{2+} or to random displacements along the $\langle 110 \rangle_{pc}$ directions.

Similarly, in the regions that present a lower degree of chemical order (the mostly disordered regions), if there is a limited amount of Ti, the displacements of Pb^{2+} are isotropic, whereas if the amount of Ti is large enough, a parallel organization of the Pb^{2+} displacements may arise. Hence, in the compositional range $0.16 \leq x \leq 0.25$, it is, at the same time, the degree of chemical order and the amount of Ti in the different regions that initiate the coexistence of regions with various organizations and directionalities of the Pb^{2+} displacements: $\text{Pb}_{anti//}$, Pb_{dir} , Pb_{iso} and $\text{Pb}_{//m}$.

In Chapter 2, because of difference in the thermal evolution of the dielectric constant with temperature, several types of relaxors were proposed to exist in the PYN-PT solid solution.

The unusual evolution of the dielectric constant with temperature of PYN-PT with $x = 0.16-0.20$ was attributed to the influence of antiferroelectricity based on the macroscopic characterization. Based on the above observations, these compositions would have a behavior dominated by $\text{Pb}_{anti//}$ and Pb_{dir} organizations. Since no SSRs due to antiparallel order were observed for these compositions, it is probable that regions with Pb_{dir} organization are more abundant or bigger compared to the ones with $\text{Pb}_{anti//}$ organization.

Furthermore, PYN-PT with $x = 0.25-0.30$ and PYN-PT with $x = 0.35-0.40$ were shown to have highly different values of degree of diffuseness δ . This difference was attributed to the presence of two types of PNRs, in the compositional range $0.25 \leq x \leq 0.30$, due to the chemical order on the B site. Anticipating on the next section, these two types of PNRs would correspond to regions with Pb_{iso} organization with correlated displacements and to regions with $\text{Pb}_{//m}$ organization.

Regions with Pb_{iso} organization will appear cubic on the "long range", regions with Pb_{dir} will appear rhombohedral and the regions with parallel organization of the Pb^{2+} displacements will appear monoclinic (since the amount of Ti remains limited). However, these structures would only appear within the corresponding region (limited in size) and in average all these structures would lead to the macroscopic cubic phase observed.

Therefore, in the compositional range $0.16 \leq x \leq 0.25$, the coexistence of regions with different degrees of chemical order and amount of Ti would lead to different directions of Pb^{2+} displacements and different correlations leading to an average cubic structure with local distortions and therefore local polar order.

PYN-PT with $0.30 \leq x \leq 0.60$

For PYN-PT $0.30 \leq x \leq 0.60$, there are no longer regions with high degree of chemical order on the B site and low amount of Ti (the ones similar to PYN). However, there are still regions that are locally more chemically ordered than others.

In the regions presenting the highest degree of chemical order, the displacements of Pb^{2+} are frustrated between the antiparallel organization (required by the chemical order) and parallel organization (required by the presence of Ti) since the amount of Ti is no longer negligible. Therefore the displacements of Pb^{2+} are isotropic (Pb_{iso}). In the regions having lower degree of chemical order, the frustration is lower and a parallel organization of the displacements favored by Ti may arise.

It is interesting to note that, for $0.16 \leq x \leq 0.25$, the Ti-rich regions exhibit a lower degree of chemical order than the rest of the sample. On the contrary, for $0.30 \leq x \leq 0.650$, the Ti-poor regions exhibit a higher degree of chemical order than the rest of the sample. Indeed, the degree of chemical ordering on the B site is not evaluated strictly speaking, but it is the effect of the increase or decrease of the chemical ordering on the organization preferably chosen by the Pb^{2+} cation that is discussed.

The regions displaying isotropic displacements will appear cubic on the long range and the regions displaying parallel correlation will appear macroscopically monoclinic.

The macroscopic structure that has been investigated using Rietveld refinement (or profile matching analysis) is an image of the coexistence of the cubic and monoclinic regions. Hence, the more regions with $\text{Pb}_{//m}$, the more the macroscopic structure will appear monoclinic on the long range. In other words, when the amount of Ti increases above $x = 0.30$, the monoclinic distortions of the perovskite cell arises.

When the Ti content increases even more, tetragonal distortion of the perovskite cell may appear. Indeed, it is energetically favorable in the environment of Ti to have tetragonal distortions since PbTiO_3 present a strongly distorted tetragonal structure. Thus, the local $\text{Pb}_{//t}$ organization will favor the appearance of a tetragonal macroscopic symmetry. And the more Ti is introduced in the solid solution, the larger the regions exhibiting tetragonal distortions and the higher the amount of macroscopic tetragonal phase.

In conclusion, in the compositional range $0.30 \leq x \leq 0.60$, regions that are more chemically ordered present isotropic displacements of Pb^{2+} , the regions that are less chemically ordered present a parallel organization of the Pb^{2+} displacements that may be tetragonally distorted depending on the amount of Ti.

Summary

In this section, the structure and polar order at room temperature of all compositions investigated in this work were explained in terms of Pb^{2+} displacements induced by different chemical natures and organizations on the B site.

For PYN with $x \leq 0.05$, the Pb^{2+} are displaced in antiparallel on the long range leading to the observed monoclinic average structure.

When larger amount of Ti is added, the chemical order is disrupted and the $\text{Pb}_{anti//}$ organization can no longer be established on the long range, but this antiparallel organization may remain on a local scale. Furthermore, the perturbation of the chemical order on the B site with addition of Ti leads to the appearance of regions with lower degree of chemical order. These chemically "disordered" regions favor Pb_{dir} and Pb_{iso} organizations.

Finally, the addition of Ti does not only break the chemical ordering on the B site but it also promotes the parallel correlation of the Pb^{2+} displacements.

It is important to note that in one composition in the PYN-PT solid solution, it is possible to have regions with several organizations of Pb^{2+} displacements. The number and size of each of these regions will depend on the chemical nature and organization of the cations on the neighboring environment.

A schematic representation of the influence of the composition on the number and size of these regions are presented in Fig.4.3. The question of which displacements patterns phases coexist exactly for a given composition remains open, but the Pb^{2+} -displacements organization predominantly present is rather well understood.

In conclusion, the room-temperature structure and polar order in the PYN-PT solid solution with $x \leq 0.60$ were explained by the coexistence of different type of local-scale organization of Pb^{2+} displacements induced by its B site environment and in particular the chemical nature and the rock-salt arrangement.

In the next section, the same reasoning as was developed here for the investigation of the room-temperature structure and polar order will be held in order to explain their thermal evolution.

4.3.2 Thermal evolution of the structure and properties

PYN with $x \leq 0.05$

For PYN-PT with $x \leq 0.05$, the room-temperature antiferroelectric structure undergoes a first order phase transition toward the high-temperature cubic phase. In this cubic phase positional disorder of the Pb^{2+} cation exists as was evidenced in Sec.3.3.4.

Hence at the Curie temperature, the $\text{Pb}_{anti//}$ organization present at room temperature is broken and the structure becomes cubic. This change of the organization of the Pb^{2+} cations and of the entire structure is related to thermal instabilities driving the perovskite structure into its highest symmetry phase: the cubic phase.

The lower value of the Curie temperature of PYN-PT 0.05 compared to the one of PYN indicates

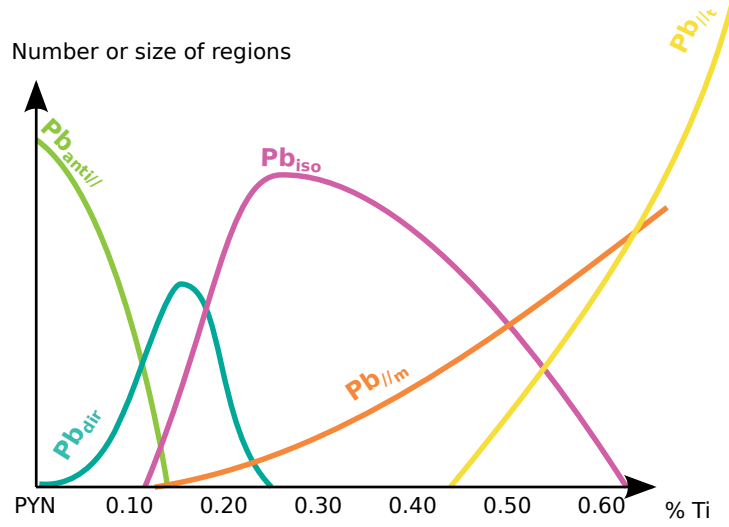


Figure 4.3: Schematic representation of the number or size of regions presenting antiparallel displacements of Pb^{2+} ($\text{Pb}_{\text{anti//}}$), random displacements with the $\langle 110 \rangle_{pc}$ directions favored (Pb_{dir}), parallel displacements of Pb^{2+} along the $[110]_{pc}$ ($\text{Pb}_{//m}$) and $[100]_{pc}$ directions ($\text{Pb}_{//t}$) and isotropic displacements of Pb^{2+} (Pb_{iso}). The compositions and the respective amounts of Pb^{2+} -displacements organizations are only indicative.

that the antiferroelectric state of PYN-PT 0.05 is less stable than the one of PYN. This lower stability of the antiferroelectric phase of PYN-PT 0.05 was ascribed to the chemical disorder introduced on the B site by the addition of Ti.

Thus, in this compositional range, the amount of Ti added is sufficient to destabilize the antiferroelectric structure, but not to alter it.

PYN-PT with $0.10 \leq x \leq 0.25$

In the compositional range $0.10 \leq x \leq 0.25$, it was proposed that, at room temperature, regions with different degree of chemical ordering coexist, as well as Ti-poor and Ti-rich regions. This coexistence of different B-site environment leads to the coexistence of $\text{Pb}_{\text{anti//}}$, Pb_{dir} , Pb_{iso} and $\text{Pb}_{//m}$.

These regions of different Pb^{2+} organization were considered, up to now, to be related to different B-site environments, but they are also influenced by temperature as all (macroscopic) polar orders are.

Hence, with temperature, the organization of the Pb^{2+} displacements inside one region could change. I also suggest that in addition to this reorganization of the displacements of Pb^{2+} inside one region, there are changes related to the interaction between regions. These changes of interaction can happen between regions having the same organization (e.g. freezing of the PNRs in a classical relaxor) or between regions having different organization (e.g. growth of regions

with one Pb^{2+} organization at the expense of regions having a different organization).

These reorganization of the Pb^{2+} displacements inside one region or due to the interaction between different regions leads to changes in the global polar state of the material probed by dielectric and hysteresis measurements, as well as to changes in the global structure observed in diffraction experiments.

A scenario for the reorganization of the Pb^{2+} displacements at the different critical temperatures (T_f , T_2 , T_3 , T_4 and T_5) is detailed hereafter.

I propose that some correlations between the Pb^{2+} displacements appear at T_5 (~ 690 K) that would correspond to the appearance of PNRs at the Burns temperature in the case of classical relaxors. In PYN-PT as in the case of the classical relaxors, the correlation between the Pb^{2+} displacements are highly local and time dependent. The particularity of the (nano)regions of PYN-PT would be that there may be regions with parallel correlation (these regions would be the equivalent to the PNRs), but also regions with antiparallel organization of the Pb^{2+} displacements. The amount of parallel or antiparallel regions, in PYN-PT, depends on the B site environment (chemical order or presence of Ti) and therefore on the composition (as it was shown at room temperature).

These regions of correlated displacements would start to interact at the temperature T_4 (that would correspond to the T^* observed in the classical relaxors). This interaction would lead to the appearance of a Curie-Weiss dependence of the dielectric constant and all regions would interact below T_2 (at T_2^* when observed).

This interaction between regions that lead to the Curie-Weiss dependence of the dielectric constant is probably related to the regions with $\text{Pb}_{anti//}$ organization since this behavior was not reported in classical relaxors (even though it may be inferred from Fig.7 of Ref.[102] for PMN). Moreover, the Curie-Weiss behavior is less pronounced at low temperature (below T_2) for compositions with larger amount of Ti that would indicate that the correlation would be disrupted by the addition of Ti and therefore would be more related to the antipolar correlation.

The freezing temperature T_f corresponds to the temperature below which the PNRs are static, in the case of classical relaxors. In the case of PYN-PT, the freezing temperature was determined using the same Vogel-Fulcher equation (Sec.2.2.2) as for classical relaxors. However, the question of the meaning of the Vogel-Fulcher relation in the case of PYN-PT in which several types of regions with local correlation arises: is the freezing temperature the temperature at which all regions with local correlations freeze or only the regions with parallel organization (i.e. the ones similar to the PNRs)? My opinion is that all regions freeze at the freezing temperature, since the freezing temperature is related to the mobility of the Pb^{2+} cations and the mobility should not be strongly influenced by the local structure, but rather by the long range one.

At T_3 , I suggest that the $\text{Pb}_{anti//}$ organization transforms into a Pb_{dir} organization or Pb_{iso} . Indeed I have proposed that Pb^{2+} must be displaced in order to favor the Pb-O bond and that the organization of the displacements is related to the B-site environment. However, Pb^{2+} is also a ferroelectrically active cation and the antiparallel organization of its displacements is

energetically unfavorable. Above T_3 , the $\text{Pb}_{anti//}$ regions are stable because of the dominating influence of the B site on the organization of the Pb^{2+} displacements, but upon cooling the influence of the ferroelectricity of the Pb^{2+} cations becomes comparable to the one of the B site and there is a change in the organization of the displacements. The reorganization of the displacements of the Pb^{2+} is probably not parallel since a parallel arrangement is unfavorable for the B-site environment and that the amount of Ti remains limited.

Hence at T_3 , the competition between the $\text{Pb}_{//m}$ organization energetically favorable for the Pb^{2+} and the $\text{Pb}_{anti//}$ organization favorable for the B site leads to a reorganization of the displacements of the Pb^{2+} in a frustrated way (Pb_{dir} or Pb_{iso}) in order to limit the global energy of the system.

Furthermore, T_3 decreases with the addition of Ti indicating that the stability of the state above T_3 increases with the addition of Ti. This larger stability induced by the addition of Ti is due to the decrease of the number or size of the antiparallel regions. Indeed, the frustration between the Pb_{dir} or Pb_{iso} organizations and the $\text{Pb}_{//m}$ one is lower than between the regions with $\text{Pb}_{anti//}$ and the $\text{Pb}_{//m}$ one. Therefore the driving force of the reorganization occurring at T_3 is lower when the number and size of $\text{Pb}_{anti//}$ (highly frustrated) regions decrease (i.e. when Ti is added).

A ferroelectric response can be obtained from this reorganized isotropic regions under the application of an electric field. Indeed, dipole moments created by the displacements of Pb^{2+} tend to align with the direction of the application of an electric field since Pb^{2+} is ferroelectrically active. This ferroelectric response induced by the applied electric field leads to the ferroelectric polarization-electric field and strain-electric field hysteresis cycles observed below T_3 . Polarization-electric field hysteresis cycle are less "square" (i.e. the ratio of the remnant polarization to the saturation polarization decreases from 1) when Ti is added. This lowering of the squareness of the hysteresis cycles is probably related to the directionality of the displacements.

Indeed, at low Ti-content, the frustrated organization of the displacements of Pb^{2+} is probably Pb_{dir} since the degree of chemical order on the B site remains relatively high. When Ti is added, the chemical order on the B site decreases and the displacements become isotropic.

The isotropic displacements can be easily aligned with the electric field: there are no potential barriers to overcome to reorient the direction of the Pb^{2+} displacements but isotropic displacements are unstable as soon as the electric field is removed (also because of the absence of potential barrier preventing the rotation of the displacements). In the case of displacements along the $\langle 110 \rangle_{pc}$ direction, more energy must be provided to the system to switch the direction of the displacements, but once the switching is done, the displacements are again stable and thus when the electric field is removed, the displacements do not switch back into their original directions (at least not instantaneously).

Therefore, in the case of the PYN-PT solid solution, below T_3 , highly directional displacements (Pb_{dir} organization) are observed in PYN-PT 0.10 and PYN-PT 0.16 leading to large values of coercive field ($\sim 15\text{-}20\text{ kV/cm}$) and square hysteresis cycles. Isotropic displacements (Pb_{iso}) are observed for PYN-PT 0.20 and PYN-PT 0.25 leading to low values of coercive fields ($\sim 5\text{-}10\text{ kV/cm}$) and slanted hysteresis cycles.

Hence, it is the applied electric field that leads to the reorientation of the Pb^{2+} displacements and

therefore to the appearance of the macroscopic hysteresis cycles observed below T_3 in Sec.2.4.2. The reorientation of the Pb^{2+} was however made possible by the reorganization of the Pb^{2+} displacements spontaneously occurring at T_3 due to the frustration of the Pb^{2+} . Thus, the reorganization of the Pb^{2+} displacements characterized macroscopically by a change in the slope in the thermal evolution of the cell parameters (in Sec.3.5) enables the electric-field induced FE-like polar order characterized in the hysteresis measurements.

In summary, in the compositional range $0.10 \leq x \leq 0.25$, the presence of chemically ordered and disordered regions as well as Ti-poor and Ti-rich regions lead to regions with different types of organization of the Pb^{2+} displacements. Not only is the B-site environment having an influence of the organization of the Pb^{2+} displacements, but also temperature and the ferroelectric activity of the Pb^{2+} cation. I have proposed possible reorganizations of the displacements of Pb^{2+} occurring at the various critical temperatures, but these are, for now, only suppositions. Dielectric measurements under application of a bias electric field may help differentiate the critical temperatures related to change of organization of antiparallel and parallel regions.

PYN-PT with $0.30 \leq x \leq 0.60$

At room temperature, for PYN-PT with $0.30 \leq x \leq 0.60$, regions that are more chemically ordered present a Pb_{iso} organization, the regions that are less chemically ordered present a parallel organization of the Pb^{2+} displacements that may be monoclinically ($\text{Pb}_{//m}$) or tetragonally ($\text{Pb}_{//t}$) distorted depending on the amount of Ti.

Macroscopically, it was shown that the room-temperature structure (mainly monoclinic for $x < 0.60$) transforms into a phase in which regions of tetragonal crystal system are spread in a cubic matrix: these tetragonally-distorted regions are the meso-domains. Hence, above T_m , coexist regions with $\text{Pb}_{//t}$ and Pb_{iso} organizations.

I proposed that, upon heating, the regions with $\text{Pb}_{//m}$ organization observed at room temperature transform in regions with Pb_{iso} organization at the temperature of the maximum of the dielectric constant T_m . This transformation probably occurs in the regions that are the most frustrated: the regions with high degree of chemical order and low amount of Ti. However, the B-site environment is not sufficient to induce the Pb_{iso} organization since the organization is different at room temperature, whereas there is no changes in the chemical order at such low temperature. I suggest that it is the thermal agitation (inducing positional disorder on all atoms) that facilitates the creation of the isotropic displacements of Pb^{2+} at T_m .

When Ti is added, the stability of the regions with parallel organization increases, as mentioned in Sec.4.3.1, and therefore the transformation of these regions in the high-temperature isotropic one requires the addition of more thermal energy (i.e. T_m increases).

With the addition of Ti, the stability of the regions presenting $\text{Pb}_{//t}$ organizations also increase as evidenced by the increase of the ratio of the macroscopic tetragonal phase at room temperature.

This increase of the stability of the ferroelectric phase with the addition of Ti is also observed in the size of the meso-domains. Indeed the domains increase in size as can be seen in the increase

of the splitting of the $(002)_{pc}$ reflections with compositions: for PYN-PT 0.30 only a widening of the peak can be observed at T_{Cr} , whereas for PYN-PT 0.60 the splitting is significant. Furthermore, the $Pb_{//t}$ is more thermally stable than the $Pb_{//m}$ since the $Pb_{//t}$ persist at high temperature. This higher thermal stability may be ascribed to a lower degree of frustration on the B site. Indeed, the regions presenting a $Pb_{//t}$ organization are the ones with the lower degree of chemical order and larger amount of Ti.

At even higher temperature, above T_{Cr} , the structure transforms into its highest-symmetry phase: the cubic one due to thermal instabilities. In this cubic phase, Pb^{2+} are out of their prototypic positions but there is no correlation between the displacements of the Pb^{2+} cations.

Hence, PYN-PT $0.30 \leq x \leq 0.60$ presents a cubic phase at high temperature. Upon cooling, meso-domains of tetragonal distortions appear in the regions presenting the lowest degree of chemical order on the B site and larger amount of Ti at T_{Cr} . At T_m , regions with $Pb_{//m}$ organizations appears in regions with intermediate degree of chemical ordering and amount of Ti. The regions with the highest degree of chemical ordering and lowest amount of Ti keep a Pb_{iso} organization down to room temperature.

4.3.3 Summary and Conclusion

A model relating the chemical arrangement and nature of the B site and the organization of Pb^{2+} displacements was proposed.

This model was applied to the description of the thermal evolution of the macroscopic polar order and structure throughout the PYN-PT phase diagram.

It was shown that the antiferroelectric structure of PYN is induced by the high degree of chemical ordering on the B site, leading to an antiparallel organization of the Pb^{2+} displacements along the $[110]_{pc}$ direction ($Pb_{anti//}$). The addition of a small amount of Ti ($x \leq 0.05$) disrupts the chemical ordering leading to the lower stability of the antiferroelectric phase (decrease of the Curie temperature). Larger addition of Ti (PYN-PT 0.10) prevents the establishment of a long-range antiparallel organization of the Pb^{2+} displacements. Actually, in PYN-PT 0.10, the amount of Ti is already large enough of to induce small frustrations and therefore some regions (especially at low temperature) present a Pb_{dir} organization.

In an intermediate compositional range $0.16 \leq x \leq 0.25$, the organization of the Pb^{2+} displacements is highly-temperature and composition-dependent and $Pb_{anti//}$, Pb_{dir} , Pb_{iso} and $Pb_{//m}$ regions may coexist.

For large amount of Ti, ($0.30 \leq x \leq 0.60$), the $Pb_{anti//}$ and Pb_{dir} organizations disappear and give way to more and more regions with isotropic displacements of Pb^{2+} (Pb_{iso}) or with Pb^{2+} displacements occurring in parallel ($Pb_{//m}$ and $Pb_{//t}$). The number or size of regions with $Pb_{//m}$ and $Pb_{//t}$ organizations increases with the addition of Ti and monoclinic then tetragonal macroscopic distortions appear. However, the $Pb_{//m}$ regions are not completely stable and they transform into Pb_{iso} regions upon heating at T_m .

Finally, for compositions with even larger amount of Ti ($x > 0.60$), that were not studied in this

work, only parallel organization of Pb^{2+} displacements in a tetragonally distorted perovskite unit cell persists leading to the observed macroscopic ferroelectric tetragonal phase [19, 49].

- CHAPTER 5 -

APPLICATIONS

This PhD work has focused on the study of the polar (Chapter 2) and structural (Chapter 3) properties of the solid solution $(1-x)\text{Pb}(\text{Yb}_{1/2}\text{Nb}_{1/2})\text{O}_3-x\text{PbTiO}_3$ (PYN-PT).

After general considerations about applications of piezoelectric, pyroelectric and ferroelectric materials (Sec.5.1), the piezoelectric measurements as a function of temperature will be presented in Sec.5.2.

Some of the results of these measurements have been already discussed in the framework of the study of the properties (in Chapter 2). Hereafter, these results will be examined from a potential applications point of view in Sec.5.3. In this section, other potential applications (electrostriction and memory devices) made possible by the versatility of the polar order in the PYN-PT solid solution will also be presented.

Finally, in Sec.5.4, suggestions to obtain properties meeting as closely as possible to the application requirements by changing the chemical content or final shape will be provided.

5.1 INTRODUCTION

This PhD work has focused on the establishment of a phase diagram based on the investigations of the polar (Chapter 2) and structural (Chapter 3) properties of the solid solution $(1-x)\text{Pb}(\text{Yb}_{1/2}\text{Nb}_{1/2})\text{O}_3-x\text{PbTiO}_3$ (PYN-PT). This solid solution is mostly known for its high-temperature high-piezoelectric properties, but this solid solution presents all polar orders (antiferroelectric (AFE), ferroelectric (FE) and relaxor (RFE)) opening an extremely large scope of possible applications presented in Sec.1.1.5 (page 23).

Indeed for compositions with $x \leq 0.05$, PYN-PT presents antiferroelectric polar ordering interesting for energy storage and actuators. These two applications gain advantage of the AFE-FE transformation taking place at large electric field associated with a large increase of polarization and strain.

In the compositional range $0.10 \leq x \leq 0.40$, PYN-PT presents relaxor properties. Relaxor materials have been used for antenna, resonators and adjustable filters. Also relaxors usually present strong electrostrictive properties that have been used for example, in the aberration correction in the mirrors of the Hubble telescope because of the absence of strain hysteresis with application of electric field.

Finally, PYN-PT with $x \geq 0.45$ displays a ferroelectric behavior. Ferroelectrics are used in data storage devices (FeRAMs) because of the possibility to switch the polarization with an applied electric field. Moreover, ferroelectric materials are also pyroelectric and piezoelectric and more applications derive from these additional properties. For example pyroelectricity is used in temperature sensors or solid-state cooling devices. Piezoelectricity, on the other hand, is used in a large domain of applications: transducers, pressure sensors, actuators, ultrasonic motors among others.

Hereafter, we will focus mainly on the strain-electric field relationship in the PYN-PT solid solution (piezoelectric and electrostrictive properties) and in particular, piezoelectricity will be discussed in regards with potential actuators applications for the industrial partner Schlumberger. Ferroelectric properties will be also briefly discussed.

Piezoelectric Figure of Merit

In the literature, several characterization coefficient or *Figures of Merit* are used to compare the intrinsic properties of materials. The most well-known Figures of Merit are the *piezoelectric strain constant* d , the *piezoelectric voltage constant* g , the *electromechanical coupling coefficient* k , the *mechanical quality factor* Q_m and the *acoustic impedance factor* Z . These different Figures of Merit will be defined and their influence on the potential applications will be discussed hereafter.

The *piezoelectric strain constant* d is the most commonly reported piezoelectric constant for bulk materials in literature. This piezoelectric constant links the strain (S) and electric field (E) or the dielectric displacement (D) and the stress (T):

$$S_{ij} = d_{ijk} \cdot E_k \quad \text{or} \quad D_k = d_{ijk} \cdot T_k \quad (5.1)$$

The *piezoelectric voltage constant* g is also commonly used, but this one relates stress and electric field or dielectric displacement and strain:

$$E_i = -g_{ijk} \cdot T_{kl} \quad \text{or} \quad S_{ij} = g_{kij} \cdot D_k \quad (5.2)$$

These two piezoelectric coefficients are actually related through the dielectric constant at constant stress: $d = g \cdot \epsilon_0 \epsilon^T$ but they are used differently depending on the intended applications. Indeed, the piezoelectric strain constant d is more significant in applications where the piezoelectric material must develop strong motions or vibrations such as actuators, whereas the piezoelectric voltage constant g is more meaningful in cases where a strong voltage response must be generated when strain is applied, e.g. sensors applications.

The piezoelectric coefficients describe the linear relationship between strain, stress, electric field and dielectric displacements. However, in applications, using the electrostrictive properties of the materials, it is no longer the linear relationship, but the quadratic one that is of interest. In these cases, the Figures of Merit are the electrostrictive coefficients, M and Q , and the previous relations become:

$$S_{ij} = d_{ijk} \cdot E_k + M_{ijkl} \cdot E_k E_l \quad (5.3)$$

$$S_{ij} = g_{kij} \cdot D_k + Q_{ijkl} \cdot D_k D_l \quad (5.4)$$

Neglecting shear strain and stress, these equations can be rearranged as

$$S_{ij} = d_{ijk} \cdot E_k + M_{ijkl} \cdot E_k^2 \quad (5.5)$$

$$S_{ij} = g_{kij} \cdot D_k + Q_{ijkl} \cdot D_k^2 \quad (5.6)$$

The *electromechanical coupling coefficient* k is also commonly reported as it measures the fraction of the electrical energy converted to mechanical energy (or vice versa) as

$$k^2 = \frac{\text{Stored mechanical energy}}{\text{Input electrical energy}} \quad \text{or} \quad k^2 = \frac{\text{Stored electrical energy}}{\text{Input mechanical energy}} \quad (5.7)$$

Other conversion rates exist, but they are less commonly documented. For example, the energy transmission coefficient λ_{max} relates the input and output energies and the efficiency η links the output and the consumed energies such as

$$\lambda_{max} = \frac{\text{Output mechanical energy}}{\text{Input electrical energy}} \quad \text{or} \quad \lambda_{max} = \frac{\text{Output electrical energy}}{\text{Input mechanical energy}} \quad (5.8)$$

$$\eta = \frac{\text{Output mechanical energy}}{\text{Consumed electrical energy}} \quad \text{or} \quad \eta = \frac{\text{Output electrical energy}}{\text{Consumed mechanical energy}} \quad (5.9)$$

The difference between all these conversion rates lies in the fact that the output energy is "stored" or "spent" and that the input energy is external or that some energy previously stored is also consumed. Indeed, the electromechanical coupling coefficient k measures the percentage of input energy stored whereas the energy transmission coefficient λ_{max} evaluates the percentage

converted. Furthermore, the efficiency η takes into account the consumption of the energy that may have been stored in previous work cycles, whereas in the energy transmission coefficient λ_{max} only the energy input in the present work cycle is taken into account.

The *mechanical quality factor* Q_m is inversely proportional to the mechanical losses in the material. This factor also represents the sharpness of the resonance peak and is defined as

$$Q_m = \frac{f_0}{2\Delta f} \quad (5.10)$$

with f_0 the resonance frequency and $2\Delta f$ the full width at $Y_m/\sqrt{2}$ with Y_m the admittance at the resonance.

The mechanical quality factor Q_m is a critical parameter in practical cases where high-accuracy are needed in the frequency or time spaces.

Finally, the *acoustic impedance* Z is of the outmost importance in transducers applications since a large impedance mismatch between the piezoelectric element and the medium limits strongly the wave transmission from the transducer to the medium. The acoustic admittance is related to the density ρ and the elastic stiffness c of the material as follows

$$Z = \sqrt{\rho c} \quad (5.11)$$

For some applications, it is not the Figures of Merit defined above that are important but a combination of them. For example, in the case of resonance actuators, more appropriate Figures of Merit are Q_md or Q_mk , whereas $k\nu$ (with ν the vibration velocity) or Q_mk^2 are more relevant for resonance transducer applications.

Characterization techniques

The Figures of Merit previously described can be determined using different characterization techniques, the most common techniques are based on

The direct piezoelectric effect The voltage generated under an external pressure is measured.

The converse piezoelectric effect The strain produced under electric field is recorded. This method has been used in this work to characterize the piezoelectric coefficient d_{33} and electrostriction coefficient Q_{33} (Sec.5.2.1.1)

The measurement of resonance modes The resonance and antiresonance frequencies of a test sample are determined. These frequencies allow the calculation of the elastic coefficient of the material and therefore of the piezoelectric constants. Several piezoelectric coefficients can be evaluated using different sample geometries. This method has been used to determine the electromechanical coupling coefficient k_t and k_p (Sec.5.2.1.2).

In the literature, more atypical method to determine piezoelectric coefficients can be found, such as acoustic spectroscopy [103] or image correlation [104].

5.2 EVOLUTION OF THE PIEZOELECTRIC PROPERTIES WITH TEMPERATURE

In this work, I have focused on the evolution of the strain-electric field response with temperature for compositions in the range $0.10 \leq x \leq 0.50$.

The strain-electric field response of PYN-PT 0.60 was measured only at room temperature because the high value of its coercive field requires the use of a special environment conditions that are not possible to put in place for measurements at high temperature.

Compositions with $x < 0.10$ were also not considered during this study for the same reason. Actually, the antiferroelectric properties of these compositions can be used for actuation because of the large strain generated during the antiferroelectric-ferroelectric electric-field induced phase transition (Fig.2.1, page 55). However, the electric-field required to induce this phase transition is extremely high and it was not possible to reach it (see Sec.2.3, page 68 for more detailed explanations).

Strain-electric field relationships were measured using the commercial piezoelectric evaluation system Aixacct 2000 in association with a cryofurnace sample holder for measurements between 180 K and 880 K. Compositions showing piezoelectric response and temperature stability interesting for potential actuator applications ($0.40 \leq x \leq 0.50$) were further characterized using the so-called "IRE-method" (Sec.5.2.1.2) to determine some of the electromechanical coupling coefficients.

5.2.1 Measurement techniques

5.2.1.1 Converse piezoelectric effect: interferometry measurements

The principle of the strain-electric field measurements in the Aixacct 2000 equipment is based on the converse piezoelectric effect: a piezoelectric material is strained when an electric field is applied to it.

In practice, it is the displacement of the top surface (monitored by a LASER interferometer) of the sample under an applied electric field that is measured and not directly the strain generated by the application of this electric field. Since the bottom surface is fixed, the change in the position of the top surface corresponds to the change in thickness of the sample. The strain generated in the sample is then simply the change of thickness due to the applied electric field normalized by the thickness of the sample without an electric field.

Therefore, the strain-electric field response can be easily obtained applying an electric field and measuring the change of position of the top surface.

Once the effect of an electric field on strain is measured, piezoelectric and electrostrictive coefficients can be determined by fitting the strain-electric field curves.

The aixPplorer software provided with the Aixacct equipment calculated the piezoelectric coefficient by taking the slope between the deformation obtained at the maximum applied electric field and the original position. This information may be extremely important for industrial

applications since it is a direct measure of the effective strain obtained for a given electric field, however this value does not correspond to the definition of the piezoelectric coefficient given in Sec.5.1: the slope in the strain-electric field curves at zero electric field. Therefore, a python program to measure the actual piezoelectric coefficient from the slope of the strain at zero electric field was developed by Ilan Shlesinger and Jean-Baptiste Bayle in the framework of a final-year research project in the SPMS laboratory. This program is capable of determining the piezoelectric coefficient for several temperatures (like the aixPlover software) and for different frequencies (an option that is not provided by the aixPlover software).

The piezoelectric coefficient d_{33} measured from this technique are presented in Fig.5.4.

5.2.1.2 Resonance measurements

The determination of the piezoelectric coefficients using the resonance method is normalized by the IRE standards [105], explaining why these measurements are commonly referred to as IRE measurements.

The measurements are carried out exciting the sample with a field at various frequencies in order to measure the resonance and antiresonance frequencies. The sample can be excited by an electrical or a mechanical signal. In the following, we will only focus on the electric excitation. The resonance and antiresonance corresponds to extrema of the impedance. The resonance frequency correspond to a minimum of impedance (maximum of admittance) and the strain in the material is large (Fig.5.1). The antiresonance frequency corresponds to a maximum of impedance and the strain in the material is smaller, and actually zero in the ideal case of material with an electromechanical coupling coefficient equal to 1, i.e. in the case when all the input energy is transformed.

Writing the piezoelectric constitutive equations and the second law of Newton assuming plane waves, a link between the material density, piezoelectric constants, geometry of the samples and the resonance and antiresonance frequencies can be derived (see for example Ref.[32] for the exact derivation).

Practically, the sound velocity of the wave can be determined directly from the resonance frequency. Knowing the density of the material the elastic compliance can be calculated from the sound velocity.

Separately, the electromechanical coupling coefficient can be determined from the resonance and antiresonance frequencies. Finally, the piezoelectric coefficient can be determined, using the previously determined elastic compliance and the electromechanical coupling coefficient and

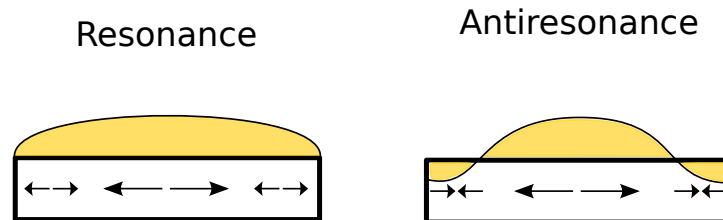


Figure 5.1: Strain distribution in the resonant and antiresonant state. Adapted from [2]

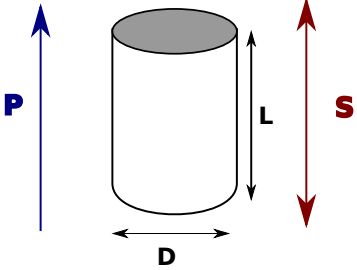
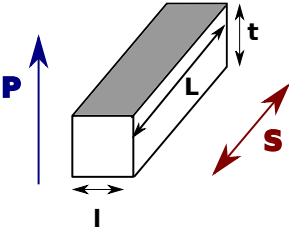
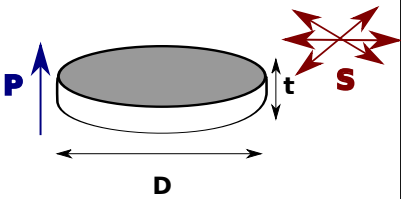
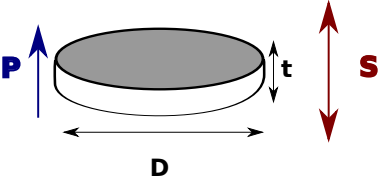
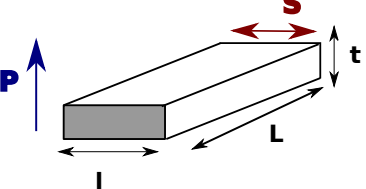
		Dimensions	constants
longitudinal		$D < \frac{L}{5}$	k_{33} d_{33} g_{33}
lateral		$I < \frac{L}{3}$ $t < \frac{L}{3}$	k_{31} d_{31} g_{31}
radial		$D > 5 t$	k_p e_{31}
thickness		$D \gg t$	k_t e_{33} h_{33}
shear		$L > 8 t$	k_{15} d_{15} g_{15}

Figure 5.2: Geometry required for the determination of the most common piezoelectric coefficient in ceramics using the resonance method.
The gray area represents the electrodes for the measurements.

measuring the permittivity at constant strain (measured at twice the resonance frequency) or at constant stress (measured at low frequency) depending on the piezoelectric coefficient under investigation.

This general procedure can be used to determine all of the piezoelectric coefficient. However each piezoelectric coefficient requires the use of a specific sample geometry in order to avoid cross-coupling between the various vibration modes.

In the case of ceramics, only a limited number of piezoelectric coefficients can be determined compared to the case of single crystals. The geometry of the samples required to determine all accessible piezoelectric constants and electromechanical coupling coefficients are summarized in Fig.5.2 (for ceramics).

In the measurement procedure, the polarization only points in one macroscopic direction. However, in the spontaneous case, the polarization is never aligned along one direction to avoid accumulation of charges at one side. Thus, poling the sample to align the polarization in one direction is necessary, otherwise the strain induced in domains with opposite directions will cancel each other.

In the case of ceramics, it is actually not possible to have the polarization of each grain pointing in the same directions as each grain is randomly oriented. However it is possible to have the polarization in a hemi-sphere centered around the desired polarization direction. The poling procedure of the PYN-PT ceramics is described in the next section.

Poling

To conduct IRE measurements, it is necessary to pole the samples in order to avoid cancellation of vibrations by oppositely polarized domains. The polarization of the samples are usually conducted using either a field-cooling procedure or an increasing-field procedure.

The field-cooling procedure takes advantage of the divergence of the dielectric constant at the Curie temperature making the sample extremely sensitive to any external fields at this temperature. Therefore, the application of a relatively small electric fields at the Curie temperature can force the domains created at this temperature to align with the electric-field.

In the increasing-field procedure, the switching of the polarization is done by applying an electric field much stronger than the coercive field at room temperature. This procedure corresponds to the first cycle of an hysteresis cycle and the polarization obtained is the remnant polarization.

Several poling temperatures and electric fields have been tried to find the best set of experimental conditions for poling PYN-PT. The evaluation of the “quality” of the poling is evaluated by looking at the planar electromechanical coupling coefficient, k_p (Fig.5.3(b)) after one day (the IRE standards demand the poling to be stable for one day).

Field cooling was considered first since it was shown on other Pb-based complex perovskites that only low electric fields ($\sim 1\text{ kV/mm}$) are required to obtain a well poled ceramic [106]. However, because in some leaky samples, the paraelectric-ferroelectric transition leads to the appearance of strong leakage currents that are too large for the voltage generator to accommo-

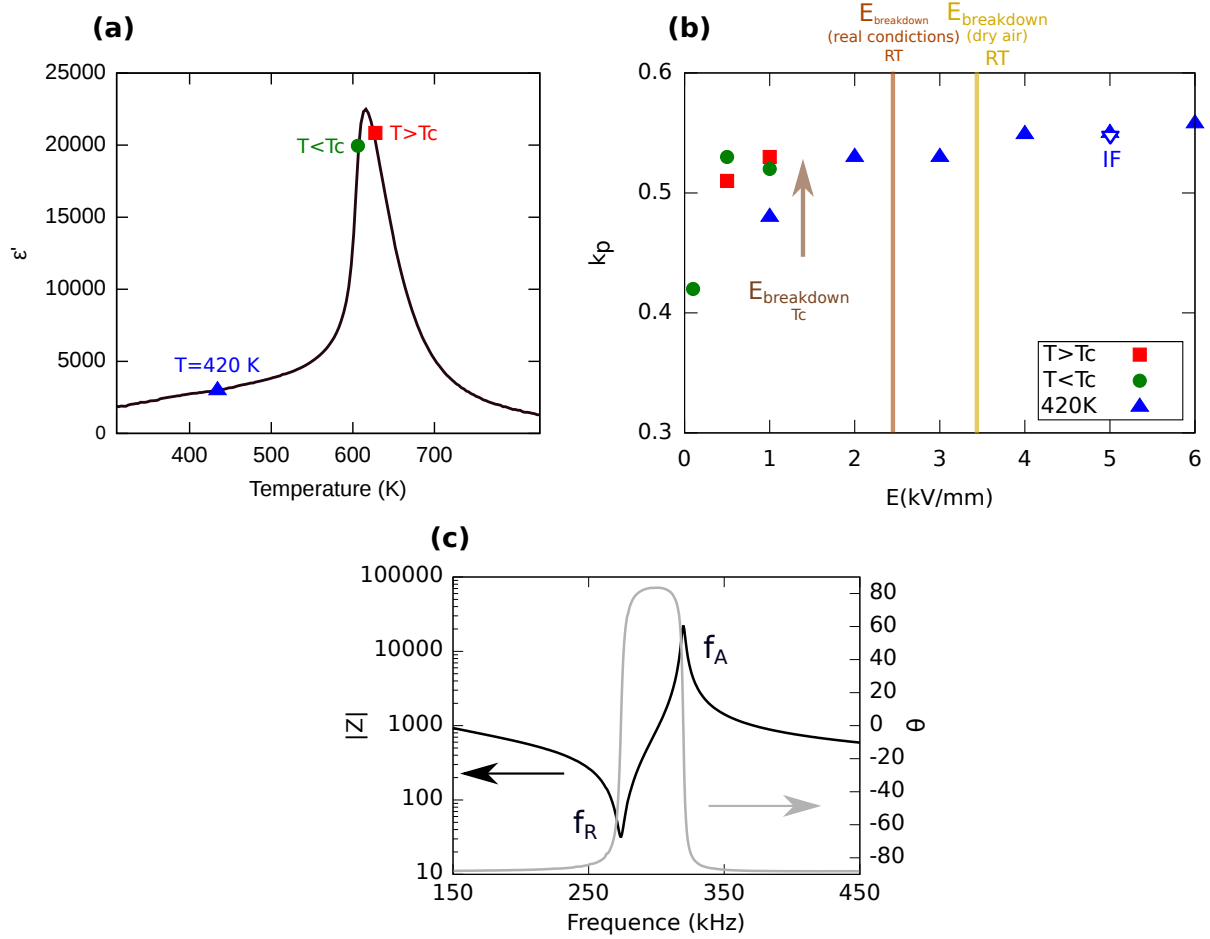


Figure 5.3: (a) Dielectric constant as a function of temperature. The different poling temperatures are indicated.

(b) Influence of the poling temperature and electric field on the planar electromechanical coupling coefficient k_p . The value obtained after poling at room temperature at 5 kV/cm is also plotted in open blue triangle and is marked as IF (increasing field). The air breakdown fields at room temperature in dry air, in real conditions as well as at the Curie temperature of PYN-PT are indicated.

(c) Impedance spectra after poling. The resonance (f_R) and antiresonance (f_A) frequencies are indicated.

date, I tried poling slightly above and slightly below the Curie temperature.

Actually, no significant differences in the planar electromechanical coupling can be seen when poling, using the same electric field, at temperatures slightly higher or slightly lower than the Curie temperature. For both poling temperatures, electromechanical coupling coefficient up to 0.52 can be obtained with applying a 1 kV/mm electric field, however larger electric field cannot be applied because of the low value of the breakdown electric-field of air at temperatures as high as the Curie temperature of PYN-PT 0.50.

Since the breakdown occurs in the air and not in the sample, larger electric field could be applied during the poling, if the poling procedure was conducted, not in air, but in a medium with a higher breakdown field. The only commercially available medium that I have found that can support high electric field and high temperature is silicone oil. Nonetheless the maximum usage temperature for the silicon oil is given to be 200 °C (~ 470 K), a temperature much lower than the Curie temperature of PYN-PT 0.50 (~ 370 °C).

We have decided to conduct the poling process at about 420 K (~ 150 °C) to be in total safety in case the heating stage overshoots, in particular considering how large electric fields are applied. 420 K is rather far from the Curie temperature and the dielectric constant is already much lower than the one at the Curie temperature (Fig.5.3(a)). Therefore the sample will be less sensitive to applied electric field and poling at 420 K requires the use of larger electric fields to obtain the same polarization state as when conducting a field cooling procedure.

To obtain the same planar electromechanical coupling coefficient as when the sample is field cooled from the Curie temperature at 1 kV/mm, an electric-field of 2 kV/mm must be applied at 420 K.

But, when applying even larger electric fields, that are attainable because of the immersion of the sample inside silicon oil, even larger, electromechanical coupling coefficients have been obtained when poling at 420 K (Fig.5.3(b)). For electric field larger than 4 kV/mm, the value of the electromechanical coupling coefficient saturated at a value of about 0.56.

Finally, since the largest electromechanical coupling coefficient was obtained for a sample poled at large electric field, but limited temperature, we also tried to pole the sample at room temperature applying a strong electric field. Indeed, the dielectric constant at room temperature is comparable to the one at 420 K making the sample almost as sensitive to electric field at room temperature as at 420 K. Poling at room temperature at 5 kV/mm (open triangle in Fig.5.3(a)) leads to the same poling as in the case of 420K, since the electromechanical coupling coefficients are identical.

In all investigated sets of temperature and electric field, the resulting poling is really good as evidenced by the strong difference in the extrema of the impedance at the resonance (f_R) and antiresonance (f_A) frequencies (Fig.5.3(c)) and as manifested by the fact that the phase is 80° between the resonance and antiresonance frequencies (in the ideal case, the phase would change from -90° to 90°).

Since poling at room temperature is technically simpler and leads to an excellent poling state, it was chosen to pole all ceramics at room temperature with an electric field of 5 kV/mm.

The results of the IRE measurements conducted on PYN-PT 0.40, PYN-PT 0.45 and PYN-PT

0.50 are plotted in Fig.5.5 and discussed in Sec.5.2.2.

5.2.2 Results and Discussion

The thermal evolution of the piezoelectric coefficient d_{33} is plotted in Fig.5.4. It has been determined from measurements conducted on the Aixacct 2000 equipment and analyzed with the program developed in the laboratory. Different temperature ranges were investigated depending on the composition based on the value of the maximum of the dielectric constant T_m measured in Sec.2.4.2.

The radial (k_p) and thickness (k_t) electromechanical coupling coefficients of PYN-PT 0.40, PYN-PT 0.45 and PYN-PT 0.50 as a function of temperature are presented in Fig.5.5.

For all investigated compositions, a maximum of the piezoelectric coefficient d_{33} can be observed as a function of temperature. The maximum of d_{33} originates from different sources for compositions with $x < 0.30$ and $x \geq 0.30$. For PYN-PT with $x < 0.30$, the maximum of d_{33} is related to the change of ferroelectric hysteresis loops to double loops at T_3 (presented in Chapter 2). For PYN-PT with $x \geq 0.30$, the maximum is due to a transition between two ferroelectric phases.

PYN-PT with $x < 0.30$

For compositions with $x < 0.30$, the maximum of the piezoelectric coefficient d_{33} occurs at the temperature T_3 characteristic of a change in the polarization-electric field relationship evidenced in Sec.2.4.2 (page 75). This change of behavior was associated with a change in the correlation between the displacements of Pb^{2+} in Chapter 4.

Above T_3 , the polarization-electric field and strain-electric field hysteresis loops are the one of a typical ferroelectric material (top of Fig.5.6), below T_3 the polarization-electric field and strain-electric field relationships can be represented by double loops (bottom of Fig.5.6) either due to antiferroelectricity or to pinched ferroelectric loops (Sec.2.1.3). At the temperature of the transition T_3 , the two ferroelectric cycles of the double loops are present at zero electric field (center of Fig.5.6). Thus, the strain at zero electric field is large: it would actually correspond to the strain induced by a AFE-FE phase transition in the case of antiferroelectric double loops. Therefore, at T_3 , the maximum of the piezoelectric coefficient d_{33} is due to the change of polarization-electric field and strain-electric field relationships that was associated with modification of the correlation between the Pb^{2+} that was proposed to take place at this temperature in Chapter 4.

PYN-PT with $x \geq 0.30$

For compositions with $x \geq 0.30$, the transition previously described cannot be observed and therefore the maximum of d_{33} must be of different origin. The maximum of the piezoelectric coefficient d_{33} is accompanied with a change in the thermal evolution of the electromechanical coupling coefficient k_p and k_t (Fig.5.5) and of the dielectric constant of the poled samples

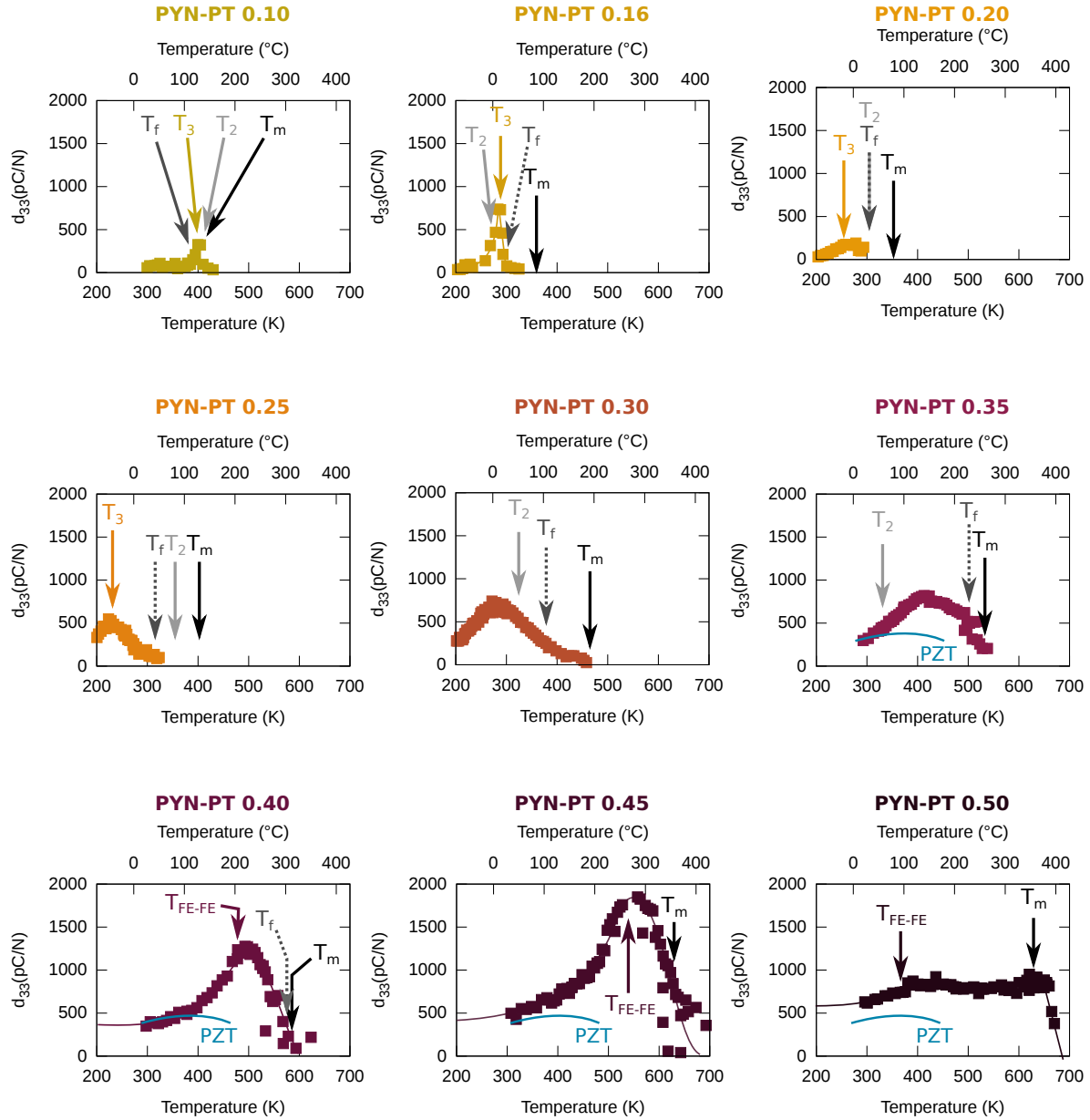


Figure 5.4: Evolution of the piezoelectric coefficient d_{33} as a function of temperature for several compositions. The evolution of PZT is given for comparison

The temperature of the maximum of the dielectric constant T_m , the freezing temperature T_f and the temperatures at which a change in the dielectric (T_2) and hysteresis (T_3) behavior was observed are indicated.

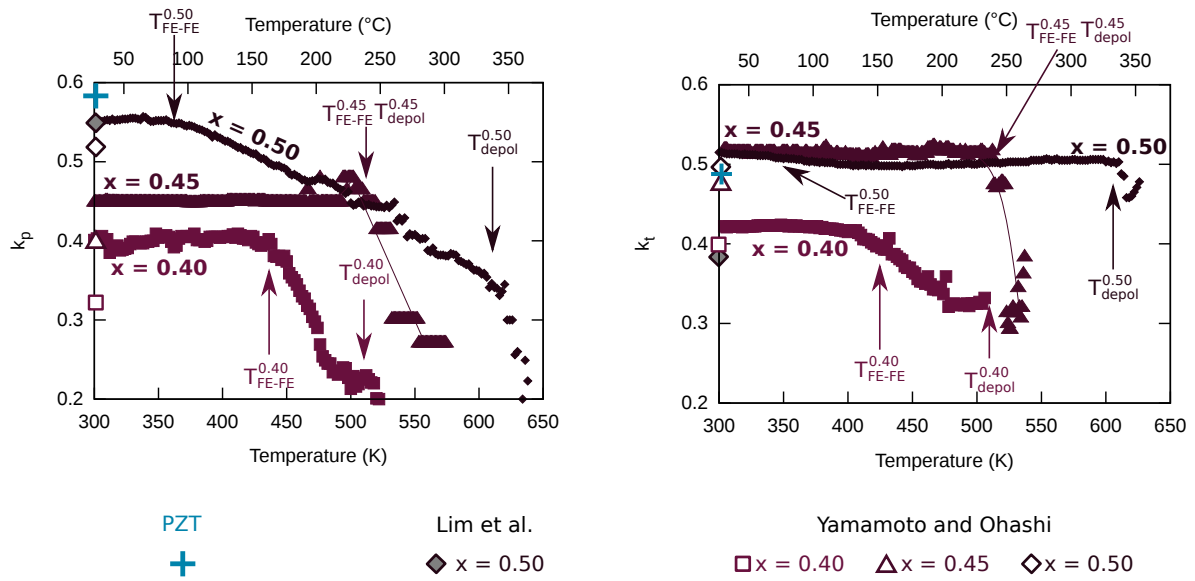


Figure 5.5: Radial (k_p) and thickness (k_t) electromechanical coupling coefficients of PYN-PT 0.40 (squares), PYN-PT 0.45 (triangles) and PYN-PT 0.50 (diamonds) as a function of temperature.

The radial and thickness electromechanical coupling coefficients for PYN-PT published by Lim et al. [47] and Yamamoto and Ohashi [19], as well as the values of PZT are reported for comparison.

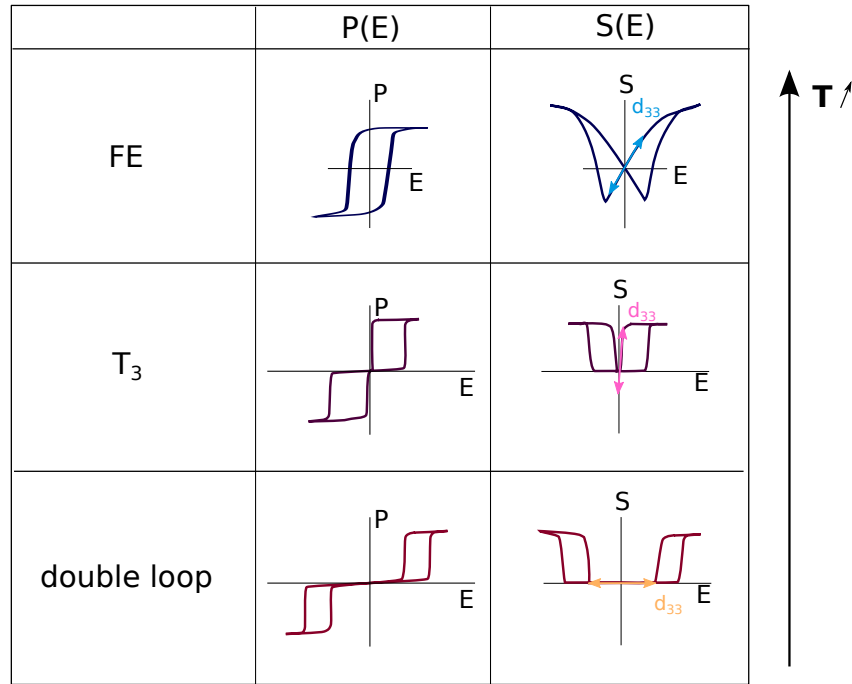


Figure 5.6: Schematic representation of the evolution of the polarization-electric field and strain-electric field relationships as a function of temperature.

(Fig.5.7(a)) can be observed for PYN-PT 0.40, PYN-PT 0.45 and PYN-PT 0.50.

The temperature of the maximum of the piezoelectric coefficient d_{33} is slightly higher than the temperature observed in the dielectric and IRE measurements. This difference can be attributed to two (possibly associated) origins: a difference in the experimental setup and in particular in the temperature measurements or an increase of the ferroelectric-ferroelectric transition temperature (leading to the increase of the piezoelectric properties that will be demonstrated hereafter) due to the large electric field impose for the interferometric measurements.

Above and below the temperature of the maximum of d_{33} , the poled dielectric constant follows the Curie-Weiss law as evidenced by the linear dependence of the inverse of the dielectric constant and therefore the temperature-independence of the derivative of the inverse of the dielectric constant ξ (Fig.5.7(b-c)) indicating the presence of two ferroelectric phases on each side of the critical temperature since these phases also demonstrate piezoelectric responses. The transition between these two ferroelectric phases will be referred as to T_{FE-FE} .

Dielectric measurements were not conducted on poled samples of PYN-PT 0.35 and PYN-PT 0.30, but the thermal evolution of the I-V curves shows that the change of behavior is extremely similar to the one of PYN-PT with $x = 0.40-0.50$ indicating that the maximum of the piezoelectric coefficient d_{33} may be also related to a ferroelectric-ferroelectric phase transition.

Furthermore, the comparison of the high-electric field dielectric constant and low-electric field one for PYN-PT 0.30 in Fig.2.19 (page 86) has shown that the application of a strong electric

field induces a phase that has a Curie-Weiss behavior. The critical temperature obtained fitting the low-temperature part of the high-field dielectric constant corresponds to the temperature of the maximum of the piezoelectric constant d_{33} indicating that the maximum of the piezoelectric constant d_{33} is related to the application of the measuring electric field.

This ferroelectric-ferroelectric phase transition induces changes in the polarization state of the poled samples lowering the values of the electromechanical coupling coefficient k_p and k_t . Indeed, when the sample is subjected to the FE-FE transition, the change of structures causes a reorientation of the polarization. Above T_{FE-FE} , the polarization is still predominantly in the poling direction, but in-plane the polarization is as much as possible compensated to lower the energy (avoiding accumulation of charges due to macroscopic polarization). This lowering of the in-plane macroscopic polarization leads to the strong reduction of the radial electromechanical coupling coefficient k_p , whereas the thickness coupling coefficient is not so strongly impaired by the FE-FE transition since the out-of-plane polarization was not heavily modified by the phase transition.

Actually, in the case of PYN-PT 0.45, both the radial and thickness electromechanical coupling coefficients drop down to zero above the FE-FE phase transition. This is due to the thermal proximity of the FE-FE transition temperature and the depoling temperature. At the depoling temperature, the material undergoes a transition toward a high-temperature state that is mainly cubic and therefore non-piezoelectrically active. Hence, in PYN-PT 0.45, the limited decrease of the electromechanical coupling coefficients due to the FE-FE is accompanied by a collapse of the same coupling coefficients due to the depolarization of the sample at a unique temperature corresponding to both the FE-FE transition and the depoling temperature.

For PYN-PT 0.40 and PYN-PT 0.50, the temperature at which the sample loses its macroscopic polarization (depoling temperature) is much larger than the FE-FE transition temperature and a piezoelectric response can be observed for temperature up to 20-50 K lower than the maximum of the dielectric constant ($T_m \sim 575$ and 640 for PYN-PT 0.40 and PYN-PT 0.50 respectively).

Finally, for PYN-PT 0.45 and PYN-PT 0.50, a piezoelectric response can be observed in the large electric-field measurements above the maximum of the dielectric constant T_m and up to the critical temperature T_{Cr} (~ 690 K) defined based on the X-ray diffraction measurements. This piezoelectric response is probably caused by the mesoscopic ferroelectric domains of tetragonal structure that were proposed (in Chapter 2) to exist in a cubic matrix in the temperature range between T_m and T_{Cr} . For PYN-PT 0.40 and PYN-PT 0.30, for which the presence of mesoscopic domains at high temperature was also inferred from the diffraction experiments, the piezoelectric response above T_m is limited and the strain-electric field relationship is dominated by the electrostrictive response making the measurement of the piezoelectric response strenuous in this compositional and temperature range.

In conclusion, for all compositions in the range $0.10 \leq x \leq 0.50$, the piezoelectric coefficient d_{33} was measured as a function of temperature using interferometric measurements. The electromechanical coupling coefficients k_p and k_t were measured in the more limited compositional

where the piezoelectric properties and temperature stability were considered sufficient for potential applications. These measurements have shown that for all compositions, the piezoelectric coefficient d_{33} goes through a maximum. This maximum is related to a change in the polarization-electric field and strain-electric field relationships for PYN-PT with $x < 0.30$ and to a ferroelectric-ferroelectric transition for $x \geq 0.30$.

5.3 APPLICATIONS OF PYN PT

Based on the results of the piezoelectric measurements discussed in the previous section, potential use of PYN-PT will be discussed in the framework of the interest of the industrial partner, Schlumberger, but also within a larger scope.

5.3.1 Piezoelectric applications

In Schlumberger, most of the applications of piezoelectricity are covering imaging systems, electric transformers and actuators for temperatures up to 200 °C (473 K). For actuator applications a strong value of the piezoelectric coefficient d_{33} is needed (Sec.5.1), a large thickness electromechanical coupling coefficient is also desired as it represents the efficiency of the material. From an application point of view, one of the aims of this PhD thesis is to develop materials with higher piezoelectric properties than the one currently in use (PZT Navy II) without degrading the stability with temperature.

Fig.5.8 presents the piezoelectric coefficient d_{33} at 200 °C as a function of composition. Since some applications of the piezoelectric properties also occur at room temperature the evolution of d_{33} with composition at this temperature is also plotted. The piezoelectric coefficients will be compared to those of ceramic $0.67\text{Pb}(\text{Mg}_{1/3}\text{Nb}_{2/3})\text{O}_3\text{-}0.33\text{PbTiO}_3$ (PMN-PT) and $\text{Pb}(\text{Zr,Ti})\text{O}_3$ (PZT) that are the most commonly used materials in industrial applications. PMN-PT displays extremely large piezoelectric properties, but it has a low temperature stability and applications are limited to room temperature. PZT, on the other hand, presents lower (but still large) piezoelectric properties and a much larger temperature stability allowing applications up to 150-250 °C, depending on the doping level.

Fig.5.8 reveals that compositions with $x < 0.30$ are not really suitable for actuator applications since their piezoelectric coefficients d_{33} are low (< 200 pC/N).

At room temperature, PYN-PT 0.30 arises as a good candidate for actuator applications since it presents a piezoelectric coefficient d_{33} similar to the one observed in PMN-PT. However, this strong piezoelectric response falls for temperature higher than 100 °C.

Another composition presenting large piezoelectric properties at room temperature is PYN-PT 0.50. This composition also presents the advantage of displaying a good temperature stability for the piezoelectric coefficient d_{33} (Fig.5.4). The thickness electromechanical coupling coefficient k_t also shows a relatively low temperature dependency. However, in Sec.5.2.2, it was shown that the slight change of slope in the thermal evolution of k_t is related to ferroelectric-ferroelectric phase transition. This phase transition may change the polarization state of the sample and

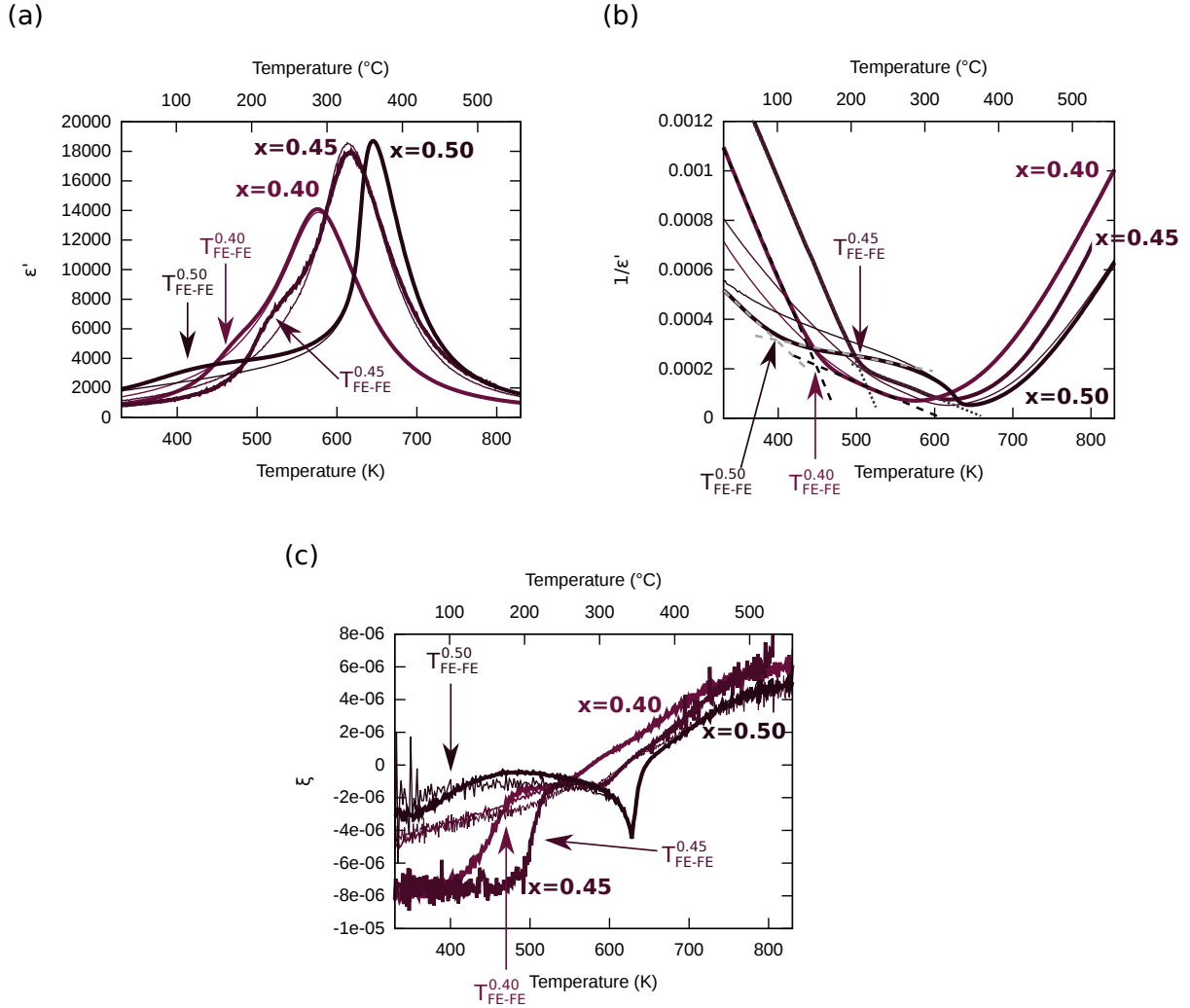


Figure 5.7: (a) Evolution of the dielectric constant of PYN-PT 0.40, PYN-PT 0.45 and PYN-PT 0.50 as a function of temperature for poled (bold line) and unpoled (thin line) samples. (b) Inverse of the dielectric constant as a function of temperature. (c) Derivative of the inverse of the dielectric constant as a function of temperature. The temperature of the ferroelectric-ferroelectric (T_{FE-FE}) phase transition is indicated with an arrow.

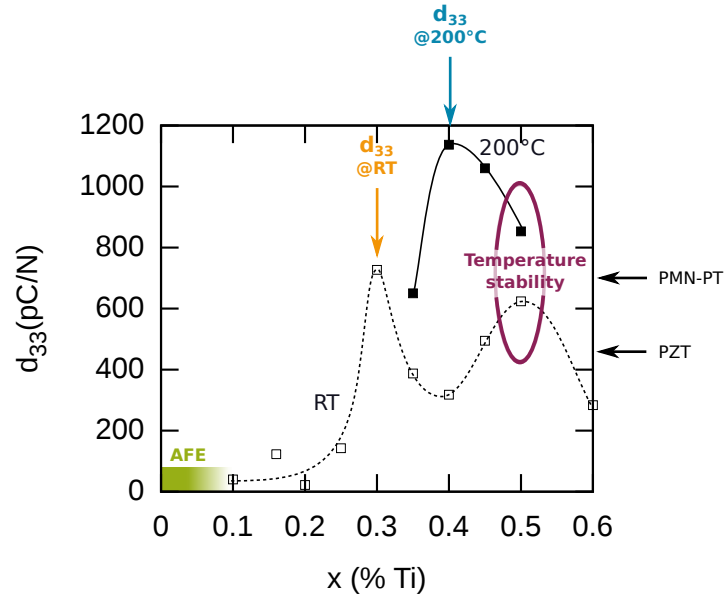


Figure 5.8: Influence of the composition on the piezoelectric coefficient d_{33} at room-temperature (open symbols) and 200 °C (filled symbols).

Typical values for the piezoelectric coefficient d_{33} at room temperature $\text{Pb}(\text{Mg}_{1/3}\text{Nb}_{2/3})\text{O}_3$ - PbTiO_3 (PMN-PT) and $\text{Pb}(\text{Zr,Ti})\text{O}_3$ (PZT 5H/NAVY VI) are indicated for comparisons.

therefore impair the use of this composition above T_{FE-FE} .

This possible limitation of the temperature usage range for this high Curie temperature material was investigated by measuring the thermal evolution of k_t after heating it up to 500 K (330 °C) to reproduce the change of polarization induced in the material up to the maximum usage temperature envisioned and cooling it back to room temperature. The results are presented in Fig.5.9 and compared to the k_t values measured just after poling, i.e. without such subsequent heating. After a thermal treatment up to 500 K, a reduction of about 10 % of the value the thickness electromechanical coupling coefficient is observed. However, the changes of slope at T_{FE-FE} in the thermal evolution of k_t is no longer viewed and the dielectric constant goes back to its “unpoled” behavior. Therefore, after the first thermal cycle, PYN-PT 0.50 would appear not to undergo a ferroelectric-ferroelectric transition and the piezoelectric properties are temperature-independent making PYN-PT 0.50 a good piezoelement for actuators designed to work between room temperature and 300 °C.

This disappearance of the FE-FE phase transition may indicate that the poling procedure modifies more intrinsically the ferroelectric state present in the material than just switching the polarization. Hence, when cooling without application of an electric field, this change of the ferroelectric state does not reappear and the material returns to its initial state but with retaining a macroscopic polarization.

Another possibility for the disappearance of the change of behavior in the piezoelectric and dielectric behavior as a function of temperature after the first thermal treatment may be that the

ferroelectric-ferroelectric transition smears, making this transition more complicated to observed experimentally.

My opinion is that, after the first thermal cycle, the ferroelectric-ferroelectric transition disappears completely since the dielectric constant presents the same behavior as in the “unpoled” state and that the diffraction experiments as a function of temperature (conducted on “unpoled” samples) have not revealed any phase transition (Sec.3.5.3). Thus, the large electric field applied during the poling procedure would induce a phase transition between two ferroelectric phases and the electrically induced ferroelectric phase is unstable with temperature leading to the appearance of a ferroelectric-ferroelectric phase transition. This induction of a different ferroelectric phase under large electric fields could be evidenced by conducting X-ray diffraction on a “poled” sample. However, differentiating the changes in the structure related to change in the domain pattern or to a change in the structure may be difficult since the “unpoled” structure of PYN-PT 0.50 has not yet been completely understood.

In all cases, the presence of a ferroelectric-ferroelectric phase transition, at least in the first thermal treatment, may induce large fatigue in the sample. It was shown that it is possible to engineer the composition in order to shift the ferroelectric-ferroelectric transition to lower temperature by doping with barium or strontium as it was demonstrated to decrease the ferroelectric-ferroelectric transition temperature in PYN-PT [47, 107].

For applications at 200 °C, PYN-PT 0.40 and PYN-PT 0.45 are two serious candidates, since at this temperature, both compositions have large piezoelectric coefficient d_{33} . At room temperature, the values of the piezoelectric coefficient are lower than the ones of PYN-PT 0.30 or PYN-PT 0.50, but remains high: $\sim 300\text{-}500$ pC/N, i.e. in the typical range of values found for PZT.

However, instability issues may arise for PYN-PT 0.40 when using at 200 °C since this composition undergoes a ferroelectric-ferroelectric (FE-FE) phase transition at about 220 °C. This issue should not arise with PYN-PT 0.45 since the temperature of the FE-FE phase transition is much higher (~ 280 °C). Nonetheless, when considering using PYN-PT 0.45, between room temperature and 200 °C, one should take into consideration the strong dependence of the piezoelectric coefficient d_{33} .

In conclusion, for actuator applications at room temperature PYN-PT 0.30 is a promising piezoelement material. For applications up to 200 °C, PYN-PT 0.45 and PYN-PT 0.50 are suitable. If temperature stability is a strong requirement, PYN-PT 0.50 may be preferred with the possible need to engineer the exact composition to be used in the actuator design.

5.3.2 Electrostriction

Piezoelectrics are the dominant transduction material for ultrasonic and medical applications [108]. However, various limitations arise from the use of piezoelectrics in transducers: mechanical, electrical and thermal limitations.

The most common mechanical failure in transducers is the fracture of the piezoelectric ceramic

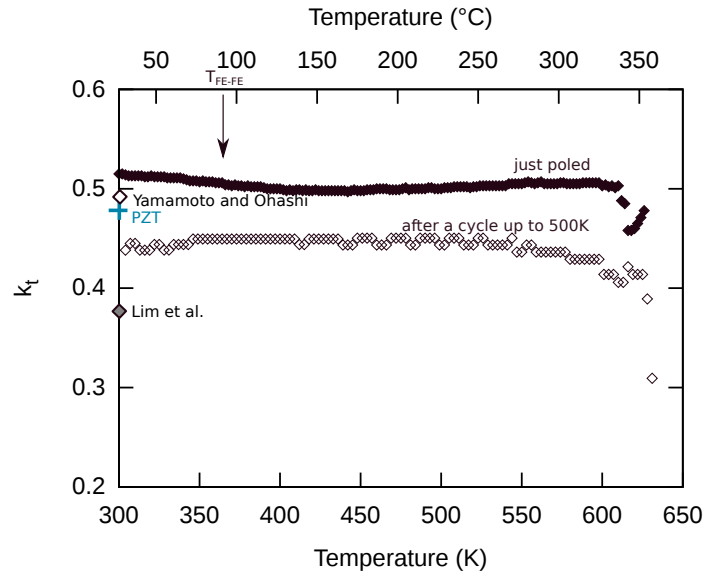


Figure 5.9: Thermal evolution of the thickness electromechanical coupling coefficient for PYN-PT 0.50 as a function of temperature measured after poling ("just poled") and after a thermal treatment up to 500 K ("after a cycle up to 500 K").

The thickness electromechanical coupling coefficients for PYN-PT published by Lim et al. [47] and Yamamoto and Ohashi [19], as well as the values of PZT are reported for comparison.

or breaking of the electrode-piezoceramic bond.

Furthermore, when operating the transducers at large electric field, electrical fatigue may arise, as well as insulation breakdown and depolarization of the piezoelectric active material leading to electrical deterioration of the transducer.

Finally, thermal limitations in the transducers emanate from the depolarization at the Curie temperature of the piezoelectric materials and from energy dissipation through electrical and mechanical losses mainly [108].

Using *electrostrictive* materials as active elements in transducers has been shown to limit the electrical and thermal limitations of the piezoelectric-based transducers.

Aging and electric fatigue mechanisms in electrostrictive materials are less pronounced than in their piezoelectric counterparts since the electrostrictive response does not involve domain wall motions as in piezoelectricity. Indeed it is mainly the pinning of domain wall motions on defects that is responsible for the decrease of the piezoelectric response with time.

Furthermore, as electrostriction exists in all dielectric materials regardless of the structure, electrostriction persists above the Curie temperature in the cubic phase. In addition the electrostrictive coefficient Q_{33} is usually viewed as temperature independent as predicted by the Landau theory even though some variations have been observed (but much lower than their piezoelectric counterpart) [109].

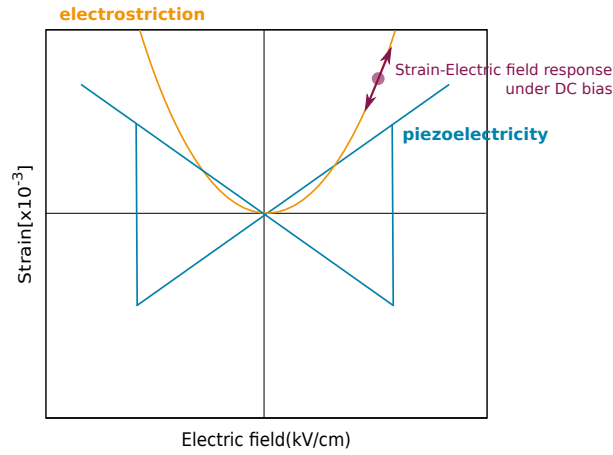


Figure 5.10: Schematic representation of the strain-electric field response of piezoelectrics and electrostrictive materials.

Nonetheless, the strain induced at zero electric field by electrostrictive materials is low compared to the one that can be obtained in piezoelectrics. However, under the application of a DC bias, the strain-electric field response of electrostrictive materials can be extremely large (larger than soft PZT) (Fig.5.10) and almost linear making electrostrictive materials good candidate for transducers or actuators, under DC bias.

Applications of electrostrictive materials

Electrostrictive materials are often used as actuators: the most famous electrostrictive actuator is probably the one design by NASA to recover the optical performance of the Hubble space telescope [110]. Moreover, electrostrictive materials are used in ultrasonic vibrators capable of generating torsional and longitudinal vibrations as well as a combination of the two vibrations [111].

Finally in the case where the electrostrictive materials is also a relaxor, applications based on the dependency of the electromechanical, dielectric and elastic properties on frequency have been developed. For example, in the medical industry, the large bandwidth of relaxors enables the usage of transducers on a broader frequency range achieving deep penetration and high resolution within one transducer, whereas two transducers were necessary to obtain both characteristics previously [112].

Electrostriction in PYN-PT

Electrostrictive properties of ceramics are usually evaluated with the coefficient M_{33} and Q_{33} presented in Eq.(5.5) and Eq.(5.6) that describe the strain response to electric field and polarization, respectively.

The electrostrictive response was measured in PYN-PT at the lowest temperature allowing the

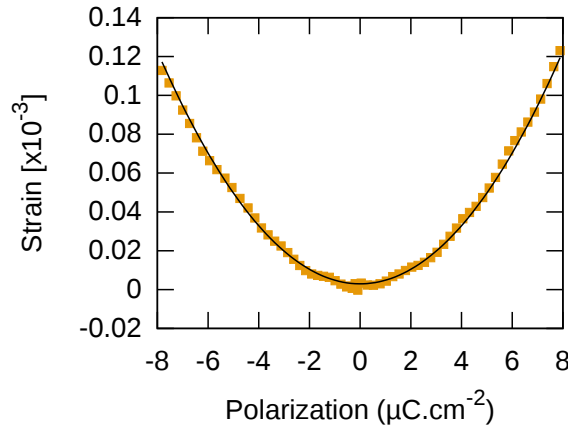


Figure 5.11: Strain-electric field relationship of PYN-PT 0.20 at 100 °C. The line represents the fit of the Q_{33} electrostrictive coefficient.

strain response to be primarily quadratic and so that the conduction is not too large. Measurements were therefore conducted at various temperatures for different compositions. In these experimental conditions, the electrostrictive coefficient Q_{33} was measured since it is temperature independent on the contrary to M_{33} .

An example of the strain-polarization response displaying an electrostrictive response is presented in Fig.5.11. The electrostrictive coefficient Q_{33} for various compositions in the PYN-PT solid solutions is presented in Fig.5.12. The Q_{33} values for PYN-PT $0.16 \leq x \leq 0.35$ are comparable to the ones observed in PMN-PT.

For PYN-PT $0.40 \leq x \leq 0.50$, the values of the Q_{33} coefficient are rather large and may be due to contribution of piezoelectricity to the strain-polarization response. Indeed, even though the Q_{33} coefficient was determined at a temperature higher than the temperature of the maximum of the dielectric constant T_m (~ 300 - 400 °C), it is possible that the meso-domains that we have proposed to exist between T_m and the pseudo-Burns temperature T_{Cr} may contribute non-negligibly to the strain-polarization response (evidenced by a slight opening of the strain-polarization response). Measurements at higher temperatures were not possible due to conduction mechanism preventing the measurement of the polarization.

Therefore, the values of Q_{33} measured in the compositional range $0.40 \leq x \leq 0.50$ should be regarded with caution.

In conclusion, in the compositional range in which the electrostriction response can be determined with certainty ($0.16 \leq x \leq 0.35$), the values of Q_{33} for PYN-PT are comparable to the ones of PMN-PT making PYN-PT a good substitute for PMN-PT, the most commonly used electrostrictive material today.

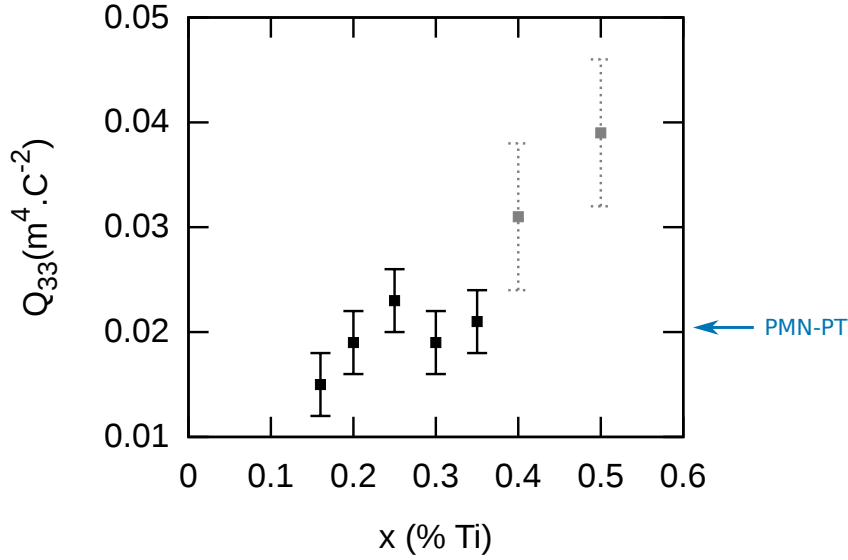


Figure 5.12: Evolution of the electrostriction coefficient Q_{33} as a function of composition. The values obtained for PYN-PT 0.40 and PYN-PT 0.50 are influence by piezoelectric response and should be considered with caution.

5.3.3 Ferroelectric Memory devices

A potential applications of the PYN-PT solid solution that is not related to its elastic properties, but to its ferroelectric properties is for ferroelectric memory devices applications. Ferroelectric memory devices (FeRAM) are used to replace flash memories because FeRAMs consume less power and offer higher speed and endurance to multiple read-and-write operations [113]. Today, the ferroelectric material used in such memory devices is PZT because of its large remnant polarization and low coercive field.

The coercive field and remnant polarization of the PYN-PT solid solution at room temperature and at 200 °C are presented in Fig.5.13.

With a maximum of the remnant polarization at $30 \mu\text{C}/\text{cm}^2$ for $x=0.40$, the PYN-PT solid solution displays lower remnant polarization than PZT. The coercive field in the PYN-PT solid solution is, on the other hand, comparable to the one of PZT in the compositional range $0.30 \leq x \leq 0.45$. Hence, replacing PZT by PYN-PT would not bring any improvement for ferroelectric memory device applications designed to work at room temperature. It is though possible that doping engineering in PYN-PT, as it has been done in PZT, may lead to a material presenting ferroelectric properties interesting enough for FeRAM applications.

Furthermore, in the compositional range $0.40 \leq x \leq 0.50$, ferroelectric hysteresis cycles persist up to 200 °C. These hysteresis cycles present reasonably high remnant polarization and significant coercive fields (that would lead to instability of the FeRAM device) indicating an excellent temperature stability of PYN-PT and possible FeRAM applications at such at high temperatures.

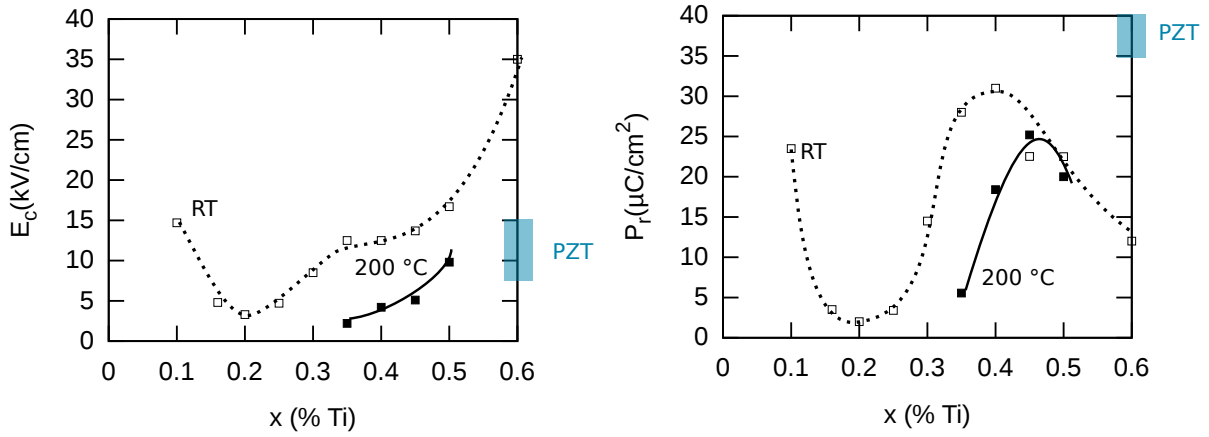


Figure 5.13: Remnant polarization (P_r) and coercive field (E_c) as a function of composition at room temperature (open symbol) and 200 °C (filled symbols). Lines are guide for the eyes.

In the event where PYN-PT would be used as the active material in FeRAMS, it would be necessary to process PYN-PT under thin-film form. Research is being carried out in the preparation of PYN-PT thin films and their possible integration on Si [114–116].

Most of the research on PYN-PT thin films has focused on the piezoelectric properties for MEMS applications. Indeed PYN-PT was shown in Sec.5.3.1 to have piezoelectric properties larger than the ones of PZT with a slightly larger temperature stability as well as piezoelectric properties comparable to the ones of PMN-PT with a much larger temperature usage range. Therefore, PYN-PT is not a temperature-piezoelectric properties compromise but displays both high-temperature stability and high piezoelectric coefficient.

5.4 FURTHER IMPROVEMENT OF THE MATERIAL

PYN-PT was shown to be suitable for a large number of applications. However, it is possible to tailor the properties to meet as closely as possible the application requirements by slightly changing the chemical content through doping as it was done in PZT or by changing the form of the material as it was done by processing PMN-PT as single crystals, for example.

In the literature, enhancement of the piezoelectric properties of ceramic PYN-PT was conducted by forming ternary solid solutions such as PYN-PZ-PT [56] or PYN-PMN-PT [57]. These ternary solid solutions display piezoelectric coefficient d_{33} up to 600 pC/N without degradation of the Curie temperature. These values of piezoelectric coefficient and Curie temperature are comparable to the values we report for PYN-PT 0.50, but $\sim 20\%$ larger than what was reported for PYN-PT 0.50 ceramic in the literature [47, 50] (see Table 1.4, page 48 for a summary of the piezoelectric coefficient measured on PYN-PT close to the MPB).

The processing method (mechanosynthesis) used to obtain the ceramics in this study leads to extremely high purity and high density ceramics with a grain size close to $1\text{ }\mu\text{m}$ that was shown to be the optimal grain size values for other Pb-based piezoelectric materials [117, 118]. Therefore, based on the literature and our results, there is no clear improvement of the piezoelectric properties by forming ternary solid solutions. However, since ternary solid solutions lead to an improvement of about 20 % compared to PYN-PT processed in similar conditions, it would be interesting to study ternary solid solution processed using mechanosynthesis to see if a 20 % improvement of the properties can also be observed compared to PYN-PT processed the same way.

To enhance the piezoelectric properties, in this work, we have focused on improving the quality of the ceramics by conducting liquid phase sintering carried out by PbO doping during the mechanosynthesis. Several amounts (1 wt%, 3 wt%, 5 wt% and 10 wt%) were tested and their effect on the density, dielectric properties and piezoelectric properties were compared (Fig.5.14). In Fig.5.14(a), it appears that adding PbO leads to a decrease of the density and an increase in the grain size. Thus, the addition of PbO helps the chemical diffusion during sintering leading to larger grain size in samples with more PbO. But PbO remains at the grain boundaries and its plaque-shape after crystallization does not fill the space at grain boundaries leading to large pores and therefore low density of the samples. Therefore, the addition of PbO improves the chemical diffusion by creating a liquid phase during the sintering process but restricts the densification process.

Actually, an optimal amount of additional PbO (1 wt%) has been found to lead to an improvement of the dielectric constant and the piezoelectric coefficient d_{33} ($\sim 30\%$ compared to the value without any addition of PbO) due to the improvement of the strength of the grain boundaries. Indeed, the SEM images (Fig.5.14(b)) taken on fractured samples show that the fracture occurs solely at the grain boundaries without addition of PbO, whereas with addition of 1 wt% PbO, the fracture happens also through the grains indicating that the mechanical toughness of the grain boundaries is similar to the one of grains for sample with 1 wt% additional PbO.

Therefore, adding a small amount of PbO enables a liquid phase sintering improving the quality of the samples, hence of the dielectric and piezoelectric properties, but further addition of PbO has a detrimental effect on both the quality of the samples and the macroscopic properties.

Doping with a small amount of PbO is a good starting point to improve the properties and trying different (additional) chemical elements may lead to further enhancement of the properties.

In addition to changes in the chemical formulation, piezoelectric properties can be altered by modifying the microstructure of the ceramic samples. In particular, texturing, i.e. orienting the grains of the ceramic into one direction, has been shown to enhance the properties of ceramics. For example, Saito et al. [119] showed that textured lead-free materials display properties comparable to PZT. However, the texturing technique used by Saito et al. [119] is not really scalable to industrial needs.

Nevertheless, texturing techniques more adaptable to industrial production have shown a doubling of the piezoelectric coefficient d_{33} without a large increase of the processing costs proving that texturing is a good way to get high properties with reasonable processing costs [120].

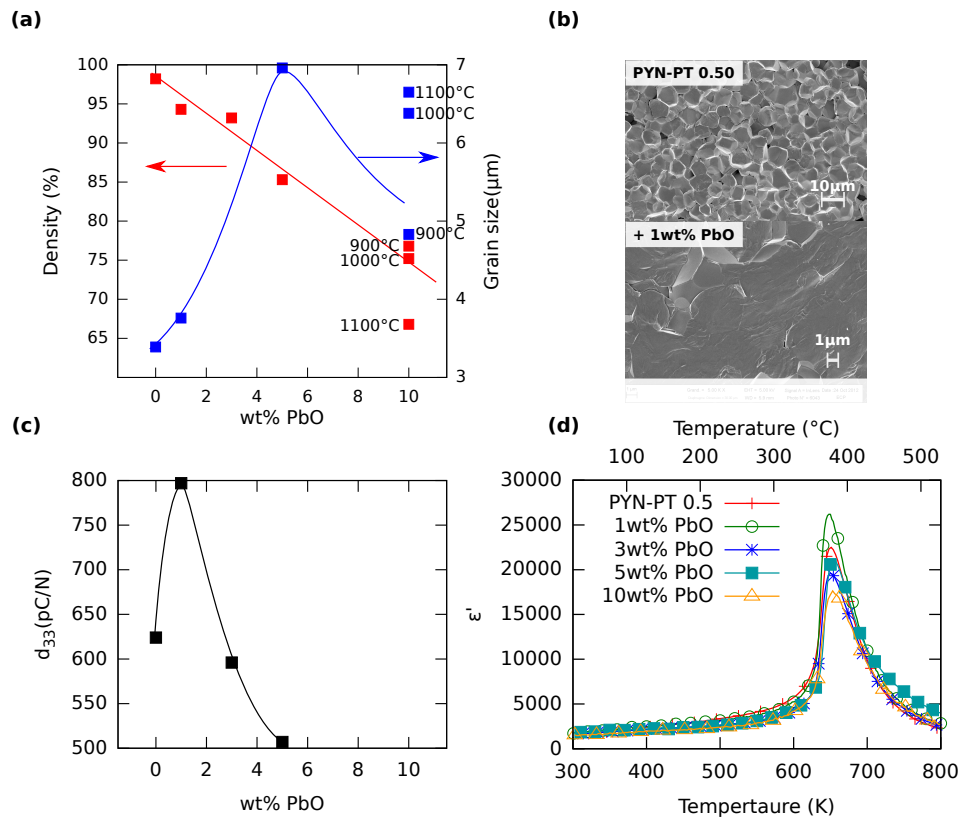


Figure 5.14: Influence of PbO doping on (a) density and grain size, (b) microstructure, (c) piezoelectric coefficient d_{33} and (d) dielectric constant.

Moreover, PYN-PT in single crystal form have been reported to achieve an improvement by a factor three in piezoelectric properties compared to ceramics (see Table 1.4, page 48). This enhancement of the properties with the use of single crystals is comparable to the one observed in PMN-PT.

In conclusion, PYN-PT is a material with the high piezoelectric properties of PMN-PT and the large temperature stability of PZT and these properties can be further developed by doping or changing the final form of the piezoelement.

5.5 CONCLUSION

In this section, some of the potential applications of the PYN-PT solid solutions have been presented, in particular within the framework of the industrial partner Schlumberger. Hereafter is a list of compositions suitable for potential actuator, electrostrictive and memory devices applications:

- PYN-PT 0.30 is a good candidate for actuators but is limited to slightly above room temperature (up to 100 °C) applications.
- PYN-PT 0.45 and PYN-PT 0.50 could be both used for actuator applications up to 200 °C with the choice between the two compositions based on the precise need of the application in terms of temperature stability and piezoelectric properties.
- PYN-PT with $0.16 \leq x \leq 0.30$ present electrostrictive properties comparable to PMN-PT, the most common electrostrictive material used nowadays.
- PYN-PT $0.40 \leq x \leq 0.50$ could be used for ferroelectric device applications desgined to work up to at least 200 °C.

Furthermore, the properties of PYN-PT could be even more enhanced by doping it or by changing the final shape using textured ceramic or single crystals for example.

Finally, all possible applications of PYN-PT were not examined and further applications of this solid solution could be found. For example, PYN-PT could also be used in a composite form for imagery applications at high temperature, given that a polymer could be found that resists well up to the needed temperature.

In conclusion, due to the versatility of the polar ordering and therefore properties present in the PYN-PT solid solution, the number of potential applications of this solid solution is extremely large (unlimited?) and some functionalities remain to be discover.

- CHAPTER 6 -

SUMMARY AND UNIFIED PHASE DIAGRAM

The perovskite solid solution $\text{Pb}(\text{Yb}_{1/2}\text{Nb}_{1/2})\text{O}_3\text{-PbTiO}_3$ (PYN-PT) is long-known to present high piezoelectric properties and high Curie temperature. This solid solution has nevertheless attracted little attention because its processing is a rather delicate task.

In this work, motivated by the potential piezoelectric applications of this solid solution at temperatures up to 200 °C (~ 470 K), the phase diagram was studied intensively.

To this end, the PYN-PT phase diagram was investigated separately from a dielectric, ferroelectric and piezoelectric properties point of view (in Chapter 2), on the one hand, and, on the other hand, from the point of view of the structure (in Chapter 3).

Summary

The study of the properties has confirmed the existence of all polar orders at room temperature: antiferroelectric (AFE), relaxor (RFE) and ferroelectric (FE). Moreover, this study has revealed that the relaxor state, in the intermediate compositional range ($0.10 \leq x \leq 0.40$), is strongly influenced by the antiferroelectricity and ferroelectricity existing at smaller and larger Ti content, respectively. This has led me to propose that three types of relaxors exist in the PYN-PT solid solution ($x = 0.16\text{-}0.20$, $x = 0.25\text{-}0.30$ and $x = 0.35\text{-}0.40$).

The examination of the structure has demonstrated that the structure of the PYN-PT solid solution is more complicated than expected from the literature, and in particular, that the structure of the morphotropic phase boundary (MPB) cannot be simply understood by analogy with other Pb-based systems. Indeed, the structure of PYN can only be partly explained by the modulation vectors proposed in the literature. I suggested that, in PYN, not only the Pb^{2+} cations are displaced in an antiparallel fashion, but also the B-site cations. Furthermore, the Pb^{2+} cations were shown to be displaced parallel to the modulation vector and not perpendicularly to it as in all other Pb-based antiferroelectrics.

Moreover, on the Ti-poor side of the MPB, the rhombohedral phase reported, up to now, in all Pb-based solid solutions could not be evidenced. This absence of rhombohedral phase was explained by a different local organization of the Pb^{2+} displacements.

The separate studies of the evolution of the dielectric, ferroelectric and piezoelectric properties (in Chapter 2), on the one hand, and, on the other hand, the evolution of the structure (in Chapter 3) with composition and temperature has enable me to propose two phase diagrams (Fig.2.23 and Fig.3.28).

The comparison of these two phase diagrams in Chapter 4 has shown an agreement for most of the compositions and temperatures. This comparison has enabled me to propose a model explaining continuously the evolution of the structure and properties in the PYN-PT solid solution. This model relies on an organization of Pb^{2+} displacements at a local scale. This organization being itself influenced by the chemical nature and arrangement of the B-site cations.

Finally, some of the potential applications of the PYN-PT solid solution were presented in Chapter 5. Focus has been made on the piezoelectric and electrostrictive applications, as well as potential FE memory devices applications.

Some of the studied compositions appeared more optimal for some applications, especially around the MPB.

Unified phase diagram: Fig.6.1

PYN is a double perovskite that presents antiferroelectric properties with a complicated structure. This structure could be described using an average monoclinic structure modulated with two modulation vectors accounting for the antiparallel displacements of both Pb^{2+} and B-site cations.

With a small addition of Ti, the PYN-PT solid solution keeps the same structure and polar order ($x < 0.10$).

For larger amount of Ti added to PYN, the antipolar properties decreases and gives way to more random organization of the Pb^{2+} displacements. This coexistence of antipolar and random (directional) organization of the Pb^{2+} displacements leads to the appearance of the rhombohedral phase with SSRs due to antiparallel ordering of PYN-PT 0.10.

With further addition of Ti ($0.16 \leq x \leq 0.40$), a relaxor state appears. This relaxor state is (even more) complex than the one of "classical" relaxors since it is highly influenced by the antiferroelectricity and ferroelectricity of the two end-members of the solid solution, as well as the chemical order on the B site present for compositions up to $x = 0.35$.

This relaxor state persists at high temperature up to the composition with the highest amount of Ti considered in this study ($x = 0.60$). However, for compositions in the range $0.45 \leq x \leq 0.60$, the high-temperature relaxor state undergoes a spontaneous transitions toward a low-temperature ferroelectric state. This ferroelectric state keeps one of the characteristic of relaxors: positional disorder of Pb^{2+} .

The structure of the compositions exhibiting ferroelectricity at room temperature can be described by a coexistence of monoclinic and tetragonal phases (whose space groups and ratio depends on the composition). Moving away from this ferroelectric phase and toward the relaxor state, the tetragonal distortions disappear completely at room temperature and the monoclinic distortions decreases until they are no longer observable ($0.16 \leq x \leq 0.25$).

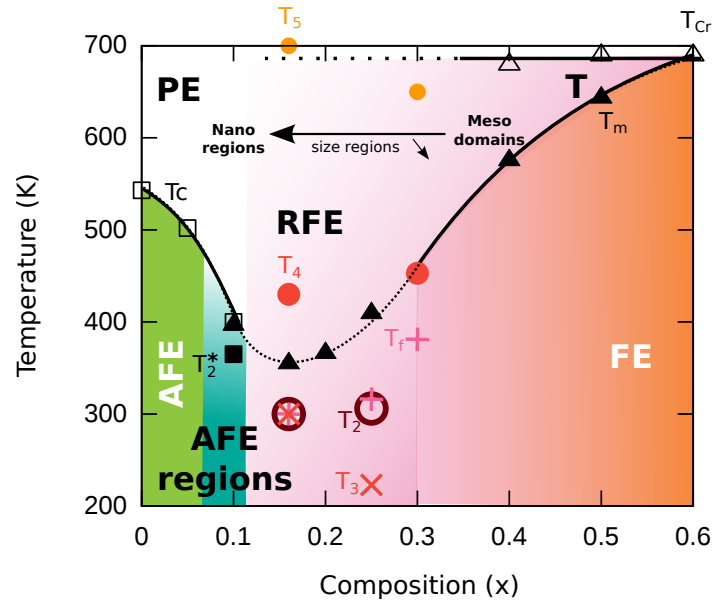


Figure 6.1: Unified phase diagram in the PYN-PT solid solution.

The various critical temperatures observed during the examination of the properties and structure are reported.

Colors represent the different macroscopic polar orders.

Finally, the evolution of the polar order and structure as a function of the composition and temperature has been proposed to be the result of the competition between the antipolar order favorable when the B-site cation are ordered in a rock-salt arrangement and the polar order favorable to Ti and Pb. In particular, it is the competition between these two orders that leads to the appearance of the relaxor state in the PYN-PT solid solution. This raises the question of whether the relaxor state in other relaxors is also the result of the competition between different polar orders.

BIBLIOGRAPHY

- [1] B Jaffe, W. R. Cook, and H Jaffe. *Piezoelectric Ceramics*. 1971.
- [2] K. Uchino. *Ferroelectric Devices*. 2009.
- [3] C Kittel. *Physcial Review*, 82:729–732, 1951.
- [4] F. Jona and G. Shirane. *Ferroelectric Crystals*. MacMillan, New York, 1962.
- [5] Karin M. Rabe. *Antiferroelectricity in Oxides: A Reexamination*, pages 221–244. Wiley-VCH Verlag GmbH & Co. KGaA, 2013.
- [6] A. A. Bokov and Z.-G. Ye. *Journal of Materials science*, 41:31–52, 2006.
- [7] G.A. Smolenskii, V.A. Isupov, A.I. Agranovskaya, and S.V. Propov. *Soviet Phys.Solid State*, 2:2584, 1961.
- [8] L.E. Cross. *Ferroelectrics*, 76:241, 1987.
- [9] Dwight Viehland, S. J. Jang, L. Eric Cross, and Manfred Wuttig. *Journal of Applied Physics*, 68(6):2916, 1990.
- [10] V. Westphal, W. Kleeman, and M.D. Glinchuk. *Phys. Rev. Lett*, 68:2469, 1992.
- [11] R. Pirc, R. Blinc, and V.S. Vikhnin. *Phys. Rev. B*, 72:014202, 1999.
- [12] P. Gehring, H. Hiraka, C. Stock, S.-H. Lee, W. Chen, Z.-G. Ye, S. Vakhrushev, and Z. Chowdhuri. *Physical Review B*, 79(22):224109, June 2009.
- [13] B. Noheda, D. E. Cox, G. Shirane, J. A. Gonzalo, L. E. Cross, and S-E. Park. *Applied Physics Letters*, 74(14):2059, 1999.
- [14] B Noheda. *Current Opinion in Solid State Materials Science*, 6:27–34, 2002.
- [15] R. Haumont. *Rotation de la polarisation dans le systèmes morphotropiques: cas de $Pb(Sc_{1/2}Nb_{1/2})O_3$ - $PbTiO_3$* . PhD thesis, École Centrale Paris, 2004.
- [16] J. Carreaud. *Effet de Taille dans les Poudres et Ceramiques de Composés Ferroélectriques Relaxeurs à base de Plomb*. PhD thesis, Ecole Centrale Paris, 2007.

-
- [17] M.T Anderson, K. B. Greenwog, G. A. Taylor, and K. R. Poeppelmeier. *Prg. Solid. St. Chem.*, 22:197–233, 1993.
- [18] L. Bellaiche and David Vanderbilt. *Physical Review Letters*, 81(6):1318–1321, August 1998.
- [19] T Yamamoto and S Ohashi. *Japanese Journal of Applied Physics*, 34:5349–5353, 1995.
- [20] A. K. Singh and Akhilesh Kumar Singh. *Integrated Ferroelectrics*, 117(1):129–138, 2010.
- [21] S. B. Park and W. K. Choo. *Jpn.J.Appl.Phys*, 39:5560–5564, 2000.
- [22] A.A. Bokov and Z.-G Ye. *Solid State Communications*, 116(2):105–108, September 2000.
- [23] O. Bidault, C. Perrin, C. Caranoni, and N. Menguy. *Journal of Applied Physics*, 90(8):4115, 2001.
- [24] P Groves. *Journal of Physics C: Solid State Physics*, 19(26):5103–5120, September 1986.
- [25] Taketoshi Fujita, Osamu Fukunaga, Takehiko Nakagawa, and Shoichiro Nomura. *Materials Research Bulletin*, 5(4):759–764, 1970.
- [26] G. Baldinozzi. *Étude des transitions de Phases des Pérovskites Complexes Ordonées au Plomb: Pb_2CoWO_6 , Pb_2MgWO_6 et Pb_2MgTeO_6* . PhD thesis, Université Paris 6, 1994.
- [27] Nathascia Lamps, Philippe Sciau, and Alessandra Geddo Lehmann. *J. Phys.:Condens. Matter*, 11:3489–3500, 1999.
- [28] A.N. Salak, N.P. Vyshatko, V.M. Ferreira, N.M. Olekhovich, and A.D. Shilin. *Materials Research Bulletin*, 38(3):453–460, February 2003.
- [29] A. A. Bokov, V. Y. Shonov, I. P. Raypevsky, E. S. Gagarina, and M. F. Kuprianov. *Journal of Physics: Condensed Matter*, 5:5491–5504, 1993.
- [30] C. Malibert. *Ordre et desordre dans la perovskite ferroelectrique relaxeur $Pb(Sc_{1/2}Nb_{1/2})O_3$* . PhD thesis, Univeristé Paris 6, 1998.
- [31] K. Z. Baba-Kishi and D. J. Barber. *Journal of Applied Crystallography*, 23(1):43–54, 1990.
- [32] K. Alilat. *Matériaux piézoélectriques pour applications transducteurs acoustiques de puissance: PIN-PT nanocéramiques et PMN-PT céramiques texturées*. PhD thesis, Ecole Centrale Paris, 2008.
- [33] A. Salaka, M. V. Bushinsky, N. V. Pushkarov, A. D. Shilin, N. M. Olekhovich, and N. P. Vyshatko. *Ferroelectrics*, 234(1):123–127, January 1999.
- [34] W Dmowski, M K Akbas, P K Davies, and T Egami. *Journal of Physics and Chemistry of Solids*, 61:229–237, 2000.

- [35] Edward F. Alberta and Amar S. Bhalla. *Ferroelectrics Letters Section*, 26(5-6):117–123, December 1999.
- [36] L.I Shvornera and *et al.* *Soviet Physics JETP*, 22:722–724, 1966.
- [37] E.G. Fensenko. *Perovskite Family and Ferroelectricity*. Moscow, atomizdat edition, 1972.
- [38] Edward F Alberta, Paul W Rehrig, Wesley S Hackenberger, Clive A Randall, and Thomas R. Shrout. *IEEE Symposium on Ultrasonics, 2003*, pages 1991–1994, 2003.
- [39] Yu. Ya Tomashpol'skii and Yu. N. Venevtsev. *Soviet Physics - Solid State*, 6(10):2388–2392, 1965.
- [40] Jeong Rok Kwon and Woong Kil Choo. *Journal of Physics: Condensed Matter*, 3:2147–2155, 1991.
- [41] Antoni Kania. *Journal of Crystal Growth*, 310(11):2767–2773, May 2008.
- [42] V Demidova, E Gagarina, T Ivanova, and V Sakhnenko. *Ferroelectrics*, 159:191–196, 1994.
- [43] N Yasuda and H Inagaki. *Japanese Journal of Applied Physics*, 30(12A):L2050–L2051, 1991.
- [44] Jeong Rok Kwon, C.K.K. Choo, and Woong Kil Choo. *Japanese Journal of Applied Physics*, 30(5):1028–1033, 1991.
- [45] R. Faye. *Structure et Propriétés d'un antiferroélectrique modèle : PbZrO₃*. PhD thesis, Ecole Centrale Paris, 2014.
- [46] H Lim, J Kim, and W L Choo. *Japanese Journal of Applied Physics*, 34:5449–5452, 1995.
- [47] Jong Bong Lim, Shujun Zhang, and Thomas R. Shrout. *Journal of Electroceramics*, 26(1-4):68–73, February 2011.
- [48] Shujun Zhang, Shashank Priya, Eugene Furman, Thomas R. Shrout, and Clive A. Randall. *Journal of Applied Physics*, 91(9):6002, 2002.
- [49] Naohiko Yasuda, Hidehiro Ohwa, Motoyuki Kume, Yasuharu Hosono, Yohachi Yamashita, Shinnichirou Ishino, Hikaru Terauchi, Makoto Iwata, and Yoshihiro Ishibashi. *Japanese Journal of Applied Physics*, 40:5664–5667, 2001.
- [50] Cihangir Duran, Susan Trolier-m, and Gary L Messing. *Journal of Electroceramics*, 10(1):47–55, 2003.
- [51] Noliac A/S. Piezo materials specification, Sept 2014. URL <http://www.noliac.com/Default.aspx?ID=141>.
- [52] Shujun Zhang, Paul W. Rehrig, Clive Randall, and Thomas R. Shrout. *Journal of Crystal Growth*, 234(2-3):415–420, 2002.

- [53] Shujun Zhang, Sorah Rhee, Clive A. Randall, and Thomas R. Shrout. *Japanese Journal of Applied Physics*, 41(Part 1, No. 2A):722–726, 2002.
- [54] Ltd. APC International. Specifications of PMN-PT single crystals (PMN-32%PT), Oct 2014. URL <https://www.americanpiezo.com/product-service/pm-n-pt.html>.
- [55] H.C. Materials Corporation. Piezoelectric pmn-pt single crystal products, Oct 2014. URL http://www.hcmat.com/Pmn_Products.html.
- [56] W.M. Zhu and Z.-G. Ye. *Ceramics International*, 30(7):1443–1448, 2004.
- [57] Chao He, Xiuzhi Li, Zujian Wang, Ying Liu, Dongquan Shen, Tao Li, and Xifa Long. *Materials Research Bulletin*, 48(1):131–136, 2013.
- [58] G Shirane, R Pepinski, and B. C. Frazer. *Acta Crystallog.*, 9:131, 1956.
- [59] A. Kania, A. Majda, S. Miga, and A. Slodczyk. *Physica B: Condensed Matter*, 400(1-2):42–46, 2007.
- [60] Ph Sciau, N Lampis, and A Geddo-Lehman. *Solid State Communications*, 116:225–230, 2000.
- [61] M.E. Lines and A. M. Glass. *Principles and Applications of Ferroelectrics and Related Materials*. 2009.
- [62] R. Haumont, J. Carreaud, P. Gemeiner, B. Dkhil, C. Malibert, A. Al-Barakaty, L. Bellaiche, and J. M. Kiat. *Phase Transitions*, 79(1-2):123–134, January 2006.
- [63] D. Damjanovic. Hysteresis in Piezoelectric and Ferroelectric Materials. In *The Science of Hysteresis*, volume 3, pages 337–461. 2005.
- [64] N. Srivastava and G. J. Weng. *Journal of Applied Physics*, 99(5):054103, 2006.
- [65] A. A. Bokov, Y.-H. Bing, W. Chen, Z.-G. Ye, S. Bogatina, I. Raevski, S. Raevskaya, and E. Sahkar. *Physical Review B*, 68(5):052102, August 2003.
- [66] M. Tyunina, M. Plekh, M. Antonova, and A. Kalvane. *Physical Review B*, 84(22):224105, December 2011.
- [67] V. A. Chaudari and G. K. Bichile. *Smart Mater. Res.*
- [68] O. E. Fesenko, R. V. Kolesova, and Yu. G. Sindeyev. The structural phase transitions in lead zirconate in super-high electric fields. *Ferroelectrics*, 20(1):177–178, January 1978.
- [69] B. Dkhil, P. Gemeiner, A. Al-Barakaty, L. Bellaiche, E. Dul’kin, E. Mojaev, and M. Roth. *Physical Review B*, 80(6):064103, August 2009.
- [70] Gerald Burns and F H Dacol. Glassy Polarization Behavior in Ferroelectric Compounds $\text{Pb}(\text{Mg}_{1/3}\text{Nb}_{2/3})\text{O}_3$ and $\text{Pb}(\text{Zn}_{1/3}\text{Nb}_{2/3})\text{O}_3$. *Solid State Communications*, 48:853–856, 1983.

- [71] Harold T Stokes, H Erich, Dorian M Hatch, and Christopher J Howard. *Acta Crystallographica B*, (B58):934–938, 2002.
- [72] R. Haumont, B. Dkhil, J. Kiat, A. Al-Barakaty, H. Dammak, and L. Bellaiche. *Physical Review B*, 68(1):014114, July 2003.
- [73] J. Carreaud, J. M. Kiat, B. Dkhil, M. Algueroo, J. Ricote, R. Jimenez, J. Holc, and M Kosec. *Applied Physics Letters*, 89(25):252906, 2006.
- [74] N Zhang, H Yokota, A M Glazer, and P A Thomas. *Acta Crystallographica B*, B67:386–398, 2011.
- [75] L Bellaiche, A Garcia, and David Vanderbilt. *Physical Review Letters*, 84(1):5427–5430, 2000.
- [76] Helen Megaw and C N W Darlington. *Acta Crystallographica A*, 31:161, 1975.
- [77] N De Mathan, E Husson, G Calvarin, J R Gavarri, A W Hewat, and Morell A. *Journal of Physics: Condensed Matter*, 3:8159–8171, 1991.
- [78] Guangyong Xu, Z. Zhong, Y. Bing, Z.-G. Ye, C. Stock, and G. Shirane. *Physical Review B*, 67(10):104102, 2003.
- [79] P. Gehring, W. Chen, Z.-G. Ye, and G. Shirane. *J. Phys.:Condens. Matter*, 16:7113–7121, 2004.
- [80] A. Lebon, H. Dammak, G Calvarin, and I. Ould Ahmedou. *J. Phys.:Condens. Matter*, 14:7035–7043, 2002.
- [81] R. Haumont, A. Al-Barakaty, B. Dkhil, J. Kiat, and L. Bellaiche. *Physical Review B*, 71(10):104106, March 2005.
- [82] A. M. Glazer. *Acta Crystallographica Section B*, 28(11):3384–3392, Nov 1972.
- [83] E Sawaguchi, H Maniwa, and S Hoshino. *Physical Review*, 83:1078, 1951.
- [84] G Baldinozzi, D Grebille, Ph Sciau, J. M. Kiat, J Moret, and J-F Bérar. *Journal of Physics: Condensed Matter*, 10:6461–6472, 1998.
- [85] P.A. Woodward. *Acta Cryst.*, B53:32–43, 1997.
- [86] L. Bellaiche and Jorge Íñiguez. *Physical Review B*, 88(1):014104, July 2013.
- [87] V. Petricek, M Dusek, and L. Palatinus. *Z. Kristallogr*, 229(5):345–353, 2014.
- [88] R.A. Young, editor. *The Rietveld Method*. International Union of Crystallography, 1993.
- [89] Gnuplot homepage, Feb 2015. URL <http://www.gnuplot.info/>.
- [90] R A Young and D B Wiles. *Journal of Applied Crystallography*, 15(4):430–438, 1982.

- [91] Crystallography open database, Oct 2014. URL <http://www.crystallography.net/>.
- [92] G Baldinozzi, Ph Sciau, M Pinot, and D Grebille. *Acta Crystallographica B*, 51:668–673, 1995.
- [93] R.L Snyder, J Fiala, and H.J. Bunge. International Union of Crystallography, 1999.
- [94] Yoshihiro Terado, Su Jae Kim, Chikako Moriyoshi, Yoshihiro Kuroiwa, Makoto Iwata, and Masaki Takata. *Japanese Journal of Applied Physics*, 45(9B):7552–7555, 2006.
- [95] Yoshihiro Kuroiwa, Yoshihiro Terado, Su Jae Kim, Akikatsu Sawada, Yasuhisa Yamamura, Shinobu Aoyagi, Eiji Nishibori, Makoto Sakata, and Masaki Takata. *Japanese Journal of Applied Physics*, 44:7151–7155, 2005.
- [96] Akhilesh Singh, Dhananjai Pandey, and Oksana Zaharko. *Physical Review B*, 74:1–18, 2006.
- [97] N. Zhang, H. Yokota, A. M. Glazer, Z. Ren, D. A. Keen, D. S. Keeble, P. A. Thomas, and Z.-G. Ye. *Nature Communications*, 5(May):5231, 2014.
- [98] P. E. Janolin, B. Dkhil, P. Bouvier, J. Kreisel, and P. A. Thomas. *Physical Review B - Condensed Matter and Materials Physics*, 73:1–9, 2006.
- [99] Bernd J. Maier, Ross J. Angel, William G. Marshall, Boriana Mihailova, Carsten Paulmann, Jens M. Engel, Marin Gospodinov, Anna Maria Welsch, Dimitrina Petrova, and Ulrich Bismayer. *Acta Crystallographica Section B: Structural Science*, 66:280–291, 2010.
- [100] Bruno Morosin, Eugene Venturini, and George Samara. *Ferroelectrics*, 377:120–136, 2008.
- [101] Z.-G. Ye, Y. Bing, J. Gao, A. Bokov, P. Stephens, B. Noheda, and G. Shirane. *Physical Review B*, 67(10):104104, March 2003.
- [102] M. Tyunina, M. Plekh, and J. Levoska. *Physical Review B*, 79(5):054105, February 2009.
- [103] Hirotsugu Ogi, Yasunori Kawasaki, Masahiko Hirao, and Hassel Ledbetter. *Journal of Applied Physics*, 92(2002):2451–2456, 2002.
- [104] Mohammad H. Malakooti and Henry A. Sodano. *Applied Physics Letters*, 102(6):061901, 2013.
- [105] IEEE. *IEEE Transactions on Ultrasonics, Ferroelectrics, and Frequency Control*, 87:717, 1996.
- [106] M. Guennou. *Modifications des propriétés structurales et électromécaniques de monocristaux piézoélectrique $\text{Pb}(\text{Zn}_{1/3}\text{Nb}_{2/3})_{1-x}\text{Ti}_x\text{O}_3$: ingénierie des domaines de dopage au manganèse*. PhD thesis, Ecole Centrale Paris, 2007.
- [107] Jong Bong Lim, Shujun Zhang, Thomas R ShROUT, Nano Functional, and Materials Group. *Phase Transitions*, 84(February 2015):95, 2011.

- [108] J. Coutte, B. Dubus, J. C. Debus, C. Granger, and D. Jones. *Ultrasonics*, 40:883–888, 2002.
- [109] L. E. Cross, Robert E Newnham, Amar S. Bhalla, J.P Dougherty, J.H. Adair, Varadan V.K, and Varadan V.V. Electrostrictive Materials For Tansducer Applications. Technical report, 1990.
- [110] J.L. Fanson. *MRS Proceedings*, 360, 1994.
- [111] S Mishiro. Ultrasonic Vibrator and a Method for Controllingly Driving Same. *United States Patent*, 4,812,697, 1989.
- [112] A Tai, J.F. Gelly, and S.E. Easterborrk. XDclear transducer technology, Feb 2015. URL www.channeltechgroup.com/publication/view/white-paper-single-crystals-ctg-powers-ges-xd-clear-technology/.
- [113] Fujitsu. Ferroelectric random acces memory (FRAM), Feb 2015. URL www.fujitsu.com/us/products/devices/semiconductor/memory/fram/.
- [114] Q. F. Zhou, Q. Q. Zhang, and S. Trolier-McKinstry. *Journal of Applied Physics*, 94(001):3397, 2003.
- [115] Wataru Sakamoto, Yoshiaki Masuda, and Toshinobu Yogo. *Journal of Alloys and Compounds*, 408-412:543–546, 2006.
- [116] N. Bassiri Gharb and S. Trolier-McKinstry. *Journal of Applied Physics*, 97(2005):064106, 2005.
- [117] K. Alilat, M. Pham Thi, H. Dammak, C. Bogicevic, A. Albareda, and M. Doisy. *Journal of the European Ceramic Society*, 30(9):1919–1924, July 2010.
- [118] J. Carreaud, P. Gemeiner, J. Kiat, B. Dkhil, C. Bogicevic, T. Rojac, and B. Malic. *Physical Review B*, 72(17):174115, November 2005.
- [119] Y Saito, H Takao, T Tani, T Nonoyama, K Takatori, T Homma, T Nagaya, and M Nakamura. *Nature*, 432(November):84, 2004.
- [120] G L Messing, S Trolier-McKinstry, E M Sabolsky, C Duran, S Kwon, B Brahmaroutu, P Park, H Yilmaz, P W Rehrig, K B Eitel, E Suvaci, M Seabaugh, and K S Oh. *Critical Reviews in Solid State and Materials Sciences*, 29(2):45–96, 2004.
- [121] J. Chaigneau, J. Kiat, C. Malibert, and C. Bogicevic. *Physical Review B*, 76(9):094111, September 2007.
- [122] American Society for Testing and Materials. pages E112–96, Reapproved 2004.
- [123] S. L. Swartz and T. R. Shrout. *Materials Research Bulletin*, 17:1245–1250, 1982.
- [124] V.V. Bhat, M.V. Radhika Rao, and A.M. Umarji. *Materials Research Bulletin*, 38(6):1081–1090, May 2003.

- [125] Yang Zupei, Zhou Shaorong, Qu Shaobo, Cui Bin, and Tian Changsheng. *Ferroelectrics*, 265(1):225–232, January 2002.
- [126] M Alguero, J Ricote, T Hungria, and A Castro. *Chem. Mater.*, 19:4982–4990, 2007.

- APPENDIX A -

INFLUENCE OF THE PROCESSING METHOD ON THE PB(YB_{1/2}NB_{1/2})O₃-PBTiO₃ SOLID SOLUTION

C. Cochard^{1,2}, F. Karolak¹, C. Bogicevic¹, O. Guedes² and P.E. Janolin¹

¹ Laboratoire Structure Propriétés et Modélisation des Solides (SPMS), Campus de Châtenay-Malabry
- CentraleSupélec, grande voie des vignes, 92295 Châtenay-Malabry Cedex, France

² Études et Productions Schlumberger, 1 rue H.Becquerel, 92140 Clamart, France

Abstract

New materials with high piezoelectric properties and a extended temperature usage range are needed for several industrial applications, such as the automobile or space industries. (1-x)Pb(Yb_{1/2}Nb_{1/2})O₃-xPbTiO₃ (PYN-PT x) solid solution is a good candidate for such high piezoelectric - high temperature applications. Ceramics were synthesized using different methods that include solid state reaction, reactive sintering, and mechanosynthesis. The effect of the processing method as well as the grain size was studied, enabling us to propose a novel chemical reaction mechanism for the formation of PYN-PT. The solid solution was investigated from a view point of crystallographic structure and dielectric properties.

A.1 INTRODUCTION

Solid solutions of complex perovskites have been extensively studied because of the large enhancement of the dielectric and piezoelectric properties at the morphotropic phase boundaries (MPB) [35, 62, 121]. To benefits from the excellent properties over a large range of temperature, a solid solution with a high Curie temperature at the MPB is needed. (1-x)Pb(Yb_{1/2}Nb_{1/2})O₃-xPbTiO₃ (PYN-PT) has been reported to have a Curie temperature of ~ 325 - 370 °C and a piezoelectric coefficient $d_{33} \sim 470$ - 510 pC/N at the MPB ($x = 0.50$)[19, 47] representing about a 30% increase of the piezoelectric properties compared to the commercially available PZT 5A with a similar Curie temperature.

In this work we shall show that the synthesis route of PYN-PT solid solution differs from other

$\text{Pb}(\text{B},\text{B}')\text{O}_3\text{-PbTiO}_3$ solid solutions as the two end members are formed before the solid solution. Binding agent appeared to be necessary to sinter powders obtained by solid state reaction into ceramics. We shall therefore compare these ceramics with those obtained by reactive sintering and mechanosynthesis and show that mechanosynthesis enables to obtain optimal ceramics with compositions ranging from $x=0$ to $x=0.60$.

A.2 EXPERIMENTAL PROCEDURE

A.2.1 Solid-State reaction

Commercial-grade oxides PbO (Interchim), Yb_2O_3 (Rhône-Poulenc), Nb_2O_5 and TiO_2 (both Alfa Aesar) with purity greater than 99.5% were used as starting materials. Raw materials were mixed in absolute purity ethanol and subsequently dried in air at 80 °C for 24 h before calcination.

The wolframite YbNbO_4 was first formed by calcining Yb_2O_3 and Nb_2O_5 at 1,200 °C for 4h. To obtain the solid solution PYN-PT, two solid state synthesis routes were envisaged: one in which the two perovskites end-members are mixed as proposed in Ref.[19, 46] hereafter called PYN+PT and a more conventional one in which the wolframite is mixed with PbO and TiO_2 hereafter called $\text{PbO}+\text{YbNbO}_4+\text{TiO}_2$. The mixed raw oxides obtained using the two methods were calcined together of a range of temperatures (800 °C - 1,000 °C) and times (2-12 h) to get the pure perovskite phase. As a prior state for the preparation of the PYN+PT mixture, the synthesis of the two end-members of the solid solution was necessary. The two mixtures of PbO and YbNbO_4 , on the one hand, and PbO and TiO_2 , on the other hand, were calcined at 850 °C for 3.5 h. The comparison of the powder X-ray pattern recorded on our powders with the JCPDS 06-0452 file for PT and with Ref.[44] for PYN attests to the formation of the perovskite phases.

The addition of a binder appeared necessary to shape the powders into green pellets, i.e. flat cylinder of compacted powder before sintering. Because of their different advantages, two types of binders were considered: an organic one (PVA) and an inorganic one PbO . On one hand, PVA deteriorates at low temperature, and residues can be eliminated by a short thermal treatment at a temperature lower than the sintering one. Hence the ceramics obtained after sintering should not have any extra phases. On the other hand, PbO is commonly used as a binder since it does not introduce any new chemical element in the ceramic and since the excess lead can compensate for the possible loss during the sintering process. The green pellets were sintered at 900 °C for 4 h.

A.2.2 Mechanosynthesis

This method, also known as ball-milling synthesis, enables the formation of a pure perovskite phase at room temperature using mechanical activation. We used a Retsch mill PM 100 specially equipped for mechanical alloying. The pure perovskite phase was obtained after a 9 h ball-milling at 450 rpm of the stoichiometric mixture of PbO , YbNbO_4 and TiO_2 using the wolframite route.

In contrast to the powder obtained from the solid state route, the powder obtained by mechano-synthesis did not require the addition of binder to be pressed into pellets, most probably due to the small grain size that enables a better compaction.

A.2.3 Reactive sintering

Reactive sintering enables preparing ceramic samples without the prior preparation of powder with the targeted composition. The mixture of raw oxides is directly shaped into green pellets without prior calcination. Only, the mixture $\text{PbO}+\text{YbNbO}_4+\text{TiO}_2$ appeared to be possible to shape into green pellets because of the presence of PbO as raw oxide playing the role of reactant and binder. Finally, one thermal treatment enables the chemical reaction and the sintering to take place.

A.2.4 Characterization methods

Powder X-ray diffraction ($\text{Cu K}_{\alpha 1,2}$) on a Bruker D2 phaser was used to check the crystallinity and the purity of the powders and ceramics. The presence of the perovskite of phase in the PYN-PT ceramics has been ascertained by comparing the powder X-ray patterns with the one reported in Ref.[46, 47]. Scanning Electron Microscopy (SEM) associated with Energy Dispersive X-ray (EDX) analysis (Leo Gemini 1530) have been conducted on fractured samples to investigate the microstructure and purity of the phase. The average grain size was obtained using the line intersection method on SEM images [122]. The relative density was measured using geometrical dimension or the Archimedes' method whenever the relative density was high enough to provide higher precision. Dielectric measurements were carried out using an Agilent 4294A impedance analyzer, on the ceramics sputtered with gold electrodes from 80 K to 800 K in the 1 kHz to 1MHz range at an applied AC voltage of 200mV.

A.3 RESULTS AND DISCUSSION

A.3.1 Chemical reaction mechanism

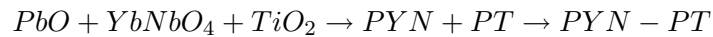
In order to determine the reaction mechanism leading to PYN-PT solid solution, we compared the two solid-state reaction routes at the same calcination stage (900 °C for 4 h) on the basis of the presence of perovskite phase, remaining reactants, and of other phases. Fig.A.1(a-b) shows the powder X-ray patterns after calcination of the powders obtained respectively by mixing PYN+PT and $\text{PbO}+\text{YbNbO}_4+\text{TiO}_2$. On both diagrams the PYN-PT perovskite phase is present as well as a few extra reflections lines indicating the presence of an impurity phase, most probably a pyrochlore. In addition, for the the $\text{PbO}+\text{YbNbO}_4+\text{TiO}_2$ route, the two end-members also appear (see Fig.A.1(b)). Since no reactants are present after this calcination step, it can be inferred that, starting from the $\text{PbO}+\text{YbNbO}_4+\text{TiO}_2$ mixture the chemical reaction to form the PYN-PT solid solution takes place in two steps: first, the two end-members are

formed; then they react together to form the solid solution.

Hence, starting from the $\text{PbO}+\text{YbNbO}_4+\text{TiO}_2$ or from the PYN+PT mixture should eventually lead to the same results. To confirm this hypothesis, the $\text{PbO}+\text{YbNbO}_4+\text{TiO}_2$ powder was further calcined at 900 °C for 2 h. The powder X-ray pattern of the corresponding powder is plotted in Fig.A.1(c) and is indeed extremely similar to the PYN+PT one (Fig.A.1(a)) in that the reflections related to the end-members have disappeared, confirming the two-step chemical reaction.

Earlier works [123–125] have demonstrated for other $\text{Pb}(\text{B},\text{B}')\text{O}_3$ and $\text{Pb}(\text{B},\text{B}')\text{O}_3\text{-PbTiO}_3$ solid solution materials that even using the wolframite (or columbite) method (that is the one analogous to mixing $\text{PbO}+\text{YbNbO}_4+\text{TiO}_2$) the raw oxides react first to form a pyrochlore phase at rather low temperature ($\sim 600\text{--}700$ °C) and that this pyrochlore phase reacts in a second step with the remaining reactants to form the desired perovskite structure.

In the case of PYN-PT, the reaction mechanism of the $\text{PbO}+\text{YbNbO}_4+\text{TiO}_2$ route appears to be more complicated: the two end-members of the solid solution (namely PYN and PT) are formed first, presumably through the formation of a pyrochlore, and then the two end-members react to form the desired perovskite phase:



However, extra peaks are present in Fig.A.1(b) and (c), most probably corresponding to a pyrochlore phase, indicating an incomplete synthesis. A pure perovskite phase was obtained with optimized calcination parameters (800 °C for 12 h). The corresponding powder X-ray pattern (Fig.A.1(d)) shows no impurity phase.

A.3.2 Influence of powder processing method on dielectric properties

As mentioned above, binders proved to be necessary to shape the powders obtained by solid state reaction into green pellets. As alternatives, reactive sintering and mechanosynthesis were also considered. The influence of different powder processing on the relative density, dielectric constant, and purity of ceramics was studied. As a first step, the presence of only the perovskite phase in the powder used to form the green pellets was checked with X-ray diffraction. It was shown above that it is possible to optimize the calcination parameters to form a powder with a pure perovskite phase using the solid-state method. As for the powder obtained by mechanosynthesis, it presents exclusively the perovskite structure of the solid solution and is composed of highly strained nanograins as can be deduced from the wide asymmetrical peaks in Fig.A.1(e).

Fig.A.2 shows the powder X-ray patterns measured on PYN-PT 0.6 ceramics obtained by the solid state route with addition of binders: PVA (Fig.A.2(a)), PbO (Fig.A.2(b,c)) as well as by reactive sintering (Fig.A.2(d)) and by mechanosynthesis (Fig.A.2(e)).

It reveals that for all methods, no additional phases is formed during sintering. However, using PbO as a binder leads to additional PbO reflections whose intensity increases with the addition of PbO. Such presence of PbO after sintering indicates that the PbO loss during the sintering is lower than what was added for binding, i.e. lower than 1 wt%. On the contrary, there are no impurity peaks for the ceramic obtained from the solid-state powder with PVA

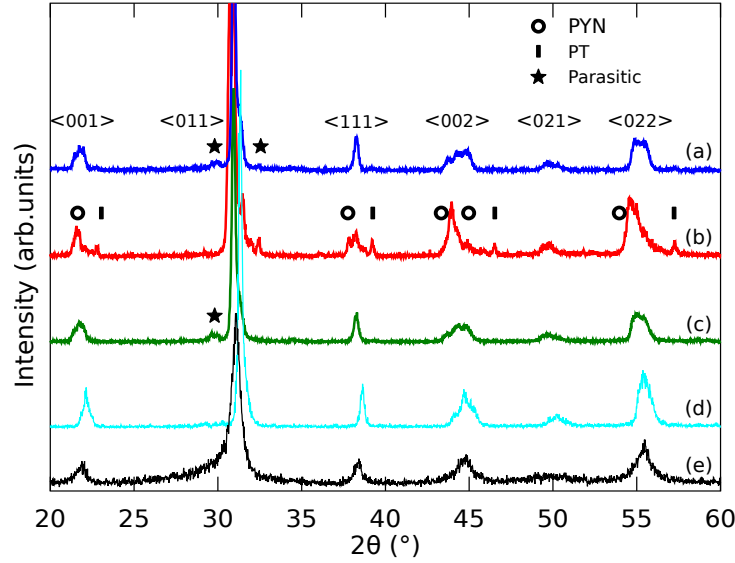


Figure A.1: Powder X-ray patterns of PYN-PT 0.5 powder obtained through different synthesis : (a) PYN+PT mixture and (b) $\text{PbO}+\text{YbNbO}_4+\text{TiO}_2$ after (900 °C for 4 h). Adding a second calcination step to the later gives (c), evidencing the two-step synthesis process. A pure PYN-PT product (d) is obtained with optimized calcination parameters. The diagram (e) is obtained by mechanosynthesis and indicates a highly strained perovskite nanopowder. Miller indices for the pseudo cubic cell.

as binder. Moreover, SEM images and EDX analysis confirm, within the detection limit, the absence of residues in this ceramic. Furthermore SEM images establish that grains have the same morphology in all ceramics regardless of the processing method of the powder.

On the other hand the processing method has a dramatic influence on the relative density (Table A.1) and the dielectric constant (Fig.A.3). The ceramic prepared from the powder formed by mechanosynthesis presents the highest relative density and dielectric constant. Conversely, the lowest relative density and dielectric constant were obtained for the ceramic reactively sintered.

Interestingly, for the samples prepared by the solid state route with addition of binder, the dielectric constant is not directly linked to the relative density. The maximal dielectric constant increases with the relative density except for the sample with 3 wt% addition of PbO as binder for which the dielectric constant is the lowest. In this sample, due to the large amount of extra PbO , the PbO contribution to the dielectric constant can no longer be neglected. Since PbO has a low dielectric constant (~ 20), the overall measured dielectric constant measured is lowered by the excess of PbO .

Additionally, the Curie temperature of the ceramic processed from the mechanosynthesized powder is slightly lower. This lowering is probably not caused by the grain size since ceramics prepared from mechanosynthesis have grain size ($\sim 1\mu\text{m}$) comparable to the ones obtained with the other routes ($5\text{-}10\mu\text{m}$). Another possibility is that the difference in the Curie temperature is due to different strain states inside the ceramics as reported in Ref.[126] or to a deficit in

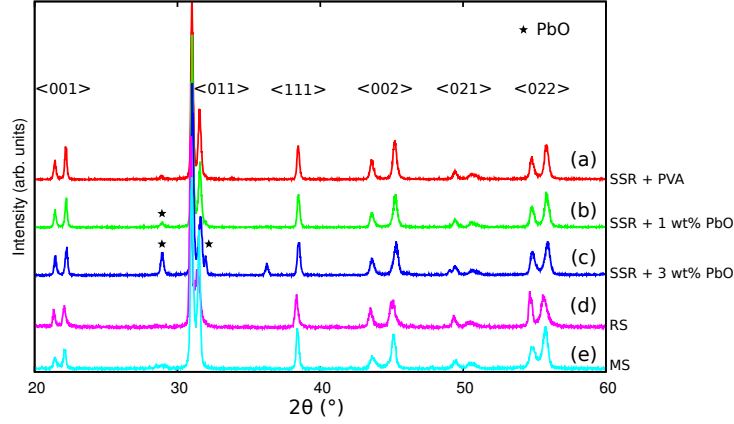


Figure A.2: Powder X-ray patterns of PYN-PT 0.6 ceramics obtained from different processing methods. Ceramics prepared by the solid state route (SSR) with PVA (a), 1 wt% (b) and 3 wt% (c) PbO as binders. The PbO reflections are marked with a filled star. Powder X-ray patterns of ceramics obtained by reactive sintering (RS, d) and mechanosynthesis (MS, e).

Processing method	relative density (d)	ϵ'	ϵ'/d
Reactive sintering	0.60	181	302
+PVA	0.81	528	652
+1.3wt% PbO	0.72	555	771
+3wt% PbO	0.86	524	613
Mechanosynthesis	0.91	867	953

Table A.1: Comparison of the relative density (d), dielectric constant (ϵ') at room temperature and the dielectric constant normalize by relative density (ϵ'/d).

Pb. Finally, it appears that the mechanosynthesis intrinsically drives the enhancement of the dielectric properties. A plausible explanation for this enhancement is that the grain size is large enough to *not* suffer from size effect[118] and nevertheless not too large to enables the density to be close to its maximum. This will be discussed in the following section.

A.3.3 Influence of microstructure and grain size on dielectric properties

As we have seen that the largest dielectric properties are obtained for ceramics obtained from powder processed by mechanosynthesis. We shall therefore restrict our study to ceramics obtained by mechanosynthesis and study the influence of the microstructure and especially the grain size on the crystallographic structure and dielectric properties, by varying the sintering conditions (800-1,000 °C and 2-6 h).

The purity and phase of the ceramics obtained under various sintering conditions were checked by X-ray diffraction (Fig.A.4). The ceramic sintered at 800 °C for 4 h is not perfectly crystallized as can be seen from the larger peaks compared to the other ceramics. For higher

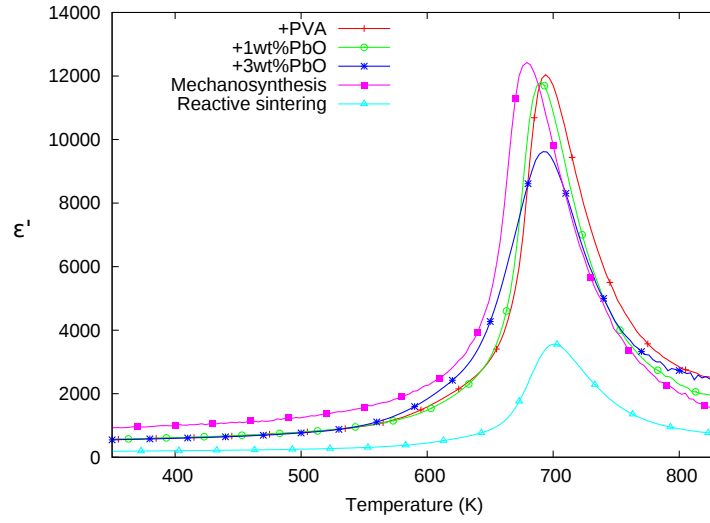


Figure A.3: Dielectric constant at 1 kHz as a function of temperature for PYN-PT 0.6 ceramics obtained from different processing methods.

sintering temperature, the sample are perfectly crystalline, but some impurity peaks (marked with a star on Fig.A.4) appear for long sintering time (6 h). The powder X-ray pattern of ceramic sintered at 1,000 °C for 4 h shows a different intensity ratio of the main peaks suggesting a strong texturing in the ceramic compared to the other samples.

SEM imaging (Fig.A.5) illustrates that the various sintering conditions lead to ceramics with comparable grain morphology. As expected, with increasing sintering temperature and time, the grain size increases and the number and size of porosity decrease (Fig.A.6).

The evolution of the dielectric constant with the sintering parameters (Fig.A.7) shows that the dielectric constant at the Curie point increases with the relative density of the ceramic, underlying the important link between relative density and dielectric response of a ceramic.

Furthermore, it is interesting to note that ceramics with similar relative density (1,000°C - 4 h and 900 °C - 6 h) display strongly different dielectric properties due to a different grain size. The ceramic sintered at lower temperature has smaller grains, and it has been shown in Ref.[117, 118] that the dielectric constant diminishes with the grain size for grain size smaller than $\sim 1 \mu\text{m}$.

Ceramics with various compositions through the phase diagram of PYN-PT were obtained using the same parameters for mechanosynthesis. The sintering conditions were optimized for each composition as described in the previous section. For all compositions, ceramics with relative density larger than 90% and pure perovskite phase (Fig.A.8) were obtained. The corresponding crystallographic structures and dielectric properties enabling the construction of a phase diagram are being investigated and shall be reported elsewhere.

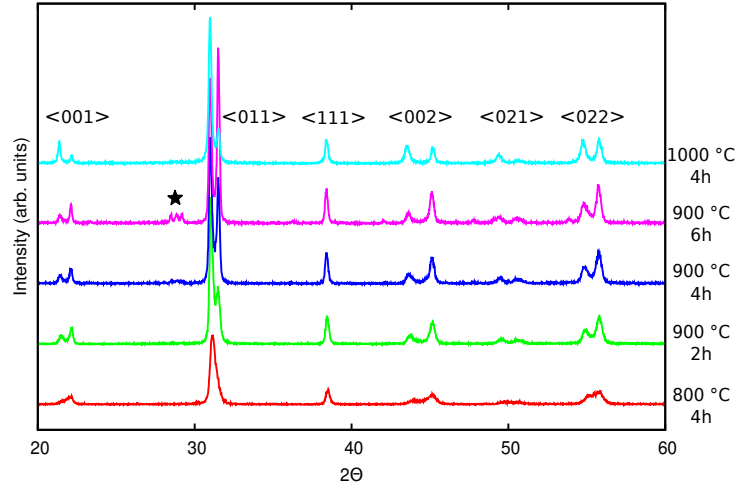


Figure A.4: Powder X-ray patterns for different sintering conditions of PYN-PT 0.6 ceramics. The starting powder was obtained by mechanosynthesis. Sintering at 1,000 °C for 4h induces a strong texturing evidenced by the change intensity ratio for the (00l) peaks.

A.4 CONCLUSION

PYN-PT ceramics have been synthesized with $x = 0$ to 0.60 using several synthesis routes including solid state reaction, reactive sintering and mechanosynthesis. Highly dense ceramics with pure perovskite phase and large dielectric properties were obtained processing powder by mechanosynthesis. The increase of the dielectric properties were found to be associated with increase in relative density and grain size. The chemical reaction mechanism for PYN-PT is more complicated than what was reported for other complex perovskites: the two end-members of the solid solution form first and then react to produce the final product. Moreover, we have shown that the mechanosynthesis can be used to successfully produce a pure perovskite phase confirming that this method is a good alternative to high pressure synthesis for processing perovskites with low tolerance factors [126].

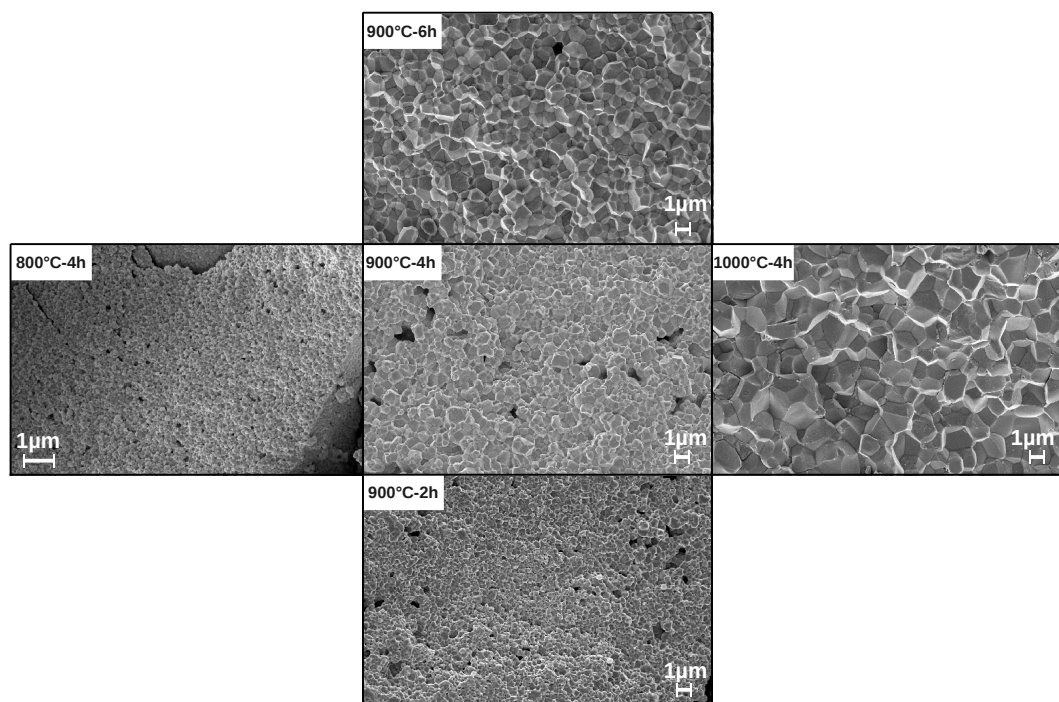


Figure A.5: SEM images obtained for PYN-PT 0.6 ceramics sintered at different temperature and different time. The corresponding relative densities and grain sizes are reported in Fig.A.6. The corresponding dielectric constant are reported in Fig.A.7

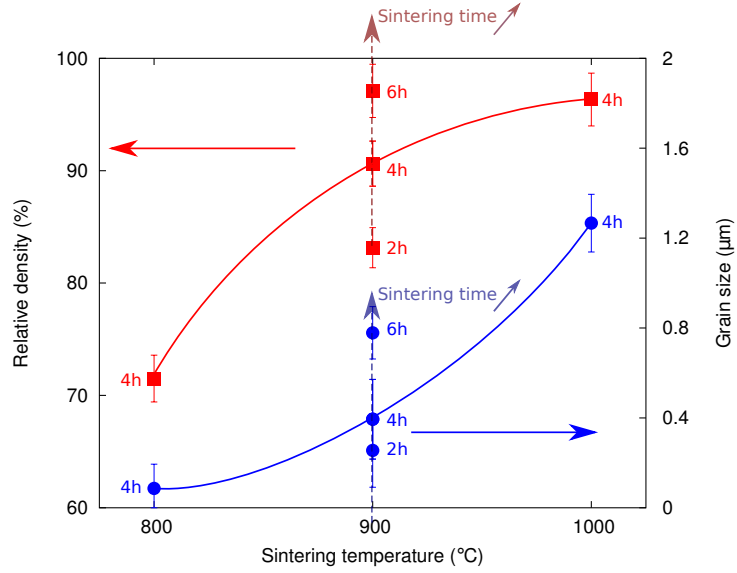


Figure A.6: Relative density and grain size for PYN-PT 0.6 ceramics sintered at different temperature and time from powder obtained by mechanosynthesis. Increasing the sintering temperature while the duration is kept constant (4 h, full line) or increasing time at constant temperature (900 °C, interrupted line) result in a increase of both the relative density and the grain size.

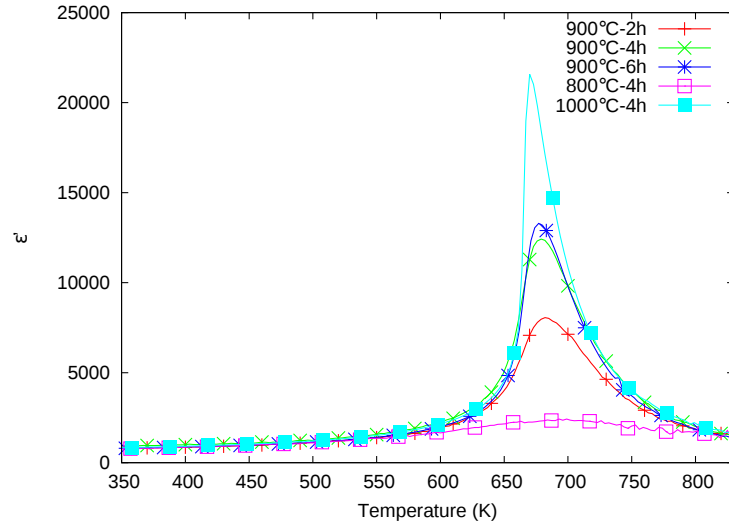


Figure A.7: Evolution of the dielectric constant for the different sintering parameters for PYN-PT 0.6 ceramics obtained from mechanosynthesis.

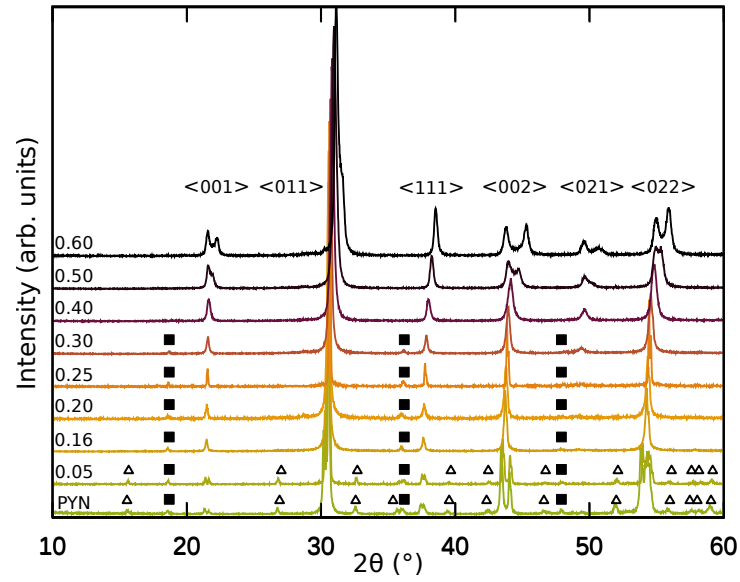


Figure A.8: Powder X-ray patterns of the ceramic with various composition with $x=0-0.60$. The full squares indicate the superstructure reflections due to B-site cation ordering. The open triangle the superstructure due to antiparallel Pb^{2+} displacements.

- APPENDIX B -

CALCULATION OF THE DERIVATIVE OF THE INVERSE OF THE DIELECTRIC CONSTANT: $\xi = \frac{\partial(1/\varepsilon')}{\partial T}$

To plot the derivative of a data with gnuplot, one can use “inline” data manipulation offered in Gnuplot 4.4. The derivative is calculated by taking the slope between the active data point and the previous data point (reading the file from top to bottom) as follow

```
y0=NaN; x0=NaN  
plot 'FILE_NAME' u 1:(dx=$1-x0, dy=$2-y0, x0=$1, y0=$2, dy/dx) w lp
```

In this case, the slope is simply the ratio between the two differences **dx** and **dy** that represent each the difference in *x* and *y* coordinates between the current data point and the previous data points. Each difference (**dx** and **dy**) is calculated by subtracting the active value (**\$1** and **\$2**) to the value of the previous line (**x0** and **y0**). Then the saved value is updated to the current value to be used in the calculation of the slope of the next data point.

More advanced methods could be used to evaluate the value of the derivative by taking for example the derivative at the data point *n* could be evaluated by taking slope between the data points *n* + 1 and *n* − 1 with *n*.

Other softwares such as Scilab or Igor have internal derivative procedure that might also be more appropriate to the calculation of derivative.

In the case of the evaluation of $\xi = \frac{\partial \varepsilon}{\partial T}$, the derivative calculated using the procedure described above appeared to be sufficient and did not lead to an important signal/noise ratio.

- APPENDIX C -

REFINED PARAMETERS FOR COMPOSITIONS IN THE RANGE
 $0.40 \leq x \leq 0.60$

Table C.1: Refined structural parameters

The refinements on neutron diffraction data, except for PYN-PT 0.45 for which X-ray data are refined (marked with *)

Refined parameter	0.40 <i>Pm/Cm</i>	0.45* <i>P4mm/Cm</i> <i>P4mm/Pm</i>	0.50 <i>P4mm/Cm</i> <i>P4mm/Pm</i>	0.60 <i>P4mm/Pm</i>
<i>Pm</i>				
Percentage	0.15	0.47	0.85	0.39
<i>a</i> (Å)	4.102(6)	4.0871(3)	4.052(3)	4.037(2)
<i>b</i> (Å)	4.081(4)	4.0994 (4)	4.111(1)	4.009(2)
<i>c</i> (Å)	4.116(5)	4.0938 (5)	4.063 (2)	4.109(2)
<i>beta</i> (°)	90.33 (5)	90.21(1)	90.1(1)	90.1(1)
Pb <i>x y z</i>	0	0	0	0
O1 <i>x</i>	0.565(21)	0.61(18)	0.52(14)	0.55(5)
O1 <i>y</i>	0	0	0	0
O1 <i>z</i>	0.428(7)	0.40(24)	0.45(7)	0.443(21)
O2 <i>x</i>	0.528(21)	0.58(21)	0.022(24)	0.551(14)
O2 <i>y</i>	0.5	0.5	0.5	0.5
O2 <i>z</i>	0.05(2)	0.11(20)	0.442(25)	0.06(5)
O3 <i>x</i>	0.073(17)	0.06(7)	0.513(4)	0.042(17)
O3 <i>y</i>	0.5	0.5	0.5	0.5
O3 <i>z</i>	0.46(3)	0.41(8)	0.051(18)	0.383(7)
Yb/Nb/Ti <i>x</i>	0.550(4)	0.5293(12)	0.545(4)	0.539(7)
Yb/Nb/Ti <i>y</i>	0.5	0.5	0.5	0.5
Yb/Nb/Ti <i>z</i>	0.461(9)	0.4392(12)	0.433(2)	0.437(7)
Pb <i>B_{iso}</i> (Å ²)	2.0(9)	2.70(32)	2.3(4)	3.4(6)
O <i>B_{iso}</i> (Å ²)	0.4 (9)	1(1)	3.4(5)	1.9(9)
Yb/Nb/Ti <i>B_{iso}</i> (Å ²)	0.10(4)	0.35(21)	0.24(7)	0.12(7)

Table C.1: (Continued) Refined structural parameters

The refinements on neutron diffraction data, except for PYN-PT 0.45 for which X-ray data are refined (marked with *)

Refined parameter	0.40 <i>Pm/Cm</i>	0.45* <i>P4mm/Cm</i> <i>P4mm/Pm</i>		0.50 <i>P4mm/Cm</i> <i>P4mm/Pm</i>		0.60 <i>P4mm/Pm</i>
<i>Cm</i>						
Percentage	0.85	0.42		0.35		
<i>a</i> (Å)	5.8018(8)	5.7873(5)		5.763(2)		
<i>b</i> (Å)	5.7879(6)	5.7736(6)		5.751(3)		
<i>c</i> (Å)	4.1052(5)	4.0927(3)		4.098(1)		
<i>beta</i> (°)	90.151(2)	90.264(8)		90.36(3)		
Pb <i>x y z</i>	0	0		0		
O1 <i>x</i>	0.443(3)	0.44(4)		0.410(4)		
O1 <i>y</i>	0	0		0		
O1 <i>z</i>	0.032(4)	0.06(4)		0.066(4)		
O2 <i>x</i>	0.237(5)	0.18(2)		0.21(1)		
O2 <i>y</i>	0.252(2)	0.24(2)		0.247(3)		
O2 <i>z</i>	0.466(4)	0.56(3)		0.497(4)		
Yb/Nb/Ti <i>x</i>	0.472(2)	0.4513(3)		0.457(4)		
Yb/Nb/Ti <i>y</i>	0	0		0		
Yb/Nb/Ti <i>z</i>	0.513(2)	0.5241(4)		0.517(4)		
Pb <i>B_{iso}</i> (Å ²)	3.7(7)	2.3(3)		3.7(6)		
O <i>B_{iso}</i> (Å ²)	1.3(2)	0.12(8)		0.9 (3)		
Yb/Nb/Ti <i>B_{iso}</i> (Å ²)	0.58(14)	0.38(4)		0.23(12)		
<i>P4mm</i>						
Percentage		0.58	0.53	0.65	0.15	0.61
<i>a</i> (Å)		4.0832(4)	4.0892(9)	4.0522(4)	4.067(4)	4.0131(3)
<i>c</i> (Å)		4.0970(6)	4.0915(9)	4.1227(8)	4.120(7)	4.1459(5)
Pb <i>x y z</i>		0	0	0	0	0
O1 <i>x</i>		0.5	0.5	0.5	0.5	0.5
O1 <i>y</i>		0	0	0	0	0
O1 <i>z</i>		0.43(3)	0.46(5)	0.470(3)	0.42(9)	0.465(2)
O2 <i>x y</i>		0.5	0.5	0.5	0.5	0.5
O2 <i>z</i>		0.03(12)	0.10(6)	0.078(3)	0.11(5)	0.092(2)
Yb/Nb/Ti <i>x y</i>		0.5	0.5	0.5	0.5	0.5
Yb/Nb/Ti <i>z</i>		0.522(14)	0.5609(7)	0.5355(11)	0.591(15)	0.5310(10)
Pb <i>B_{iso}</i> (Å ²)		3.8(3)	3.7(4)	3.3(3)	2.3(3)	2.2(2)
O <i>B_{iso}</i> (Å ²)		3.7(9)	2.2(9)	1.6(6)	3.3 (9)	1.1(4)
Yb/Nb/Ti <i>B_{iso}</i> (Å ²)		0.74(7)	0.45(5)	0.33(3)	0.24(4)	0.22(3)